NATIONAL UNIVERSITY OF IRELAND MAYNOOTH

Motion Artifact Processing Techniques for Physiological Signals

by

Kevin Sweeney

A thesis submitted in partial fulfillment for the
degree of Doctor of Philosophy

in the
Faculty of Science and Engineering
Department of Electronic Engineering

April 2013

Declaration of Authorship

I, Kevin Sweeney, declare that this thesis titled, 'Motion Artifact Processing Techniques for Physiological Signals' and the work presented in it are my own. I confirm that:

- This work was done wholly or mainly while in candidature for a research degree at this University.
- Where any part of this thesis has previously been submitted for a degree or any other qualification at this University or any other institution, this has been clearly stated.
- Where I have consulted the published work of others, this is always clearly attributed.
- Where I have quoted from the work of others, the source is always given. With the exception of such quotations, this thesis is entirely my own work.
- I have acknowledged all main sources of help.
- Where the thesis is based on work done by myself jointly with others, I have made clear exactly what was done by others and what I have contributed myself.

Signed: _____

Date: _____

"A journey of a thousand miles begins with a single step."

Lao Tzu

Abstract

The combination of reducing birth rate and increasing life expectancy continues to drive the demographic shift toward an ageing population and this is placing an ever-increasing burden on our healthcare systems. The urgent need to address this so called healthcare "time bomb" has led to a rapid growth in research into ubiquitous, pervasive and distributed healthcare technologies where recent advances in signal acquisition, data storage and communication are helping such systems become a reality. However, similar to recordings performed in the hospital environment, artifacts continue to be a major issue for these systems. The magnitude and frequency of artifacts can vary significantly depending on the recording environment with one of the major contributions due to the motion of the subject or the recording transducer. As such, this thesis addresses the challenges of the removal of this motion artifact removal from various physiological signals.

The preliminary investigations focus on artifact identification and the tagging of physiological signals streams with measures of signal quality. A new method for quantifying signal quality is developed based on the use of inexpensive accelerometers which facilitates the appropriate use of artifact processing methods as needed. These artifact processing methods are thoroughly examined as part of a comprehensive review of the most commonly applicable methods. This review forms the basis for the comparative studies subsequently presented. Then, a simple but novel experimental methodology for the comparison of artifact processing techniques is proposed, designed and tested for algorithm evaluation. The method is demonstrated to be highly effective for the type of artifact challenges common in a connected health setting, particularly those concerned with brain activity monitoring. This research primarily focuses on applying the techniques to functional near infrared spectroscopy (fNIRS) and electroencephalography (EEG) data due to their high susceptibility to contamination by subject motion related artifact.

Using the novel experimental methodology, complemented with simulated data, a comprehensive comparison of a range of artifact processing methods is conducted, allowing the identification of the set of the best performing methods. A novel artifact removal technique is also developed, namely ensemble empirical mode decomposition with canonical correlation analysis (EEMD-CCA), which provides the best results when applied on fNIRS data under particular conditions. Four of the best performing techniques were then tested on real ambulatory EEG data contaminated with movement artifacts comparable to those observed during in-home monitoring.

It was determined that when analysing EEG data, the Wiener filter is consistently the best performing artifact removal technique. However, when employing the fNIRS data, the best technique depends on a number of factors including: 1) the availability of a reference signal and 2) whether or not the form of the artifact is known. It is envisaged that the use of physiological signal monitoring for patient healthcare will grow significantly over the next number of decades and it is hoped that this thesis will aid in the progression and development of artifact removal techniques capable of supporting this growth.

Acknowledgements

First and foremost, I would like to express my sincerest thanks to my two supervisors Dr Tomás Ward and Dr Seán McLoone for their constant direction and support throughout my PhD. Their approachability, enthusiasm and in-depth knowledge in the area have made the overall experience a very enjoyable one.

I would also like to express my gratitude to all the members of staff in the Electronic Engineering Department in Maynooth for generating a atmosphere in which work, and fun, came easily. In particular I would like to thank John Maloco and Denis Buckley for their technical help throughout the research and Joanne Bredin and Ann Dempsey for always being at the end of the phone/email when needed. Thanks to all the postgrads in the department for the company throughout the four years, particularly Anthea, Aodhan, Darren, Francesco, Giogio, Niall, Shane B and Violeta. Particular thanks are due to Dr Hasan Ayaz, Dr Meltem Izzetoglu and Prof. Banu Onaral, and all in Drexel university who were kind enough to share both their knowledge and their offices with me. This research would not have started without the support from the Irish Research Council for Science, Engineering and Technology, so again I give my thanks.

I would like to thank my parents, Kevin and Cecelia, who have been unwavering in their love, not only during this PhD, but throughout my life. I could not have completed this work without your help. To my sisters, Ciara and Siobhán, your support has always meant the world to me. I thank you for looking after your "student brother" more than you might have had to. Thanks to all of the great friends I have had throughout my time in Maynooth both during undergrad and postgrad. To Graham, Leanne, Shelley and Sinead, thank you for being great housemates (even after I left). To Annie, Kate and all the girls in Biology, thanks for the constant cups of tea and chats! A special thanks to Ian Hatch and Mark Creevey who have been some of my closest friends for the last 24 years! Long may it continue.

Finally I would like to thank Ciarán Pollard, Damian Kelly, Helen O'Dowd, Lorcan Walsh and Shane Lynn for being the best housemates and friends a person could ask for. Each of you have made my time here some of the best in my life; thank you.

Contents

List of Figures

List of Tables

Abbreviations

ADC	**A**nalog to **D**igital **C**onverter
AMR	**A**nistropic **M**agneto**R**esistive
ANSI	**A**merican **N**ational **S**tandards **I**nstitute
APD	**A**valanche **P**hoto-**D**iode
AR	**A**uto**R**egressive
ATrou	Fast Dyadic Wavelet Transform (“*algorithme à trous*”)
BCI	**B**rain **C**omputer **I**terface
BOLD	**B**lood **O**xygenation **L**evel **D**ependent
BSS	**B**lind **S**ource **S**eparation
BV	**B**lood **V**olume
CCA	**C**anonical **C**orrelation **A**nalysis
CMS	**C**ommon **M**ode **S**ource
CWT	**C**ontinuous **W**avelet **T**ransform
DC	**D**irect **C**urrent
DCT	**D**iscrete **C**osine **T**ransform
DE	**D**ynamical **E**mbedding
DFT	**D**iscrete **F**ourier **T**ransform
DRL	**D**riven **R**ight **L**eg
DST	**D**iscrete **S**ine **T**ransform
DWT	**D**iscrete **W**avelet **T**ransform
ECG	**E**lectro**C**ardio**G**raphy
EEG	**E**lectro**E**ncephalo**G**raphy
EEMD	**E**nsemble **E**mpirical **M**ode **D**ecomposition
EKF	**E**xtended **K**alman **F**ilter
EMG	**E**lectro**M**yo**G**raphy
EMI	**E**lectro**M**agnetic **I**nterference
EOG	**E**lectro**O**culo**G**raphy
FIR	**F**inite **I**mpulse **R**esponse
FFT	**F**ast **F**ourier **T**ransform
fNIRS	**f**unctional **N**ear-**I**nfra**R**ed **S**pectroscopy

GDP	**G**ross **D**omestic **P**roduct
GTC	**G**round **T**ruth **C**omponent
Hb	**H**emoglo**b**in - deoxygenated
HbO	**H**emoglo**b**in - **O**xygenated
HOS	**H**igher **O**rder **S**tatistics
ICT	**I**nformation and **C**ommunications **T**echnology
IC	**I**ndependent **C**omponent
ICA	**I**ndependent **C**omponent **A**nalysis
IMF	**I**ntrinsic **M**ode **F**unction
IRV	**I**ndependent **R**andom **V**ariables
LDCT	**L**ocal **D**iscrete **C**osine **T**ransform
LDSCT	**L**ocal **D**iscrete **S**ine **C**osine **T**ransform
LED	**L**ight **E**mitting **D**iode
LMAV	**L**east **M**ean **A**bsolute **V**alue
LMS	**L**east **M**ean **S**quare
LTI	**L**inear **T**ime **I**nvariant
LWP	**L**ocal **W**avelet **P**acket
MA	**M**oving **A**verage
MBLL	**M**odified **B**eer **L**ambert **L**aw
MCA	**M**orphological **C**omponent **A**nalysis
MCR	**M**iss**C**lassification **R**ate
MDL	**M**inimum **D**escription **L**ength
MEG	**M**agneto**E**ncephalo**G**raphy
MMSE	**M**inimum **M**ean **S**quare **E**rror
NLMS	**N**ormalised LMS
NN	**N**eural **N**etwork
OD	**O**ptical **D**ensity
PCA	**P**rinciple **C**omponent **A**nalysis
POX	**P**ulse **OX**imetry
PPG	**P**hoto**P**lethysmo**G**raphy
PSD	**P**ower **S**pectral **D**ensity
QOS	**Q**uality **O**f **S**ignal
RF	**R**adio **F**requency
RLS	**R**ecursive **L**east **S**quare
RRMSE	**R**elative **R**oot **M**ean **S**quare **E**rror
SCICA	**S**ingle **C**hannel-ICA
SD	**S**tandard **D**eviation
SNR	**S**ignal to **N**oise **R**atio
SOS	**S**econd **O**rder **S**tatistics

SSA	**S**ingular **S**pectrum **A**nalysis
STFT	**S**hort **T**ime **F**ourier **T**ransform
TDL	**T**ap **D**elay **L**ine
TMS	**T**ranscranial **M**agnetic **S**timulation
TUG	**T**imed **U**p and **G**o
USB	**U**niversal **S**erial **B**us
WHO	**W**orld **H**ealth **O**rganisation
WICA	**W**avelet-ICA
WSS	**W**ide **S**ense **S**tationary

Dedicated to my parents, Kevin and Cecelia; without their unwavering love and encouragement, this document would not exist.

Chapter 1

Introduction

The worlds population has been steadily increasing and is set to continue to do so over the next number of decades. The current estimated population of the world is over 7 billion [143], however this figure is expected to reach anywhere between 9 and 10.5 billion by 2050 [142] [139]. In addition to the increasing number of people, the average life span around the world is also rising and is set to do so over the next forty years [126]. It is expected that the proportion of the world's population over 60 years of age will double from about 11% to 22%, from 605 million to 2 billion over the same period [140]. The *Old Age Dependency Ratio*, which is the ratio of the number of people over 65 to the number of working age adults, is therefore expected to increase dramatically from 25.9 % in 2010 to 52.6 % in 2060 in Europe and from 16.8 % to 36.7 % in Ireland [189].

This ageing of the population demographic will inevitably lead to a rise in the number of people living with chronic illnesses such as cardiovascular diseases, diabetes, cancer, epilepsy and respiratory diseases. Chronic diseases are long-lasting conditions that can be controlled but are not currently curable. Chronic illnesses affect the population worldwide. As highlighted by the Center for Disease Control in the U.S., chronic disease is the leading cause of death and disability in the United States. It accounts for 70 % of all deaths in the U.S., which is 1.7 million each year [105]. Data from the World Health Organisation (WHO) show that chronic disease is also the major cause of premature death around the world even in places where infectious disease are rampant [148].

The combined increases in both the worlds population and the ageing demographic will place further stress on already stretched healthcare systems. Since the 1960s, expenditure on national healthcare has grown faster than the gross domestic product (GDP) in most EU member states. A study conducted by the Ministry of Health and Social Affairs in Sweden found that the expenditure has risen from an average of 3.1 % in 1960

to 8.8 % in 2006 [63]. In the U.S., healthcare costs were eight times higher in 2008 than in 1980 and accounted for 16.2 % of the national GDP [144]. Additionally, due to the rise in the *Old Age Dependency Ratio*, there will be proportionally less people contributing tax for government expenditure in the future. The increase in national healthcare expenditure is unsustainable and, as a result, a more cost-effective delivery of health services is imperative.

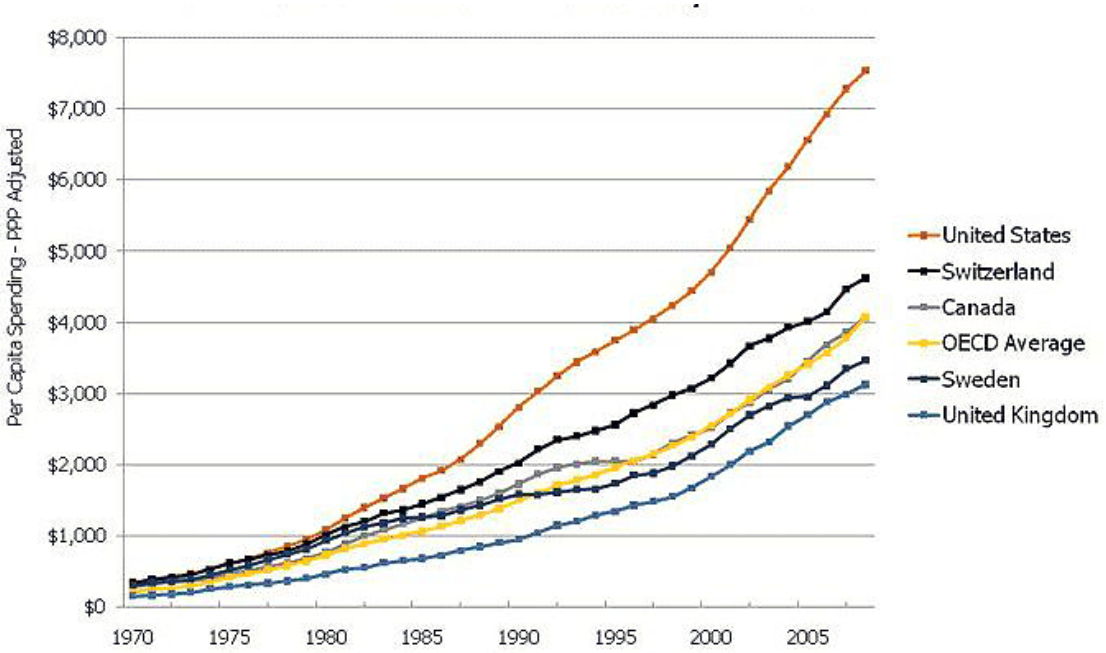

FIGURE 1.1: Growth in healthcare expenditures over the last 40 years. Source: [56]

Recent advances in information and communications technology (ICT) have allowed for the generation of cheaper and more widely available monitoring systems and have enabled many clinic-based examinations to be performed using connected-health in a community-clinic or personal healthcare (p-health) domain. Connected health is a model for healthcare delivery that uses technology to provide healthcare remotely. Connected health is becoming increasingly utilised due to the advent of smart phones, tablets etc. [18]. Connected health is primarily used in the areas of cognitive monitoring, behavioural monitoring, activity recognition and cardiology. This ability to monitor the patient outside of the hospital environment can greatly improve quality of life, while out-patient care can cost as little as 50 % of in-patient counterparts, thus making them a more feasible option in many instances [198]. However despite the recent advances in monitoring systems, the presence of undesired artifacts on the desired physiological signals is still a significant area of concern and thus further advances in the area of signal processing are required in order to allow for the recording of clean useful clinical data.

1.1 Objective

During recording of the various physiological signals, both within and outside of the hospital environment, contamination of the desired signals due to artifacts is a constant problem. Artifacts are defined as being any unwanted variations in a signal caused by an external source. These unwanted variations can manifest themselves in a number of different forms depending on the source of the artifact. For example, Figure 1.2 illustrates the difference between clean, clinically recorded, EEG data and data recorded while the subject was in motion. It can be observed that the presence of these artifacts seriously contaminates the recorded physiological signals. Artifacts contaminate signals recorded in all domains, however their presence is more difficult to prevent outside of the hospital environment. Due to its *ad hoc* nature, motion artifact can often be the most difficult artifact to remove whilst also commonly having the largest detrimental affect on the desired signal. Therefore, there is a considerable need for automated algorithms capable of detecting and removing these artifacts from the desired true signals.

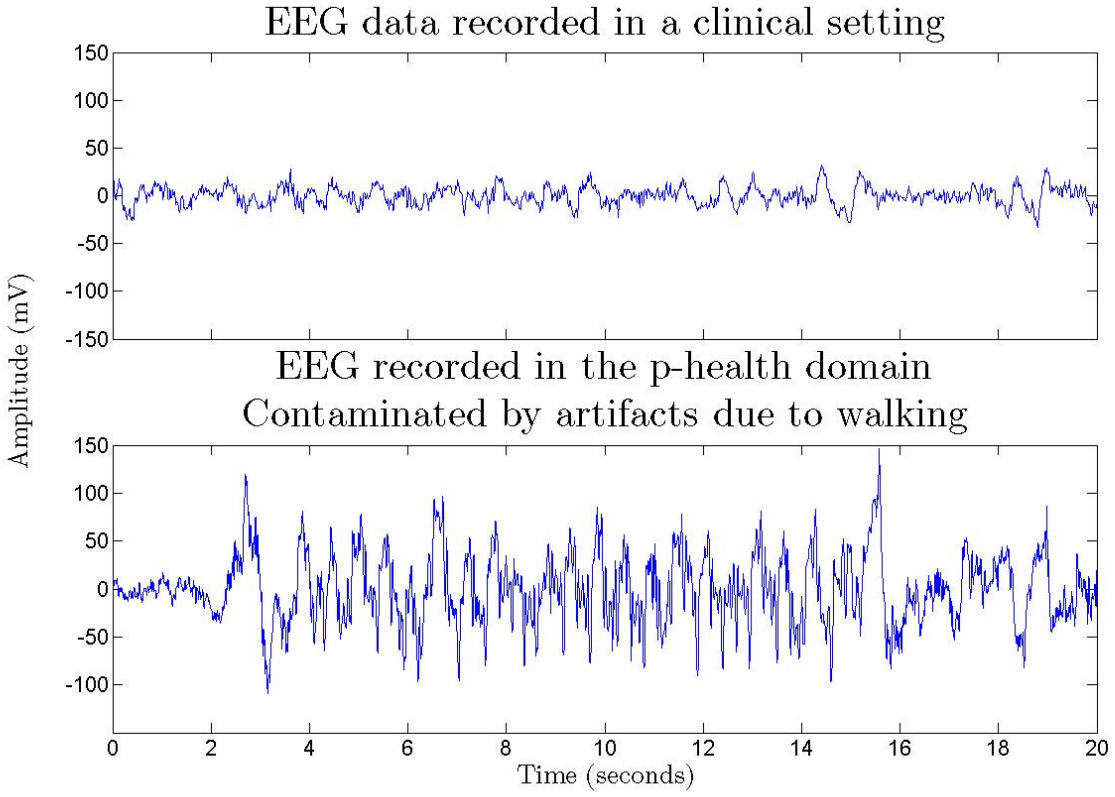

FIGURE 1.2: Contaminating effect of artifacts on recorded EEG signals. In the lower figure, the subject began walking after 5 seconds. Data recorded using EEG system described in Section 4.1.2.

The objective of this thesis is to analyse novel and existing artifact removal techniques and validate the efficacy of each algorithm. The thesis focuses on the artifacts

arising from subject motion using both the electroencephalography (EEG) and the functional near-infrared spectroscopy (fNIRS) signal modalities.

1.2 Contributions of the Thesis

This thesis aims to analyse both novel and existing artifact removal techniques to determine the best techniques to employ in given situations and environments. In its entirety, this thesis has produced a number of contributions which are described below.

1. A comprehensive literature review of the state of the art in artifact removal techniques utilised in physiological signal analysis is presented. The review consists of a short description of the operation of each of the selected techniques, example results obtained using the algorithms on different signal modalities as well as any comparisons completed between the different algorithms.

2. To allow for an accurate evaluation and comparison between the analysed techniques, a novel recording methodology was developed. This methodology, presented to record either electroencephalography (EEG) or functional near-infrared spectroscopy (fNIRS) data, permits the recording of two separate but highly correlated channels, allowing for the recording of an artifact-contaminated and an artifact-free signal concurrently. Using the two available signals, accurate measurements of an artifact removal technique's efficacy can be determined.

3. A novel tagging algorithm is presented which employs dual accelerometers to generate a quality-of-signal (QOS) metric. This QOS metric can be used for a number of different purposes:

   (a) To inform a technician as to the epochs of contaminated data within a signal.

   (b) Classification of motion artifact types, permitting the use of the correct artifact removal technique for each specific corrupting artifact.

   (c) To permit the activation of artifact removal techniques. This switching of the technique allows the algorithms to be used solely when required, thus improving their efficacy.

4. A novel artifact removal technique is presented which combines the decomposition method of the ensemble empirical mode decomposition (EEMD) algorithm with the source separation canonical correlation analysis (CCA) technique. The use of this combination allows for the CCA algorithm to be employed on recordings with a lower number of channel recordings than underlying sources. This method

is shown to have improved performance over all existing similar techniques when employed on fNIRS data.

5. A detailed evaluation and comparison of the most commonly implemented artifact removal techniques is presented using both simulated data and data collected using the novel recording methodology. The efficacy of the techniques is measured by the change in signal-to-noise ratio (SNR) and the change in correlation between the contaminated signal and the available "ground truth" signal.

6. A comparison between two previously implemented artifact component selection techniques is presented. A number of tested artifact removal techniques are only able to separate the signal and the artifact into source components. The selection of the components relating to artifacts is a current area of research. The use of the autocorrelation function and the Hurst exponents are both tested and the best technique for use with the EEG and fNIRS data identified.

7. A case study is presented which employs a number of the best artifact removal techniques determined in the thesis on real ambulatory recorded EEG data. This novel recorded dataset is contaminated with artifacts ranging from those due to simple head movements, to artifacts present due to the subject running on a treadmill. The efficacy of the removal techniques is evaluated on their ability to remove or reduce the contaminating effect.

8. The benchmark datasets collected to test the efficacy of the various artifact removal techniques, namely the fNIRS and EEG data recorded using the novel methodology and the EEG data recorded during the case study, have been made available online. This contribution provides a valuable resource for future artifact removal research.

1.3 List of Publications

A list of the publications produced from the thesis is presented below. A further description of each paper is provided in Appendix A.

1. Sweeney, K.T. Ward, T.E. and McLoone, S.F., "The use of empirical mode decomposition with canonical correlation analysis as a novel artifact removal technique", *IEEE Transactions on Biomedical Engineering, (Accepted)*, 2012.

2. Sweeney, K.T. Ayaz, H. Ward, T.E. Izzetoglu, M. McLoone, S.F. and Onaral, B., "A methodology for validating artifact removal techniques for physiological brain

signals", *IEEE Transactions on Information Technology in Biomedicine*, vol. 16, no. 5, pp 918-926, Sept., 2012.

3. Sweeney, K.T. Ward, T.E. and McLoone, S.F., "Artifact Removal in Physiological Signals -Practices and Possibilities", *IEEE Transactions on Information Technology in Biomedicine*, vol. 16, no. 3, pp 488-500, May, 2012.

4. Sweeney, K.T. Ayaz, H. Ward, T.E. Izzetoglu, M. McLoone, S.F. and Onaral, B., "A Methodology for Validating Artifact Removal Techniques for fNIRS", *In proceedings of the IEEE Engineering in Medicine and Biology Society (EMBC)*, pp 4943-4946, Sept., 2011.

5. Sweeney, K.T. Kelly, D. Ward, T.E. and McLoone, S.F., "A Review of the State of the Art in Artifact Removal Technologies as used in an Assisted Living Domain", *IET Conference on Assisted Living*, pp 1-6, April, 2011.

6. Sweeney, K.T. Leamy, D.J. and Ward, T.E. and McLoone, S.F., "Intelligent artifact classification for ambulatory physiological signals", *In proceedings of the IEEE Engineering in Medicine and Biology Society (EMBC)*, pp 6349-6352, Sept., 2010.

7. Sweeney, K.T. Ward, T.E. and McLoone, S.F., "A simple bio-signals quality measure for in-home monitoring", *In proceedings of the 7th IASTED International Conference*, Feb., 2010.

1.4 Outline of the Thesis

This thesis is comprised of seven subsequent chapters, the content of which is described below.

Chapter 2 provides a background to the physiological signals that are most commonly measured for clinical purposes. These signals are separated into two groups: Photoplethysmography (PPG) and electrocardiography (ECG) signals which monitor the cardiovascular system, and EEG, fNIRS and electromyography (EMG) which monitor the central and peripheral nervous systems. A description of each of the signal modalities and their utility in diagnosis, health and wellness is provided in the chapter. Additionally, the chapter presents a description of the artifact modalities which can affect recorded physiological signals.

Chapter 3 presents a comprehensive review of the current research into artifact removal methods which are frequently employed in the biomedical field. A description of

each of the techniques is provided as well as any comparisons between techniques presented in the literature. The review separates the techniques into two groups, namely single stage and two stage algorithms. Single stage algorithms can directly remove the artifact signal from the desired signal of interest while two stage algorithms decompose the signal and artifact into individual sources but require additional techniques to identify the artifact components and facilitate their removal.

Chapter 4 outlines the various methods used to analyse the artifact removal techniques described in the thesis. A novel recording methodology is proposed which allows for the concurrent recording of two channels of either EEG or fNIRS data with one channel contaminated with artifacts while the second channel remains artifact-free. The benefit of the recording methodology is that the two channels of recorded data are highly correlated. Therefore the artifact-free signal acts as a "ground truth" signal from which the efficacy of the various artifact removal techniques can be evaluated. This chapter also details a number of techniques used to aid in the selection of artifact components for the two stage techniques outlined in Chapter 3. The chapter concludes by describing the generation of simulated data that is used to test the efficacy of the analysed artifact removal techniques.

Chapter 5 begins by documenting a novel tagging algorithm which is used to provide a QOS metric. The QOS metric can be used to inform a trained clinician as to the location of the artifact components in a signal, to determine which artifact removal technique should be employed (depending on the artifact) or to permit the switching of the artifact removal techniques thus allowing them to be used only when required. The chapter continues by providing a detailed evaluation of four of the single stage artifact removal techniques described in Chapter 3. These techniques are compared, using both the simulated data and the real EEG and fNIRS datasets, and the best techniques to use for motion artifact removal are presented.

Chapter 6 continues on from Chapter 5 by reporting on the evaluation of a number of novel and existing two stage artifact removal techniques. The operation of the techniques and their determined efficacy are again presented and compared with the other two stage techniques as well as the single stage techniques presented in Chapter 5. The chapter also analyses a number of the artifact selection techniques presented in Chapter 4. A comparison of results is presented and the best technique to employ for both EEG and fNIRS is determined.

Chapter 7 concludes the analysis of the artifact removal techniques by employing four of the best algorithms determined from the previous two chapters on ambulatory recorded EEG data. This EEG data is recorded using a mobile EEG system while the

subject performed a number of described tasks. Each task represents a normal daily movement that could be performed by patients in a p-health environment, providing a realistic dataset for examination.

Chapter 8 concludes the thesis by providing a summary of the novel contributions of the thesis and discussing possible further avenues of research arising from the work performed for this thesis.

Chapter 2

Physiological Background

Physiological signal monitoring has long been an important and widely implemented form of patient observation and supervision. As stated previously recent advances in ICT have allowed some of the monitoring systems to be employed outside of the hospital environment. There are a number of advantages of this shift; for the patient it represents a reduction in healthcare costs and a greater quality of life as more time can be spent in the comfort of their own home while also alleviating the burden on healthcare professionals, the health care system and caregivers. This chapter provides a background introduction into a number of the different physiological signals monitored both within and outside of the hospital environment as well as their utility in diagnosis, health and wellness. These measurements include ECG/PPG and POX, which are used to monitor the cardiovascular health of a patient, EEG and fNIRS, which measure the function of the neural system and EMG which records the electrical activity produced by skeletal muscles. The origin and form of these signals, their diagnostic value and the methods employed to monitor them are described.

The chapter also presents a description of the different artifact modalities that can affect all recorded physiological signals. These modalities include environmental artifacts, experimental error as well as artifacts arising from the concurrent recording of undesired physiological signals. The origin of the different forms of artifacts are detailed as well as their contrasting contaminating effect on the different available recording modalities.

2.1 Circulatory System

The circulatory system is a collection of organs whose purpose is the transport of the required gases, nutrients and blood etc. around the body to the demanding cells. These

transported compounds are then used to maintain the daily operation of the body by fighting diseases, stabilising the body temperature and pH and to maintain homeostasis. The cardiovascular system, which distributes the blood around the body, is a closed loop system implying that the blood never leaves the network of veins, arteries and capillaries, although other substances such as nutrients, and gases do.

The main organ of the cardiovascular system is the heart. This muscle is designed to pump the required gases and nutrients around the cardiovascular system to the required cells. The heart is divided into four main chambers, namely the right and left Atrium and the right and left Ventricle (see Figure 2.1). The Atria are used to store the blood returning from the body or lungs and the Ventricles are used to pump the blood from the heart [172].

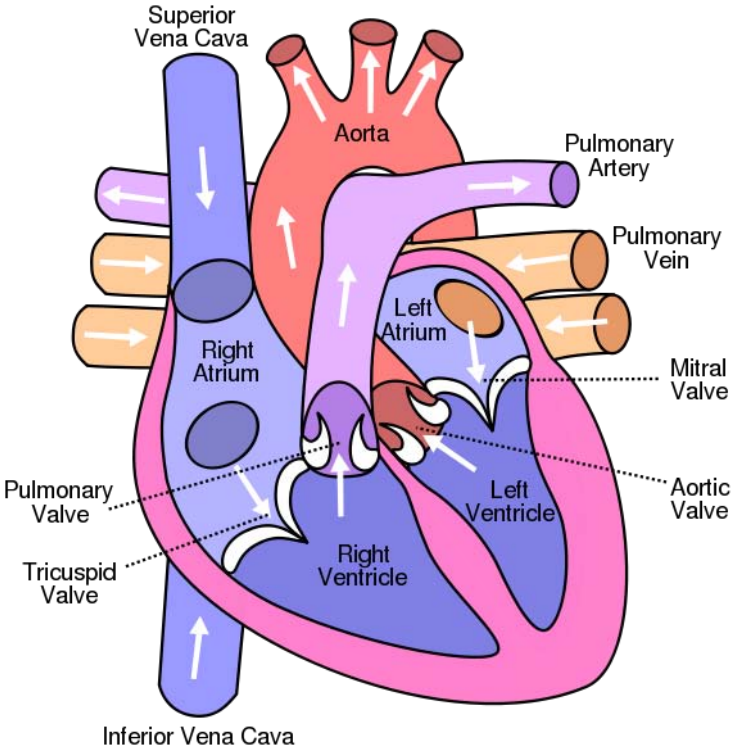

FIGURE 2.1: Diagram of the human heart.

Monitoring of the heart, or the cardiovascular system in general, is therefore extremely important. In addition to the obvious complications with a problematic heart (including angina, heart attacks or cardiac arrest), improper blood circulation can also reduce the bodies capability to rid the body of its wastes, weaken the ability maintain a constant body temperature and increases the possibility of infectious diseases [67].

Three methods often employed to monitor the cardiovascular system are described below. Photoplethysmography (PPG) and pulse oximetry (POX) monitor the volumetric

change and haemoglobin concentration of the blood while electrocardiography (ECG) monitors the electrical activity of the heart.

2.1.1 Photoplethysmography (PPG)

Photoplethysmography (PPG) is the optically obtained volumetric measurement of an organ. In conventional PPG the system monitors the changes in blood volume from a position on the body and is usually obtained from transmissive absorption (as in the finger tip or ear) but can also be obtained reflectively (as on the forehead). During each cardiac cycle (contraction/relaxation) the heart pumps blood to the periphery. Each contraction sends a wave of oxygenated blood into the arteries. This wave can then be recorded using the PPG at any position on the body which has a detectable pulse. The shape of the PPG waveform can vary depending on the subject and also in the manner and location where the sensor is attached. Figure 2.2 presents an example of a PPG recorded from a finger when the hand is held at two different positions. It can be observed that the pulse rate of the heart can be easily determined from the recordings. The PPG signal is slow varying compared to some other physiological signals and has a frequency range of between 0.04 Hz and 0.6 Hz [128].

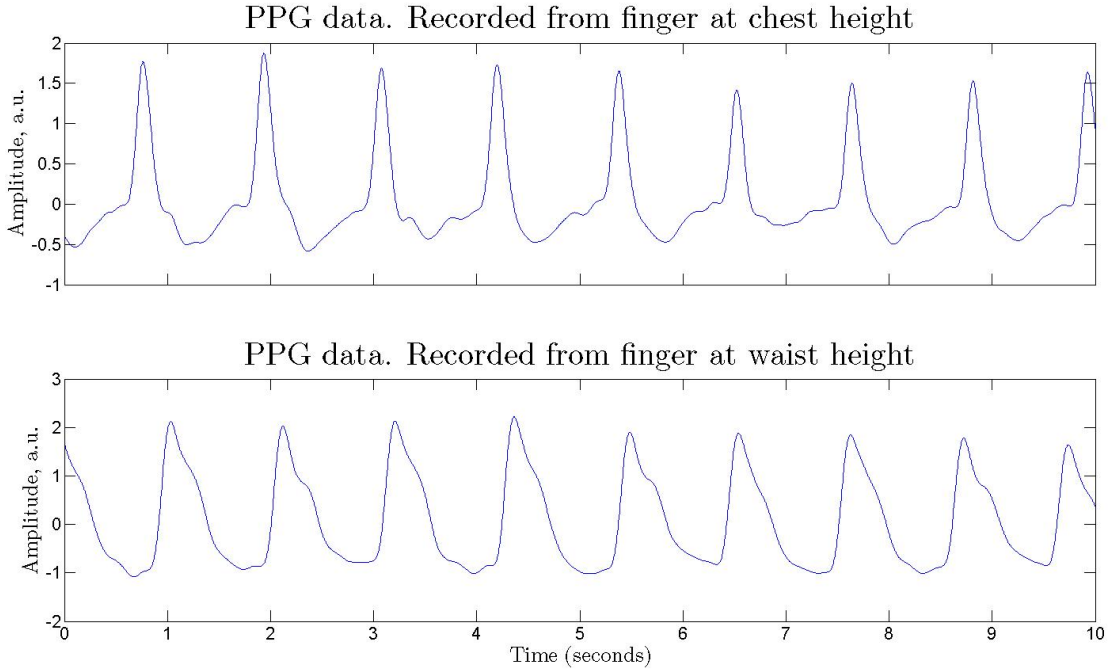

FIGURE 2.2: Examples of Photoplethysmography (PPG) output. Top plot presents an example where the recording was taken from the middle finger with the hand supported at chest height. The lower plot represents a recording from the same finger with the hand relaxed by the waist. Signals recorded using the BioSemi system (Section 4.1.2) with the PPG adaption.

A PPG sensor consists of a light source, which can take the form of a light emitting diode (LED) or a laser, and a detector (photodiode). Although laser sources have been used by a multitude of researchers [116], LEDs are still predominantly used [204][199]. Laser sources can pose a safety risk due to the possibility of interaction with the users retina or cornea where the lasers can cause thermal damage, or burning, if sustained for a period of time [10]. As the LED sources do not have the same safety issues, they are most often employed in the clinical setting where inaccurate patient usage can often lead to misuse of systems.

The source transmits light, at two different wavelengths, into the tissue to be studied and the detector determines the changes in blood volume over time, inferred from the change in light intensity received [168]. This is typically determined using the modified Beer-Lambert law (MBLL) which states

$$a = log_{10}\left(\frac{i_0}{i}\right), \tag{2.1}$$

where a is the absorption of the blood, i_0 is the incident light intensity and i is the transmitted intensity. The MBLL can then be utilised to calculate the relative change in concentration levels of oxy and deoxy-hemoglobin using the following formula [41]:

$$\Delta a = (\alpha_{HbO}\Delta C_{HbO} + \alpha_{Hb}\Delta C_{Hb})\, LB, \tag{2.2}$$

where Δa is the change in absorption, α_{HbO} and α_{Hb} are the specific extinction coefficients of oxy-hemoglobin and deoxy-hemoglobin respectively. These extinction coefficients describe the levels of absorption of light for certain media at predefined wavelengths. C_{HbO} and C_{Hb} are the concentration levels for oxy-hemoglobin and deoxy-hemoglobin respectively, L is the distance between the source and detector optodes and B (constant) is the differential path-length factor. Using the concentration levels (C_{HbO} and C_{Hb}) the volumetric variations can be determined.

Figure 2.3 shows how the absorption spectra of both the HbO and Hb compounds changes with varying incident light wavelength. As the two compounds have independent spectra, by recording the light absorption at two wavelengths spectroscopic separation of the chromophore concentrations is possible. Throughout recording there are a number of absorption factors that remain relatively constant including the absorption levels of the skin, tissue and venous blood. The absorption level of the arterial blood changes however with the rhythmic pulsing of the cardiac cycle. If the absorption of the incident light is detected separately at both the trough (which should include all the constant absorbers)

and crest of the pulse, then the difference in these absorption levels is equivalent to the absorption of the added blood volume only. This is called pulse oximetry (POX).

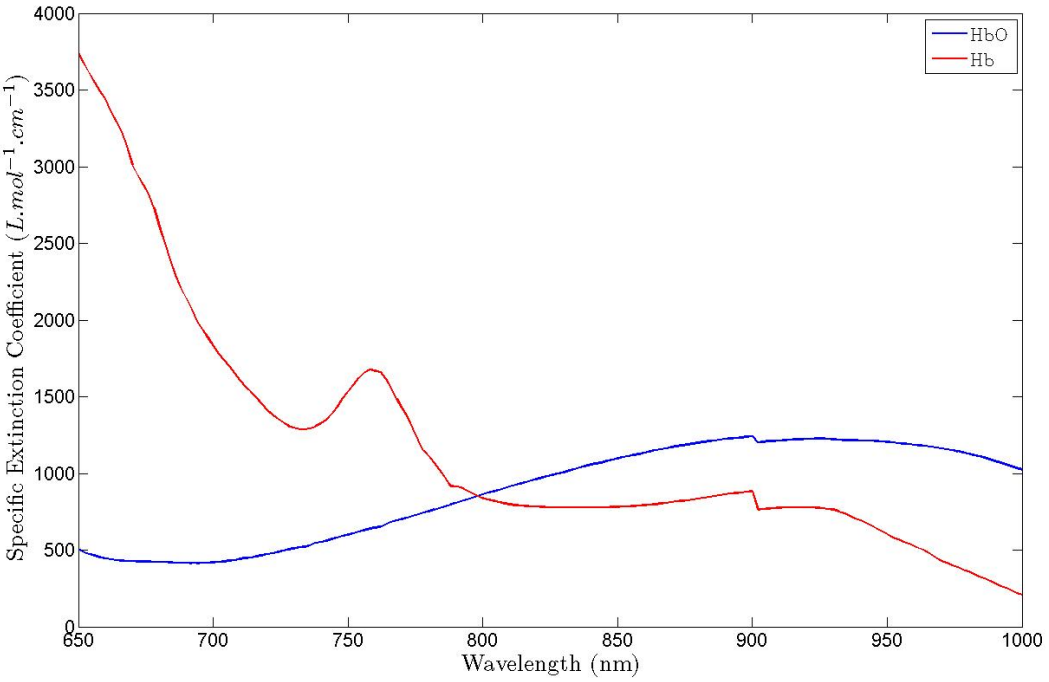

FIGURE 2.3: Absorption spectra for oxy-haemoglobin (HbO) and deoxy-haemoglobin (Hb). Values taken from [164] and [134].

Pulse Oximetry (POX) uses the PPG wave form, as stated above, to create an indicator of arterial oxygen saturation (SpO_2). This quantity responds rapidly to hypoxemic events and is very simple to interpret [150]. It is often used in situations where there is a need to monitor a patients oxygenation levels, as in intensive care, critical care, and emergency department areas of a hospital, but can also be utilised in a p-health environment to supervise recovery after heart problems or to aid the diagnosis of some sleep disorders such as apnea and hypopnoea [27]. The PPG waveform is often used as a heart rate and cardiac cycle monitor due to its ease of use in comparison to other techniques such as ECG. The application of the PPG monitor simply requires the connection to a finger or ear lobe and thus error due to poor patient usage is not a major concern. PPG can also be used for monitoring respiration due to the respiratory systems effect on the pressure placed on the heart during inhalation and exhalation as described by Shelley *et al.* [167].

Due to the relatively inexpensive nature of the systems, this measurement is increasingly utilised in a p-health environment. A more sophisticated variation of PPG

is functional near-infrared spectroscopy (fNIRS) which uses the same principles as the PPG to measure the changing oxygen levels in the brain and is described in Section 2.2.2.

2.1.2 Electrocardiography (ECG)

Electrocardiography (ECG) is a transthoracic measurement of the electrical activity of the heart recorded externally by skin electrodes. As the heart muscles contract and expand (for the purpose of pumping the oxygenated and deoxygenated blood around the circulatory system and to the lungs respectively) they generate a small voltage difference that can be measured non-invasively across the chest.

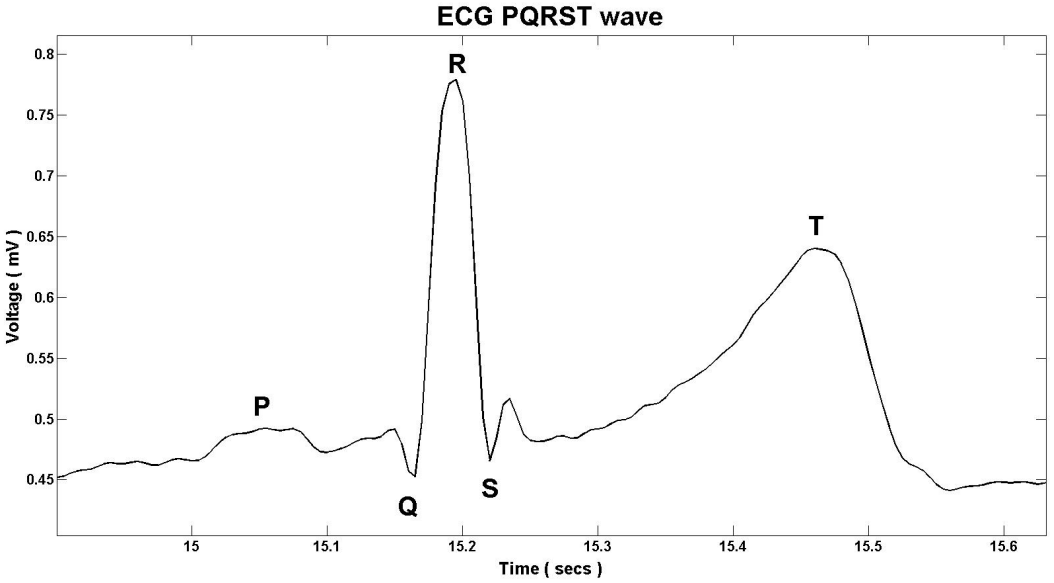

FIGURE 2.4: Example P QRS and T wave for ECG.

A typical ECG recording consists of P, QRS and T waves, each a consequence of the independent contraction or expansion stages of the cardiac cycle. Figure 2.4 presents an example epoch of an ECG recording. The P wave can be directly related to the spread of changes in electrical activity through the atrial musculature of the heart. This wave has a duration of not more than 0.11 seconds and should be gently rounded in shape. The QRS wave is the most dominant complex in the ECG recording as it represents the spread of the electrical impulse through the ventricular muscle which pumps the blood around the periphery [82]. This complex is usually around 0.05-0.12 seconds in duration and its amplitude is greater than the P or T waves and varies depending on the recording location but is commonly not larger than 2.5-3.0 mV. The T wave then represents the recovery of the ventricles and usually lasts around 0.16 seconds. Again the amplitude is dependent on the location of the recording electrodes but is usually

around 0.2 mV. The interval between consecutive waves is known as the RR interval and is dependent on a number of different parameters including the sex, fitness and health of the patient, however normal durations range from 0.6 to 1.2 seconds. The frequency range of a normal ECG signal is 0.1 - 250 Hz however 1 ms accuracy heart rate detection is obtainable at a 0.5-35 Hz frequency range [75]. The wider frequency range is required if arrhythmia detection is required.

ECG signals are obtained through the amplification of the tiny electrical changes associated with cardiac activity via electrodes applied to the skin. ECG instrumentation usually consists of a 3, 5 or 12 lead setup depending on the scenario and duration of the recording. In the p-health domain, 3 and 5 lead setups are most common as a 12 lead system is more complicated to structure. The systems employed for monitoring outside of a clinical environment primarily use adhesive active electrodes [207] to detect the voltage changes. Active electrodes have a high input impedance preamplifier placed very close to the skin which reduces the susceptibility of the system to power-line interference and cable motion artifacts, thus improving signal quality. Also no preparation of the skin, such as skin abrasion, is required prior to adhesion when using active electrodes. The use of highly conductive electrode gel placed between the electrode and the skin also aids in the securing of low noise data, however this can often degrade over long term use. This limits the number of complications which can arise from recording the physiological signals outside of the hospital environment.

The ECG recording is one of the most predominantly employed monitoring systems utilised by clinicians due to the variety of ailments which can be detected. Any variation of the signal from the model ECG signal morphology can inform a trained technician as to the presence of a large number of different disorders. As an example, the detection of low-level, alternating changes in T wave amplitude, is established as an indicator of increased risk for sudden, life threatening arrhythmias [170]. Arrhythmias often arise within a limited time span and occur quite infrequently thus are not often detected during routine ECG examination due to the conventional short measurement time. Therefore longer ECG measurements during a patients normal activity are required to diagnose arrhythmias and to determine the effectiveness of treatment [102], giving merit to in-home measurements. The detection of atrial fibrillation and flutter after acute stroke also calls for prolonged measurements of the ECG signal [89]. These are just a few of the many ailments where the use of the p-health systems can, and do, aid in the monitoring of a patients health and increase the likelihood of a correct diagnosis.

2.2 The Nervous System

The nervous system is an organ system which contains a network of neurons and other cells which are used to control the functions of the body. The organ system contains all the parts required for the human body to interact with the outside world including the brain, spinal cord, and the nerves. The brain and spinal cord are part of the central nervous system which controls the activity of the human body. The nerves outside of the brain and spinal cord form the peripheral nervous system.

The brain is the driving force behind the nervous system with the other elements used to send/receive and channel the information. Therefore, accurate recordings of the function of the brain can inform a great deal of information regarding the workings of the body. The signals transmitted to and from the brain are electrochemical in nature and so signal monitoring in the form of electroencephalography (EEG) can be employed. These recordings operate in a similar manner to the ECG recordings described above in that EEG records the small changes in voltage that can be detected over the scalp. However, as the brain also requires oxygen to function, the change in blood oxygenation throughout the various cortical regions can also divulge information as to the functions currently being executed.

The non-invasive measurement of brain activity outside a clinical setting is difficult, and the only two practical methods available are electroencephalography (EEG) and to a lesser extent functional near-infrared spectroscopy (fNIRS). The function of the peripheral nervous system can be monitored using a technique known as electromyography (EMG). The next section describes these measurements at a level appropriate for the applications described in this thesis.

2.2.1 Electroencephalography (EEG)

Electroencephalography (EEG) is the recording of electrical activity along the scalp, produced by the firing of neurons within the brain [141]. When neurons in the brain need to communicate with their neighbours they do so by discrete electrochemical signals called action potentials. These individual action potentials are however too small to be detected. The detected EEG activity is therefore always a reflection of the sum of the synchronous activity of the thousands or millions of neurons that are orientated in a similar spatial manner. The EEG signal also usually reflects the processes taking place at positions close to the surface of the brain. Activity from sources deep in the brain are more difficult to detect than sources in closer proximity to the skull as the potential fields fall off with the square of the distance from the source [99].

The amplitude of the EEG recorded data can vary between subjects however a typical adult human EEG signal is about 10 to 100 μV in amplitude when measured from the scalp [7] and is about 10 to 20 mV when measured from subdural electrodes as described below. The analysis of the EEG data is most commonly focused on the low frequency ranges however the frequency can range from 0 to 100+ Hz. The EEG signal is normally broken down into a number of frequency bands during analysis as shown in Table 2.1.

TABLE 2.1: Frequency bands of signal recorded by electroencephalography (EEG).

Name	Frequency Band	Predominantly Observed
Delta	Up to 4 Hz	Adult slow wave sleep In babies
Theta	4 to 8 Hz	Young children Drowsiness in adults
Alpha	8 to 13 Hz	Resting in adults Eyes closed
Beta	13 to 30 Hz	Alert/Working Active concentration
Gamma	30 to 100+ Hz	Multisensory semantic matching Perceptual functions

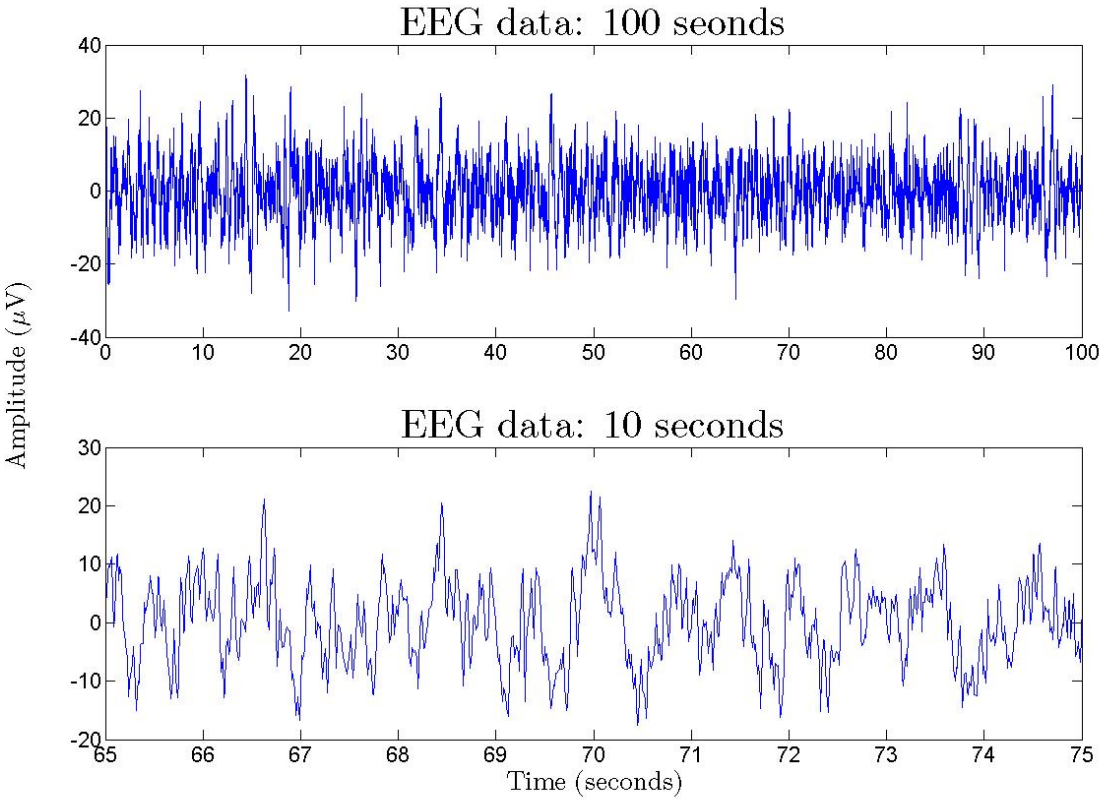

FIGURE 2.5: Example of EEG recorded data shown over a 100 second and 10 second epoch. Data recorded using the system described in Section4.1.2.

The EEG signal can be recorded in two ways; either non-invasively, with the electrodes secured to the scalp with conductive gel, or invasively with the subdural, or depth electrodes placed on the surface or within the substance of the brain respectively [159]. The invasive technique produces results with less noise and higher amplitude than the noninvasive technique, however it is a far more complicated manner in which to record the EEG data. The contrast in information content between the two recording methods is due to the path that the signal must pass through before being measured. The invasive method measures the signals directly from the surface of the brain, whereas the signals recorded by the non invasive method must pass through the dura matter, the cerebrospinal fluid, the skull bone and the skin of the scalp (also possibly the hair on the scalp) before it reaches the scalp electrode [4]. This additional path length distorts the recorded signal due to the differing volume conduction effects [190] and the low pass filter effect of the skull [70]. However, for the p-health domain, non-invasive EEG data acquisition is the only viable option available.

EEG recording systems used outside of the clinical setting generally employ a relatively low number of electrodes (< 8), due to the limitations of the available power of the system. These electrodes are active electrodes, similar to those used for the ECG recording. An example of an ambulatory recording system commonly used is the Starstim® (Neuroelectrics, Barcelona, Spain) system which allows for 8 channels of EEG recordings. Recordings acquired using this system can be seen in Chapter 7 where a number of the best performing algorithms analysed in this thesis are tested on real ambulatory EEG data.

EEG has a wide range of applications in modern medicine. One of the most common uses is in the area of epilepsy [169]. Epileptic activity can be very difficult to measure due to the (sometimes) uncertainty in the occurrence of events. Therefore long term monitoring is often employed to increase the probability of detection. This long term monitoring can cause discomfort to the patient who must remain in a motion free state for a extended period of time. The recording of the EEG signals in an in-home, p-health, domain can increase the users level of comfort and allow for longer recording durations while still recording the data to a satisfactory level of quality. Advances in data reduction techniques have also aided in the reduction in the quantity of recorded data being stored [33], [32] and have therefore facilitated longer recordings. The EEG setup is more complicated than some other recording techniques, requiring the user to be given some basic training in its configuration before implementation. Other uses of EEG include the detection of sleep/drowsiness levels [16], [15], [149], cognitive workload [15], [173] and in brain-computer interfaces (BCI) [13], [108], [175], [203].

2.2.2 Functional near-infrared spectroscopy (fNIRS)

In order to function properly, the human brain requires a sufficient level of oxygen which is delivered as required by the blood supply in response to local metabolic needs. As specific areas of the brain are employed, more energy is required necessitating an increase in oxygen which is achieved through changes in the neurovasculature system (typically a dilation of capillaries and related vessels). By recording these changes in blood oxygenation in specific areas it is therefore possible to analyse the activation of the brain. NIRS is a imaging technique to determine the oxygen concentration in the haemoglobin in the blood. Functional NIRS is the use of the technique to monitor the functional activity of the brain. fNIRS imaging is gaining popularity in cognitive and clinical neuroscience as it can be used in settings and on populations, where the use of other functional imaging techniques would be too expensive, difficult, or impossible [155].

Functional near-infrared spectroscopy (fNIRS) employs light at multiple wavelengths (in the infrared band) to penetrate the skull, and to indirectly measure the change in the concentration levels of oxygenated (HbO) and deoxygenated hemoglobin (Hb) in the brain, through changes in the optical absorption [28]. Figure 2.6 presents the absorption values from an example recording of fNIRS recorded from the prefrontal cortex. fNIRS, when applied in human neuroimaging, produces a narrowband signal with frequencies ranging from 0.01 Hz to 0.8 Hz [81].

The fNIRS apparatus consists of a low level light source (typically between 5 to 10 mW) which transmits the light into the tissue and a detector which receives the rebounded light. These sources and detectors are placed non-invasively onto the scalp of the subject. The near-infrared frequency range is chosen as the biological tissue and water in the head both have a low absorption rate at these wavelengths and thus the light can penetrate a few centimeters into the scalp [28]. This allows the NIRS technique to detect the changes in the outermost cortex, allowing optical measurements to be used for imaging brain functions [81]. Applications of NIRS center on the non-invasive measurement of the quantity and oxygen content of hemoglobin. These measurements are then used in the determination of cognitive tasks [86] and in BCI [124]. Recent technological advances are allowing for the development of fNIRS systems for use outside of the clinical setting. An example system currently available is the Artinis PortaLite system (Artinis, AS Zetten, Netherlands) which provides a three light source device capable of an absolute measure of HbO for up to 10 hours.

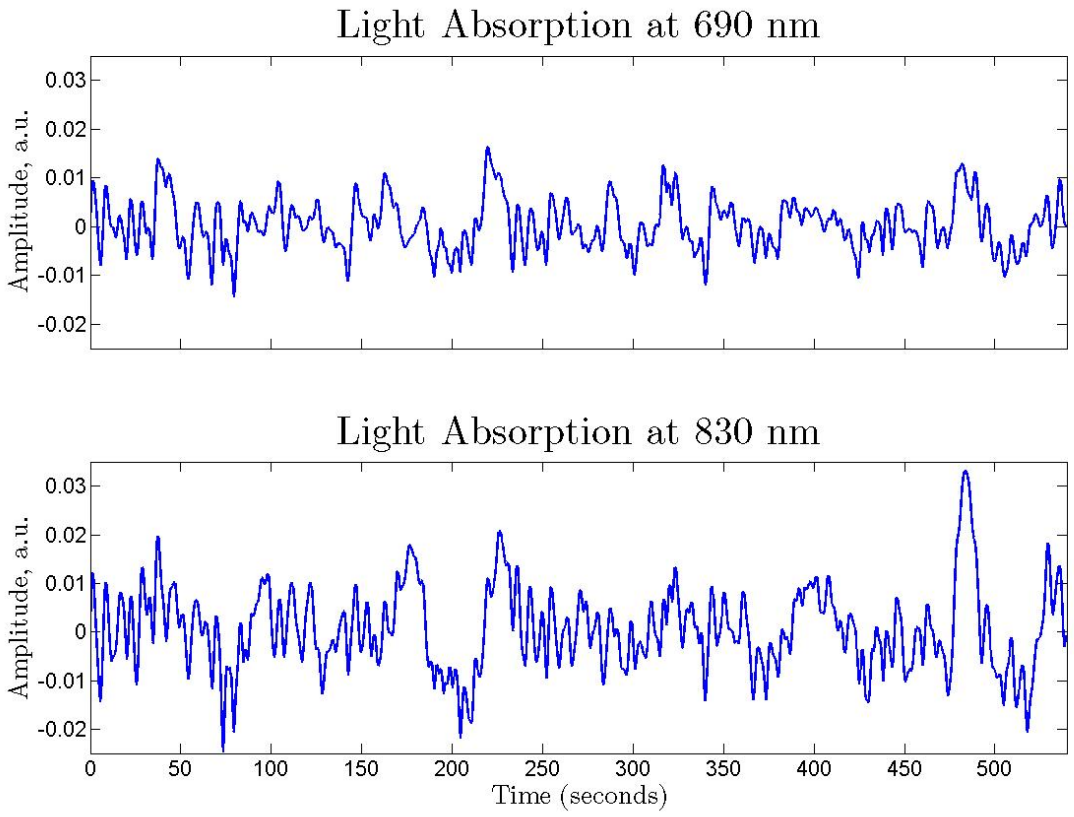

FIGURE 2.6: Example recording of light absorption using fNIRS.

2.2.3 Electromyography (EMG)

Electromyography (EMG) is a technique for evaluating the electrical activity of the skeletal muscles [156]. An electromyograph detects and measures the electrical potential produced by muscle cells when these cells are electrically or neurologically activated. This electric potential has a range of less then 50 μV up to 20 to 30 mV while having a typical repetition rate of muscle motor unit firing of between 7 and 20 Hz, depending on the muscle group under observation. Figure 2.7 presents an example signal recorded using EMG.

There are two types of EMG in widespread use, surface EMG and intramuscular EMG. In the out-patient domain, the non-invasive surface EMG technique is most common as intramuscular EMG is seen as too invasive. However, as the electrodes during surface EMG are placed on the skin and not on the muscle directly, there is a greater chance of artifact contamination and the signal strength is also diminished due to the extra path length of the signals through the subcutaneous tissue and epidermis. The EMG system uses similar active electrodes and electrolyte gel as that employed when recording ECG signals.

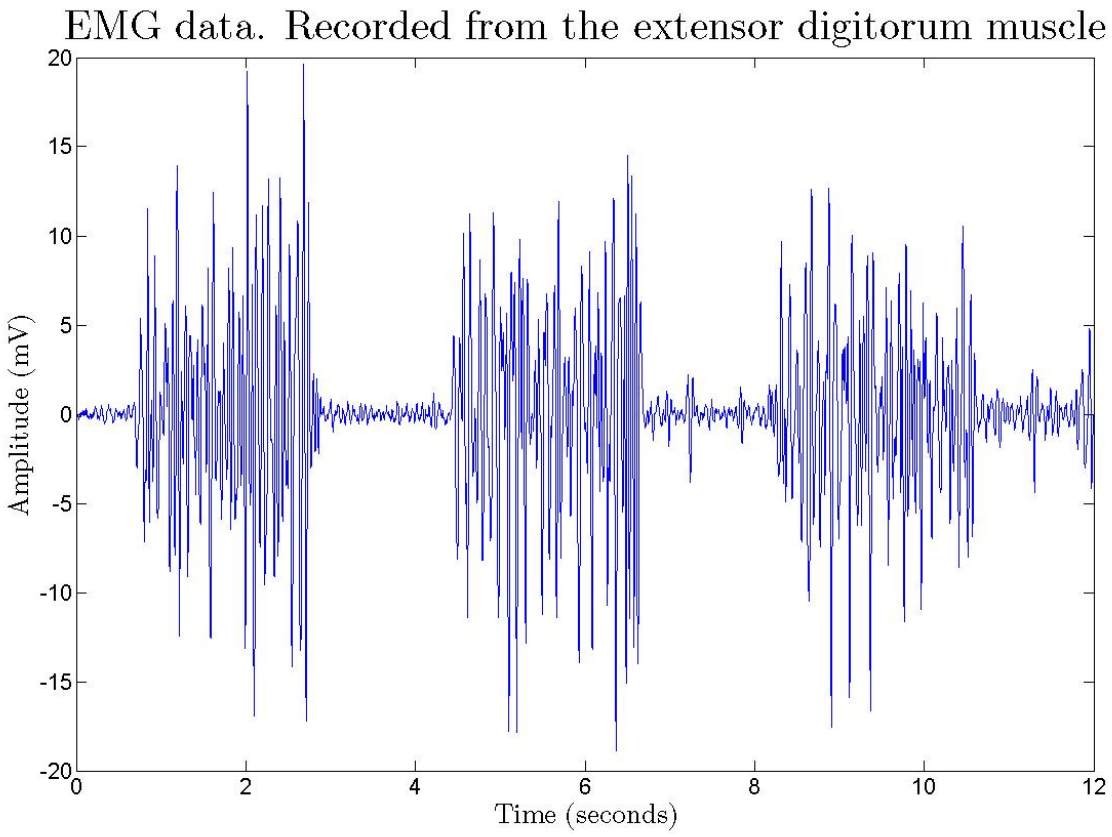

FIGURE 2.7: Example recording of EMG recorded from the extensor digitorum muscle on the forearm. Plot shows variation from rest to muscle activation.

EMG recordings are employed in a number of different areas of both research and treatments [151]. Azzerboni et al. [9] used long term EMG recordings to differentiate between parkinsonian and essential tremor and correctly diagnosed in 93% of their cases. In 2002 researchers [157] used EMG patterns to determine the effect of medication on individuals with Parkinson's disease. Another major application of EMG recordings is in the control of prosthesis [109], [20], [174]. By utilising the available functional muscles in the body, a subject is capable of controlling an inactive muscle group or limb through the use of a prosthetics system. All the uses of EMG stated above, along with many others, require long term or constant operation thus presenting the requirement for accurate out-patient measurements.

There are many other clinically relevant signals that can be measured from the human body. Some of these include body temperature, blood pressure, pH levels and perspiration levels [42]. These signals exhibit only slow fluctuations and consequently do not normally warrant the use of continuous monitoring and thus are considered spot measurements. Therefore for the purpose of this thesis only the physiological signals already described above will be explored further. In particular the next section describes the various sources of noise and artifact that can corrupt such signals.

2.3 Artifact Modalities

The presence of artifacts seriously degrades the clinical utility of recorded physiological measurements. This is particularly true for recordings made outside of the hospital environment where the lack of a trained technician can add additional complications. There are three distinct sources of artifacts that impact all physiological recordings; environmental artifacts, experimental errors and systemic physiological artifacts [81]. These three sources have different properties and thus manifest themselves distinctively on the individual measured signals.

2.3.1 Environmental Artifacts

Environmental artifacts primarily originate from the mains power leads that surround the body during day to day living and can be seen in the form of 50/60 Hz hum. The artifacts can additionally arise from electromagnetic interference (EMI); a disturbance that affects the signal due to the electromagnetic radiation emitted from an external source. This EMI can interact with the measurement cables, or the human body which acts as an antenna to the RF interference. Instrumentation artifact is a type of environmental artifact which is said to originate from within the circuit components themselves and can be observed in the form of thermal noise (due to the changing temperature of components), shot noise (due to the quantised nature of the electric charge) or 1/f (pink) noise (due to the slow fluctuations of the condensed-matter materials of the devices). A further major source of interference in bioelectric measurements is due to the capacitive coupling of the measurement cables with the mains (C_{ca} and C_{cb} in Figure 2.8) [191] and other devices.

A poor electrode-skin interface can be the source of undesirable artifacts, however this impact can be greatly reduced by using a suitable electrode-skin interface electrolyte gel and an active electrode system. However the electrolyte gel is not suitable for long term monitoring. The recording leads can also be susceptible to magnetically induced interference, but this can be reduced by shortening the lead lengths and twisting the cables so both receive the same interference. Further, the recording leads are also shielded to avoid RF interference and capacitative coupling. Optical measurement devices, such as PPG and NIRS, are not intrinsically susceptible to capacitive coupling interference as no bioelectric measurement is conducted (Figure 2.8(a)). However, they are sensitive to environmental artifacts from other natural and artificial light sources. These interferences can be reduced by using correct procedure and ensuring that no external lighting can affect the recording.

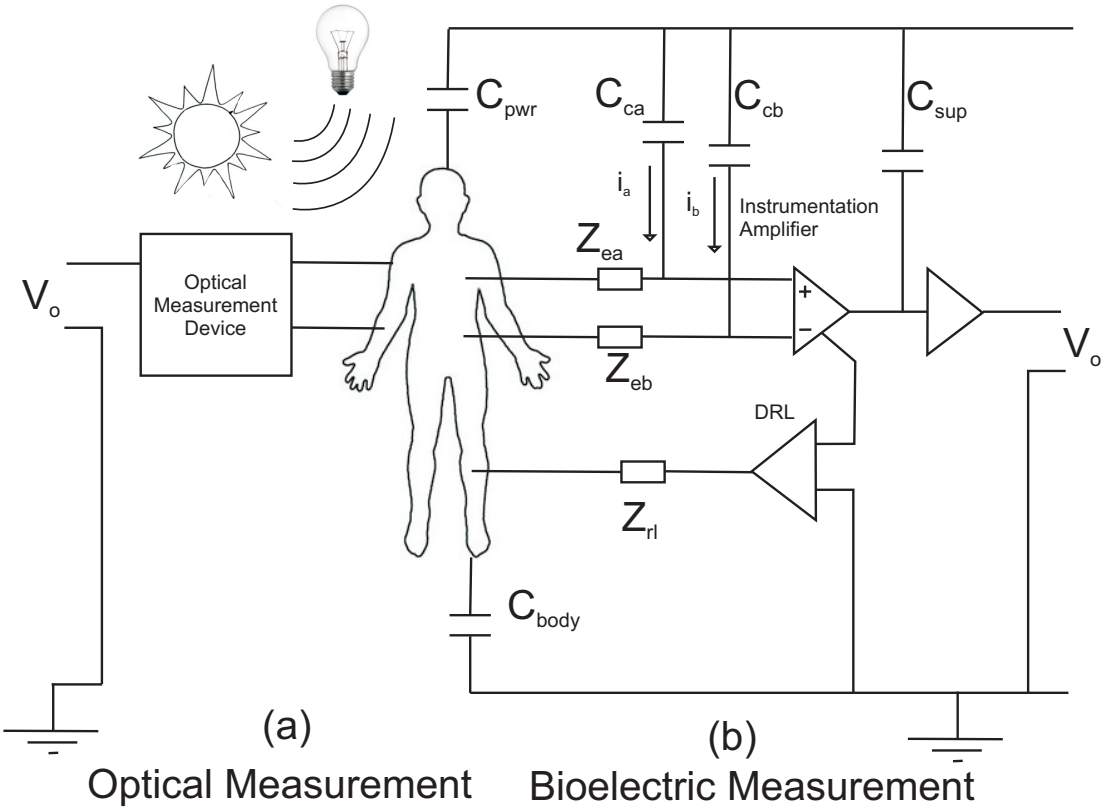

FIGURE 2.8: Block diagram of sources of artifact on an optical measurement (a) and bioelectric measurement (b) system [191].

2.3.2 Experimental Error

Experimental error is seen as uncontrolled/unwanted variation in the experimental setup. This category of error can be reduced by proper procedure and planning, but it is almost impossible to eliminate completely. This inability to completely eradicate the error is, in most part, due to human error during experimental setup or subject motion during data acquisition. Incorrect procedural setup, for example the poor application of the electrodes, can create discrepancies in the measured signal. In the p-health environment, the user is not always a trained technician, and thus the correct procedure in preparation and recording may not always be adhered to. However these errors can often be observed prior to recording, and thus corrected. Motion of the subject can create a large amount of experimental error and is commonly the most detrimental for many physiological signal recordings, due to changes in the underlying measurement geometry. This source of error, although present in most recordings, is far more prominent in the p-health environment due to the patient having more freedom of movement. Subject motion can also cause changes to the coupling between the sensors and the tissue surface introducing further distortion to the recorded signals.

With respect to optical methods, PPG and fNIRS for example, motion of the subject causes two distinct types of artifact. Firstly, movement of the source or detector optodes with respect to the skin causes a change in the path-length taken by the light transmitted by the source optode before it enters the detector. Subject movement also causes a blood pooling effect observable in the measurements. This blood pooling creates an increase in the overall blood levels at the recording site [179] and disrupts the ability to resolve the functional induced change.

Motion also has a damaging effect on bio-potential measurements in the body, such as ECG and EEG. Subject motion can cause the position of the electrode on the skin to alter. This movement can cause a variation in the distance (d) between the recording electrode and the skin (Figure 2.9), which results in a corresponding change in the electrical coupling, causing signal distortion. Subject motion can also cause a change in the conduction volume between the electrode and the signal source which induces potential changes at the recording sites [180]. These changes culminate in the production of artifact on the recorded output. The movement of the recording devices with respect to the underlying skin can be reduced by correct preparation of the interface surface by abrasion and cleansing of the skin and ensuring a strong adhesion of the electrodes [80].

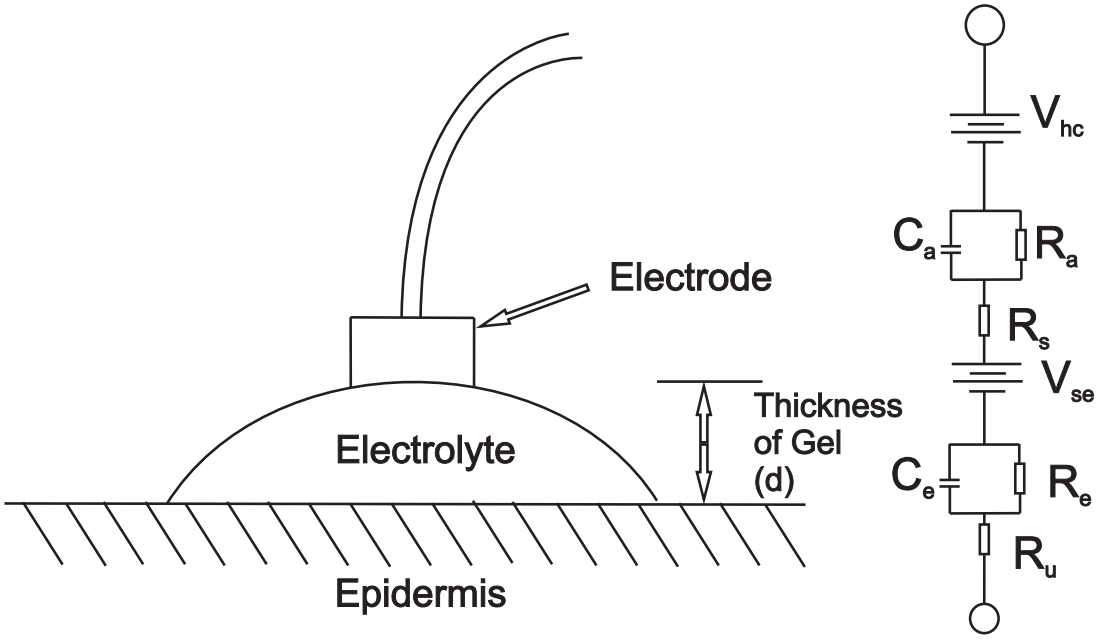

FIGURE 2.9: Block diagram of the interface between an electrode and the skin.

2.3.3 Physiological Artifacts

Physiological artifacts are variations in the desired signal due to other physiological processes in the body. Major contributors of artifacts most commonly detected in physiological measurements are eye movement-related artifacts, cardiac signals, respiration signals and muscle tension signals measured using EMG. Other physiological signals, such as brain signals, do not have sufficient signal strength to cause major complications to the desired measurements.

Eye movement-related artifacts have the largest detrimental effect on EEG recordings. As the eye alters position the resting potential of the retina changes and can be measured using an electrooculogram (EOG). Blinking also causes involuntary movement of the retina as well as muscle movements of the eye lid. Due to the eyes' close proximity to the brain, as the signal propagates over the scalp it can appear in the EEG signal as an artifact that can present serious complications in EEG analysis [73]. The amplitude of these signals can be many times greater than the EEG signals of interest. This ocular signal can easily be measured using electrodes placed above and below the eye.

Muscle movements can cause artifacts on a broad range of electrophysiological signals as they can originate from any muscle on the body, and thus can be in very close proximity to the signal recording site. The muscle fibres have a typical repetition (firing) rate of about 7-20 Hz, depending on the size of the muscle. In terms of EEG recording, the tension of the facial or jaw muscles has a large detrimental effect on the desired signal as the magnitude of the EMG signal can be many times larger than the desired EEG signal. EMG signals do not however have an adverse effect on the signals recorded using light, for example fNIRS and PPG, due to the different recording modalities.

The cardiac signal can cause artifacts on a number of different recordings including EEG and EMG. The electrical signal outputted from the heart has a high signal strength and so can be picked up at numerous positions around the body. The beating of the heart also causes pulse artifacts where the expansion and contraction of the vessel introduce voltage changes into the recordings [100]. The ECG and pulse signals have a frequency range of around 0.5-40 Hz and 1.2 Hz respectively making it difficult to remove them from most physiological signals, due to the overlapping frequency spectra.

2.4 Conclusion

The accurate non-invasive measurement of physiological signals has a number of different and important applications. These signals provide information that can be used to

inform a trained technician of the presence of a wide range of different ailments and conditions ranging from heart problems to epilepsy. The recordings can also be used as part of a person's treatment especially when used as part of a closed loop system, for example in operation of a prosthetic device or as biofeedback for a rehabilitation technology.

The feasibility of the above hinges on the viability of appropriate quality measurement in uncontrolled environments. This chapter served to describe this context and in particular highlighted a number of the most common physiological measurements in use today for such systems. The physiological origin, examples and characteristics of these signals are given to allow for a comparison between the different signal modalities. For example, it can be seen that the amplitude of the signals recorded using EEG are smaller by at least an order of magnitude to those measured using ECG and EMG, thus making them more sensitive to artifact contamination.

In addition to the physiological signals, different categories of artifact which can contaminate these measurements are described. These include artifacts from environmental sources (such as 50 Hz hum), experimental error (subject motion) and from the recording of unwanted independent physiological signals (such as eye movement on EEG signals). It is the presence of these artifact signals which degrades the desired signal quality and therefore the ability to perform the measurements in uncontrolled environments. An important area of research is therefore in the removal of these undesired artifacts.

Chapter 3 will next provide a review of a number of artifact removal techniques which are most commonly implemented in the physiological signal monitoring domain.

Chapter 3

Review of Existing Artifact Removal Methods

The accurate separation of artifact components from the desired signal of interest is an important processing step for all physiological measurement and it is an especially challenging one for measurements acquired outside laboratory and clinical conditions. This chapter presents a thorough review [178] [181] of the most commonly implemented artifact removal techniques employed in physiological signal analysis. The review consists of a short description of the operation of the techniques, example results obtained using the algorithms on different signal modalities as well as any comparisons completed between the different algorithms.

There are a number of general techniques used for artifact separation and removal. This removal can often be accomplished using simple classical filtering techniques (for example low-pass filtering). However, these simple methods can only be employed when the frequency bands of the artifact and the desired signal do not overlap. When there is spectral overlap alternative techniques must be adopted.

Figure 3.1 presents the general form of the artifact suppression techniques discussed in this review. The signal recorded during an experiment ($\mathbf{x}(n) \in \mathbb{R}^P$) is a combination of the original desired signal $\left(\mathbf{s}(n) \in \mathbb{R}^M\right)$ and contaminating artifact $\mathbf{v}(n)$. P is the number of recorded signals and M is the number of underlying sources. The function f is used to describe how the two signals are combined to produce the signal at the recording site. This allows for both multiplicative [61] and additive artifacts, however additive artifacts are predominantly assumed as this leads to tractable problem formulations, i.e.

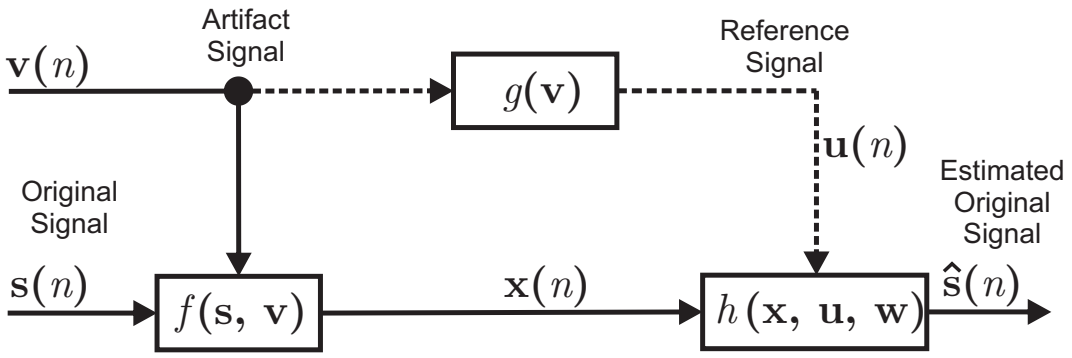

FIGURE 3.1: A General Framework for Artifact Removal

$$\mathbf{x}(n) = \mathbf{s}(n) + \mathbf{v}(n). \tag{3.1}$$

Therefore, Figure 3.1 evolves to Figure 3.2. Label (i) depicts situations in which a reference signal $\mathbf{u}(n)$ is used by the function h to aid in the estimation of $\mathbf{v}(n)$ (for example adaptive filtering) and (ii) depicts where $\mathbf{v}(n)$ is estimated directly from $\mathbf{x}(n)$ (for example BSS techniques). As $\mathbf{u}(n)$ will seldom be a direct proxy for the contaminating artifact $\mathbf{v}(n)$, the function g is presented to imply that the two signals are related. While both (i) and (ii) can be employed together, in practice the methods developed usually fall into one or other of (i) or (ii). Many of the artifact removal techniques using (ii) also assume that the number of recorded signals must be equal to or larger than the number of sources, i.e. $P \geq M$. Section 3.6 describes algorithms that operate when this is not the case.

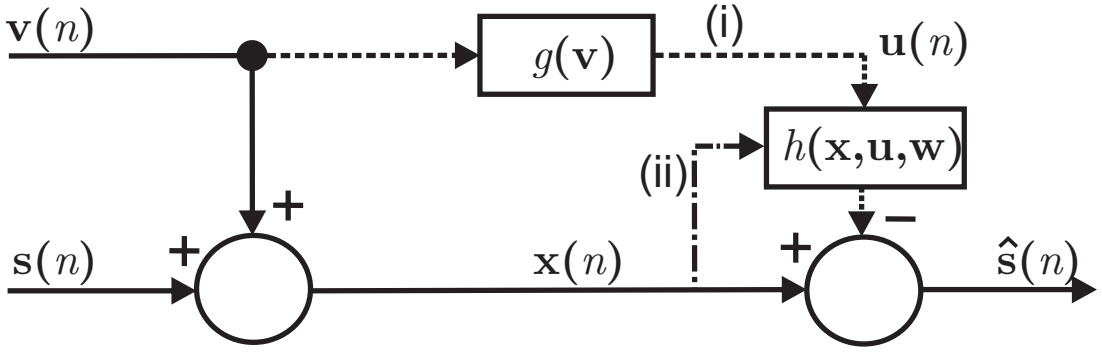

FIGURE 3.2: A Linear Framework for Artifact Removal

The remainder of this chapter will expand on a number of the most commonly implemented artifact removal techniques employed on physiological signals. A review is presented of the signals with which they have been used and also their calculated

efficacy. Section 3.7 then analyses the reviewed techniques and classifies them into techniques which are either single stage or two stage in nature (see Table 3.1).

3.1 Adaptive Filtering

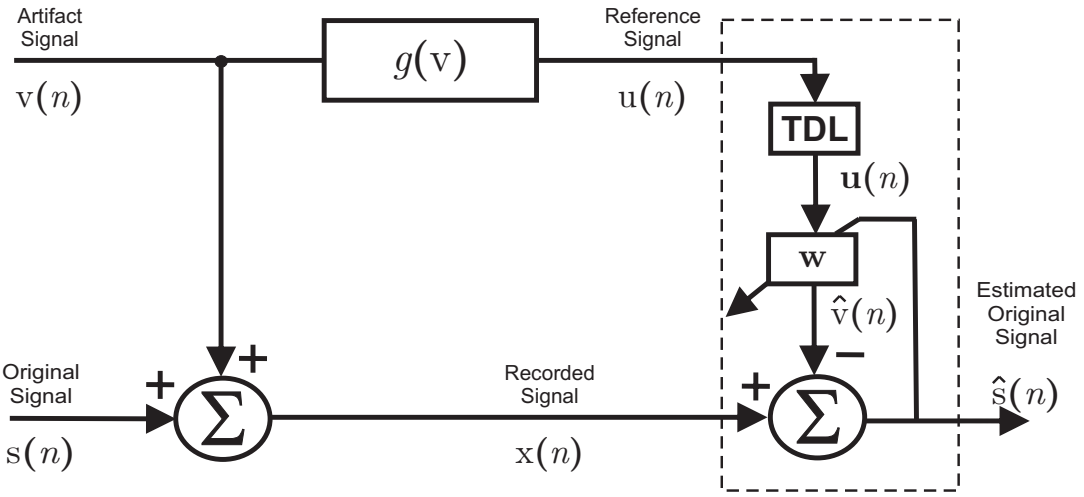

FIGURE 3.3: Adaptive Filter Framework for Artifact Removal

Adaptive filtering operates under the assumption that the desired signal $s(n)$ and the artifact $v(n)$ are uncorrelated, i.e.

$$E[s(n)v(n)] = 0, \tag{3.2}$$

where $E[.]$ is the expectation operation. Using a tapped delay line (TDL) the filter generates a signal $\hat{v}(n)$ which is correlated with the actual artifact signal $v(n)$ from a reference signal $u(n)$. This estimate of the artifact is then subtracted from the recorded signal $x(n)$ and the residual $\hat{s}(n)$ is an estimate of the original signal $s(n)$ [121]. The filter coefficients continue to adapt until the artifact in the output, which is correlated with the provided reference, has been minimised.

Reference Signals

The choice of artifact reference $u(n)$ is very important when utilising an adaptive filter as the reference is used as a proxy for the contaminating artifact. The higher the correlation between the reference and the contaminating artifact the better the adaptive filter will perform. For motion artifact, accelerometers are predominantly selected [40] [131] due to their high sensitivity combined with an ease of application, however other

sources such as anisotropic magnetoresistive (AMR) sensors [188], optical bend sensors, impedance sensors [69] and skin stretch sensors [68] have also been considered.

References for artifacts originating from undesired electrophysiological signals can often be recorded using general recording techniques. Examples of this include the recording of EOG for the removal of eye movement artifact from EEG signals [73] and EMG recording for removing muscle movement artifact from ECG signals [214]. However, other methods have also been proposed which develop a model of the artifact to use as a reference [186]. These model based methods can however add unnecessary complexity to the system and are not often implemented.

Algorithms

The choice of algorithm dictates the computational cost and accuracy of the adaptive filter. The most common algorithm employed in adaptive filtering is the least mean-square (LMS) algorithm with a computational complexity of O(L) (L is the filter length) [5] and which has a weight update equation [94]:

$$\hat{s}(n) = x(n) - \mathbf{w}^T(n)\mathbf{u}(n) \tag{3.3}$$

$$\mathbf{w}(n+1) = \mathbf{w}(n) + 2\mu\hat{s}(n)\mathbf{u}(n). \tag{3.4}$$

This algorithm produces an estimate of the desired signal $\hat{s}(n)$ through adaption of the filter coefficients $\mathbf{w}(n)$. The filter coefficients are adjusted so as to minimise the mean squared amplitude of the estimated signal. The step size μ controls the rate of adaption and hence the overall stability of the filter.

Another family of algorithms commonly used in adaptive filtering is based on the recursive least square (RLS) algorithm. This is a computationally more complex algorithm with a computational complexity of O(L^2) [5] and an update equation [14]:

$$\mathbf{G}(n) = \frac{\mathbf{R}^{-1}(n-1)\mathbf{u}(n)}{\lambda + \mathbf{u}^T(n)\mathbf{R}^{-1}(n-1)\mathbf{u}(n)} \tag{3.5}$$

$$\mathbf{R}^{-1}(n) = \lambda^{-1}\mathbf{R}^{-1}(n-1) - \mathbf{G}(n)\mathbf{u}^T(n)\lambda^{-1}\mathbf{R}^{-1}(n-1) \tag{3.6}$$

$$\mathbf{w}(n) = \mathbf{w}(n-1) + \hat{s}(n)\mathbf{G}(n), \tag{3.7}$$

where $\mathbf{R}(n)$ is an estimate of the input signal covariance matrix and λ is a forgetting factor. The RLS algorithm exhibits extremely fast convergence due to its 2nd order nature. Many papers describe the advantages of both families of algorithms including

others such as least mean absolute value (LMAV) and sign (SIGN) [122]. The RLS family of algorithms consistently perform to a higher accuracy than the other algorithms but in doing so have a higher computational cost [131] [152]. In [122] the authors tested 5 different algorithms from the two families of algorithms and found that the RLS algorithms achieved the highest accuracy (computed using correlation values) in 23 of the 28 computed tests when removing ECG artifacts from EMG recordings. This was especially true when the signal was assumed stationary and a simplified formulation was used. In 2009, Zia Ur Rahman *et al.* [214] used a normalised signed LMS algorithm in the calculation of simulated artifacts on an ECG signal. This algorithm was found to converge faster than the basic LMS algorithm, had a lower computational cost and also had a greater signal to noise ratio (SNR) improvement (3.9 dB versus 9.2 dB in some cases) all of which are desired for operation in the p-health domain.

The adaptive filter is easy to implement and it also has an ability to operate on-line and without preprocessing or calibration, but the requirement of additional sensors to provide reference inputs can add to the complexity of the hardware system. Further, if the reference signals do not provide an accurate representation for the artifact signal the technique will not perform well.

3.2 Wiener Filtering

Wiener filtering is another parametric technique used to remove unwanted artifacts from the measured signals [49]. The Wiener algorithm is based on a statistical approach and thus does not require the use of an external reference signal. The signal and the (additive) artifact are assumed to be stationary linear stochastic processes with known spectral characteristics or known autocorrelation and cross-correlation. The desired signal and artifact are also assumed to be uncorrelated with each other.

The purpose of the Wiener filter is to produce a linear time invariant filter so that the mean square error between the true desired signal $s(n)$ and the estimated one $\hat{s}(n)$ is minimised [88] as stated in Equation 3.10. This filter is determined using the power spectral densities (PSD) of the signal and the artifact as described in [88] and in Section 5.3. These PSD are generally not available *a priori* and must be estimated from measurements.

The necessity for calibration prior to usage, and its inability to be employed in realtime applications, is a disadvantage of the Wiener filter with respect to the adaptive filter. However it eliminates the requirement for additional hardware on the recording device necessary with the adaptive filter. In 2005, Izzetoglu *et al.* [88] used both adaptive

filtering and Wiener filtering individually to try to remove motion artifact from recorded NIRS data. After calibration of the Wiener filter, the output was discovered to have a better SNR than that achievable using the adaptive filter (average ΔSNR = 3.25dB determined using epochs of clean data as the true signal) demonstrating the advantage of the Wiener filter.

3.3 Bayes Filters

Bayesian filtering is a method of probabilistically estimating a given systems state from available noisy observations. Bayes filters express the state at the current time sample as $\mathbf{x}(n)$. The probability distribution over these random variables $\mathbf{x}(n)$ (known as *belief*, $Bel(\mathbf{x}(n))$) is a representation of the uncertainty. Bayes filters operate by estimating the beliefs over the state space using all the available information encompassed in the observed data [58] using the assumption that the dynamic system is Markov. Markov systems assume that the current state variable $\mathbf{x}(n)$ contains all the relevant information about the system.

Bayes filters are implemented using a predictor-corrector methodology. The predictor uses a time update model to describe the relationship between the states from one time sample to the next. The corrector step then utilises a measurement model to describe the relationship between the observed data and the internal state.

This approach overcomes some of the limitations of adaptive filtering and Wiener filtering. Like Wiener filtering, the Bayes filter technique does not require a reference signal to be capable of removing the embedded artifact. However, unlike the Wiener algorithm, Bayes filtering is capable of operating in real time due to its recursive nature.

The Bayes filter technique is not itself implemented as it is computationally intractable. There are however, a number of different methods that implement approximations of the technique. Two of the most popular are detailed next.

3.3.1 Kalman Filtering

Kalman filtering was first described by Rudolph E. Kalman in 1960 [96]. The Kalman filter essentially implements a mathematical predictor-corrector type estimator as stated above. The filter uses feedback control to estimate a process: the filter first estimates

the process state at a given time and then obtains feedback in the form of (noisy) measurements [200]. This creates 2 layers of calculations; time update equations and measurement update equations as detailed by Welch and Bishop in [200] and are discussed in detail in Section 5.4.

After each time and measurement update pair have completed, the process is repeated with the previous *a posteriori* estimate used to predict the new *a priori* estimate [200]. The filter models must be created prior to implementation of the algorithm. These models can be determined using a number of different modeling methods, such as autoregressive (AR) and moving average (MA) models. The requirement that the algorithm be calibrated before use [87] could lead to problems in the personal health care environment.

There are a number of approaches to achieving artifact removal using a Kalman filter. Firstly, a model of both the desired signal and the contaminating artifact can be produced. The recorded signal can be described as the summation of these two model signals and thus the process and measurement models can be determined. The Kalman filter can then be implemented to estimate the unknown system parameters by reducing the variance of the error between the recorded output and the modeled output. With the system parameters now known, artifact removal can be accomplished by setting the parameters affiliated with the artifact in the measurement model to zero. This method was implemented by both Seyedtabaii *et al.* [166] and Morbidi *et al.* [136] to remove motion artifact and transcranial magnetic stimulation (TMS)-induced artifact from PPG and EEG signals respectively, with promising results. A second method models just one of the combined signals, either the desired true signal or the contaminating artifact. Using this model the Kalman update equations are then produced. Again the Kalman filter update equations are employed and the desired signal can be determined either as the function of the state space equation or as the residual [87] [154]. Reference signals can be used as an aid in the modeling of the signals [166] if available. The Kalman filter has also been implemented as part of an adaptive filtering scheme in [19], in which the Kalman filter update equations were employed to update the tap weights of the adaptive filter.

The Kalman filter operates on the assumption that the initial uncertainty (belief) is Gaussian and that the system dynamics are linear functions of the state [58]. However as most systems are not strictly linear, the Kalman filter has also been extended to the non-linear domain through the extended Kalman filter (EKF) [200]. This EKF is capable of performing to the same degree by linearising around the current mean and covariance. The main advantage of the Kalman filter is in the computational efficiency of the algorithm due to its efficient use of matrix operations. However the filter can only

function with unimodal distributions which can be a problem in biomedical applications where many signals are multimodal.

In 2001, Rohalova *et al.* [158] presented results showing the advantage of the EKF in the detection of artifacts in sleep EEG data. Their results show that for that application, the non-linear Kalman filter has a sensitivity of almost twice that of the linear Kalman filter. The EKF was also utilised by Sameni *et al* in 2005 [161] and 2007 [162] for denoising simulated ECG signals. Here the filter was used to remove environmental and muscle artifact from noisy ECG signals showing positive results with a Δ SNR ranging from 8.5dB to 0.8dB depending on the input SNR.

If the process and measurement models are available for the required system, the Kalman filter stands as a very attractive alternative to the adaptive filter for two major reasons. Firstly it produces a superior SNR and secondly it does not require an external reference thus reducing the hardware costs of the system.

3.3.2 Particle Filtering

Particle filtering also implements the Bayes filter technique but unlike the Kalman filter, does not require the model to be linear or the distribution to be unimodal. In order to overcome the mathematical intractability of the Bayes method while incorporating multi-modal distributions, a Monte Carlo sampling approach is implemented as described in [51]. In order to be capable of expressing the state changes, N samples (particles) are randomly selected from the probability density function (pdf). These particles have weights proportional to the amplitude of the pdf at their sample point and the weights have the property that their sum is equal to 1. Each particle is then passed through the process model to determine the next state of that particle. As a result, the particle filter becomes more computationally complex but more accurate the more samples you choose, to the point where if $N = \infty$ then the system will give the optimal Bayesian solution. The weights of the new particles are determined using an update equation that incorporates the measurement model, and the estimated state is the mean of the determined pdf. One issue with the particle filter is that over time a small number of the particles become dominant, to the point where only a single particle will have a non-zero weighting. To prevent this from occurring, a number of different solutions have been described [31]. One of the most common techniques used to stop degeneracy is called the sampling-importance-resampling (SIR) technique. Using this technique, if the number of effective particles is less than a given threshold then the particles are sampled with replacement from the current batch of particles proportional to the weights of the particles. Once N particles have been sampled the weights of each particle are reset to

1/N. These new particles are then passed through the process model to determine the new states and the algorithm repeats.

Little work has been done to date on artifact removal using the particle filter in physiological signals. However, artifact removal using the particle filter is similar to that accomplished using the Kalman filter. Process and measurement models are required prior to employing the algorithm. In 2010 Hongxia and Jifang [76] used the particle filter to remove noise from simulated and actual motor bearing vibration signals. This was accomplished by determining a non-linear process model for the system and having the measurement model as the current state plus the added noise. Therefore by determining the next state of the system, the algorithm is determining the best estimate of the signal without the added artifact.

Kalman filters require sensors with high accuracy levels and fast update rates to perform optimally [58]. They are one of the most efficient filtering techniques, that use the Bayes' method, in relation to computation time and memory. However, if accurate sensors are not available, or if there is no detailed model of the process and measurements then particle filtering becomes the more viable option. Particle filters do not require a detailed model of the systems and thus are a very flexible tool with a relatively low implementation overhead [58].

3.4 Blind Source Separation

Blind source separation (BSS) is based on a wide class of unsupervised learning algorithms with the goal of estimating sources (which are not necessarily independent) and parameters of a mixing system [37]

$$\begin{bmatrix} \mathbf{x}_1 \\ \mathbf{x}_2 \\ \vdots \\ \mathbf{x}_P \end{bmatrix} = \begin{bmatrix} a_{11} & a_{12} & \cdots & a_{1(M+Q)} \\ a_{21} & a_{22} & \cdots & a_{2(M+Q)} \\ \vdots & \vdots & \ddots & \vdots \\ a_{P1} & a_{P2} & \cdots & a_{P(M+Q)} \end{bmatrix} \begin{bmatrix} \mathbf{s}_1 \\ \vdots \\ \mathbf{s}_M \\ \mathbf{v}_1 \\ \vdots \\ \mathbf{v}_Q \end{bmatrix} + \mathbf{N} \tag{3.8}$$

where $\mathbf{s}_i$, $\mathbf{v}_i$, $\mathbf{x}_i \in \mathbb{R}^{1\times L}$ are row vectors of L samples for the i^{th} original underlying source signal with specific statistical properties, the i^{th} contaminating artifact signal and the i^{th} recorded signal. $\mathbf{A}$ is the unknown mixing matrix and $\mathbf{N}$ is an unknown matrix representing noise and error values. For the remainder of this thesis, the combined source and artifact signal matrix will be referred to as $\mathbf{S}$.

Source separation is performed using only the recorded sensor signals and some assumptions on the underlying signals; therefore no additional reference signal is required. Most BSS models can be expressed algebraically in terms of matrix factorisation: given observation $\mathbf{X}$ perform the matrix factorisation, $\mathbf{X} = \mathbf{AS}$. This is the general form of the additive artifact model in which Equation 3.1 is a special case, that is Equation 3.1 is obtained when $P = M = Q$ and $\mathbf{A} = [\mathbf{I}_M; \mathbf{I}_M]$, where $\mathbf{I}_M$ is the $M \times M$ identity matrix. As only the observations $\mathbf{X}$ are known, BSS techniques estimate an un-mixing matrix to determine the original sources.

$$\hat{\mathbf{S}} = \mathbf{WX}, \tag{3.9}$$

where $\hat{\mathbf{S}}$ is the estimation of the original sources (and artifact) and $\mathbf{W}$ is the un-mixing matrix. Once the estimations of the original sources are known, the sources representing the artifact signals can be removed.

There are number of different algorithms available to perform BSS, including independent component analysis (ICA) and canonical correlation analysis (CCA) described below. Each algorithm performs matrix factorisation with the aid of some particular assumptions about the signals, such as independence for ICA. The fundamental approaches underpinning source separation algorithms, as described in Choi *et al.* [37], are: (i) the use of higher order statistics (HOS) including skewness and kurtosis; (ii) second order statistics (SOS) including delayed correlations and spectral diversity; (iii) SOS with non-stationarity; and (iv) the use of the signal characteristics (time, frequency) to separate the sources.

The choice of the best algorithm to employ depends on *a priori* knowledge of the signal. Below, some of the most common BSS algorithms employed in research are described.

3.4.1 Independent Component Analysis (ICA)

Independent component analysis (ICA) is a blind source separation technique [39] in which recorded, multi-channel, signals are separated into their independent constituent components or sources [83]. There are many assumptions that the sources and mixing must adhere to for ICA to be allowed to be employed, including linear mixing, square mixing and stationary mixing. These assumptions are here clarified further: [90].

1. Linear Mixing: This assumes that the recorded signals are mixed linearly (and generally instantaneously). This assumption holds true for most physiological

signals, however it has been reported that, for example, the propagation of the EOG signal through the scalp creates a time delay in the signal viewed at separate positions [100].

2. Noiseless Mixing: This assumption states that the underlying sources are noiseless and remain so until mixed with the noise at the sensors. This assumption may not be fully accurate, however it allows the ICA algorithm to isolate the desired sources even if the sources are themselves contaminated with noise.

3. Square Mixing: For ICA it is assumed that the number of sources is equal to the number of measurement sensors. This assumption is less then desirable in certain cases in which there are a large number of sensors recording over a short period of time. Often data reduction techniques are used prior to ICA to reduce this problem [83], however this can cause additional problems in certain cases.

4. Stationary Mixing: The fourth assumption made is that the mixing of sources does not change over time. This assumption holds strong for most recordings, however can cause some problems when recording ECG where the act of breathing can change the signal mixing.

5. Statistical Independence of Sources: The final and probably most important assumption is in the independence of the sources. Other BSS techniques assume the sources are un-correlated, this however does not guarantee independence. Independence states that each source signal is generated by a random process which is independent of the random processes generating the other sources. Data must have independent components for ICA to be able to accurately separate.

One of the major limitations of ICA is the requirement for the independent sources to be non-Gaussian. ICA can obtain an estimate $\hat{\mathbf{s}}$ of the sources $\mathbf{s}$ iff (if and only if) the sources are non-Gaussian. If a single independent component is Gaussian it can be estimated as the residual that is leftover after extracting all other independent components, but ICA cannot account for more than one Gaussian component. Unfortunately a component is generally not known to be Gaussian or non-Gaussian *a priori*. The data is commonly whitened prior to the computation of the ICA. This can be achieved with principle component analysis (PCA). By doing so, the correlation between the signals is canceled and the dimensionality of the data can often be reduced.

There are a number of different algorithms used to determine the un-mixing matrix $\mathbf{W}$. Some of the most commonly employed include fast ICA [83], the Bell-Sejnowski algorithm [12], extended ICA [110] and JADE [52]. Fast ICA separates the sources by

maximising the magnitude of the kurtosis or by maximising the negentropy. The Bell-Sejnowski algorithm uses negentropy to try and separate the sources. The extended ICA algorithm is similar to that proposed by Bell and Sejnowski but allows for sources that have a negative kurtosis. Finally the JADE algorithm maximises the kurtosis of the probability density function through a joint diagonalization of the fourth order cumulants.

When the recorded signals have been passed though the un-mixing matrix $\mathbf{W}$ the outputs are deemed to be the original independent sources. The sources considered to be artifacts can then be removed. The artifact signals can often be determined using heuristics such as signal shape, frequency and amplitude [65]. The remaining sources are thus the original desired signal sources and when put through the inverse of the un-mixing matrix $\mathbf{W}^{-1}$ the resulting outputs are the artifact corrected signals [112] [95] [34].

While propagation delays associated with physiological signals are generally small they could potentially be sufficient to violate the ICA assumptions of instantaneous mixing of the sources. An extension to the ICA algorithm, known as Convolutive ICA (CICA), has been developed which takes into account both weighted and delayed contributions of sources in the generation of the observations [192]. In doing so, the coefficients of the unknown mixing matrix $\mathbf{A}$ are substituted by finite impulse response filters and the product term of Equation 3.9 is replaced by the convolution operator $\star$. Milanesi *et al.* [132] used a frequency domain approach with the CICA algorithm for the removal of motion artifacts from ECG signals and illustratively showed it to provide improved results compared to basic ICA. The algorithm has also been shown to improve the separation of EEG components [206] compared to the ICA algorithm.

ICA, as a non-parametric algorithm, has a major advantage over some other parametric algorithms, such as adaptive filtering, in that no *a priori* information is required for the algorithm to function. Thus no reference signals are required, reducing the number of sensors allowing for a more portable device. However if *a priori* information is used in the model the ICA algorithm becomes much more informative as a technique [90].

There have been a number of papers detailing the differences between a number of the different ICA algorithms described above. The studies however do not clearly nominate a single method as the optimal, instead it depends on the problem [52]. Zibulevsky and Pearlmutter [216] ran tests on simulated data comparing JADE, Fast ICA and Infomax and found very little difference in the error rate detected, 8.8 %. 8.6 % and 7.1 % respectively. In a separate study, Karvanen et al. [97] report that JADE slightly out

performed Fast ICA, with the Infomax algorithm performing significantly worse. Again, Ziehe et al [217] report no significant difference between the Fast ICA and JADE algorithms when removing noise from a MEG signal. However, due to the computational complexity of the JADE algorithm it is usually restricted to operate solely in low dimensional data sets with the result that the Fast ICA algorithm becomes the algorithm of choice.

3.4.2 Canonical Correlation Analysis (CCA)

Canonical correlation analysis (CCA) [77] is another BSS method for separating a number of mixed or contaminated signals. The CCA method uses second order statistics (SOS) to generate components derived from their uncorrelated nature. CCA solves the BSS problem by forcing the sources to be maximally autocorrelated and mutually uncorrelated [46]. By looking for uncorrelated components, the approach uses a weaker condition than statistical independence sought by the ICA algorithm. ICA does not take temporal correlations into account, thus the samples can be arranged arbitrarily in time and the method will return the same solution. CCA addresses this point by being capable of finding uncorrelated components that, in addition, have maximum spatial or temporal correlation within each component. Details on the algorithm used to find the un-mixing matrix $\mathbf{W}$ using CCA can be found in [23] and are described in detail in Section 6.4. Artifact removal can then be introduced by setting the columns of the estimated source $\hat{\mathbf{s}}$ matrix which represent the artifacts in the recording to zero when performing the reconstruction.

Borga and Knutsson [23] compared both CCA and Fast ICA for the problem of separating 5 different EEG channels. Both methods had qualitatively the same results, but as CCA employs SOS, where ICA employs HOS, the CCA method is more computationally efficient. The authors repeated this test with fMRI data in [22] and again showed that the CCA algorithm performed better in terms of computational complexity by at least an order of magnitude while having similar qualitative results thus lending itself towards implementation in the p-health domain. It is also noted that the CCA method always returns the same result when employed with a given data set, this however is not true when using the ICA algorithm.

In 2006 Clercq *et al.* [46] used CCA to successfully remove muscle artifacts from EEG signals. This method was also shown on simulated data to outperform an ICA-based technique (JADE) where the overall Relative Root MSE (RRMSE) for CCA was on average 2.48 times lower than that achieved using ICA. This result was again documented

by Gao *et al.* [62] in 2010. The possible reason for CCA's improved performance over the ICA method is due to the form of the muscle activity. As ICA employs statistical independence to separate the sources it is able to isolate those artifacts with stereotyped scalp topographies into a single independent component. Muscle artifacts, however, involve the movement of a group of muscles, which do not have a stereotyped topography and thus ICA does not function correctly.

3.5 Single-Channel Decomposition Methods

Artifact removal using signal decomposition methods has become more widely used over the last number of years. These decomposition methods are capable of operating on single channel signals which increases their ability to be used in the home healthcare domain where the number of recorded signals is usually far less than that recorded in the hospital domain. Three such decomposition methods are described below.

3.5.1 Wavelet transform

The wavelet transform decomposes the noisy signal into approximations and details using a specified mother wavelet (see Section 6.1). These approximations and details can then be examined and the components corresponding to the artifact signals can be removed. The wavelet transform has been used previously by a number of authors to remove artifacts from biomedical signals [104] [160] [114]. Kumar *et al.* [104] used the algorithm to remove ocular artifacts from recorded EEG signals where the "artifacts were adequately attenuated, without removing significant and useful information" while Rosso *et al.* [160] used the wavelet algorithm to remove muscle artifacts from EEG signals recorded during epileptic activity again with positive results.

3.5.2 Empirical Mode Decomposition

The empirical mode decomposition (EMD) method was first described in 1998 [79] as a technique for non-linear signal processing and is well suited to non-stationary signals. The EMD algorithm decomposes the signal into components called intrinsic mode functions (IMF) with well defined instantaneous frequencies. When decomposed, the IMF can then be analysed and the components relating to artifacts can be removed, before recombining the clean IMF to generate the cleaned signal.

Wang *et al.* [197] used the EMD algorithm to remove motion artifact from recorded PPG signals. Using the algorithm the SNR was observed to rise from 1.7 dB to 6.2 dB and the peak detection rose from 39.3 % to 86.9 %. Tang *et al.* [184] also employed the EMD algorithm to de-noise a simulated ECG signal contaminated with Gaussian white noise. The algorithm was shown to produce a 6.24 dB increase in SNR, slightly outperforming the DWT algorithm which was employed as a reference technique.

Liu *et al.* [117] employed the EMD algorithm to remove tissue artifact from respiratory signals. Simulations showed that the EMD algorithm was an effective alternative to low-pass filters and ICA-based techniques, as it did not require *a priori* knowledge for choosing the cutoff frequency as was the case for the LPF, and was computationally more efficient than ICA.

3.5.3 Morphological Component Analysis (MCA)

Morphological component analysis (MCA) operates by decomposing the recorded signal into components that have different morphological characteristics. Each component is sparsely represented in an overcomplete dictionary which is comprised of a collection of waveforms, called atoms, which can be used to describe the different underlying signals. The overall signal is thus a linear combination of these individual atoms multiplied by their coefficient vectors. The basis pursuit denoise model [210] is then used to find the sparsest representation. Once this has been completed, the bases that represent the artifact signal(s) can be removed.

In [210] the authors used the MCA algorithm to remove artifacts originating from eye-brow raising, jaw clenching swallowing and eye blinks from a single channel EEG recording. Three dictionaries were chosen to represent the EEG signal, namely the Daubechies wavelet, the discrete cosine transform (DCT), and the Dirac basis. These bases were chosen as they are capable of representing the different morphologies of the recorded EEG and artifact [210]. Their results visually demonstrate that the MCA algorithm reduces the artifacts in the simulated contaminated EEG signal while also producing an improved correlation with the true signal ($R = 0.5485$) over that produced using the stationary wavelet transform ($R = 0.2925$). The artifacts due to 60 Hz hum are not removed using this method however, as this artifact is also represented using the DCT basis. This can be removed by post processing using basic filtering. The system can be improved by adding more applicable dictionaries to the already over-complete dictionary. This method has also been applied in multi-channel systems by Yong *et al.* [211] and was shown to provide a decrease in mean square error following the removal of artifacts from EEG data.

3.6 Extension of BSS Methods for Single Channel Measurements

Many of the BSS algorithms described above are incapable of operating on single channel measurements. However decomposition techniques generate multidimensional data from the single channel measurements thus permitting the combined use of decomposition methods with the BSS methods. Four algorithms are described below which make use of the presented combination.

3.6.1 Single-Channel ICA (SC-ICA)

As stated in Section 3.4.1, the independent sources $\hat{\mathbf{s}}$ can only be separated from the recorded mixed signals $\mathbf{x}$ if the inverted matrix $\mathbf{W}$ of the mixing matrix $\mathbf{A}$ can be determined, i.e. $\hat{\mathbf{s}} = \mathbf{W}\mathbf{x}$. However basic ICA does not function if there are more sources than sensors. In 2007 Davies and James [45] demonstrated that ICA can be implemented on single channel signals, if the power spectral density of the mixed signals is disjointed. If this is the case, the recorded time series is then fragmented into a sequence of contiguous blocks. With these new vector observations, the problem of single-channel ICA (SCICA) transforms into a multiple channel ICA (MICA) problem. Using the original ICA method each signal can be decomposed and reconstructed in the observation domain achieved through the implementation of the mixing and un-mixing matrices as described by Davies and James [45]. This algorithm was shown to be able to extract a number of spikes, seizure components and ocular artifacts from a recorded single channel EEG signal.

3.6.2 Dynamical Embedding (DE)

Dynamical embedding (DE) creates a series of delay vectors of the recorded signal and uses these vectors to create an embedded matrix, also known as a trajectory matrix, as observed in [91]. This matrix needs to be further decomposed so as to access the information required from the signal. There are a number of different methods used to decompose these matrices, two of which will be described in more detail below.

James and Lowe [91] used fast ICA to deconstruct the embedding matrix, created using single channel recordings from both EEG and magnetoencephalogram (MEG) signals embedded with ocular and 50 Hz hum artifact, into to its informative components. The Fast ICA algorithm was chosen due to its ease of implementation and speed of

operation. The fast ICA algorithm performs as stated in Section 3.4.1 and deconstructs the embedded matrix into m IC's. The next step in the process is the selection of the IC's that are not a result of artifacts, which is not always a trivial task. With these IC's chosen, they are then projected back onto the measurement space in isolation, where the embedding is reversed thus producing the resultant single channel signal free of the detected artifacts.

Teixeira *et al.* [185] used an alternative method to extract the desired information from the embedded matrix. In this work the authors used local singular spectrum analysis (Local SSA) to extract high amplitude and low frequency artifacts from single channel EEG recordings. Similar columns of the trajectory matrix are grouped together using a clustering algorithm such as k-means creating a number of sub-trajectory matrices. PCA is then used to determine each individual cluster's eigenvalues and eigenvectors. Denoising is achieved by projecting the data onto the eigenvectors corresponding to the k largest eigenvalues, with the value of k (which can be different for each cluster) determined using the minimum description length (MDL) criterion [185]. After de-noising, each sub-trajectory matrix is reconstructed as described in [185]. Each column of the new sub-trajectory matrices is then assigned to a column of a new trajectory matrix. The columns, to which they are assigned, are determined according to the columns of the original trajectory matrix used to create the sub-trajectory matrix. Finally, the one-dimensional signal is regenerated by averaging over the entries of the corresponding descending diagonals of the reconstructed trajectory matrix. This technique, unlike conventional ICA methods, does not require any user input in the selection of components of the reconstruction thus allowing for fully automatic artifact removal. It is capable of removing artifacts such as line noise, baseline drift and eye and head movements, all common in the p-health measurement domain [185].

3.6.3 Wavelet ICA (WICA)

WICA utilises both the wavelet transform and ICA in the removal of artifacts from the desired signal. The discrete wavelet transform (DWT) is unable to remove artifacts which overlap in the spectral domain, for example ECG artifact embedded on an EMG signal. ICA also has limitations as described above in Section 3.4.1. One main assumption and limitation is the requirement that the number of sources is equal to the number of measurement sensors. The method of wavelet ICA (WICA), as described in [9], combines the positive aspects of both independent algorithms to overcome some of their individual shortcomings. WICA can be used for single channel recordings due to the wavelets creating multi dimensional data from a single channel measurement as

described by Lin and Zhang in 2005 [115]. The DWT is first applied to the single channel recording. The resulting wavelet resolutions are analysed and the resolutions that contain artifacts components are manually selected. These artifact corrupted wavelet resolutions are then used to create a new data set which is used as the input to the chosen ICA algorithm. ICA is applied as specified in Section 3.4.1 and the components determined to be artifacts are removed. Wavelet reconstruction is then performed using both the unselected coefficients and the coefficients cleaned during the ICA step. This produces the multichannel signals with the artifact removed. Mijović *et al.* [129] demonstrated how this approach can be used to remove ECG artifacts from contaminated EMG recordings.

The WICA algorithm has currently only been compared to the basic ICA algorithm in [9] in which WICA showed a visual improvement in being able to remove the artifacts in the case where there were not enough redundant recordings. In the p-health domain, there is a greater likelihood that there will be a reduced number of recording sources and thus the WICA algorithms advantages become more relevant.

3.6.4 Empirical Mode Decomposition ICA (EMD-ICA)

As stated in Section 3.5.2 the EMD algorithm generates a decomposition of the data into IMF's. These IMFs can then be used as inputs to an ICA algorithm and the mixing and un-mixing matrices can be found [129]. The IC's corresponding to the artifact can be removed and the original signal minus the artifact can be obtained by adding all the new derived IMFs.

Ensemble EMD-ICA was tested against WICA and SCICA as a method for the removal of simulated artifacts from recorded physiological signals [129]. EEMD-ICA was seen to perform slightly better than the WICA algorithm (Relative Root Mean Square Error (RRMSE) ranging from 50.73 % to 64.79 % for EEMD-ICA and RRMSE = 66.22 % for WICA) at removing the artifacts from EMG and EEG data, with both outperforming the SCICA algorithm. As most biological signals are non-stationary and non-linear, the EEMD-ICA algorithm adapts itself effectively to real world situations.

3.7 Discussion and Conclusion

The requirement for algorithms, capable of removing the undesired artifacts from recorded physiological signals, has increased over the past number of decades due to the increased clinical usage of the recorded signals. This chapter has reviewed the most commonly

implemented artifact removal techniques in use today [181]. Although each technique differs in the manner in which it performs the artifact removal, it is possible to classify each technique into two distinct groups; those which directly remove the artifact signal from the desired signal of interest (Single stage techniques) and those which decompose the signal and artifact into individual sources but still require the use of additional techniques to identify the artifact components therefore facilitating their removal (Two stage techniques).

Single stage artifact removal techniques

Algorithms within the first group include adaptive filters, Wiener filter, Bayes filters, MCA etc. These algorithms use a number of different techniques to reduce the power of the artifact. For example the adaptive and Wiener filter use parametric and statistical methods respectively to reduce the mean squared error between the output $\hat{\mathbf{s}}(n)$ and the desired original signal $\mathbf{s}(n)$, i.e.

$$\min_{\mathbf{w}} \parallel \mathbf{s}(n) - \hat{\mathbf{s}}(n) \parallel^2, \tag{3.10}$$

MCA on the other hand separates the artifact signal from the desired signal using the assumption that the two signals have different morphological characteristics. As the basis contributing to the artifact is known, it can be automatically removed from the reconstructed signal post separation. Although the artifact removal process is different for each technique, when each technique belonging to this single stage group has completed, the artifact signal has been removed to the best ability of the particular technique and therefore no further processing is required.

Two stage artifact removal techniques

The algorithms belonging to the second group use a different methodology to reduce the effect of the artifact signal. These techniques do not reduce or remove the artifact signal themselves but instead decompose the signals into components such that artifacts and the desired signals are contained in different components. After separation these artifact components can then be removed, with the combination of the residual components generating the desired signal. Examples of algorithms within the second group include ICA, CCA and EMD. When employing techniques belonging to this second group the artifact components are not explicitly identified by the technique. Therefore further analysis is required to determine which components are artifacts. These techniques are

thus known as two stage techniques. This 2-stage requirement adds an extra level of complexity to the techniques. Section 4.7 describes a number of the currently available techniques for automatic artifact component identification which are used as the second stage of the techniques.

Table 3.1 (viewable at the end of the chapter) provides an overview of all the techniques described in this chapter and outlines under which of the two groups (single stage or two stage) each technique falls. It can be seen from the table that the adaptive filter is the sole technique analysed in this chapter which requires additional sensors for a reference signal. However, the inclusion of a reference signal to other techniques can also aid in their capability to accurately remove the artifact as is shown with the Kalman filter in Section 5.4. Although the single stage techniques do not require the use of additional techniques to remove the artifacts, the majority do require some input from the user prior to employment, such as the development of signal models or filter parameters. The majority of the two stage systems are incapable of operating on-line, due to the requirement for signal decomposition. For example, when using the EEMD algorithm, the signal is decomposed N times and so is incapable of operating in real time. This induced delay can be minimal however if short epoch of data are analysed (see Figure 6.17). However, with the use of automatic artifact selection techniques (Section 4.7) many of these techniques are capable of running in quasi real time, where there is a small delay between recordings and the output of the cleaned signals. Finally, only MCA and dynamical embedding SSA have yet to be shown be capable of operating in the non-linear domain.

Chapter 5 expands on some of the single stage techniques described in this chapter. The formulation of the Wiener and Kalman filters, the MCA algorithm and the adaptive filter are described and their efficacy is analysed using both fNIRS and EEG data. The chapter also describes a novel use of accelerometers to develop a data tagging algorithm and quality of signal (QOS) measurement which is capable of determining between different forms of contaminating artifacts [180] [179]. By doing so, the appropriate artifact removal techniques can be used for the particular artifact type. Chapter 6 continues by describing a number of the two stage methods (EEMD, wavelets, ICA and CCA). This chapter also describes the novel combination of the EEMD and wavelet algorithms with the CCA algorithm [182] allowing for more accurate removal of the contaminating artifacts. The chapter concludes by providing a comparison of the artifact removal techniques developed and analysed in the thesis.

Prior to the extended description and analysis of the techniques described in this chapter, Chapter 4 describes a novel recording methodology [177] developed to allow an accurate comparison of the efficacy of the different techniques. This methodology also

allows for an evaluation of the automatic artifact component identification techniques not previously available.

TABLE 3.1: A comparison of the advantages and disadvantages of various artifact removal techniques.

		No additional sensors required	No *a priori* user input required	Can operate on-line	Can operate single channels	Can operate in the non-linear domain
Single Stage	Adaptive filter	×	×	✓	✓	✓
	Wiener filter	✓	×	✓	✓	✓
	Kalman filter	✓	×	✓	✓	✓
	Particle filter	✓	×	✓	✓	✓
	Morphological Component Analysis	✓	×	×	✓	×
	Dynamical Embedding SSA	✓	✓	×	✓	×
Two Stage	Independent Component Analysis	✓	✓	✓	×	✓
	Canonical Correlation Analysis	✓	✓	×	×	✓
	Wavelet Transform	✓	×	×	✓	✓
	Empirical Mode Decomposition	✓	✓	×	✓	✓
	Single Channel ICA	✓	✓	×	✓	✓
	Dynamical Embedding ICA	✓	✓	×	✓	✓
	Wavelet ICA	✓	×	×	✓	✓
	Empirical Mode Decomposition ICA	✓	✓	×	✓	✓

Chapter 4

Methodology for Comparison of Artifact Removal Techniques

Since the introduction of electrophysiological recording, the contamination of the signal of interest by undesired artifacts has been a consistent hinderance. Researchers have been competing to determine the best algorithms or techniques to remove these artifacts for many decades and the search for the optimum artifact removal technique will continue for many more. A number of signal processing algorithms have been previously employed to remove motion artifacts from physiological signals [181]. One dilemma, faced by all researchers, when trying to remove motion artifact from the desired signal, is the lack of knowledge of the true form of the original (noise-free) signal. Without knowledge of this signal it is not possible to accurately determine the efficacy of a given artifact removal technique. It also proves to be difficult to perform a valid comparison of the different possible methods.

Currently, the efficacy of a particular artifact removal technique is most commonly calculated using either simulated data or artifact contaminated real world data. Simulated data generally consists of two components; real recorded physiological data, such as ECG or EEG signals, and an artifact segment which is either manually generated or recorded separately (for example 50/60 Hz hum [215] or EMG signals [46]). The complete simulated data signal can then be created by combining the two components in some known manner (i.e. linearly [46]). By creating an artifact contaminated signal using this simulation method, the true desired signal is known and thus the artifact removal techniques can be tested to determine how proficiently they each remove the artifact from the contaminated signal. However, the method of combining the true signal and the artifact signal is usually overly simplistic (i.e. purely linear) and thus the results are not directly comparable to real world data. The second method of data acquisition

uses real artifact contaminated recorded signals (e.g. fNIRS signals contaminated with motion artifact [87]). Although, using this method, the combination of the artifact and the desired signal is real, the researchers are incapable of acquiring any accurate knowledge of the true form of the underlying clean signal. The efficacy of the artifact removal techniques, when using this data type, is therefore most often quantified by a reduction of a particular evaluating metric, such as the SNR of the signal. Unfortunately, using this data type, researchers cannot accurately determine the effect that the artifact removal technique has on the true signal and thus the results may not reflect the true performance of the system.

This chapter details a novel recording methodology for physiological signals which facilitates a more accurate comparison of artifact processing methods alleviating some of the problems highlighted above. This novel methodology permits the recording of two separate but highly correlated channels [176] [177], allowing for the recording of a noise-contaminated and a noise-free signal concurrently. The noise-free signal, labeled the "ground truth" signal, can then be used by researchers for a number of different applications. Firstly, it can be used to test the efficacy of individual motion artifact removal techniques employed on the noise-contaminated data as the "true" underlying signal is now known. This can be seen as a combination of the two techniques currently used to analyse artifact contaminated data, in that the contamination of the artifact onto the signal is not simulated but the underlying signal is known. Therefore, the methodology also allows for an accurate comparison between a multitude of artifact removal methods, which was not previously attainable. Secondly, the new availability of this "ground truth" signal also permits methodical testing of the various automatic artifact component selection techniques required for the two stage artifact removal algorithms, as described in Chapter 3. Using the "ground truth" signal, the best case results can be determined for each of the artifact removal techniques as described in Section 4.7 and then the automatic component selection algorithms can be compared to this best case.

The artifacts analysed in this thesis are focused on those due to movement of the subject or recording optodes/electrodes as these are often the most detrimental to the signals. The described methodology therefore also incorporates accelerometer recordings, used to determine the time and magnitude of the induced motion. The information from these accelerometers can then be used for illustration purposes as well as a reference signal, as required in certain artifact removal techniques such as the adaptive filter technique, described in Section 5.6.

The remainder of the chapter describes the steps performed to record the required signals. The measurement systems used to record the analysed physiological signals are described in Section 4.1 followed by the novel experimental setup and protocol used to

record the required signals (Section 4.2). The chapter also describes the post-processing performed on all the recorded signals to ensure that they each adhere to the desired form.

In addition to the novel recording methodology, the chapter also discusses a number of different automatic artifact component selection techniques required by the two stage techniques reviewed in Chapter 3, and from these the best performing artifact component selection techniques for the EEG and fNIRS data are determined. Finally the techniques described in this thesis are also tested on synthetic data and the generation of this data is portrayed in Section 4.8.

4.1 Recording Systems

To detail and verify the new methodology proposed in this chapter, recordings using both EEG and fNIRS were acquired. In the sections below the two systems used to record the different data modalities are described.

4.1.1 fNIRS

A TechEn continuous-wave (CW6) system (TechEn Inc., USA) was used to record the change in both oxygenated and deoxygenated haemoglobin in the blood cells of the brain as described in Section 2.2.2. This system is capable of measuring up to 32 individual channels simultaneously. The input light intensity recorded at each individual detector is passed by optical fibre to the receiver module before being transported to the computer through the control module. A 16-bit successive approximation register (SAR) ADC was used to convert the analog data to digital and the sampling rate was set to 25 Hz.

The system uses a series of frequency encoded lasers as sources and an array of avalanche photo-diodes (APD's) as detectors. APD's are highly sensitive electronic devices that exploit the photoelectric effect to convert light to electricity. Each source optode is connected to two laser sources of differing wavelengths through a bifurcated fibre cable. The CW6 system uses source wavelengths of 690 nm and 830 nm for reasons described in Section 2.2.2. The output at each of the 32 individual source optodes is a modulation of the two chosen wavelengths at a different frequency (between 6,400 Hz and 12,600 Hz at 200 Hz spacing and a duty cycle of 50 %). The system is therefore capable of determining which source signal is being recorded at the detector site and allows each individual channel to be resolved independently. The typical power settings of the lasers is 12 mW for the 690 nm source and 6 mW for the 830 nm source, both

below the American National Standards Institute (ANSI) standard. The power required for the 690 nm source is greater than that for the 830 nm source as the lower frequency requires more power to obtain the same penetration into the tissue.

4.1.2 EEG

A BioSemi ActiveTwo biopotential measurement system (BioSemi Inc., Netherlands) was used to record the electrical impulses in the brain as described in Section 2.2.1. The system is capable of recording up to 256 channels of EEG concurrently with a user defined sampling rate of 2, 4, 8 or 16 kHz per channel. The recorded channels are passed through an analog-to-digital converter (ADC) before being multiplexed into a serial data stream. This data can then be passed, through an optical cable to a USB2.0 receiver before finally being connected to the PC for post processing.

The raw EEG signals are recorded using active electrodes, thus offering a solution to some of the environmental artifacts described in Section 2.3.1 such as high electrode impedance and cable shielding. The silver-silver chloride (Ag-AgCl) sintered electrodes have an integrated amplifier stage which allows for an output impedance lower than 1 Ohm and therefore measurements with extremely low noise levels are possible. Further, due to the use of the active electrodes, common procedures such as skin abrasion are no longer required. A highly conductive electrolyte gel (see Figure 2.9) should be used for all measurements as it ensures that there is a satisfactory connection between the electrode and the scalp.

The BioSemi ActiveTwo system makes use of both the common mode sense (CMS) and the driven right leg (DRL) electrodes. These electrodes are used to drive the average potential of the patient as close as possible to the ADC reference potential. This ensures that the common mode voltage (the average potential of the subject) is within the normal range of the ADC. The CMS is usually placed around the top of the head (approx. Cz on the 10-20 system - see Figure 4.1) however the exact position is not overly critical. The DRL electrode can be connected to anywhere on the body away from the location of recording.

4.1.3 Accelerometer Data

The acceleration data was collected in conjunction with the EEG and fNIRS data to allow for accurate visualisation and tagging (see Section 5.1) of the time, magnitude and direction of the induced motion as well as acting as a reference for some artifact

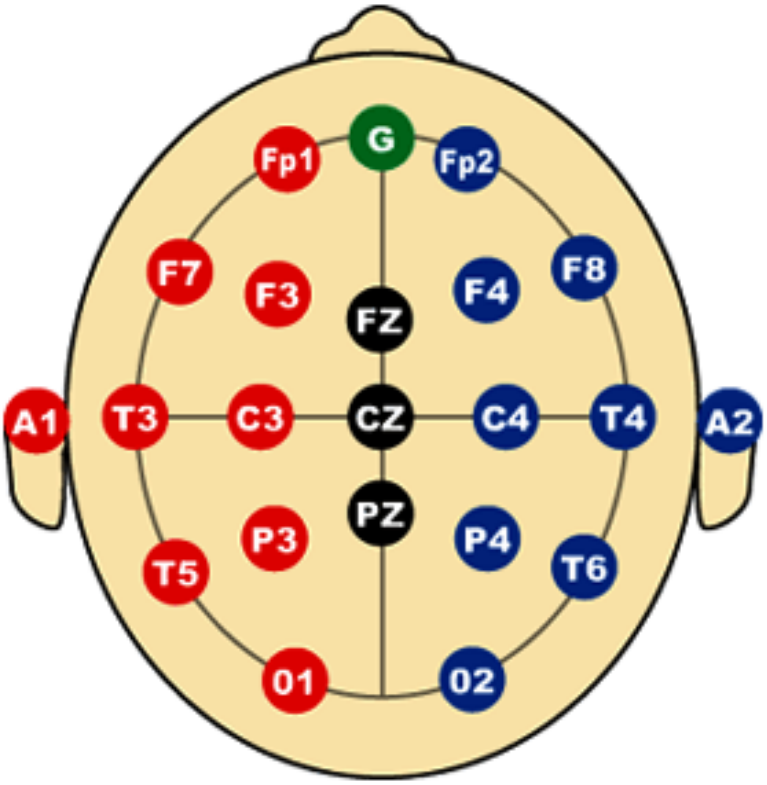

FIGURE 4.1: The International 10-20 electrode placement.

removal, techniques such as the adaptive filter. The accelerometer employed was the Analog Devices ADXL327 (Analog Devices Inc., USA). This is a low-power, complete tri-axial accelerometer with signal conditioned voltage outputs. It has a minimum full scale range of ±2 g and is capable of recording both the static acceleration due to gravity and the dynamic acceleration resulting from motion. The full specifications of the accelerometer are available in Appendix B.

The outputs of the accelerometers are passed to a fabricated circuit to perform some basic processing steps before progressing to the PC. The first stage of the circuit consists of an input buffer. This buffer is required to stop any loading effects on the accelerometer outputs due to their low output current and high impedance. The second stage of the circuitry encompassed a summing amplifier to remove the DC offset. The DC offset has to be removed prior to the amplification of the signal to ensure the signal does not become saturated. As the frequency of the accelerometer signal can be quite low, a very high order filter would be required to remove the DC offset without affecting the desired frequencies. Therefore instead of employing a filter, a simple summing amplifier was used to remove the offset from the signal. The third stage of the circuitry applied a gain to the system using an instrumentation amplifier (INA114) and the gain was set to 35. Finally the output signal was passed through a low pass filter circuit for anti-aliasing

purposes. A schematic of the circuitry described above for the three channels (i.e. x,y,z axis) can be found in Appendix B.

The output of the accelerometer circuitry is then connected to a PC-based data acquisition system (Humusoft S.R.O., Czech Republic). The data can then be read into the PC using the real-time Simulink toolbox in MATLAB (2008b, The Mathworks Inc., Natwick, MA) at a sampling frequency of 200 Hz, where it is stored for later processing as described in Section 4.3.

4.2 Recording Methodology

This section describes the novel experimental setup of the equipment used to record the fNIRS and EEG data. It also details the protocol adhered to during recording to ensure that the measured data encapsulated the ideology of the methodology. Recording of the two modalities (EEG and fNIRS) was performed independently.

4.2.1 fNIRS Experimental Setup

The fNIRS optodes are held in position using a housing called a probe. These probes can be designed to encase any number of source and detector optodes. An example probe, used to house a single source and detector, is shown in Figure 4.2. The plastic housing, comprised of low-density polythene, allows for a rigid and secure connection between the fNIRS optode and the head; however it is also flexible and therefore capable of reforming to the curvature of the head. This plastic housing is backed by a polyurethane foam which grants a more comfortable fit for the user. The probe can then be attached to the head in the required position using the attached velcro straps.

The purpose of the methodology is to record two highly correlated signals concurrently; one noise-contaminated and the second noise-free. The aim is to acquire a "ground truth" signal for the artifact corrupted signal, thus allowing for accurate testing of the various artifact removal techniques. To be capable of fulfilling this aim there is a necessity for two separate recording optodes, so the artifact induced to one will have no effect on the second. The first probe encompasses both a source and detector optode, as can be seen on the lower strap of Figure 4.3. The spacing between the two optodes is set rigidly to 30 mm conforming with common practice. The second detector is housed on a separate probe which is not coupled to the first, save the coupling through the head itself. This second detector is strategically positioned above the first, as shown in

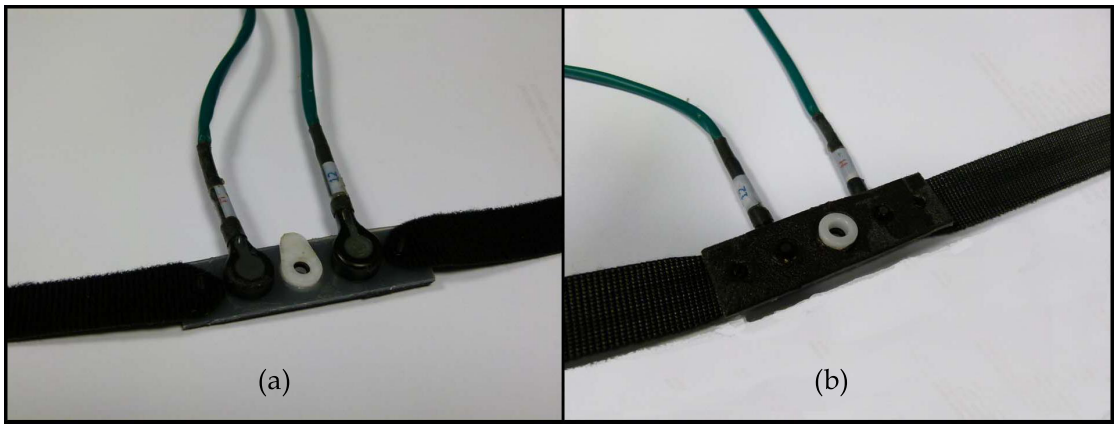

FIGURE 4.2: An example probe used to house the fNIRS source and detector optodes. (a) presents the front of the probe while (b) shows the back, which is in contact with the subjects scalp.

Figure 4.3, so as to preserve the 30 mm inter-optode spacing between it and the source optode on the lower probe. Moreover, the spacing between the detectors is kept very small (approx. 20 mm) so that the overall monitored volume within the head highly overlaps between these two channels. The distance between the centroid points of each source-detector pair is approximately 10 mm. Section 4.6 details the importance of having this distance between centroids as small as possible.

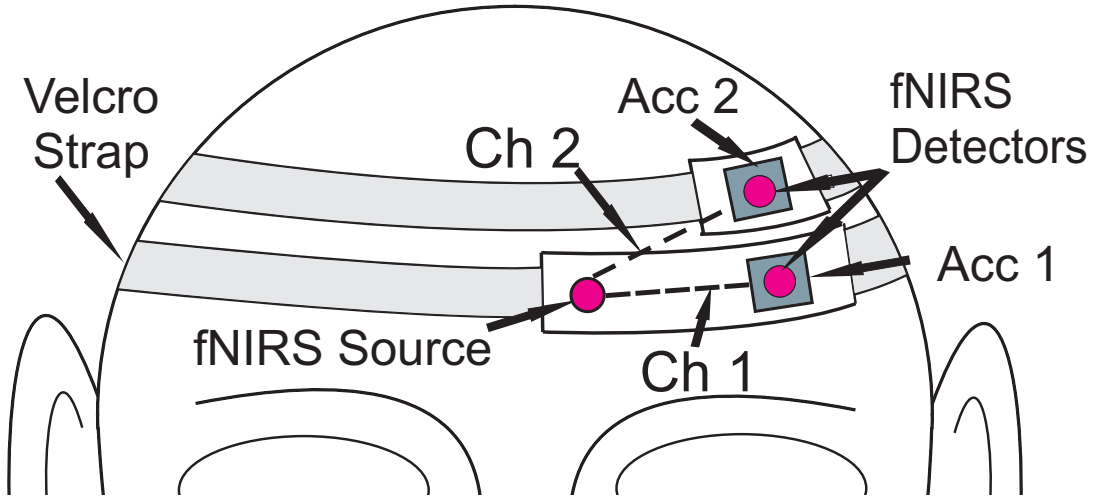

FIGURE 4.3: Positioning of the fNIRS optodes and the accelerometers.

As stated previously, the two accelerometers utilised during the experiment are employed to determine a measure of the differential acceleration of the detector optodes. To accomplish this, one accelerometer is placed securely onto each individual detector as shown in Figure 4.3. Any differential acceleration between the two accelerometer outputs can now be used to determine the motion induced on the detectors. Care is taken to ensure the orientation of each individual accelerometer is kept consistent with

respect to the other. When the system is connected to the subject, the leads of the fNIRS system and the accelerometers are secured to ensure that there is no undesired movement of the recording optodes. It should be again noted that the two detectors and accelerometers are not directly coupled (i.e. not on the same probe) and therefore the movement of one will have little or no effect on the position of the second.

4.2.2 EEG Experimental Setup

The setup of the EEG experiment is similar to that of the fNIRS experiment. The EEG (Ag-AgCl) active electrodes, used to record the two separate channels, are secured to the scalp of the subject using a 256 array electrode cap (Electro-cap International, Inc., USA) shown in Figure 4.4. The cap covers the cranium and is held in place using the available chin strap. The cap is manufactured using a fabric material allowing for the movement of a single electrode without altering the position of any of the adjacent electrodes. The spacing of the recording electrodes is fixed by the cap at 20 mm allowing for the two channels to be recorded in close proximity as required by the methodology. The close proximity ensurers that the recorded signals are as correlated as possible as described in Section 4.6.

FIGURE 4.4: The 256 array electrode cap used to house the EEG electrodes. (Electro-cap International, Inc., USA)

Electrolyte gel is placed below each electrode prior to recording to ensure that the electrode maintains the required coupling with the scalp as outlined in Section 2.2.1. Similar to the fNIRS experiment, the two accelerometers are attached to the individual recording electrodes, again ensuring that the orientation of each individual accelerometer is kept consistent with respect to the other. The accelerometers will record the acceleration of each electrode and therefore any differential acceleration between them.

4.2.3 fNIRS Experimental Protocol

fNIRS measurements were obtained from ten healthy subjects in order to demonstrate the validity of the proposed methodology. The cohort comprised of 4 males and 6 females (mean age: 29 years, standard deviation: 5.62 years). Each recording resulted in two useable trials for each channel due to recording at the two wavelengths (690 nm and 830 nm). Therefore in total, 4 signals were recorded simultaneously for each subject; 690 nm and 830 nm light intensities for both Channel 1 and Channel 2. Recording took place in a contained room with no natural light to reduce the possibility of contaminating artifacts due to light contamination as described in Section 2.3.2.

The 3 fNIRS optodes (1 source and 2 detectors) were positioned on the left pre-frontal cortex of each subject, as illustrated in Figure 4.3. This particular optode positioning was chosen to reduce the possibility of contamination of the signal due to interference by the subjects hair. If positioned elsewhere on the head, the movement of the optodes could allow hair to fill the space between the optode and the scalp and thus disrupt the baseline signal. Further, as the methodology proposed is designed to allow for the recording of two highly correlated signals, one with and the second without motion artifact contamination, the underlying cortical activity was not of significance. Therefore the positioning of the recording optodes was not of great concern and was chosen so as to invoke the least number of complicating issues. In addition, the subjects were not required to perform any specific activity for the duration of the experiment as again the cortical activity itself was not of importance.

Due to the setup of the new methodology, the two channels were recorded in close proximity. As the fNIRS optode measures from the volumetric region in between the light source and detector [8], by using the same light source and two separate detectors in close proximity, the optode measurement volumes overlap and the measured cortical activities are expected to be highly correlated for the two optodes. Each individual trial of the experimental session lasted a total of 9 minutes. At regular 2 minute intervals the experimenter induced a positional disturbance to the detector attached to Accelerometer 2 for a random duration of between 10 and 25 seconds. This source detector pairing

was labeled Channel 2 (Figure 4.3). This slight disturbance, which was performed manually by pulling on the optode cable, induced motion artifact on Channel 2. However, as the detector optode, connected to Accelerometer 1, and the source optode were not disturbed, Channel 1 remained free of contamination throughout the duration of the experiment. This result can be observed in the optical density plots in Figure 4.5. A spectrogram of the data in Figure 4.5 is shown in Figure 4.6. The artifact signal is visible in Channel 2 at the time epochs highlighted in Figure 4.5, and it is also possible to see that the artifact resides in the frequency band of the desired fNIRS signal making it impossible to remove using simple filtering techniques alone.

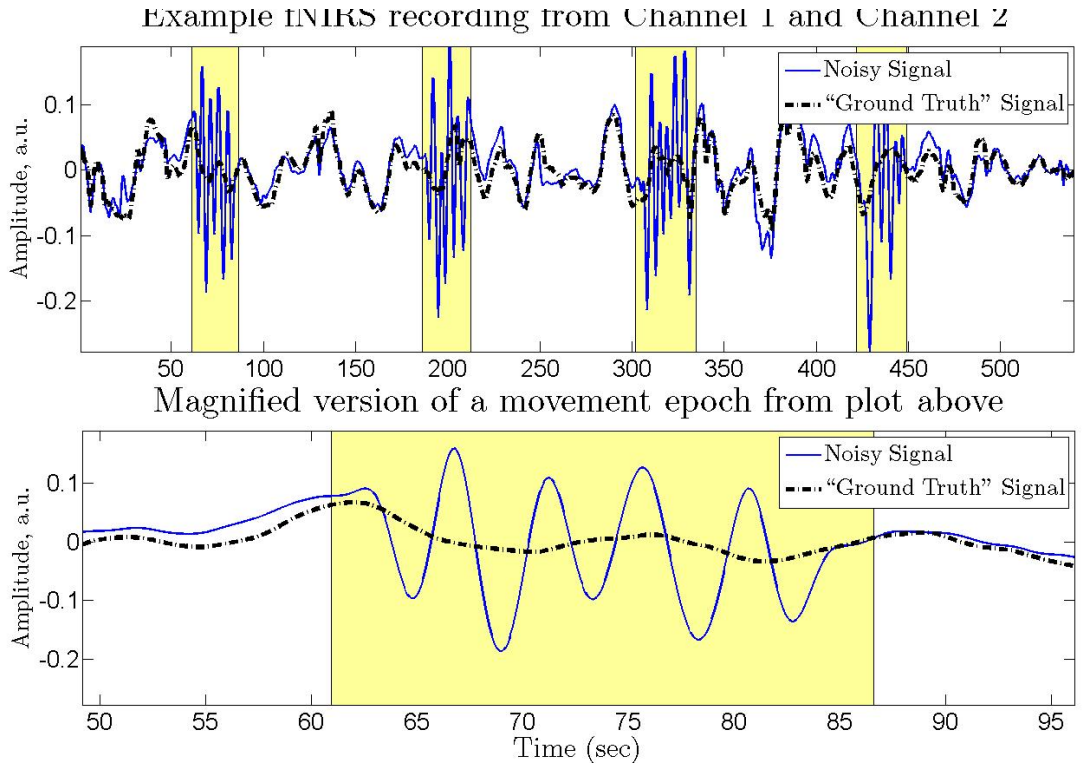

FIGURE 4.5: An example output from an fNIRS recording. The plot shows the optical density values for the 830 nm signal. The shaded sections highlight the regions containing motion artifact as determined using the tagging algorithm described in Section 5.1. Average correlation over clean epochs for trial shown: 0.87. Average correlation over movement epochs for trial shown: 0.31.

The sections of the signal which are not shaded in Figure 4.5 are epochs of motion free data where Channel 2 can be observed to follow the output of Channel 1 closely. The epochs of corrupted data (shown in highlighted sections) were determined using a simple tagging algorithm [179] using the available data outputted from the accelerometers (see Section 5.1).

Tamura *et al.* [183] describes the use of NIRS trajectory plots to better understand the different brain activities engaged at given points in time. The NIRS trajectory uses

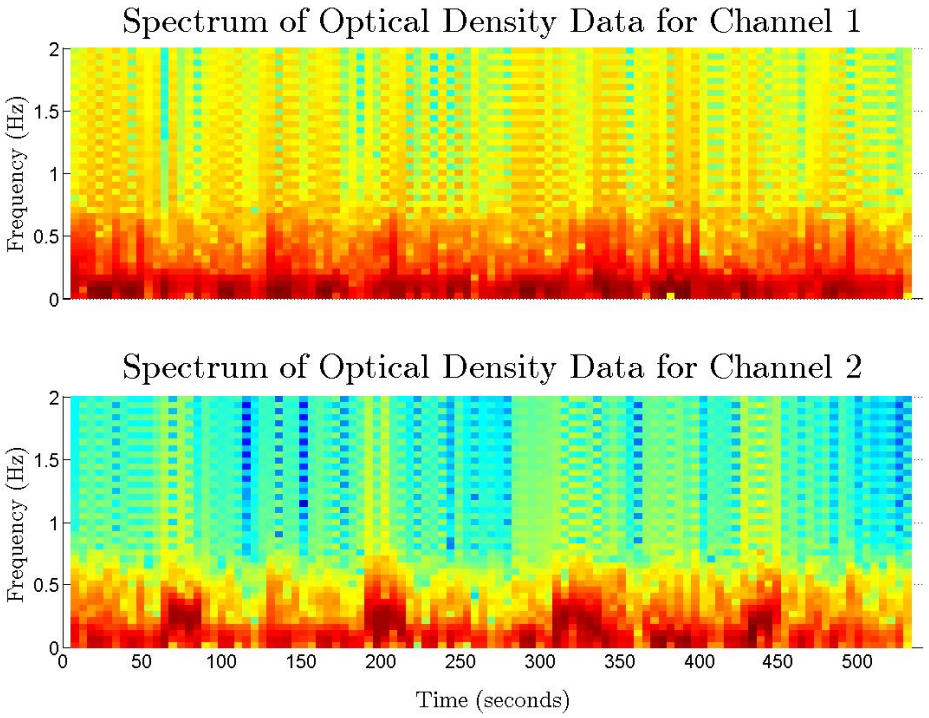

FIGURE 4.6: Spectrogram of the two channels of fNIRS data from Figure 4.5.

both the oxygenated (HbO) and the de-oxygenated (Hb) haemoglobin to create a plot of their variation over time. These plots can then be used to easily demonstrate the phase of the signals. If the signals are out of phase (i.e. HbO = -Hb) then the trajectory will have an average slope of -1. Due to the setup of the experiment protocol, there will be a low level of blood flow into the area being monitored. In these situations the trajectory plot often reflects the diagram typical to oxygen consumption and deoxy Hb production, which have round cocoon like shapes. An example of this can be seen in Figure 4.7(a) where the trajectory plot is displayed for Channel 1 for the trial shown in Figure 4.5. Figure 4.7(b) shows the trajectory plot for the artifact contaminated data. It can be clearly seen that when the artifact signal is present, the HbO and Hb signals become highly correlated and thus the trajectory plot has a positive slope of approximately 1. These plots can therefore be very useful in displaying the success of the artifact removal techniques employed.

Before each individual recorded trial (combination of "ground truth" and noisy signal shown in Figure 4.5) was selected for use in analysing the different algorithms, the artifact contaminated signal was analysed against its corresponding "ground truth" signal. Signals whose clean epochs had an average correlation lower than 0.65 (calculated using the Pearson product-moment correlation coefficient and decided upon empirically) with the corresponding epoch of the "ground truth" signal were discarded. This ensured

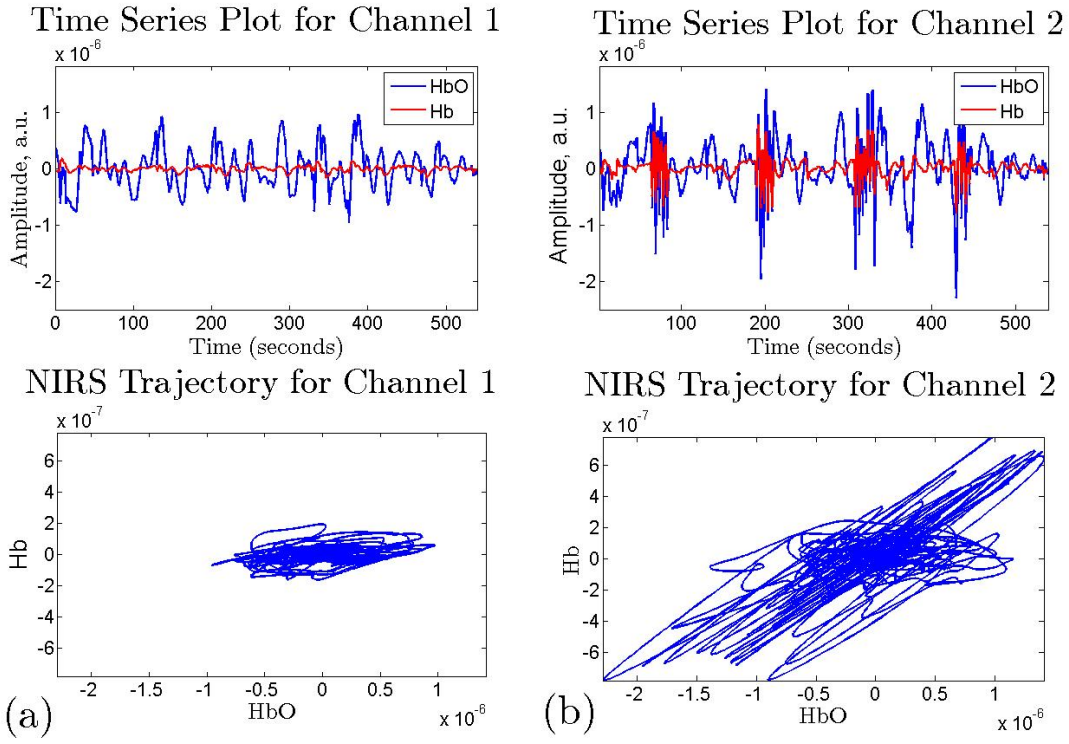

FIGURE 4.7: NIRS trajectory plot for the data shown in Figure 4.5. (a) "Ground Truth" signal recorded from Channel 1. (b) Artifact contaminated signal recorded from Channel 2.

that only the most correlated signal pairs were employed to analyse the artifact removal techniques. Low correlation values during the clean epochs could be due to many factors including poor connection between the optode and the skin.

Following the removal of the low correlated trials there remained 16 fNIRS trials for analysis. These 16 trials were calculated to have an average correlation (r) of 0.77 (std = 0.2) during motion free epochs over all trials. However the average correlation over the full signal for all trials is significantly lower (r = 0.58, std = 0.16) due to the intermittent presence of motion artifacts. Over all trials it has been calculated that motion artifacts are deemed to be present in 19.75 % of the data.

4.2.4 EEG Experimental Protocol

EEG recordings were obtained, over 4 sessions, from 6 healthy subjects (mean age: 27 years, standard deviation: 4.29 years) resulting in 24 useable trials. The cohort consisted of 3 males and 3 females. Two channels of EEG were simultaneously recorded from the frontal cortex from positions FPz and FP1h (using the 10-5 system as described in [145]), labeled Channel 1 and Channel 2 respectively. The DRL (Driven Right Leg) and

CMS (Common Mode Source) electrodes were placed at positions P2 and P1 respectively using the 10-20 system.

Similar to the fNIRS recording, an understanding of the underlying EEG signals was not important in this study and thus subjects were not required to perform any cognitive activity during recording. During experimentation each subject was instructed to keep their eyes closed and to maintain a stationary head position throughout the experiment, therefore limiting the number of artifacts originating from sources such as eye blinks, saccades and head motion (Section 2.3.3). The sources of artifact arising from eye movement were of no consequence when recording the fNIRS data due to the optical nature of the recording, however, when recording the EEG signals these artifacts could contaminate both signals (i.e. "ground truth" and artifact contaminated) in a distinct manner and thus reduce the effectiveness of the methodology. Again, each trial lasted a total of 9 minutes with motion induced to Channel 2's electrode at regular 2 minute intervals. This motion artifact was induced by mechanically disturbing the electrode by pulling on the connecting lead. An example output from the two channels can be observed in Figure 4.8 with the corresponding spectrogram provided in Figure 4.9.

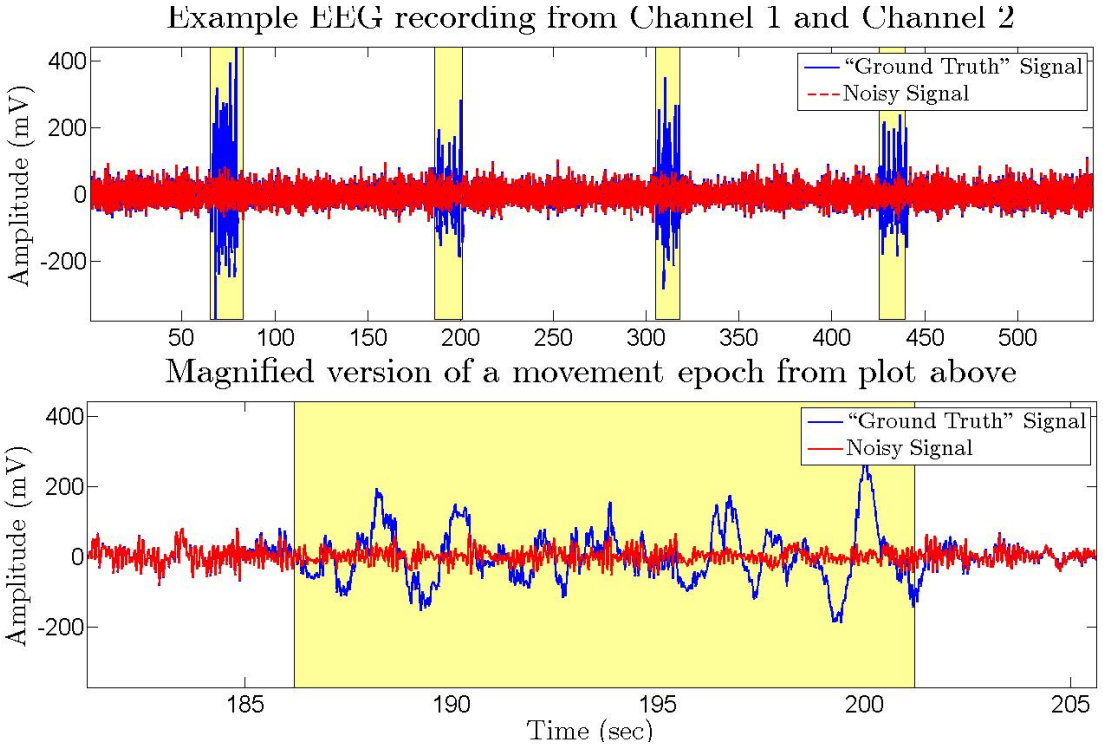

FIGURE 4.8: An example output from an EEG recording. The shaded sections highlight the regions containing motion artifact as determined using the accelerometer data. Average correlation over clean epochs for trial shown: 0.83. Average correlation over movement epochs for trial shown: 0.09.

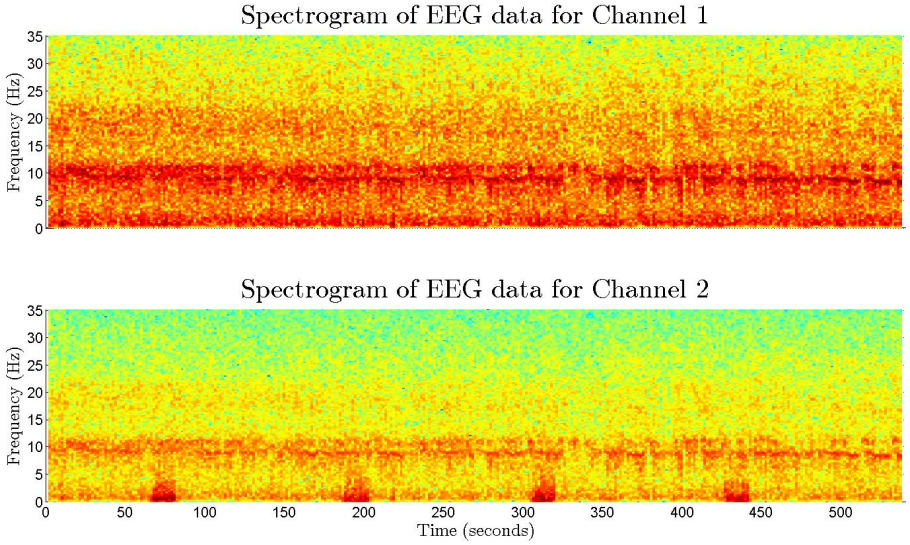

FIGURE 4.9: Spectrogram of the two channels of EEG data from Figure 4.8.

During epochs of no motion the two recording channels were calculated to have an average correlation coefficient (r) of 0.83 (std = 0.2) over all trials but this value again drops (r = 0.40, std = 0.19) when analysing the full signal due to the presence of artifacts. The artifact components are present in 15.74 % of the total recorded data.

4.3 Postprocessing of Recorded data

Following the recording of the EEG, fNIRS and accelerometer data a number of post processing techniques were performed to ensure that each trial was consistent (in terms of length, frequency spectrum etc) prior to further analysis to allow for accurate comparisons. The following section will describe the multiple processing steps undertaken on each modality for each of the individual recorded trials.

4.3.1 Triggers

When recording signals of different modalities using different recording equipment it is very important to be able to determine a consistent start and end point for the recorded data. This ensures that when analysing the data for a particular event in the EEG data, for example, the corresponding event recorded in the accelerometer data can be accurately selected.

A program (compiled using Visual C#) was used to generate a trigger signal which was then capable of signifying the start and end of the experiment. The program outputs

a pre-determined voltage, on the parallel port of the PC, depending on the current state of the trigger. This trigger signal is then available to each individual modalities recording equipment. Before beginning and following the conclusion of the experiment, a voltage of 0 Volts (V) is outputted by the trigger. When the trigger signal is activated by the program, signaling the commencement of the experiment, the output voltage increases to 5 V.

The output signal from the parallel port can be read in simultaneously by the employed recording equipment (i.e. the EEG and accelerometer recording devices or the fNIRS and accelerometer recording devices). In doing so, the start and end times of each of the recordings can be aligned accurately in the time domain after post processing the data as described below.

4.3.2 EEG Post Processing

In comparison to the other recordings employed, the EEG data did not require a great deal of post processing prior to being employed in the analysis. The first step undertaken was to filter the EEG data so as to analyse only the frequency range of interest. It has been previously documented that the primary frequencies of interest recorded by the EEG lie below $\sim$ 35 Hz, which are often grouped into pre-defined frequency bands (Delta: up to 4 Hz, Theta: 4-8 Hz, Alpha: 8-13 Hz, Beta: 13-35 Hz). The EEG data was therefore filtered using a 2^{nd} order butterworth bandpass filter with a low frequency cut-off of 0.5 Hz and a high frequency cut-off of 35 Hz. The 0.5 Hz cut-off frequency removes any DC drift affecting the underlying signal while the 35 Hz cut-off removes all un-desired high frequency components.

Following the filtering of the data, it is truncated to correspond to the information in the trigger signal. The Bio-Semi recording system has an available trigger input port and so a trigger signal is recorded at the same sampling frequency as the EEG. Only the EEG data which is recorded when the trigger is high is retained. Following the truncation of the data, it was next down-sampled to reduce the sampling frequency from 2048 Hz to 80 Hz to reduce data size. This new sampling frequency was chosen in order to reduce the overall number of samples in the recording while still remaining above the Nyquist frequency (twice the highest frequency component in the signal), ensuring that all required frequency components could still be reconstructed. Figure 4.10 shows an example of all the post processing steps undertaken for one recording of a contaminated EEG channel.

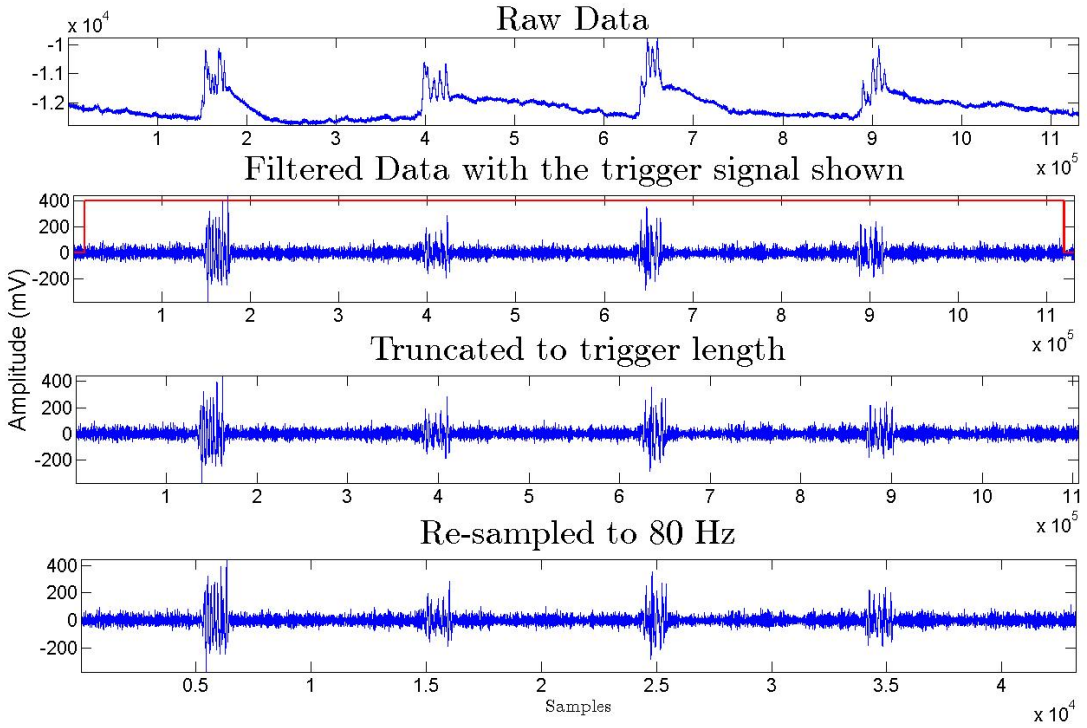

FIGURE 4.10: Post processing steps undertaken with each trial of the EEG data.

4.3.3 fNIRS Post Processing

When analysing the fNIRS data in this thesis, two separate representations of the data were used. The first representation was the change in optical density at the two wavelengths, namely ΔOD_{690} and ΔOD_{830}. The second form presents the change in concentration levels of the oxygenated and deoxygenated haemoglobin in the blood, namely ΔC_{HbO} and ΔC_{Hb}. The former representation was employed in analysing the artifact removal techniques while the latter was primarily used for illustration.

The fNIRS TechEn CW6 system records the raw intensity of the light received from the source (I) that has passed through the scalp at a sampling rate of 25 Hz. This raw data is first bandpass filtered using a 4^{th} order butterworth filter with a low frequency cut-off of 0.01 Hz and a high frequency cut-off of 0.4 Hz. These frequencies were chosen to remove any DC drift present in the signal and also any higher frequency fluctuations due to heart-beat and respiration. Following the filtering of the data, the amended signals were next truncated to the length of the trigger signals, processed in the same manner as that performed for the EEG data. This again insured that the analysed data would be aligned correctly in time with the accompanying accelerometer data. The optical density values (also known as absorption (A)) for the 690 nm and the 830 nm data could then be calculated using

$$\begin{aligned} \Delta OD_{690,830} &= -\log_{10}(I_{690,830}) \\ A &= \begin{bmatrix} \Delta OD_{690} \\ \Delta OD_{830} \end{bmatrix}. \end{aligned} \tag{4.1}$$

In order to perform the next step and to calculate the change in concentration levels of ΔC_{HbO} and ΔC_{Hb} the modified Beer Lambert law (MBLL) described in Equation 2.2 must be implemented. A rearranged form of this equation is shown below.

$$\begin{aligned} C &= \frac{1}{\alpha}\left(\frac{A}{BL}\right) \\ C &\equiv \begin{bmatrix} \Delta C_{Hb} \\ \Delta C_{HbO} \end{bmatrix}. \end{aligned} \tag{4.2}$$

The parameter (L), known as the path length, is calculated as the distance between the source and detector for that particular channel. When setting up the recording, using the TechEn CW6 system, the source and detector optode positions are defined and this information is outputted by the system in conjunction with the transfer of the recorded data. The path length can therefore be easily calculated using the simple Euclidean distance formula. The differential path length (B) is a pre-selected number used to describe the adjustment of the path length due to the curvature of the light through the scalp, set to 6 for fNIRS recordings. Finally, the extinction coefficients (α) are a set of coefficients that have been pre calculated to describe the absorption of light at specific wavelengths for specific media [41].

Once the change in ΔC_{HbO} and ΔC_{Hb} have been calculated the corresponding overall change in blood volume (BV) can be easily determined as:

$$BV = \Delta C_{HbO} + \Delta C_{Hb}. \tag{4.3}$$

An example of the post processing steps taken for a single trial of the fNIRS data is provided in Figure 4.11.

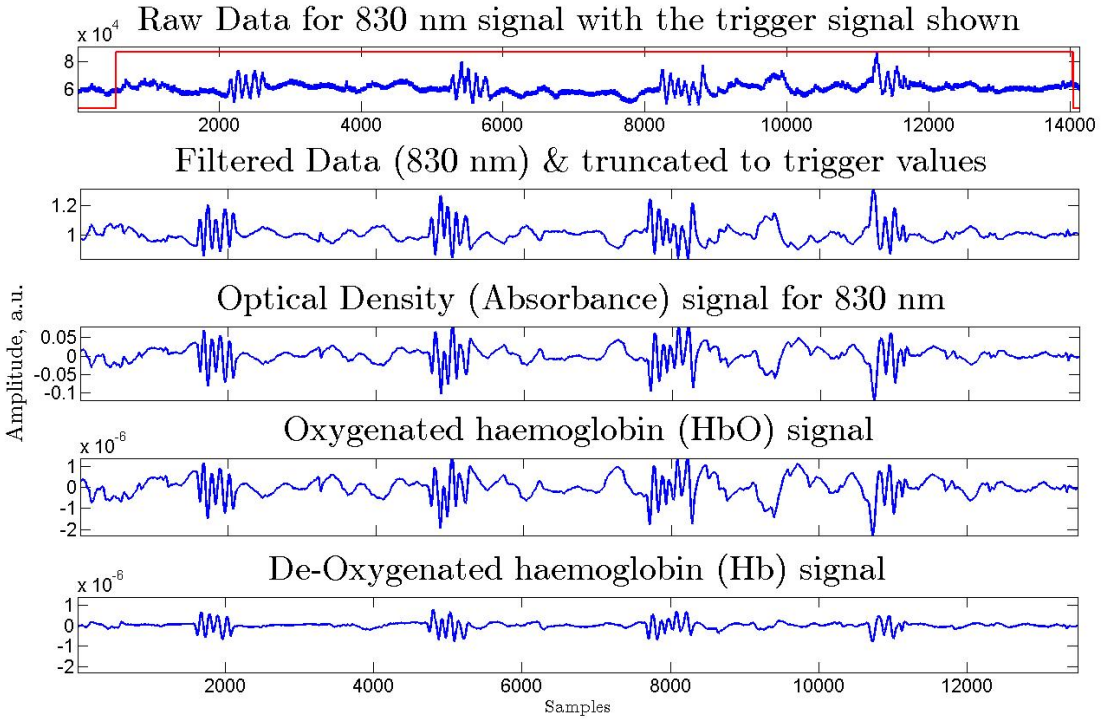

FIGURE 4.11: Post processing steps undertaken with each trial of the fNIRS data.

4.3.4 Accelerometer Post Processing

The recorded accelerometer data is primarily used for data tagging, which is used for illustration purposes (to show where the motion artifact was induced into the signal) as can be seen in Figure 4.5 and Figure 4.8. However, the data can also be employed as a reference signal for the reference aided artifact removal techniques (e.g. an adaptive filter). The additional processing steps taken to generate this reference signal are not described here but instead are described in the section relating to the use of the adaptive filter (Section 5.6).

The raw accelerometer data was first bandpass filtered using a 4^{th} order butterworth filter with cut-off frequencies of 0.05 Hz and 2 Hz. The low-pass frequency was chosen to remove the DC offset of the signal and the high-pass cut-off frequency was chosen as it removed the undesired high frequency components while still encapsulating the frequency content of the movement of the optodes/elecrodes. The filtered data was next truncated using the available trigger information which was read in using the Humusoft card. The accelerometer data was then re-sampled to the sampling rate of the methodology being used (80 Hz for EEG or 25 Hz for fNIRS).

As the interest surrounds the differential acceleration of the optodes/electrodes, i.e. how one optode/electrode moves in relation to the other and therefore with respect to the

underlying skin, the differential acceleration of the accelerometers must be calculated. To begin, the differential acceleration (DA) over each individual axis is calculated by simply calculating the difference between the two filtered outputs and then the overall differential acceleration was calculated as follows:

$$\mathrm{DA}_{x,y,z} = \mathrm{Acc1}_{x,y,z} - \mathrm{Acc2}_{x,y,z} \tag{4.4}$$

$$\mathrm{DA} = \mathrm{DA}_x + \mathrm{DA}_y + \mathrm{DA}_z. \tag{4.5}$$

As the output signals from the accelerometer have a very small amplitude, the baseline noise can often cause problems, therefore to combat this the low amplitude noise is removed from the signal by setting all values below an empirically calculated threshold to zero. Figure 4.12 displays the steps taken in the post processing of the accelerometer data.

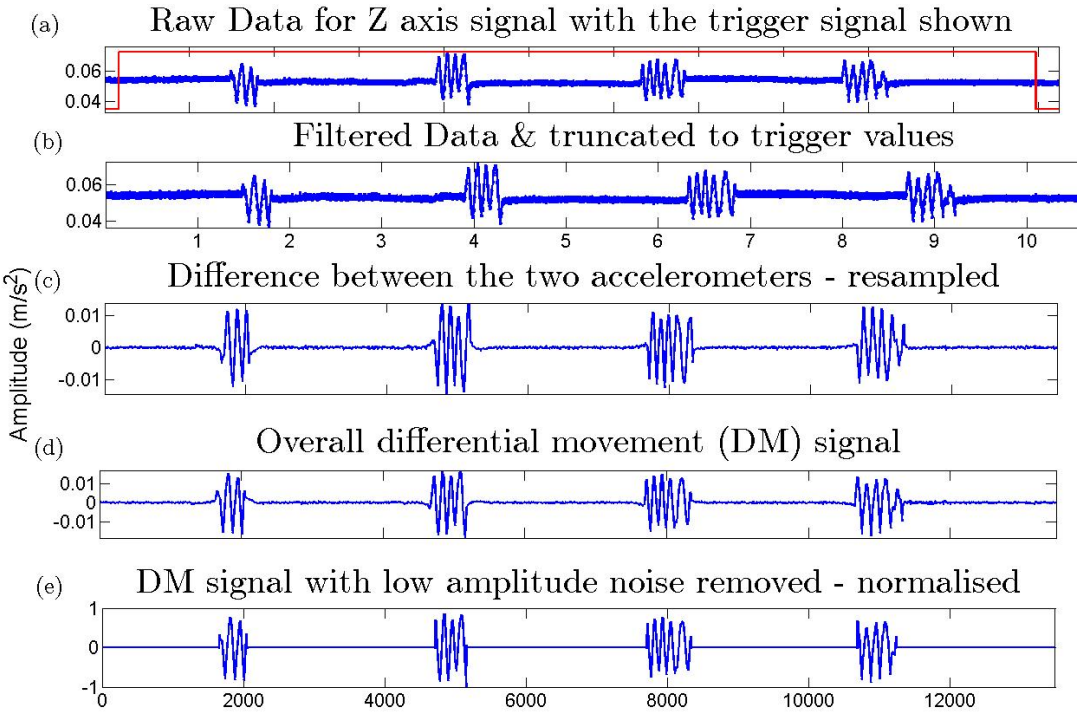

FIGURE 4.12: Post processing steps undertaken with each trial of the accelerometer data. The accelerometer data shown here was recorded from the same trial as the fNIRS data in Figure 4.11. Plots (a-c) show the outputs for the Z-axis only, whereas plots (d,e) represent the overall differential acceleration (i.e. Equation 4.4)

4.4 Split of Training and Testing Data

This section provides a brief overview as to the initialisation of the training and test datasets used throughout the thesis. When analysing each of the individual techniques, a separate training and test dataset is imperative to ensure that over-fitting of the data does not occur. This split allows the various analysed techniques to be trained on a small portion of the available data whilst the results are presented from a separate independent test dataset.

For both the fNIRS and EEG data, two recorded trials were randomly selected to represent the training data. This resulted in 14 fNIRS trials and 22 EEG trials to be available to be used as the test dataset. The training data is used in a different manner for each technique. For example, each of the single stage artifact removal techniques described in Chapter 5 require the use of the training data to initialise some model parameters *a priori*, whilst the two stage techniques described in Chapter 6 only require the training data to determine the optimum threshold value for the automatic artifact component selection techniques. In each of the techniques analysed in this thesis, a brief description will be provided as to the use of the training data to initialise the required parameters.

4.5 Efficacy Metrics

In order to fairly compare any artifact removal techniques employed on data recorded using the recording methodology described in this chapter, the following two efficacy metrics will be employed. The signal-to-noise (SNR) of a signal is a commonly employed metric which is used to specify the power of the signal with respect to the power of the contaminating noise. A SNR value greater than 0 dB indicates that the power of the signal is greater than the power of the noise. Using the SNR metric, the improvement in a signals SNR post artifact removal can be calculated using a metric known as Δ SNR [87]. First, SNR is commonly defined as:

$$SNR = 10 \log_{10} \left(\frac{P_{signal}}{P_{noise}} \right). \tag{4.6}$$

However, a signals power is equivalent to its variance when the signal has zero mean (i.e. $\sigma_x^2 = P_x - \mu_x^2$). Therefore the signal variance can be used to calculate the Δ SNR metric (the difference between the SNR after artifact removal and the SNR before) when the signals are known to have zero mean using the following formula [87]:

$$\Delta SNR = 10\ \log_{10}\left(\frac{\sigma_x^2}{\sigma_{e_{after}}^2}\right) - 10\ \log_{10}\left(\frac{\sigma_x^2}{\sigma_{e_{before}}^2}\right) \tag{4.7}$$

where σ_x^2 is the variance of the "ground truth" signal and $\sigma_{e_{before}}^2$ and $\sigma_{e_{after}}^2$ are the variances of the error signal before and after employing the artifact removal technique. The error signal is determined as the difference between the noisy signal and the "ground truth" recording, assuming that the motion artifact is additive.

In order to describe the signal improvement more comprehensively a second metric, based on the correlation function, was also employed. This metric, namely the percentage reduction in artifact λ, is used to describe how the correlation between the contaminated signal and the "ground truth" signal changed following the use of the artifact removal techniques, and is defined as:

$$\lambda = 100\left(1 - \frac{R_{clean} - R_{after}}{R_{clean} - R_{before}}\right). \tag{4.8}$$

Here R_{before} is the correlation between the full "ground truth" (clean) signal and the artifact contaminated signal, whereas R_{after} is the correlation of the full "ground truth" signal with the contaminated signal following processing by an artifact removal algorithm. R_{clean} is calculated as the correlation between the "ground truth" and noisy signals but only over the epochs of known clean data (i.e. the non-shaded areas of Figure 4.5 and 4.8) and is an estimate of the maximum achievable correlation between the two signals for the experimental setup considered. As such, the denominator of Equation 4.8 is the improvement in correlation possible if complete artifact removal is achieved while the numerator is the actual correlation improvement obtained for a given artifact removal technique. A high λ therefore equates to good efficacy in artifact removal.

4.6 Importance of electrode/optode distance

In Section 4.2 the experimental setup for recording both the EEG and fNIRS data was described. During the description of the steps, it was stated that the electrodes/optodes should be positioned as close as possible to each other to ensure that the underlying signals were as correlated as possible. By ensuring these signals were highly correlated, the assumption that the clean signal available from Channel 1 could be employed as a "ground truth" signal for Channel 2 becomes legitimate.

Figure 4.13 shows how the correlation values of the recorded signals change with increasing distance between the recording electrodes. A similar plot is shown in Figure 4.14 for the fNIRS data. It can be seen from both figures that as the distance between the recording electrodes/optodes increases, the correlation between the underlying signals decreases. Therefore, in order to confidently assume that the "ground truth" signal from Channel 1 provides an adequate reference signal for the underlying true signal from Channel 2, the distance between the electrodes/optodes should be kept to a minimum.

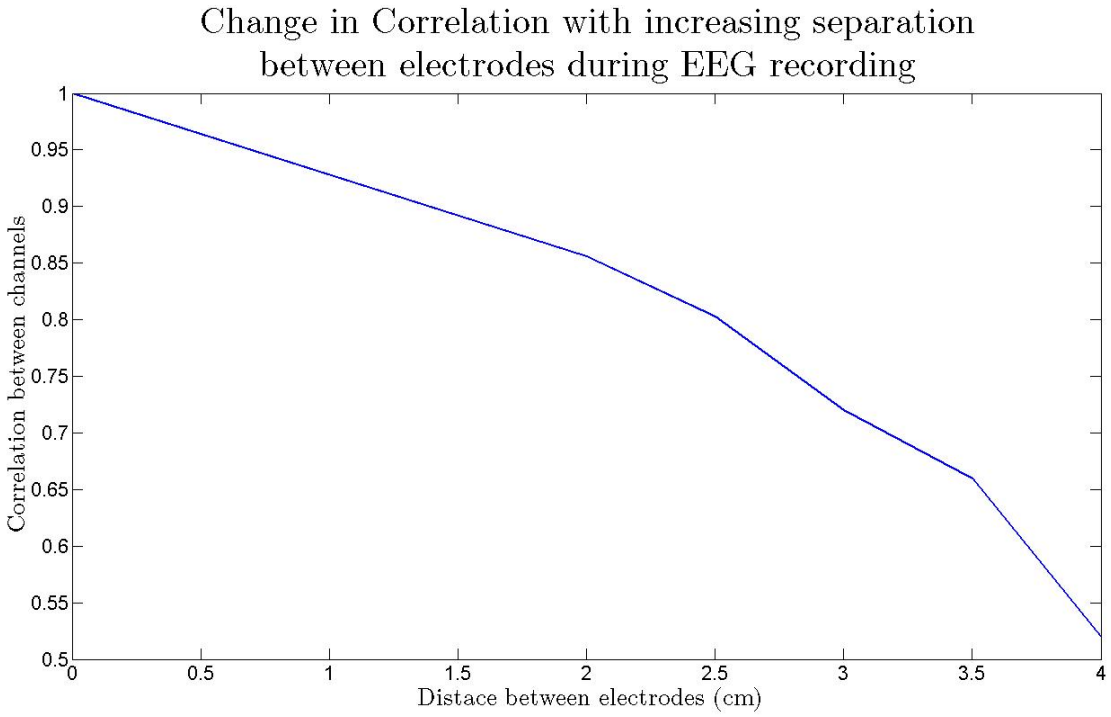

FIGURE 4.13: Changing correlation between recorded EEG signals with increasing distance between recording electrodes.

4.7 Automatic Artifact Removal

A number for the artifact removal techniques described in Section 3 (e.g. ICA, CCA, EEMD, wavelet), known as two stage techniques, require that the decomposed signals artifact components be selected and removed prior to the reconstruction of the signal. Quite often these components are selected manually using a number of properties such as frequency content, amplitude or morphological characteristic. However, this manual selection can be time intensive and is prone to human errors and bias when being performed by different technicians. This selection technique also prohibits the artifact removal techniques from being employed on-line and in real-time. Therefore the development of an automatic artifact component selection criterion is desired. A number of

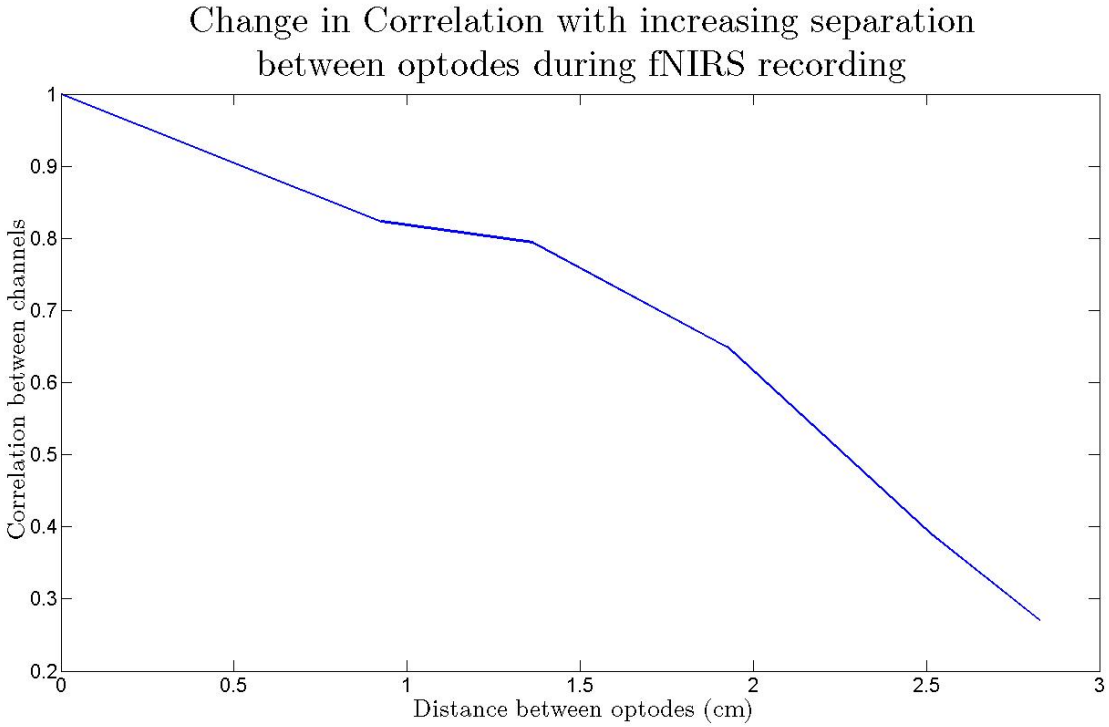

FIGURE 4.14: Changing correlation between recorded fNIRS signals with increasing distance between recording optodes.

authors have described many techniques which are capable of selecting the artifact components automatically when some assumptions are made on the signal and the artifact [1, 47, 53, 71, 92, 111, 113, 135, 163, 194, 195, 213, 218].

Hassan *et al.* [71] describe the use of the autocorrelation function to determine artifact components when using the CCA algorithm to denoise labor electrohysterograms. An algorithm is employed to determine the optimum threshold value below which all components, whose autocorrelation falls below this threshold, are removed. The technique therefore assumes that the desired signal components will have a greater autocorrelation than the contaminating artifact signal. A number of other authors have also detailed methods for automatic artifact removal when using the CCA algorithm due to the decreasing order of the correlation coefficients. For example, Zhao and Qiu [213] removed ocular artifacts from EEG signals by first using CCA to decompose the signals. The first component was then consistently determined to be ocular in origin and was then further decomposed using the wavelet transform. Each individual level was then compared to their corresponding threshold and were removed if they exceeded this threshold. Finally the signal was reconstructed with the ocular artifact removed. Vorobyov *et al.* [195] also used the autocorrelation of the signals, but instead used it to calculate the Hurst exponent which is the rate at which the autocorrelation of a signal changes with increasing lag. The assumption was then made that this exponent remains

constant for artifacts of the same type and so the corresponding components could be identified and removed.

Reference signals have also been utilised to improve the automatic artifact reduction. Vos *et al*. [47] removed any components from a decomposed neonatal EEG signal that were correlated with a simultaneously recorded polygraphic signal while James *et al*. [92] used an EOG reference signal to remove any component, from a cICA decomposition, that had similar characteristics. Viola *et al*. [194] used a similar technique which employed a user defined template to determine the artifact components.

A further method proposed in a number of papers details the use of the artifact signals characteristics (such as amplitude, frequency, skewness etc.) [53] [113] or spatial and temporal features [135] [111] to determine the artifact components. Each of these techniques operated well for the particular situation (signal and artifact combination) that they were utilised in, however the artifacts must have highly defined characteristics in order to be distinguishable.

Two automatic artifact removal techniques are analysed for this thesis. The first novel method, described in Section 4.7.1 uses the available "ground truth" signal to determine the optimum components to remove so as to increase the correlation of the cleaned signal with the available "ground truth". This situation is the ideal case, in that the result will always give the best possible result for each of the analysed techniques. However, as the "ground truth" signal will not always be available, two further techniques are described in Section 4.7.2 and 4.7.3 for fNIRS and EEG that function in the absence of a "ground truth" reference. For practical applications, the "ground truth" methodology can be employed in a calibration experiment to enable optimisation of the tuning parameters of the practical artifact selection methods.

4.7.1 Ideal Automatic Artifact Removal for both fNIRS and EEG

As the purpose of this thesis was to study a number of different and novel artifact removal techniques, the selection of the correct artifact components was imperative to ensure a fair comparison. In order to be capable of performing this fair comparison the authors utilised the available "ground truth" signal to determine the correct components to remove. As the "ground truth" signal (Channel 1) was assumed to be the equivalent to the true underlying signal of Channel 2, which was later contaminated with artifact, the purpose of each the artifact removal techniques was to "return" the contaminated signal to this "ground truth" signal.

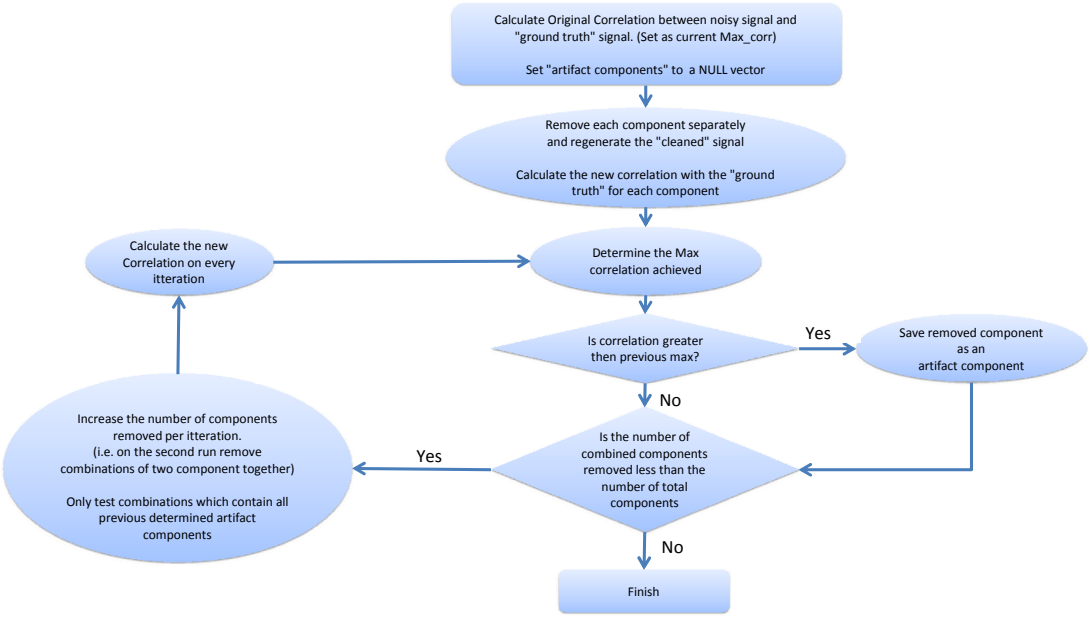

FIGURE 4.15: Flow chart depicting the steps undertaken to chose the optimum artifact components using the "ground truth" signal, known as the "ground truth" component (GTC) selection technique.

Figure 4.15 provides a flow chart of the steps undertaken to determine the artifact components using the available "ground truth" signal. It was proposed that any component that, when removed, increased the correlation of the cleaned signal with the "ground truth" signal was an artifact and therefore should be removed. To begin, the correlation of the noisy signal with the "ground truth" was calculated and was set as the current maximum correlation. Next, the first component from the decomposed signal was removed and a "cleaned" signal was generated. The correlation of this new signal was then calculated against the "ground truth" signal. This step was next repeated for each of the individual components and it was assumed that whichever component showed the greatest increase in correlation was the component most correlated with the artifact.

This process was then repeated, but for each iteration of the next run a combination of two components were removed; the artifact component determined from the first run, and each of the remaining components. By doing so, the aim was to find the second component most correlated with the artifact. It should be noted that the components are only determined to be artifacts if by their removal, the correlation of the "cleaned" signal with the "ground truth" is greater than the previous maximum correlation. This loop was then completed for combinations of $3, 4, ..., N$ components where N was the total number of components.

Figure 4.16 displays the change in maximum correlation obtained for an example

fNIRS signal decomposed using EEMD. For this example the original correlation of the noisy signal with the "ground truth" signal was 0.33. It can be seen that up to a combination of 5 different components the maximum determined correlation of the cleaned signal with the "ground truth" increased. Following this, any additional components that were removed did not increase this maximum correlation. Therefore, for the example shown, the "ground truth" component (GTC) selection technique determined that the components removed to generate the maximum correlation on that 5^{th} run are the artifact components (as their removal provided the highest correlation of the cleaned signal with the "ground truth" signal).

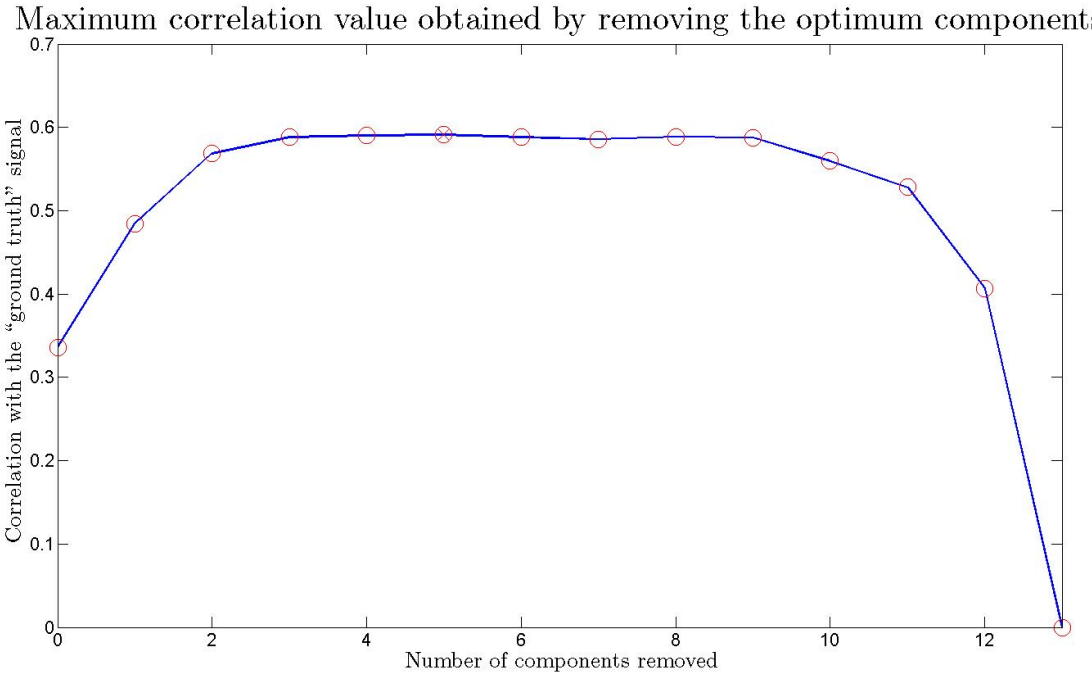

FIGURE 4.16: Choice of optimum artifact components using "ground truth" signal.

Using this process guaranteed that each individual technique removed the components that would ensure that it performed optimally during evaluation. Although it is not possible to employ this technique for determining artifact components in practical applications, as the required "ground truth" signal will not be available, it effectively decouples the artifact separation process from the component selection process and thus provides the fairest method for comparing the two stage algorithms considered in this thesis.

To ensure completeness of the two stage artifact removal techniques, an automatic artifact component selection criterion for both the fNIRS and EEG are described below. These techniques were deemed to be the best at selecting the artifact components in the described scenarios for when the "ground truth" signal was not available.

4.7.2 Automatic Artifact Selection for fNIRS

A number of the techniques mentioned above were analysed for selection of the artifact components from the decomposed fNIRS signals. The method of using the autocorrelation of the signal components, as described by Hassan *et al.* [71], was determined to be the best tested technique due to its simplistic nature and its consistency with the results returned using the GTC selection technique.

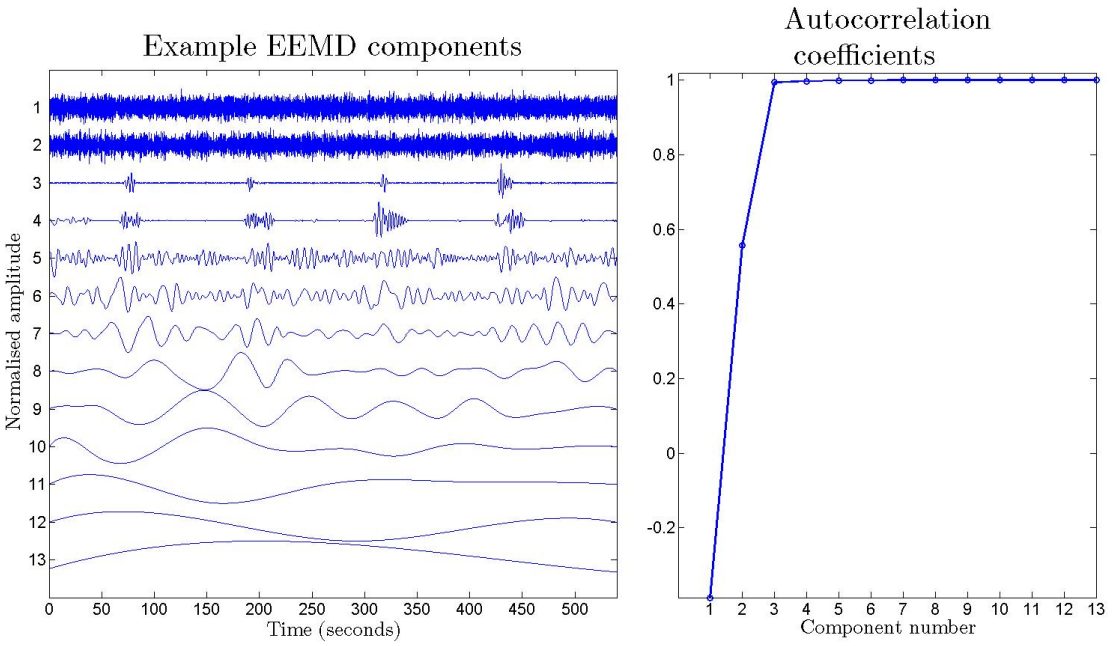

FIGURE 4.17: An example output of the EEMD algorithm for contaminated fNIRS data. Artifact components can be clearly seen in components 1-4, with the fNIRS data in components 5 - 13. The corresponding autocorrelation values can been seen in the right plot.

This technique calculates the autocorrelation, at lag 1 (assumed from here on), of the individual signal components after decomposition, performed using either EEMD, wavelets, ICA or CCA. Autocorrelation, which can also be seen as cross-correlation of a signal with itself, is the similarity of a signal with itself as a function of the time between them. The autocorrelation of x at lag k can be calculated as

$$R_{xx}(k) = \frac{\sum_{i=1}^{N-k} (x_i - \bar{x})(x_{i+k} - \bar{x})}{\sum_{i=1}^{N-k} (x_i - \bar{x})^2}, \tag{4.9}$$

where $\bar{x} = \sum_{i=1}^{N} x_i$ is the overall mean and N is the total number of samples.

Figure 4.17 shows an example signal decomposed using the EEMD technique and the corresponding autocorrelation coefficients for each of the components. It can be seen from this figure that the artifact components (i.e. components 1-4) have a lower autocorrelation coefficient than the true fNIRS signal due to their more random nature. The fNIRS signal consistently have coefficients close to one, and so a threshold value was required to determine the boundary between artifact and real signal components.

This threshold value was chosen with the aid of the available "ground truth" signal. Using the GTC selection technique the optimum components to remove to maximise the correlation with the cleaned signal can be determined. Therefore, as the autocorrelation coefficients are known for each component and it is known whether each component is an artifact (according to the GTC selection technique) the threshold value can be tuned so as to reduce the number of false positives and false negatives, known as the misclassification rate (MCR). A false positive indicates that the autocorrelation coefficient was below the threshold but the "ground truth" analysis determined the component to be true signal. A false negative indicates that the autocorrelation coefficient was above the determined threshold but the "ground truth" analysis determined the component to be artifact. Figure 4.18 shows the change in MCR with changing threshold value when calculated using the available training data. The square pointers show the minimum values obtained and thus the optimum threshold values for each technique. These threshold values were then used in the resulting analysis to determine the efficacy of the individual artifact removal techniques.

4.7.3 Automatic Artifact Selection for EEG

Two techniques performed well for selection of the artifacts from the EEG signal decomposition and were thus fully analysed. The first was the autocorrelation function described above for the fNIRS modality and the second used the Hurst exponent. As can be seen from Figure 4.19, when using EEG data the autocorrelation of components corresponding to the true EEG data is less than that of the artifact components. Therefore, in contrast to the fNIRS data, a threshold needs to be determined above which all components are deemed to be artifacts. A plot of the misclassification rate was again created using the training data to determine the optimum threshold value for the EEG as shown in Figure 4.20.

The second technique used the Hurst exponent as described by Vorobyov *et al.* [195]. The Hurst exponent can be seen as a measure of the long range dependence within a

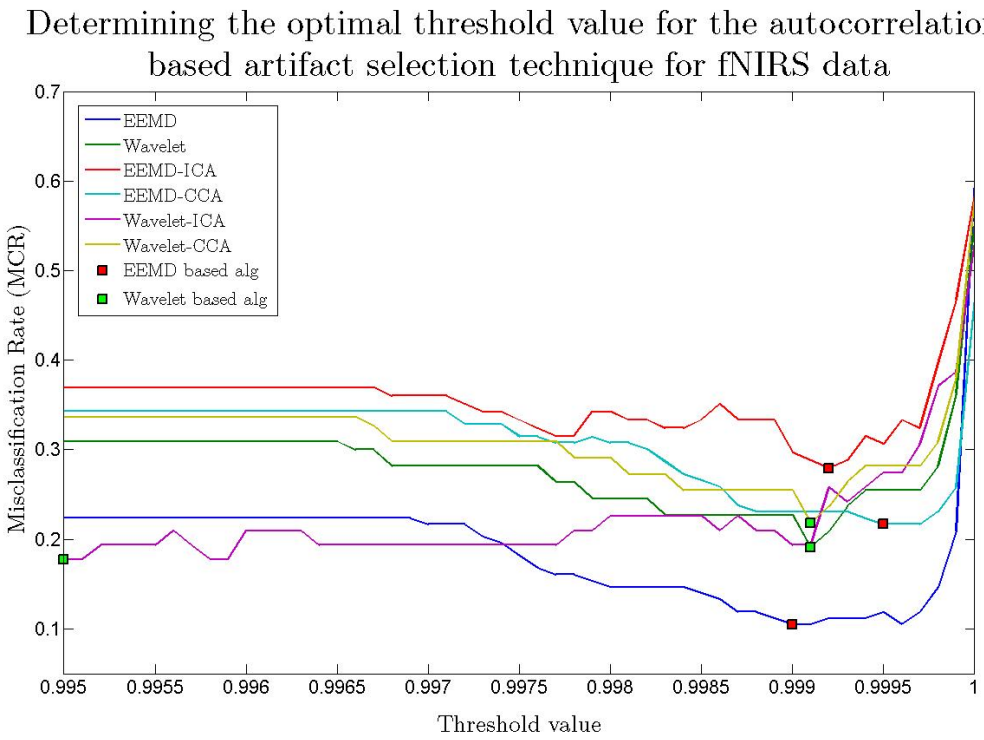

FIGURE 4.18: Miss classification rate (MCR) as a function of the threshold value for the described techniques. The threshold value that minimised the number of false positives and negatives (MCR) for each technique is shown by the square pointer.

signal and relates to the autocorrelations of the time series and the rate at which they decrease as the lag between the pairs increases. The Hurst exponent lies between 0 and 1. Although the Hurst exponents were observed to be more variable than the corresponding autocorrelation components (i.e. they were not as tightly bunched), the EEG exponents were still discovered to have a lower value then the artifact components. Therefore a threshold value was again required. Figure 4.21 displays the determined threshold values for the different techniques used. This threshold could then used to select the artifact components and therefore aid in the cleansing of the signal.

Results from the two stage artifact removal techniques using both the autocorrelation function and the Hurst exponent are provided in the results section of Chapter 6.

4.8 Synthetic Data

As well as testing the algorithms on the real data recorded using the methodology described in Section 4.2 the different techniques were also tested on synthetic data. The purpose of this synthetic data was to create ideal scenarios in which the true signal, the

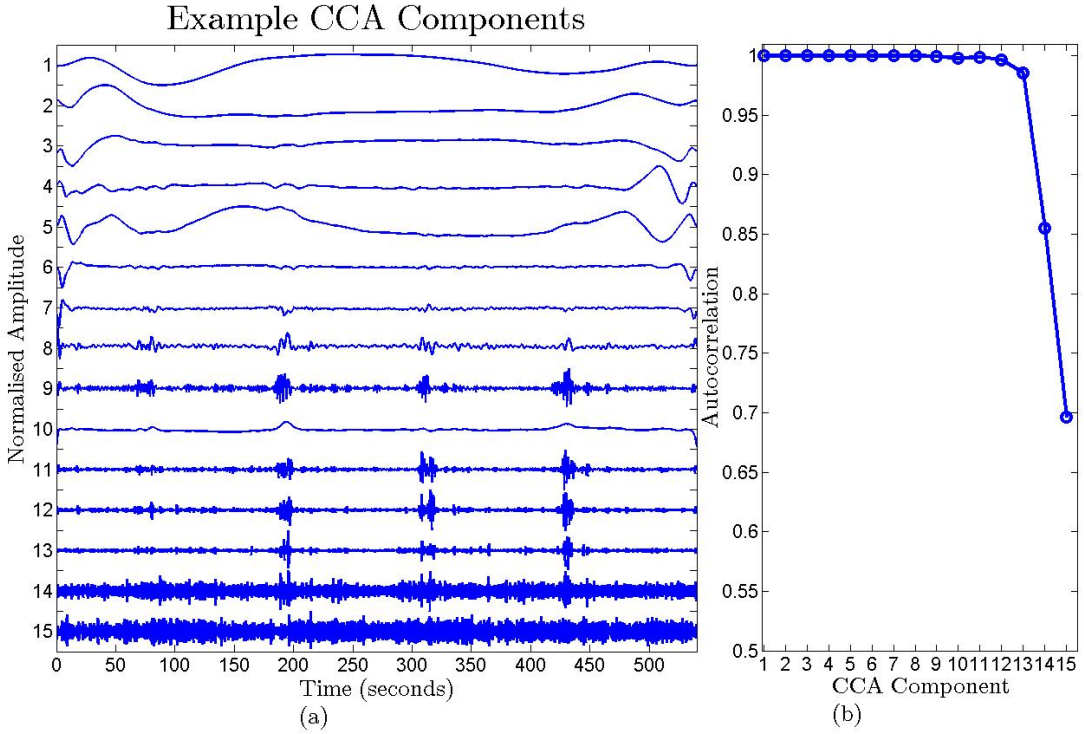

FIGURE 4.19: An example output of the CCA algorithm for contaminated EEG data. Artifact components can be clearly seen in components 8-13, with the EEG data in components 14 and 15.

artifact signal and the form of the combination (i.e. linear) was known. Comparisons could then be made between the ideal results and the true signal results.

For the purpose of this thesis, two types of artifact contaminated signals were created for both the EEG signal and the fNIRS signal; the first created artifacts similar to those observed in the real signal and the second were of a more basic form in which the artifact signal takes the form of a single intermittent sine wave crests. These artifacts were then combined with accurate representations of the underlying EEG or fNIRS signals. The methods used to create the different synthetic data are described below.

4.8.1 EEG

As stated above, an accurate representation of the EEG signal characteristics is required when producing simulated data. Simulated EEG data has previously been developed by Yeung *et al.* [208] [209] for evaluating different detection methods of synchronised oscillations in the EEG data. This simulated data has been shown to match the empirical data well and thus the simulation setup described was repeated for this thesis. The EEG signal was generated by first creating short trials of data. These trials consisted of a summing together of 100 sinusoids of randomly varying frequencies in the range of 1 Hz to

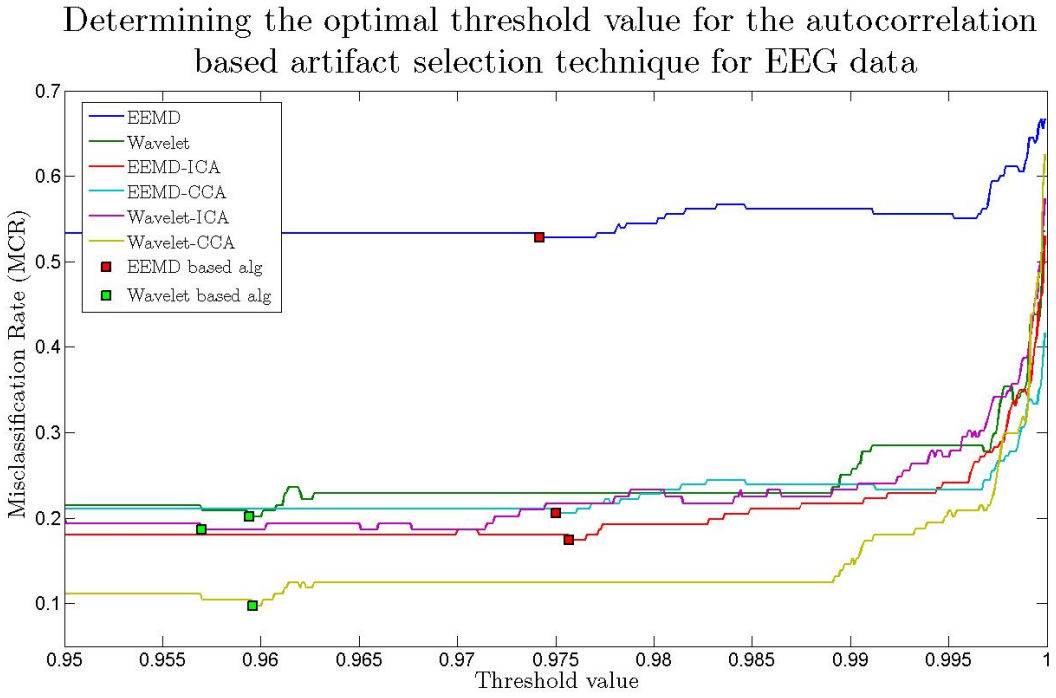

FIGURE 4.20: Choice of the threshold value for automatic artifact removal using the Autocorrelation function.

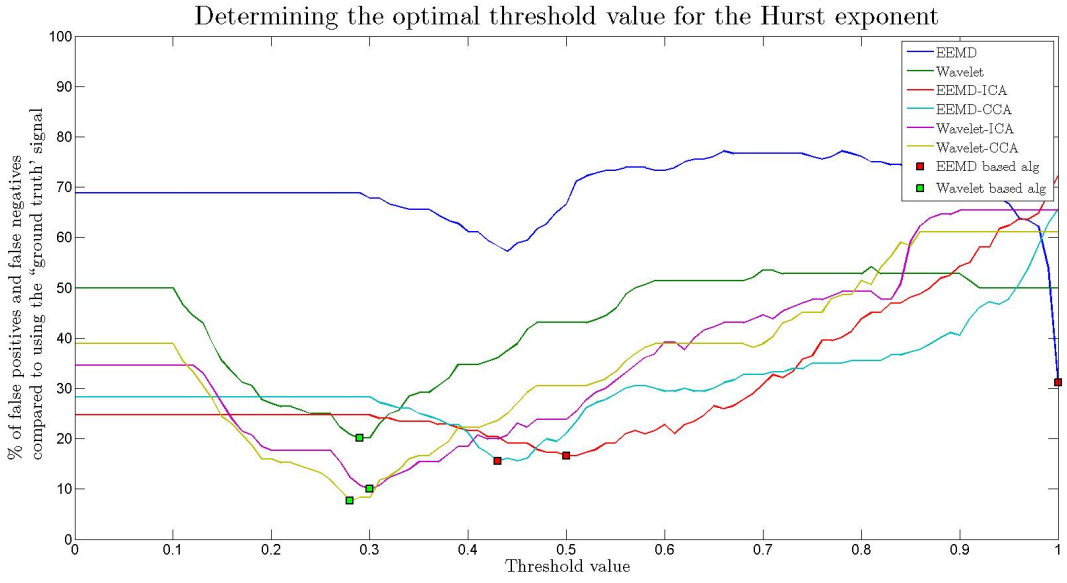

FIGURE 4.21: Choice of the threshold value for automatic artifact removal using the Hurst exponent.

80 Hz. Each individually generated sinusoidal wave also had a random phase associated with it in the range of 0 to 2 π (Equation 4.10). The full simulated EEG signal was then created by concatenating together the desired number of trials therefore ensuring that the final signal is non-periodic.

$$\text{EEG Trial} = \sum_{i=1}^{100} A \sin\left(2\pi f_i t + \phi_i\right), \begin{cases} f_i & \in [1 \text{ Hz}, 80 \text{ Hz}] \\ \phi_i & \in [0, 2\ \pi]. \end{cases} \tag{4.10}$$

$$\text{EEG Signal} = \left(\text{EEG Trial}_1,\ \text{EEG Trial}_2, \ldots \text{EEG Trial}_n\right). \tag{4.11}$$

When creating the individual trials care was taken to ensure the simulated data would approximate the true EEG signal as much as possible. Therefore the amplitude (A) of each sinusoid added to the signal was scaled to match the power spectrum of the EEG for that particular frequency. Accordingly, the frequency spectrum of the simulation signal closely mirrors that of the real data as can be seen in Figure 4.22 and so it can be said that, although very simple in structure, the simulated data accurately replicates the primary features of the empirical data.

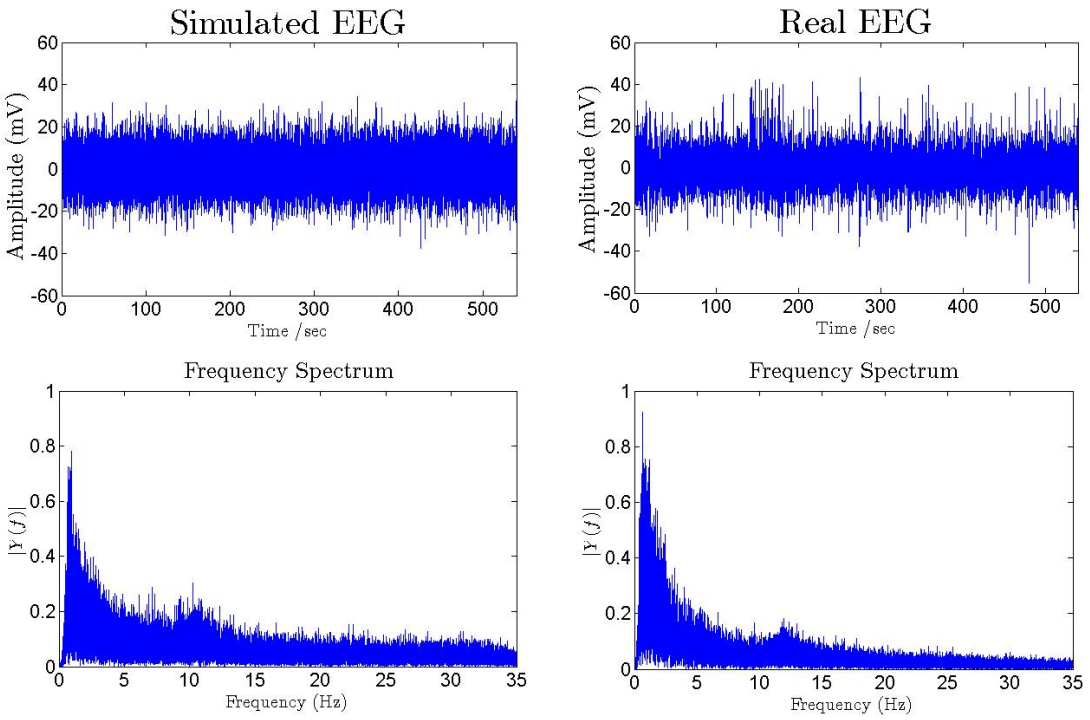

FIGURE 4.22: The simulated signal is plotted in both the time and frequency domain and is shown to closely mirror the characteristics present in the real data.

4.8.2 fNIRS

In order to reproduce the results of the artifact removal techniques on the real data, using simulated data, an accurate representation of the fNIRS data was required. In

1998, Buxton *et al.* [30] developed a biomechanical model for the dynamic changes in deoxygenated haemoglobin content during brain activation. This model incorporated the conflicting effects of the dynamic changes in blood oxygenation as well as the increase in blood flow and was shown to match well with measurements of the blood oxygenation level dependent (BOLD) signal recorded using MRI. Leamy *et al.* [107] extended this work to develop a model for synthetic fNIRS data generation and proved it capable of accurately modeling real-world signals in both the time and frequency domain, shown using both temporal and spectral features. As stated previously this thesis uses both the optical density (OD) and the oxygenated and deoxygenated haemoglobin (HbO & Hb) forms of the data, and therefore the employed model has to be capable of recreating each signal. The model produced by Leamy *et al.* consisted of a model of the vascular response (to produce ΔC_{HbO} and ΔC_{Hb}) in addition to a spectrophotometric model which related the hemodynamics to changes in optical density (OD). The model is further extended to incorporate the other signals commonly contained within the recorded fNIRS signal including the cardiac pulse, the Meyer wave, broadband interference due to environmental and instrumental noise and signal offset. For the purpose of this thesis only the pure underlying signals are desired and thus the additional steps mentioned above are not undertaken.

The change in ΔC_{HbO} and ΔC_{Hb} due to the activation of a particular area of the brain, as measured using fNIRS, is due to the vascular response. The Buxton balloon model [30] models this vascular response as a function of the blood flow. A differential equation description for the model is presented in [43] as follows:

$$E(t) = 1 - (1 - E_0)^{\frac{1}{f_{in}(t)}} \tag{4.12}$$

$$\dot{q}(t) = \frac{f_{in}(t)}{\tau_0}\left(\frac{E(t)}{E_0} - \frac{q(t)}{v(t)}\right) + \frac{1}{\tau_v}\left(f_{in}(t) - v^{\frac{1}{\alpha}}\right)\frac{q(t)}{v(t)} \tag{4.13}$$

$$\dot{v}(t) = \frac{1}{\tau_v}\left(f_{in}(t) - v^{\frac{1}{\alpha}}\right) \tag{4.14}$$

$$\dot{p}(t) = \frac{1}{\tau_v}\left(f_{in}(t) - v^{\frac{1}{\alpha}}\right)\frac{q(t)}{v(t)}. \tag{4.15}$$

$E(t)$ is the unidirectional extraction fraction of oxygen where E_0 is the net oxygen extraction fraction. $E(t)$ can be seen as the fraction of oxygen molecules that are available for tissue metabolism (which is a function of the blood flow $f_{in}(t)$) while E_0 is the fraction that is extracted and metabolised (constant) [29]. $q(t)$, $v(t)$ and $p(t)$ represent deoxygenated haemoglobin (ΔC_{Hb}), blood volume and total haemoglobin respectively. A measure for oxygenated haemoglobin (ΔC_{HbO}) can be determined by subtracting deoxy haemoglobin from total haemoglobin. τ_0 is the mean transit time, given by the ratio

of the blood volume to blood flow at rest, and τ_v describes an additional resistance to rapid volume changes [133]. Finally α is the Grubb's relation between cerebral blood volume and cerebral blood flow [153]. The constant parameters were set similar to [43]; $E_0 = 0.4$, $\tau_0 = 2$, $\tau_v = 30$ and $\alpha = 0.4$. The input blood flow ($f_{in}(t)$) is specified by the user and was set as a combination of variable frequency and amplitude sine waves within the sampling frequency of the fNIRS data.

In order to increase the similarity between the simulated signal and the real data, the resultant values for ΔC_{HbO} and ΔC_{Hb} were scaled to a typical amplitude before further processing. Figure 4.23 displays an example output of the simulated data generation.

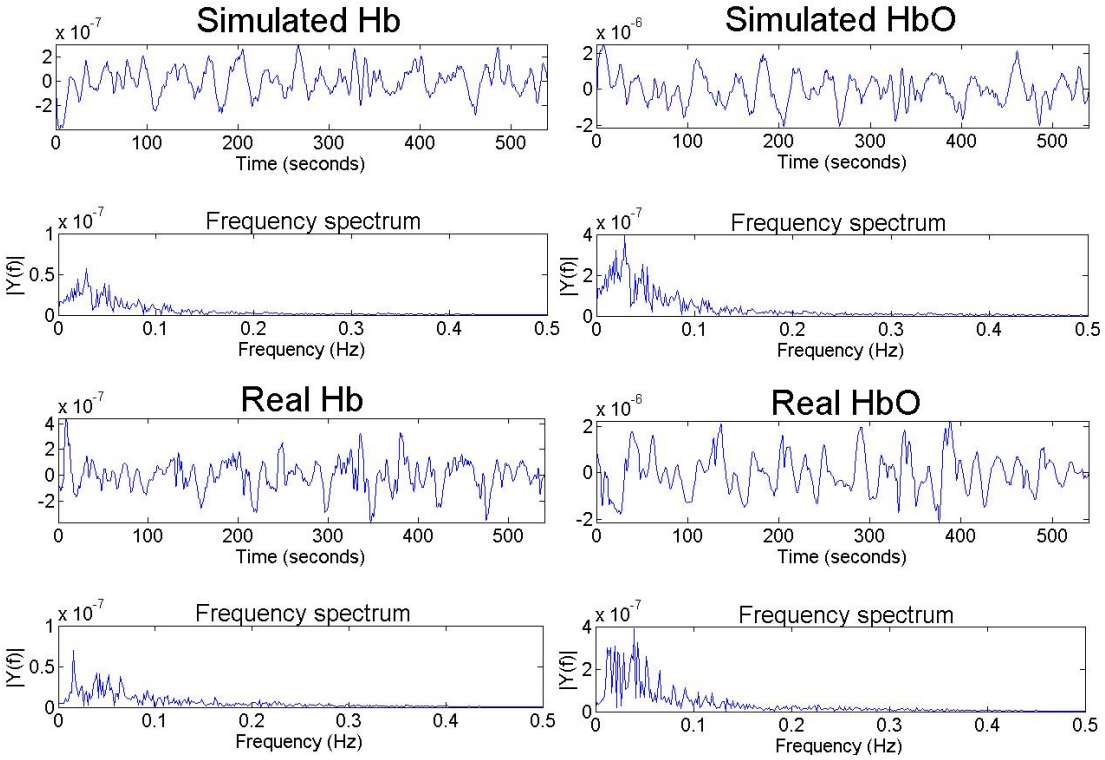

FIGURE 4.23: An example output of ΔC_{Hb} and ΔC_{HbO} using the simulated fNIRS data generated using Equation 4.12-4.15. Time series and frequency spectrum of the real fNIRS data is plotted for comparison.

With ΔC_{HbO} and ΔC_{Hb} now calculated, the next step was to determine the optical density values for both 690 nm and 830 nm. The change in optical density for a particular wavelength (λ) can be calculated using the modified Beer-Lambert law as follows:

$$\Delta A^{\lambda}(t) = \left(\alpha^{\lambda}_{Hb}\Delta C_{Hb}(t) + \alpha^{\lambda}_{HbO}\Delta C_{HbO}(t)\right) BL, \tag{4.16}$$

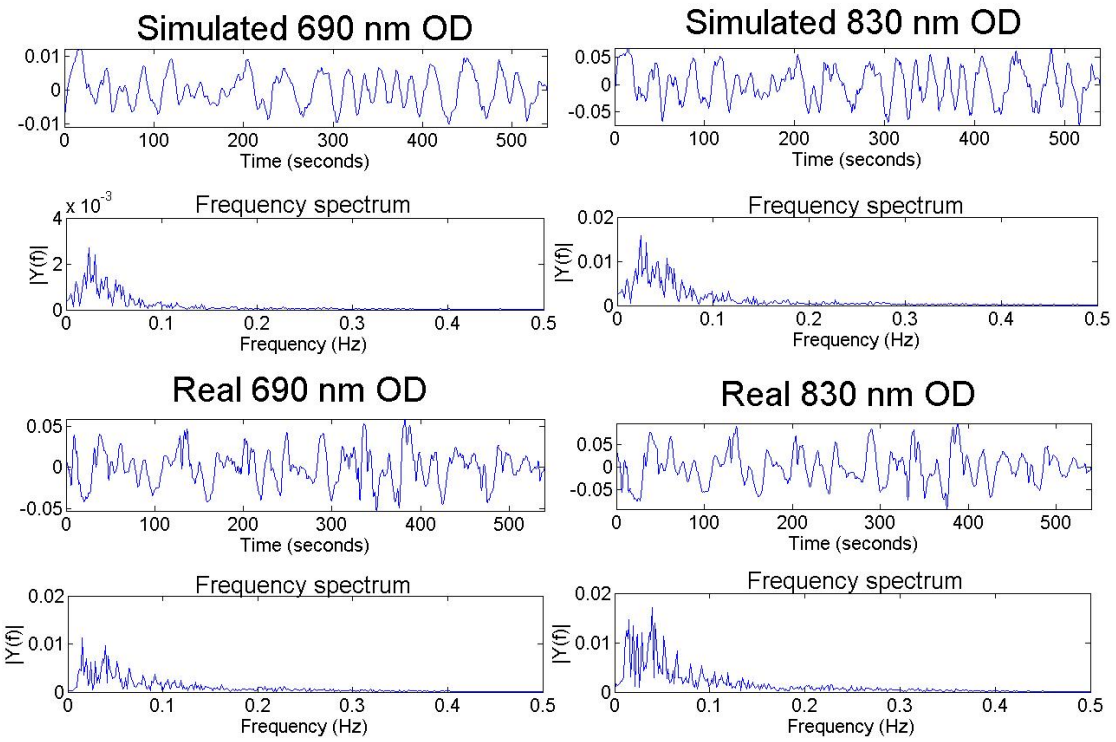

FIGURE 4.24: An example output of optical density for 690 nm and 830 nm using the simulated fNIRS data generated using Equation 4.16. Time series and frequency spectrum of the real fNIRS data is plotted for comparison.

where the parameters are as described in Section 2.2.2 and 4.3.3. An example of the optical density signals can be seen in Figure 4.24. Using these steps, a database of optical density signals were generated on which to test the implemented algorithms.

4.8.3 Motion Artifact

In order to be capable of testing the artifact removal techniques described in this thesis with the simulated data outlined above, the contaminating artifact also needs to be modeled. Two different types of motion artifact were generated for both the fNIRS and EEG data. The first is described in detail below for both modalities and represents the morphology of the real artifact observed on the recordings. The second artifact that will be tested will be more rudimentary in nature, and consists of waves of limited duration and of single frequencies etc.

fNIRS

In order to model the motion artifact contaminating the fNIRS signal an understanding was first required into how motion affected the signal. As stated in Equation 4.16 the

absorbance of light is proportional to the distance between the source and detector optode, i.e $A = \alpha CBL$. Therefore a change in this length $(L + \Delta L)$ due to motion would create a signal contaminated with artifacts $(\bar{A})$. The artifact signal due to the changing path length can thus be determined as the difference between the two signals $(\bar{A} - A)$ as shown in Equation 4.17.

$$\begin{aligned} A &= \alpha CBL \\ \bar{A} &= \alpha CB\,(L + \Delta L) \\ &= \alpha CBL + \alpha CB\Delta L \\ \text{Noise Signal}(\eta) &= (\bar{A} - A) \\ &= \alpha CB\Delta L \\ \eta &= \frac{A\Delta L}{L} \end{aligned} \tag{4.17}$$

This artifact signal is therefore multiplicative in nature as it is affected by both a change in L and by a change in A. However as the offset of the parameter A is on average a factor of around 10 times larger than the variation in the signal, the parameter A can be assumed stationary. With this new assumption the equation above now becomes linear with the noise signal proportional to the change in length $\eta = \beta\Delta L$.

Figure 4.25 demonstrates the addition of the motion artifact to the simulated fNIRS data. The third subplot shows the noise signal (η) for both the 690 nm and 830 nm signals as well as the changing length signal (ΔL). It can be seen from this figure that the assumption that the contaminating noise is proportional to the changing length is legitimate, thus permitting the use of techniques such as the adaptive filter which assume linear addition of the noise signal (see Section 5.6).

EEG

Unlike for fNIRS there is no simple relationship available to map a change in the position of the electrode to the addition of artifact to the signal. This change in electrode position can have multiple effects including an effect on the impedance associated with the electrode-electrolyte interface and with the resistance associated with the electrolyte itself.

To induce artifacts, similar to those observed during the experiments described in Section 4.2, intermittent short duration sine waves or differing frequencies were added.

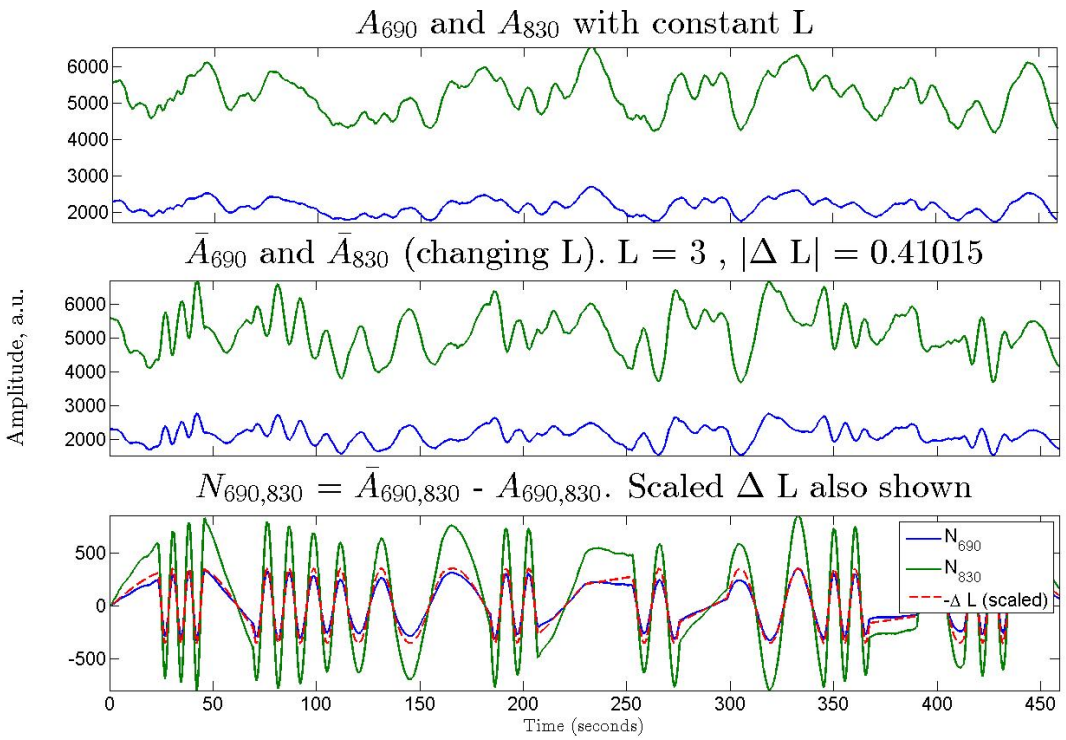

FIGURE 4.25: Effect of changing the path length (L) during recording. Data plotted is simulated using the step described in Section 4.8.2.

As can be seen from Figure 4.26 the addition of these simulated artifact signals create a signal of similar morphology, in both the time and frequency spectrum, to the real signal.

Therefore when analysing the artifact removal techniques using the simulated data (for both the EEG data and the fNIRS data), the form of the data will be very similar to the real recorded data, however the true underlying signal is now accurately known. In this way the results produced using the real data and the "ground truth" data can be supported using the simulated data.

4.9 Conclusion

In this chapter a number of important techniques which will be employed over the remainder of the thesis have been described. To begin, a novel recording methodology was detailed [181] which provides a number of important possibilities in terms of the evaluation of different artifact removal techniques. This methodology provides the researcher with both a real signal contaminated with motion artifacts as well as a "ground truth" signal which is highly correlated with the true (uncorrupted) underlying signal. Using these two signals the interested researcher can now effectively and accurately compare

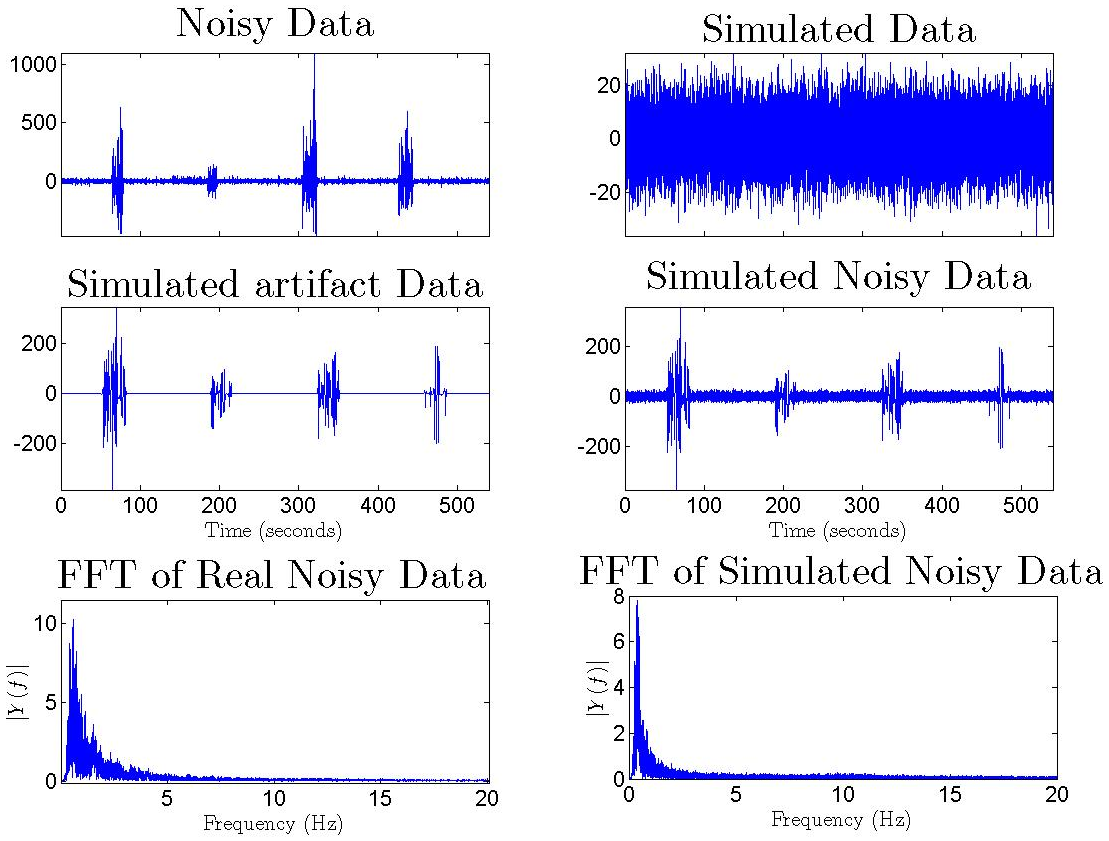

FIGURE 4.26: An example of the simulated motion artifact added to the EEG data.

the efficacy of a number of different artifact removal techniques. An added advantage to this methodology is the ability to determine the optimum components to remove from the two stage artifact removal algorithms, described in Chapter 3, so as to remove as much of the artifact from the desired signal as possible.

It follows that the "ground truth" signal also allows for an accurate measure of the effectiveness of the currently available automatic artifact component selection techniques. A description of some of the currently available automatic artifact component selection techniques was given and the best techniques for operation with the EEG and fNIRS modalities were described. The use of the autocorrelation function to determine the artifact components functioned well the fNIRS data, while both the autocorrelation function and the Hurst exponent showed promising results when operating on the EEG data.

The techniques expanded upon and analysed in Chapters 5 and 6 are also evaluated on synthetic data and the production of this data for both fNIRS and EEG was described. When using the synthetic data, the exact underlying signal is available and thus the results obtained using the data from the novel recording methodology can be verified.

In the next chapter, the data obtained using the recording methodology described in this chapter is used to test the efficacy of a number of the single stage artifact removal techniques described in the literature review. The algorithms are tested on the fNIRS, EEG and simulated data and an evaluation is provided comparing the methods.

Chapter 5

Single Stage Artifact Removal Techniques

The content of this chapter is divided into two parts; firstly the chapter details a novel tagging algorithm developed with the use of multiple accelerometers. This novel algorithm provides an accurate quality-of-signal (QOS) metric which can be used to reliably inform a technician as to the epochs of contaminated data within a signal [180]. Through the novel use of dual accelerometers this QOS metric is also capable of distinguishing between different motion artifact types, thus permitting the use of the correct artifact removal technique for the specific corrupting artifact [179]. Finally the data tagging also permits the switching of artifact removal techniques allowing the best technique to be used for a particular artifact type, therefore enhancing individual methods contributions while permitting the algorithms to be employed only when required.

Secondly, the chapter provides a critical and rigorus evaluation of the principal single stage artifact removal techniques, as introduced in Chapter 3. Initially some basic filtering methods will be described which can be used to remove contaminating artifacts in situations where the frequency spectrum of the artifact and the signal do not overlap. However, as the frequency range of many artifact signals lie within the frequency spectrum of the desired signals, more complex techniques must be employed. These include the Wiener filter, Kalman filter, morphological component analysis (MCA) and adaptive filter, all of which either use signal models to reduce the artifact or use the morphology of the signals to separate the signal from the artifact.

The operation and mathematical description of each of these methods is first described. The techniques will be benchmarked for motion artifact removal on real fNIRS

and EEG datasets, recorded using the methodology described in Section 4.2, and the generated simulation data introduced in Section 4.8 using the performance metrics outlined in Section 4.5. Results are presented, for two scenarios: (1) the algorithms are employed over the full signal and (2) the algorithms are only applied to the epochs identified as being contaminated by motion artifact, as determined by the tagging algorithm.

5.1 Data Tagging

Reference signals have a very important role to play in a number of artifact removal techniques. When available, these signals can convey information regarding the form and position of a contaminating artifact. These reference signals can be from a number of different sources, such as accelerometers [180] [179] or additional physiological signal recordings (e.g. EOG [73] EMG [214]).

In this section the use of reference signals for data tagging [180] is described, allowing for an accurate representation of the position and type of artifact in the signal [179]. Data tagging is a method of using an available reference signal to assign a metric to specific epochs of the data. These assigned metrics are usually in the form of a "quality of signal" (QOS) measure which can be used to define the quality of the data in the given epoch. This information can be useful in determining where in a signal an artifact is likely to be present; with this information the artifact contaminated epoch can either be removed or can be processed using artifact removal techniques. A number of authors have previously employed reference signals to generate QOS metrics, with the vast number used in conjunction with ECG recordings. One possible reasoning for this would be that a large number of the available ECG monitoring devices have in-built accelerometers which can be easily employed as a reference.

In 2004, Muhlsteff *et al.* [138] tested a new design for a wearable ECG belt, with integrated dry electrodes. Although attempts to remove the motion artifacts using the accelerometer data failed, the accelerometer output was used to determine states of rest and activity of the subjects. By using these known states of activity, the author was able to apply a simple QOS metric and thus determine the epochs of clean, artifact free, data. In 2005 Healey and Logan [74] used the accelerometer data in their "Wearable Wellness Monitoring System" to estimate the quality of the signal data and give a confidence rating on the results of their analysis algorithms. As the subjects activity level increased the quality of the ECG signal deteriorated, thus giving merit to their approach. Kishimoto *et al.* [98] recorded ECG signals from subjects as they slept. Any positional changes in the sleeping subject caused a disruption in the observed ECG signal. An

accelerometer was attached to the body to detect when these body movements took place and used this detected movement as a basis for a QOS measure for the recorded ECG signal.

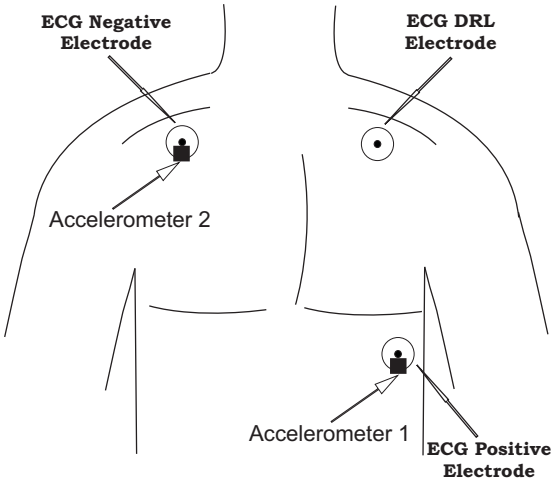

FIGURE 5.1: Accelerometer placement for generating quality of signal (QOS) metric for ECG signal.

Although all the methods mentioned above do provide a QOS metric signal, they were all deemed to have an important limitation. ECG is used to measure the changing voltage across the torso as described in Section 2.1.2. When subject motion causes the torso to contort, the path between the two recording electrodes is altered, creating an artifact on the desired signal. However, if movement of the subject doesn't cause this path to change then there will be no artifact contamination. The previously mentioned QOS techniques would however class this type of movement as generating a low QOS and thus would label the data incorrectly as being of bad quality. Therefore, in a number of recording situations the presence of subject motion does not mean that artifact will be created. While it is a necessary condition it is not a sufficient condition. It is changes to the electrophysiological properties of the tissue under measurement due to motion which is important. Not all motion will have an appreciable change in such properties. The same is true when analysing the EEG and fNIRS data. An algorithm was therefore developed to generate a QOS metric for ECG signals calculated with the use of two individual accelerometers [180]. These two accelerometers were placed on each of the recording electrodes as shown in Figure 5.1. Using these two accelerometers both overall body acceleration and the differential electrode acceleration could now be calculated.

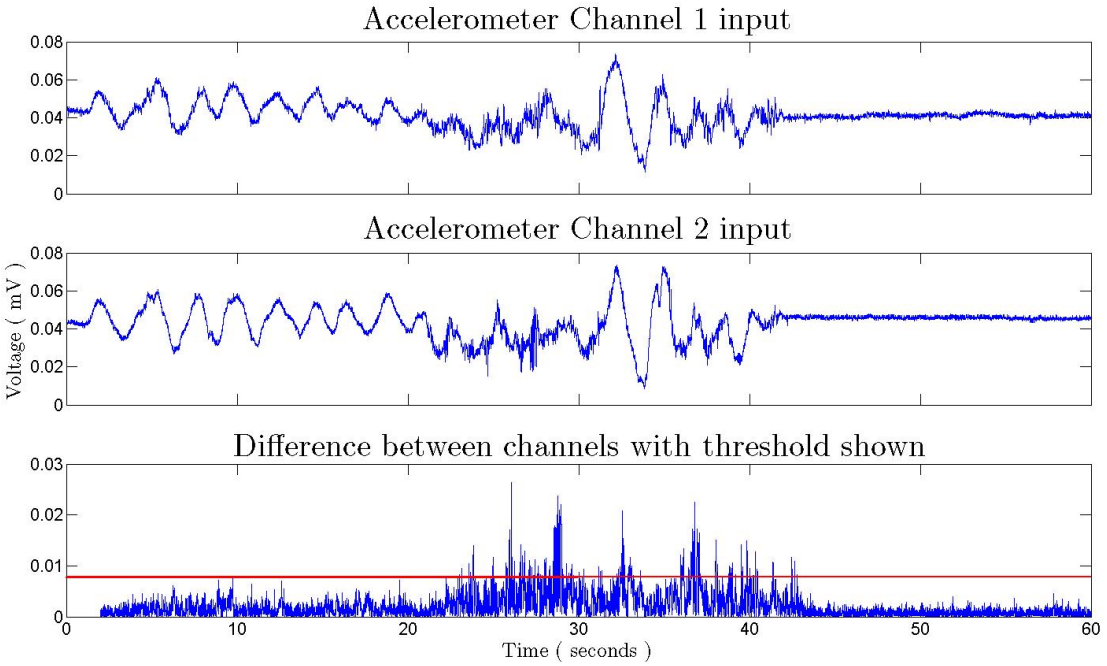

FIGURE 5.2: Determining the novel QOS metric. Lower plot shows the absolute value of the difference between the two accelerometer signals. Threshold is shown in red. All samples above this line are determined to be movement samples.

This preliminary novel QOS metric operated solely on the differential acceleration between the two accelerometers and thus any movement which did not alter the path length of the ECG signal was not analysed. Figure 5.2 shows the output of the accelerometers during an example experiment, where the accelerometers were located as shown in Figure 5.1. During this experiment 60 seconds of ECG data was recorded with three separate epochs of activities. During the first 20 seconds the subject was instructed to move their body "freely" without distorting the torso. These movements included twisting and bending from the waist. Over the second 20 seconds epoch the subjects were asked to move their body including their torso so as to alter the path length between the electrodes and finally over the last 20 seconds the subject was at rest. The absolute value of the difference between the accelerometers (calculated using Equation 4.4) was used as the measurement criterion for the QOS. A threshold value β, determined empirically, was set and all differential acceleration sample points, whose amplitude was greater than the set threshold, were assigned as detected motion. Finally the QOS metric could be determined. This algorithm calculated the number of movements that were detected over a 1 second period, centered at the current sample. The current sample (k) was then assigned a QOS value between 0 and 1 indicating the number of movements detected in that one second epoch. A value of 1 was given to a detected clean signal (ie no detected movements) with 0 implying all surrounding samples had also detected movement.

$$\text{QOS}(k) = 1 - \sum_{i=k-\frac{n}{2}}^{k+\frac{n}{2}-1} \frac{\alpha(i)}{n}, \quad \alpha(i) = \begin{cases} 1 & \text{if } |DM(i)| > \beta \\ 0 & \text{otherwise} \end{cases} \tag{5.1}$$

where n is the number of samples per second, k is the current sample, DM is the differential movement of the accelerometers determined using Equation 4.4 and β is the chosen threshold value.

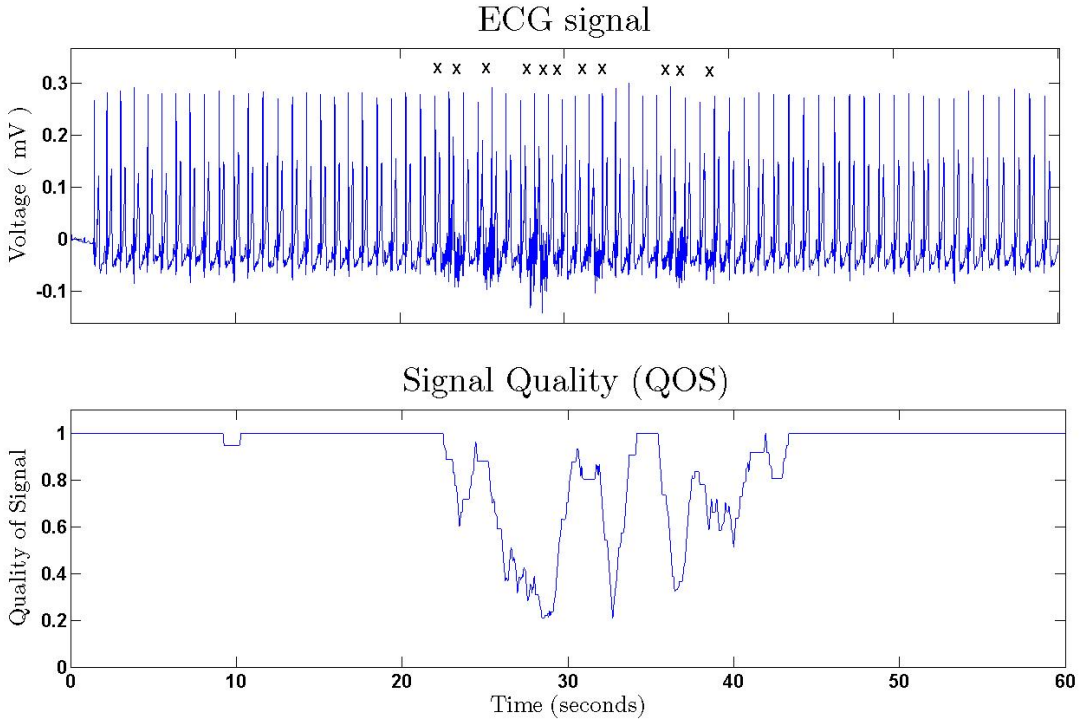

FIGURE 5.3: Recorded ECG signal with respective QOS signal. P-QRS and T waves which could not be manually deciphered are marked with an "X".

An example of the ECG recorded in conjunction with the accelerometer data shown in Figure 5.2 can be viewed in Figure 5.3. The ECG data was manually analysed and the P-QRS-T waves that could not be accurately determined manually are marked with an "X". The data was tagged using the QOS as described [180] and can be seen to correlate well with the noisy ECG signal. Figure 5.4 shows the same ECG data over shorter epochs to allow for a greater understanding.

The QOS metric specified above was also expanded in [179] to operate with both EEG and fNIRS data. In this paper it was demonstrated that the different possible variations of motion which can effect fNIRS and EEG recordings can have different effects on both signals, as can be seen in Figure 5.5. For the selected modalities two different QOS metrics were calculated. The first employed only one of the available accelerometer signals, and thus the QOS metric would decrease when any movement was detected.

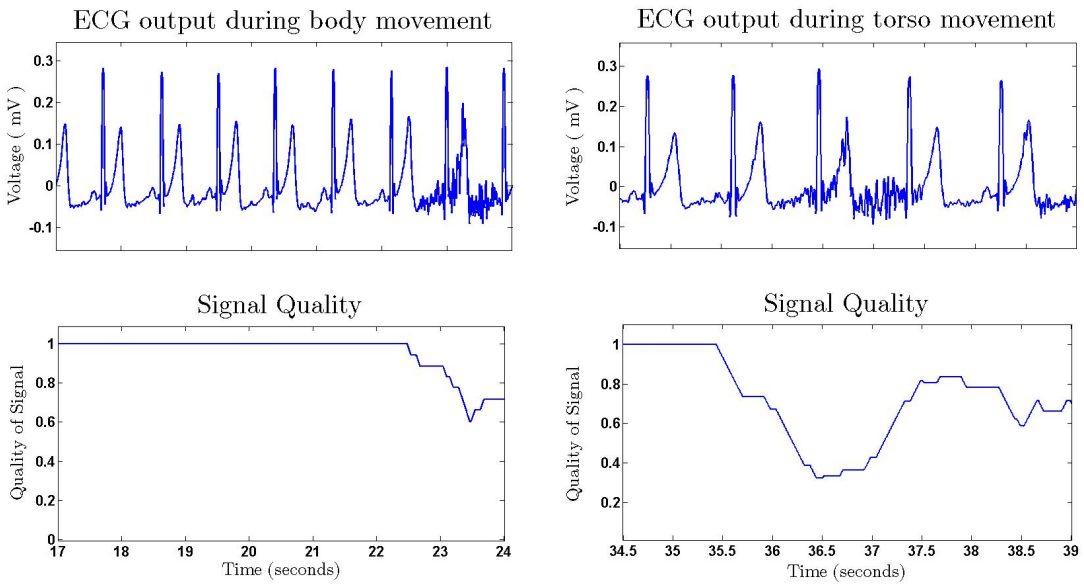

FIGURE 5.4: Magnified version of Figure 5.3. It can be observed that over the first 20 seconds, although there is subject motion this does not generate artifact on the signal. The QOS metric can be seen to accurately represent the artifact position in the data.

The second QOS metric was similar to that described for the ECG signal above, and used both available accelerometers to detect differential movement. The location of the accelerometers is described in Section 4.2 and can be seen in Figure 4.3 for the fNIRS setup. Results showed that differential movement, generated due to the movement of the recording optodes or electrodes with respect to the head created artifact signals on both signal modalities (shown by yellow shading). However, overall head motion, in which there was no differential movement, only generated artifacts on the fNIRS signal due to blood pooling (blue shading in Figure 5.5); the EEG signal remained artifact free. These results again showed the importance of using the differential movement of the accelerometers as an individual QOS tagging metric. If only a single accelerometer was employed all data shaded in both blue and yellow would be regarded as containing artifacts for the EEG signal which can be observed to be inaccurate.

In addition to tagging the data, the QOS metric can also be used to aid in the decision of which artifact removal technique to use or the pre-processing steps to take. When using fNIRS, for example, the artifact can either be due to a change in blood volume (due to blood pooling) or due to a change in light intensity due to movement of the optode. If due to blood pooling (determined using overall head movement) then the artifact removal techniques would be better performed on the HbO and Hb data as these directly relate to blood volume ($\Delta BV = \Delta HbO + \Delta Hb$). However if the artifact is due to the movement of the optode then the artifact removal techniques should be applied to the optical density values discussed in Section 2.2.2. As will be demonstrated later in

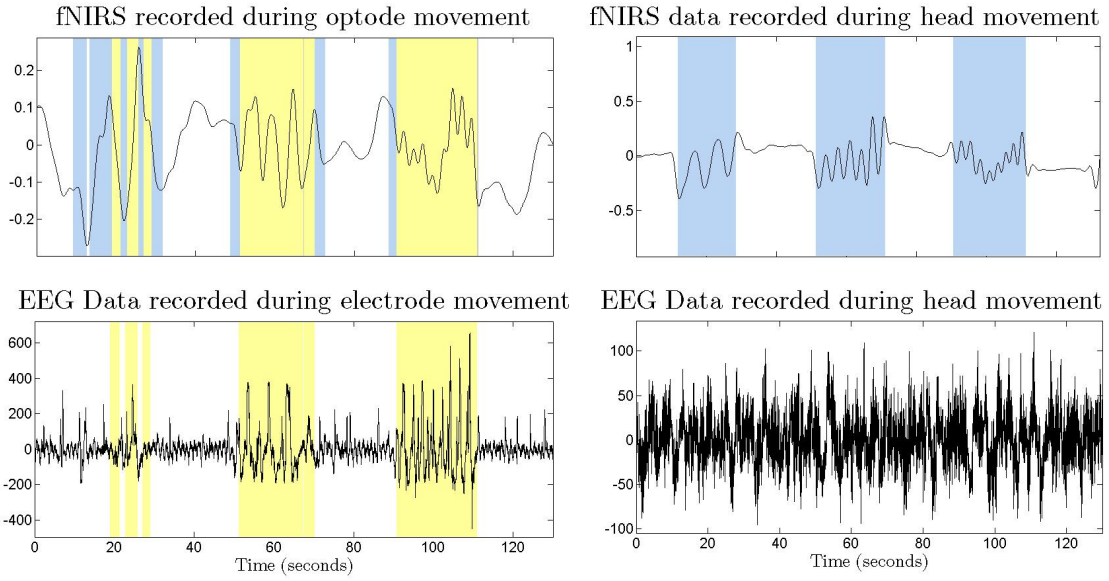

FIGURE 5.5: How different movements affect the different signal modalities. Optode/-electrode movement (shown in yellow) affects both signals whereas head movement (shown in blue) only affects fNIRS. Shading generated using tagging algorithm.

the chapter, tagging offers the possibility of determining when to apply artifact removal techniques, and in the case of some algorithms, inform the tuning of their operating parameters.

5.2 Linear Time Invariant (LTI) Filtering Methods

Before attempting to remove contaminating artifacts from the desired signals using the more elaborate techniques discussed in this thesis, a number of standard linear filtering methods can be used to first reduce their number and power. Most noise is broadband (with white noise having a flat spectrum), and most signals are narrowband. Therefore, it should always be possible to improve a signal's signal-to-noise ratio (SNR) by reshaping the spectrum of the waveforms using a filter. Thus, although contaminating white noise is a broadband signal, and therefore corrupts all frequencies, including the frequencies containing the signal of interest, filtering the undesired frequency components can greatly reduce the noise power, thereby improving the SNR of the remaining signal. Accordingly, a filter can be seen as a linear method of reshaping a signals spectrum in some well-defined and desirable manner [165].

Depending on the morphology of the desired signal, artifacts from environmental sources (Section 2.3.1) can normally be suppressed by means of a simple LTI filter. For example, if the artifact signal has a narrow frequency band (e.g. 50/60 Hz hum), which is disjoint from the spectrum of the desired signal, then a notch filter can be

employed to attenuate the power of the signal at these chosen frequencies. Similarly if the frequency range of the signal and artifact are disjoint (e.g. fNIRS-measured neurovascular response and the cardiac pulse [24]) then standard LTI filtering methods can again be implemented.

Experimental artifacts (particularly those relating to motion) in the recorded signals are more difficult to remove than instrumental artifact as they generally do not have a predetermined narrow frequency band and their spectrum often overlaps that of the desired signal [186]. Further, artifacts due to motion are often non-stationary in nature. A signal is said to be non-stationary if the frequency or spectral content can change with respect to time. This changing of the frequency spectrum therefore further invalidates the use of the LTI filters for the removal of artifacts of this type.

Due to the overlapping spectra of the various physiological signals, the majority of artifacts that can be embedded on a signal have to be removed in a way that does not involve basic LTI filters so as to minimise information loss. In the remainder of this chapter and in Chapter 6 a number of the most commonly used algorithms, available at present, which are capable of artifact removal, in situations where basic filtering methods will not suffice, are compared.

5.3 Wiener Filter

Wiener filters were first introduced by Norbert Wiener in the 1940's for use in extrapolating, interpolating and smoothing stationary time series [202]. Wiener filters, which are a type of optimum linear filter, can be used to estimate a desired signal from a contaminated recorded signal. The filter uses a statistical approach to the linear filtering problem and thus makes certain assumptions on the availability of particular signal characteristics such as correlation or power spectrum. The goal is to determine the optimum filter weights so as to minimise the error between the true underlying signal and the estimated signal, calculated using some statistical criterion. The most common statistical criterion implemented for the Wiener filter is the reduction of the mean-square value of the error signal (Equation 5.3).

5.3.1 The mathematics behind the Wiener filter

With a recorded wide-sense-stationary (WSS) signal $x(n)$ the Wiener filter attempts to find the weights of the linear-time-invariant (LTI) system, with an impulse response $h(n)$,

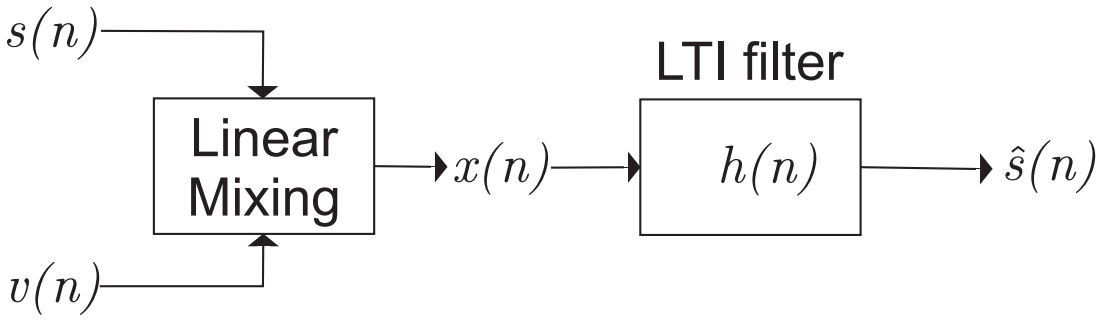

FIGURE 5.6: Discrete time LTI filter for linear MMSE estimation.

such that the filter output $\hat{s}(n)$ is the minimum-mean-square-error (MMSE) estimate of the true desired signal $s(n)$ prior to being contaminated by noise $v(n)$ as shown in Figure 5.6. There are three main variations of the LTI system; the causal filter, the non-causal filter and the finite impulse response (FIR) filter. For the purpose of this thesis the discrete time FIR form of the filter, with tap weights $\mathbf{w}$ ($\mathbf{w} = [w_0, ..., w_{L-1}]$ where L is the number of tap weights), will be used to represent the LTI impulse response. The output of an L tap FIR Wiener filter can be calculated as

$$\hat{s}(n) = \sum_{k=0}^{L-1} w_k x(n-k), \tag{5.2}$$

the error signal $e(n)$ can therefore be defined as:

$$e(n) \triangleq \hat{s}(n) - s(n) \tag{5.3}$$

and the minimisation of the error in the MMSE sense can be described as:

$$\min_{\mathbf{w}} e = E\{e^2(n)\}. \tag{5.4}$$

The resulting filter $\mathbf{w}$ is then known as the Wiener filter for estimation of $s(n)$ from $x(n)$ [146]. In order to determine the optimal choice for $\mathbf{w}$, Equation 5.4 must first be expanded.

$$e = E\left\{\left(\sum_{k=0}^{L-1} w_k x(n-k) - s(n)\right)^2\right\} \tag{5.5}$$

The L weights of $\mathbf{w}$ that minimise the error can be determined by setting the derivative of the equation with respect to $\mathbf{w}$ equal to zero, i.e. $\frac{\delta e}{\delta \mathbf{w}} = 0$ where $\frac{\delta e}{\delta \mathbf{w}} = [\frac{\delta e}{\delta w_0}, ... \frac{\delta e}{\delta w_m}, ... \frac{\delta e}{\delta w_{L-1}}]$. Therefore for the m^{th} element we can write,

$$\frac{\delta e}{\delta w_m} = E\left\{ 2 \underbrace{\left(\sum_k w_k x(n-k) - s(n) \right)}_{e(n)} x(n-m) \right\} = 0. \tag{5.6}$$

This equation therefore specifies that

$$\begin{aligned} E\{e(n)x(n-m)\} &= 0, \text{ or equivalently} \\ R_{ex}(m) &= 0 \text{ for all } m. \end{aligned} \tag{5.7}$$

R_{ex} corresponds to the cross correlation between the error signal and the input. These equations, specifying the relationship between the input and the error signal, are forms of the commonly known *orthogonality principle* which states that the error vector is orthogonal to any possible estimator [48]. Using the equations above it is also possible to show that

$$\begin{aligned} R_{ex}(m) &= E\{e(n)x(n-m)\} \\ &= E\{(\hat{s}(n) - s(n))\, x(n-m)\} \\ &= R_{\hat{s}x}(m) - R_{sx}(m), \text{ and therefore} \\ R_{\hat{s}x}(m) &= R_{sx}(m). \end{aligned} \tag{5.8}$$

This equation states that for the optimum filter, the cross-correlation between the input and the estimated signal is equal to the cross-correlation between the input and the actual signal. As the estimate $\hat{s}(n)$ is calculated by filtering $x(n)$ with the LTI filter $\mathbf{w}$ the following relationship applies:

$$\begin{aligned} R_{\hat{s}x}(m) &= w_m * R_{xx}(m), \text{ which from Equation 5.8 means} \\ w_m * R_{xx}(m) &= R_{sx}(m) \text{ and therefore} \\ \sum_k w_m R_{xx}(m-k) &= R_{sx}(m), \end{aligned} \tag{5.9}$$

where R_{xx} is the autocorrelation of the input $x(n)$.

Therefore for a filter of length L there will be L equations to determine the L values of the filter weights $\mathbf{w}$. These linear equations, with as many equations as unknown, can be also viewed in matrix form as follows:

$$\begin{bmatrix} R_{xx}(0) & R_{xx}(-1) & \cdots & R_{xx}(1-L) \\ R_{xx}(1) & R_{xx}(0) & \dots & R_{xx}(2-L) \\ \vdots & \vdots & \ddots & \vdots \\ R_{xx}(L-1) & R_{xx}(L-2) & \cdots & R_{xx}(0) \end{bmatrix} \begin{bmatrix} w_0 \\ w_1 \\ \vdots \\ w_{L-1} \end{bmatrix} = \begin{bmatrix} R_{sx}(0) \\ R_{sx}(1) \\ \vdots \\ R_{sx}(L-1) \end{bmatrix} \tag{5.10}$$

These equations, known as the Wiener-Hopf equations, can now be solved to determine the impulse response values, i.e. $\mathbf{w} = \mathbf{R}_{xx}^{-1}\mathbf{r}_{sx}$. As autocorrelation ($R$) and power spectral density (S) form a fourier transform pair (i.e. $\mathbf{S}_{xx}(f) = \mathscr{F}\{\mathbf{R}_{xx}(n)\}$) the Wiener-Hopf equations can also be transformed into the frequency domain [88]:

$$\begin{aligned} \mathbf{w} &= \mathbf{R}_{xx}^{-1}(n)\mathbf{r}_{sx}(n) \\ \mathbf{w}(f) &= \frac{\mathbf{S}_{sx}(f)}{\mathbf{S}_{xx}(f)} \\ \mathbf{w}(f) &= \frac{\mathbf{S}_{ss}(f)}{\mathbf{S}_{ss}(f) + \mathbf{S}_{vv}(f)}. \end{aligned} \tag{5.11}$$

Therefore if the power spectral density of the true signal $\mathbf{S}_{ss}$ and the noise $\mathbf{S}_{vv}$ are known then the Wiener filter weights can be calculated as the inverse fourier transform of $\mathbf{w}(f)$.

5.3.2 Requirements and limitations of the filter

The Wiener filter differs from some of the other filtering techniques described in this chapter in a number of ways. Unlike the adaptive filter, described in Section 5.6, the Wiener filter does not require a reference signal to be employed. This is a major advantage to the algorithm as the addition of reference signals also requires additional hardware which can often be a limiting factor for any system to be employed outside of the clinical environment. However, due to the statistical nature of the Wiener filter it is inadequate for dealing with situations in which non-stationarity of the signal and/or noise is intrinsic to the problem. As stated previously the algorithm only requires the autocorrelation or the power spectral density (PSD) of the true signal and the noise in order to operate. The filter also assumes that the signals are zero-mean and uncorrelated with each other. The Kalman filter, described in Section 5.4, is capable of solving the corresponding filtering problem in greater generality for non-stationary signals but with a greater computational complexity.

5.3.3 Employing the Wiener filter

In order to apply the Wiener filter, the PSD of the clean signal ($\mathbf{S}_{ss}$) and the noise signal ($\mathbf{S}_{ss} + \mathbf{S}_{vv}$) must be estimated *a priori*. This measurement can be performed off-line prior to employing the filter. The PSD is a measurement which describes how the power of a signal is distributed with frequency and can be calculated for a signal $z(t)$ as :

$$\begin{aligned} \mathcal{F}(\omega) &= \frac{1}{\sqrt{T}} \int_0^T z(t) e^{-i\omega t} dt \\ \text{PSD}(\omega) &= \lim_{T \to \infty} E[|\mathcal{F}(\omega)|^2]. \end{aligned} \tag{5.12}$$

The measurement of the clean signal PSD ($\mathbf{S}_{ss}$) was performed using the "ground truth" signals from the available training data. The noisy signal PSD can be calculated independently for each trial prior to employment. Once the PSD have been determined the vector $\mathbf{w}$ containing the frequency domain filter weights can be calculated as described in Equation 5.11.

The time domain noisy signals which require the artifact removal are then transformed into the frequency domain prior to processing, i.e. $\mathbf{x}(f) = \mathscr{F}\{\mathbf{x}(n)\}$. Once in the frequency domain the noisy signals can be cleaned by simply multiplying them by the filter weights:

$$\hat{\mathbf{s}}(f) = \mathbf{x}(f) \odot \mathbf{w}(f), \tag{5.13}$$

where $\odot$ denotes component-wise multiplication.

The inverse fourier transform of $\hat{\mathbf{s}}(f)$ yields the time domain estimate of the clean signal ($\mathbf{s}(n)$). This process is repeated for each trial of the fNIRS and EEG benchmark test datasets. An example output of the technique plus the efficacy results for both datasets are presented in Section 5.7 with Section 5.8 presenting an evaluation and comparison of the technique with the other analysed single stage artifact removal techniques.

5.4 Kalman Filter

The Kalman filter can be viewed as a set of mathematical equations, used to provide an efficient computational means to estimate the state of a process. This state is approximated in a way that minimises the variance of the estimation error [200]. The filter is

an optimal linear estimator, similar to the optimal Wiener filter developed by Norbert Wiener [202], however the Kalman filter does not require that the deterministic dynamics or the random processes have stationary properties. This is an important extension as many real applications have non-stationary data distributions. The Kalman filter can be seen as optimal with respect to virtually any criterion that makes sense [125]; that is to say that the average performance of the Kalman filter, over a finite number of runs, on the same application will always exceed the average performance from any other filter.

One of the major benefits of the Kalman filter is its ability to exploit all of the available information (regardless of the precision of that information) when trying to estimate the values of the variables of interest. As a result, no information, no matter how insignificant, is unused when estimating the required state. Examples of these elements of information can include a knowledge of the system and measurement device dynamics, initial conditions or system noise and measurement error statistics. As no mathematical system model is perfect (due to approximations or indeterminacies) and also sensors do not provide perfect and complete data about a given system (due to imprecise sensors or noise), the combined use of all information will always prove to increase the performance of the filter. A further advantage of the Kalman filter is its recursive nature. Consequently, all previous recorded data is not required to be stored and re-processed at each iteration and hence the complexity of the algorithm is reduced, improving the practicality of the filter.

As stated previously, the basic Kalman filter is an optimal linear estimator and thus only capable of operating on processes that can be described using a linear system. However, the filter has also been extended to be capable of operation in the non-linear domain through the Extended Kalman filter [200]. The EEG and fNIRS signals that are being analysed as part of this thesis are assumed to be linearly corrupted by the undesired artifact, and thus the progression onto the Extended Kalman filter is not necessary for this work. The interested reader should refer to Welch and Bishop [200] for more information. Two further assumptions underpinning the Kalman filter are that the system and measurement noises are 1) white and 2) Gaussian. Whiteness implies that the noise signals contain equal power at all frequencies and are not correlated with time while the Gaussianity describes the distribution of the probability density function of the signal. These 3 basic assumptions help to reduce the complexity of the mathematics involved and thus make the filter more tractable.

The basic equations used to describe the linear systems used by the Kalman filter are described in Equations 5.14 and 5.15 [200].

State equation:

$$\mathbf{s}_{n+1} = \mathbf{A}_n\mathbf{s}_n + \mathbf{B}_n\mathbf{u}_n + \mathbf{w}_n, \tag{5.14}$$

Output Equation:

$$\mathbf{x}_n = \mathbf{H}_n\mathbf{s}_n + \mathbf{v}_n, \tag{5.15}$$

where $\mathbf{s}_n$ is the k-dimensional state vector (*unknown*, *desired*), $\mathbf{u}_n$ is the m-dimensional input vector (*known*, *optional*), $\mathbf{x}_n$ is the p-dimensional output vector (*known*, *measured*), $\mathbf{A}_n$, $\mathbf{B}_n$, $\mathbf{H}_n$ are appropriately dimensioned system matrices (*known*) and $\mathbf{w}_n$ and $\mathbf{v}_n$ are zero-mean, white Gaussian noise with (*known*) covariance matrices $\mathbf{Q}_n$ and $\mathbf{R}_n$ respectively.

$$p(\mathbf{w}) \sim N(0, \mathbf{Q}), \tag{5.16}$$

$$p(\mathbf{v}) \sim N(0, \mathbf{R}). \tag{5.17}$$

In practice the process noise covariance matrix $\mathbf{Q}$ and the measurement noise covariance matrix $\mathbf{R}$ might change over the length of the measurement signal, however they are assumed to be constant. This assumption is analysed further later in the section. The $\mathbf{A}$ matrix relates the state at the previous time sample $(n-1)$ to the state at the current time sample (n). Although $\mathbf{A}$ may change slightly with respect to time it is assumed to remain constant. The matrix $\mathbf{B}$ relates the (optional) control input $\mathbf{u}$ to the state $\mathbf{s}$. Finally, the matrix $\mathbf{H}$ relates the state $\mathbf{s}$ to the measurement $\mathbf{x}$ and is again assumed constant over time.

Although desirable, it is not possible to measure the state $\mathbf{s}$ directly. Instead measurements $\mathbf{x}$ which are a function of the state are available, but are also contaminated by some noise factor $\mathbf{v}$, shown in Figure 5.7. It is therefore not possible to simply use the information from the measured signal to determine the current state; instead the extent to which the measurement values are used is determined by the "trust" that can be placed on their estimated accuracy. This "trust" value is determined using a parameter known as the Kalman gain factor, and will be described in the next section.

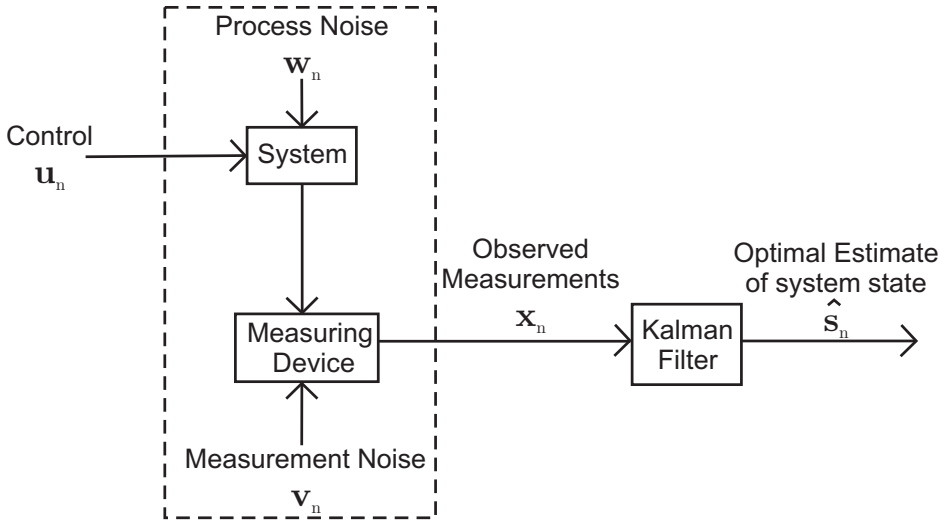

FIGURE 5.7: Block diagram of the basic Kalman filter application [125]

5.4.1 The mathematics behind the filter

The Kalman filter addresses the problem of estimating the state $\mathbf{s}$ using both a model of the state and the recorded noisy measurements. The filter uses a method of formulation known as prediction-correction; it uses the process model to predict the next state of the system given the current state, and then corrects that prediction based on the available noisy measurements. The prediction stage projects the current state $\mathbf{s}_{n-1}$ forward in time to generate the *a priori* estimates for both the state $\hat{\mathbf{s}}_n$ and the error covariances $\mathbf{P}_n^-$ for the next time sample using the time update equations shown in Equation 5.18-5.19.

$$\hat{\mathbf{s}}_n^- = \mathbf{A}\hat{\mathbf{s}}_{n-1} + \mathbf{B}\mathbf{u}_{n-1} \tag{5.18}$$

$$\mathbf{P}_n^- = \mathbf{A}\mathbf{P}_{n-1}\mathbf{A}^T + \mathbf{Q} \tag{5.19}$$

The Kalman filter can thus be seen to be projecting forward the conditional probability density function, described by the first two moments of the state distribution (mean and variance). As the system is described through a linear model and both the process and measurement noise are assumed Gaussian, the mean and variance of the system completely describe the processes conditional probability density function. The measurement update equations, shown below in Equation 5.20-5.22, are then employed to perform a correction of the *a priori* estimate of the current state $\hat{\mathbf{s}}_n^-$ using the available noisy measurements $\mathbf{x}_n$.

$$\mathbf{K}_n = \mathbf{P}_n^- \mathbf{H}^T (\mathbf{H}\mathbf{P}_n^- \mathbf{H}^T + \mathbf{R})^{-1} \tag{5.20}$$

$$\hat{\mathbf{s}}_n = \hat{\mathbf{s}}_n^- + \mathbf{K}_k(\mathbf{x}_n - \mathbf{H}\hat{\mathbf{s}}_n^-) \tag{5.21}$$

$$\mathbf{P}_n = (\mathbf{I} - \mathbf{K}_n\mathbf{H})\mathbf{P}_n^- \tag{5.22}$$

The matrix $\mathbf{K}$ is known as the Kalman gain and determines the "trust" that should be placed on the measurement value. From Equation 5.20 it can be seen that as the measurement error covariance matrix $\mathbf{R}$ approaches zero, the Kalman gain matrix increases, i.e.

$$\lim_{\mathbf{R}_n \to 0} \mathbf{K}_n = \mathbf{H}^{-1}. \tag{5.23}$$

Conversely, if the *a priori* estimate error covariance $\mathbf{P}$ approaches zero then the Kalman gain matrix also tends to zero, i.e.

$$\lim_{\mathbf{P}_n^- \to 0} \mathbf{K}_n = 0. \tag{5.24}$$

Therefore, from Equation 5.21, it can be seen that when the measurement error covariance $\mathbf{R}$ is low (i.e. $\mathbf{K}$ is high) the measurement $\mathbf{x}_n$ is trusted more and the state estimate gets corrected by $\mathbf{K}$ times the difference between the current measurement and the predicted estimate. However if the estimate error covariance $\mathbf{P}$ is low or the measurement error covariance $\mathbf{R}$ is high (i.e. $\mathbf{K}$ is low) then there is very little, if any, correction to the state estimate. The difference between the measured value and the predicted value $(\mathbf{x}_n - \mathbf{H}\hat{\mathbf{s}}_n^-)$ is known as the innovation or the residual.

Figure 5.8 illustrates the prediction correction loop performed by the Kalman filter. Using initial estimates for the state and error covariance, the time update equations predict the next state and error covariance matrix. The filter then updates the Kalman gain matrix using the current *a priori* error covariance matrix $\mathbf{P}_n^-$, and the measurement error covariance matrix $\mathbf{R}$. The state and estimate covariance is next corrected to determine the *a posteriori* estimates $\hat{\mathbf{s}}_n$ and $\mathbf{P}_n$. The loop then repeats with the *a posteriori* estimates becoming the previous sample estimates in the time update equations.

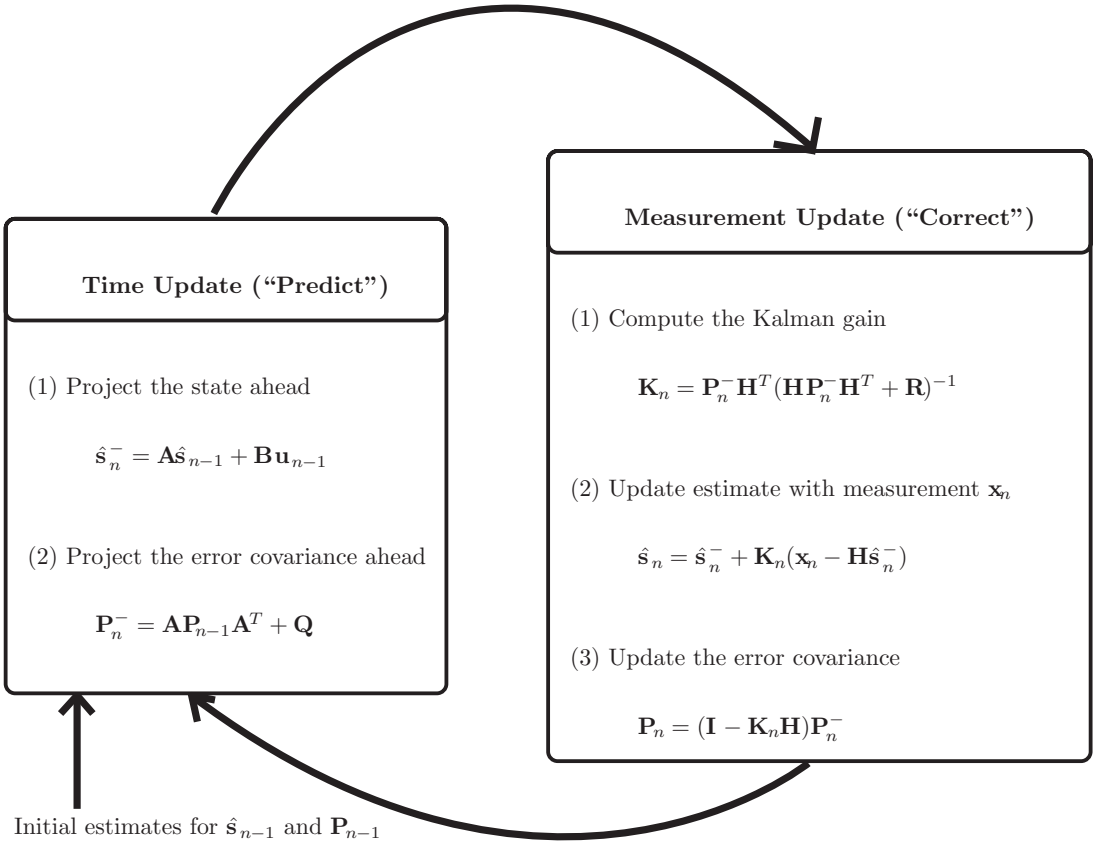

FIGURE 5.8: A flow diagram of the prediction correction formulation of the Kalman filter [200]

5.4.2 What input parameters are required by the user *a priori*?

Before the Kalman filter can be employed on any given process, a number of parameters must be first initialised. The initial estimate of the state, $\hat{\mathbf{s}}_{n-1}$, is usually set to zero as normally an accurate estimate of the state is not available. An incorrect initial estimate will not prevent the filter from converging on the correct answer, but instead will only cause the initial convergence speed to be slower. The initial estimate error covariance $\mathbf{P}_{n-1}$ must also be set. The choice of this parameter is arbitrary, so long as it is not set to zero. If set to zero the filter would initially and always believe the choice for $\hat{\mathbf{s}}$ (Equation 5.24). Therefore, any other choice (i.e. $\mathbf{P}_{n-1} \neq 0$) and the filter will eventually converge. For the purpose of this thesis the initial $\mathbf{P}_{n-1}$ was set to the initial signal value (i.e. $\mathbf{x}_n(1)$) as implemented by Izzetoglu et al. [87].

The covariance matrices for the (zero-mean, white, Gaussian) process $\mathbf{Q}$ and measurement $\mathbf{R}$ noise parameters also have to be set *a priori*. The choice of $\mathbf{R}$, as stated above in Section 5.4.1, will determine how much "trust" the filter will place on the acquired measurements. When employing the filter to operate on the EEG or fNIRS

signals, recorded using the methodology described in [177], the measurement error covariance $\mathbf{R}$ was initially set as the variance of the artifact signal, where this signal was calculated as the difference between the recorded clean and noisy signals. However this static selection of $\mathbf{R}$ is a disadvantage of the Kalman filter. The Kalman filter assumes that the noise signal is consistent throughout the signal and therefore a static $\mathbf{R}$ is adequate. In the recordings analysed in this thesis the variance of the artifact signal is changing quite dramatically between epochs of movement and no movement. If a single value for $\mathbf{R}$ is used the filter output will be of one of two types. Either the $\mathbf{R}$ value will be too high meaning that there is very little "trust" placed on the recording even during the epochs of no movement (Figure 5.9(a)). During these epochs the signal will be highly attenuated thus reducing the effectiveness of the algorithm. Or, conversely, the value of $\mathbf{R}$ will be too low and the artifact will not be removed due to the high "trust" placed on the recorded signal (Figure 5.9(b)). Figure 5.9(c) provides an example of the output of the novel algorithm when a variable $\mathbf{R}$ value is employed. It can therefore be easily seen that a variable value for $\mathbf{R}$ is required. Unfortunately this requirement also requires a method for determining when the artifact has occurred in the signal, however using the recording system described in Chapter 4 a reference signal in the form of an accelerometer is available and thus the tagging algorithm, described in Section 5.1, can be employed. Using the training data, two values for $\mathbf{R}$ were determined. The first was calculated as the variance of the epochs of clean data from the artifact signal (i.e. difference between clean and noisy signal) ($\mathbf{R} = 1.351 \times 10^{-5}$) while the second was calculated similarly but instead employed the epochs of known noisy data ($\mathbf{R} = 1.1 \times 10^{-3}$). The process error covariance is often difficult to determine, and can be "tuned" to help improve the performance of the filter. For use with the EEG and fNIRS signals, $\mathbf{Q}$ was calculated as the variance of the true signal times the error of the AR model, as implemented by Izzetoglu *et al.* [87] ($\mathbf{Q} = 3.5 \times 10^{-10}$).

The system matrices $\mathbf{A}$, $\mathbf{B}$ and $\mathbf{H}$ must also be initialised prior to the use of the Kalman filter. As stated previously the $\mathbf{A}$ matrix relates the state at the previous time sample to the state at the current time sample. The Yule-Walker method was used to calculate the parameters of a 5^{th} order auto-regressive (AR) model for both the EEG and fNIRS data. A model order of 5 was determined to be sufficient to model both signal modalities using the "System Identification Tool" in MATLAB which determines the optimal tradeoff between model fidelity and model complexity. Therefore the next estimate of the state was a function of the previous 5 samples. The final $\mathbf{A}$ matrix thus has the following form:

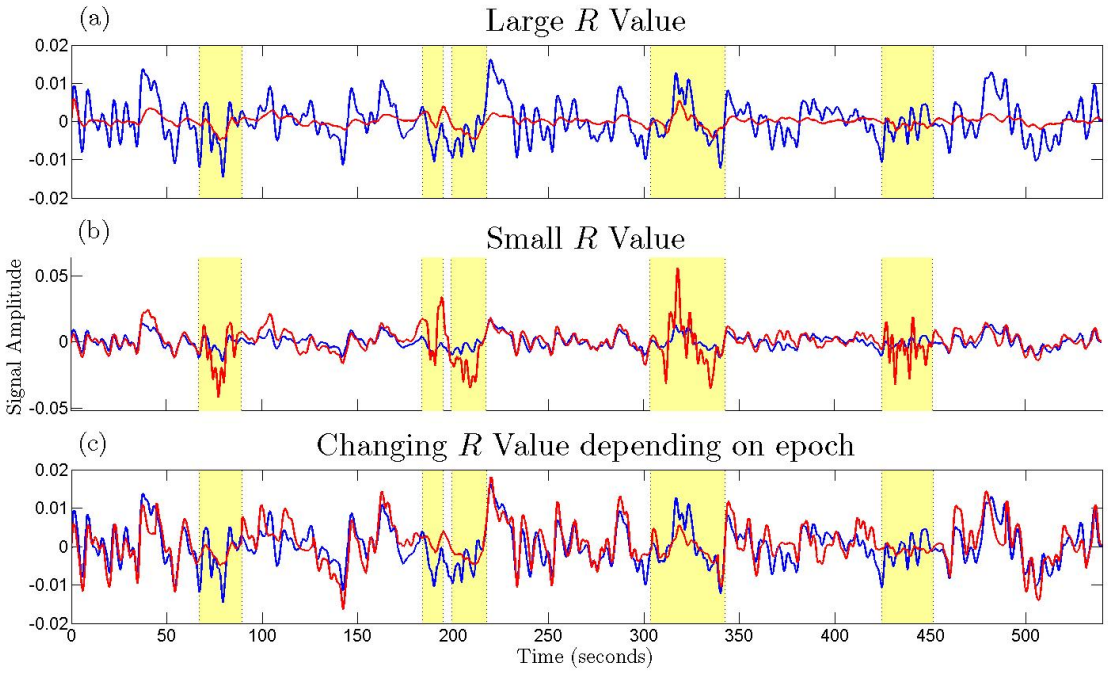

FIGURE 5.9: Effect of changing R value when using the Kalman filter. The output of the filter is shown in red, with the true signal shown in blue. A static value for R can be seen to be sub-optimal with intermittent artifacts.

$$\mathbf{A} = \begin{bmatrix} -\mathbf{yw}(2) & -\mathbf{yw}(3) & -\mathbf{yw}(4) & -\mathbf{yw}(5) & -\mathbf{yw}(6) \\ 1 & 0 & 0 & 0 & 0 \\ 0 & 1 & 0 & 0 & 0 \\ 0 & 0 & 1 & 0 & 0 \\ 0 & 0 & 0 & 1 & 0 \end{bmatrix}, \tag{5.25}$$

where **yw** are the parameters of the AR model determined using the Yule-Walker equations. As no control input, **u**, was being applied to the employed system, there was no requirement for the **B** matrix and therefore it was set to zero. As the measurements were a direct recording of the current state, with added noise, the **H** matrix could simply be initialised as:

$$\mathbf{H} = \begin{bmatrix} 1 & 0 & 0 & 0 & 0 \end{bmatrix}. \tag{5.26}$$

5.4.3 Employing the Kalman filter

Prior to employing the Kalman filter the training data was used to determine the AR model coefficients and, using these coefficients, the process error covariance **Q** was calculated. With all the required *a priori* parameters initialised, the Kalman filter can

then be employed to estimate the underlying desired signal $\hat{\mathbf{s}}$. The filter passes through each sample of the signal, performing both the time update (Equation 5.18-5.19) and the measurement update equations (5.20-5.22) as shown in Figure 5.8. During epochs of no detected movement, the value of the variance $\mathbf{R}$ is low and so the filter places a lot of "trust" on the actual recorded signal. However, during epochs of motion, determined using the detailed data tagging algorithm , the value of $\mathbf{R}$ is changed to the pre-defined variance of the artifact signal. During these epochs, the recorded measurements have less "trust" placed in them and consequently the model of the signal output is trusted more. By doing so, the Kalman filter removes the artifact from the measurement signal. Figure 5.23 and 5.24 provide examples of the outputs of the Kalman filter when employed on contaminated fNIRS and EEG data. The improvement in SNR and correlation after employing the Kalman filter is detailed in Section 5.7.

5.5 Morphological Component Analysis

Morphological component analysis (MCA) was first described by Stark *et al.* [171] in 2005 as a means for separating sources which have differing underlying morphological characteristics. Unlike other techniques such as ICA or CCA which separate the contaminated signal into sources which are deemed independent or uncorrelated, the MCA technique uses the morphological diversity of the individual sources contained in the data and uses this diversity to associate each morphology to a particular dictionary of atoms for which a fast transform is available [17]. The morphology of a signal describes the shape or form of the signal, i.e. does it have a smooth or spiky impulse-like waveform.

As the assumption is that the recorded single channel signal is a combination of the desired EEG or fNIRS signal $\mathbf{s}(n)$ plus the undesired artifact $\mathbf{v}(n)$, i.e.

$$x(n) = s(n) + v(n) \tag{5.27}$$

it becomes possible to use the MCA technique to separate the components that are known to be morphologically dissimilar.

5.5.1 Operation of the Morphological Component Analysis technique

As stated previously the artifact signal $\mathbf{v}$ ($\mathbf{v} = [v(1), ...v(N)]$, where N is the length of the signal) can be viewed as an individual independent source signal and thus the recorded signal $\mathbf{x}$ can be calculated as the sum of k sources, each with differing morphologies, i.e.,

$$\mathbf{x} = \sum_{i=1}^{k} \mathbf{s}_i. \tag{5.28}$$

The MCA technique makes the following assumptions on these individual sources [171]:

- For every possible source signal $\mathbf{s}_i$ there exists a dictionary $\mathbf{\Phi}_i$ (which can be overcomplete), such that solving

  $$\boldsymbol{\alpha}_i^{opt} = \underset{\boldsymbol{\alpha}}{\operatorname{argmin}} \|\boldsymbol{\alpha}\|_0, \text{ subject to } \mathbf{s} = \mathbf{\Phi}\boldsymbol{\alpha}$$

  leads to a very sparse solution. Sparse representations are representations that account for most or all information of a signal with a linear combination of a small number of elementary signals called atoms (i.e. $\|\boldsymbol{\alpha}_i^{opt}\|_0$ is very small). $\|\mathbf{z}\|_0$ denotes the ℓ_0 pseudo-norm of the vector $\mathbf{z}$, i.e. the number of non-zero coefficients of $\mathbf{z}$ ($\ell_0 \equiv \|\mathbf{z}\|_0 \triangleq \#(i; \mathbf{z}_i \neq 0)$).

- Also for every possible source signal $\mathbf{s}_j$, where $j \neq i$

  $$\boldsymbol{\alpha}_j^{opt} = \underset{\boldsymbol{\alpha}}{\operatorname{argmin}} \|\boldsymbol{\alpha}\|_0, \text{ subject to } \mathbf{s}_j = \mathbf{\Phi}_i\boldsymbol{\alpha}$$

  leads to a very non-sparse solution (i.e. $\|\boldsymbol{\alpha}_j^{opt}\|_0$ is very large).

Therefore the obtained dictionary is composed of atoms built by associating several transforms $\mathbf{\Phi} = [\mathbf{\Phi}_1, ..., \mathbf{\Phi}_k]$ such that, for each i ($i = 1, ..., k$), $\mathbf{s}_i$ is sparse in $\mathbf{\Phi}_i$ and is non-sparse in $\mathbf{\Phi}_j$, i.e.

$$\forall i, j \neq i \quad \|\mathbf{\Phi}_i^T \mathbf{s}_i\|_0 < \|\mathbf{\Phi}_j^T \mathbf{s}_i\|_0. \tag{5.29}$$

In order to obtain the sparsest of the possible representations over the overcomplete dictionary ($\mathbf{\Phi}$) the MCA technique is required to solve the following equation:

$$\begin{aligned} \{\boldsymbol{\alpha}_1^{opt}, ..., \boldsymbol{\alpha}_k^{opt}\} \quad &= \underset{\{\boldsymbol{\alpha}_1, ..., \boldsymbol{\alpha}_k\}}{\operatorname{argmin}} \sum_{i=1}^{k} \|\boldsymbol{\alpha}_i\|_0 \\ &\text{subject to } \mathbf{x} = \sum_{i=1}^{k} \mathbf{\Phi}_i \boldsymbol{\alpha}_i. \end{aligned} \tag{5.30}$$

However, the problem formulated in Equation 5.30 can be difficult to solve due to the use of the ℓ_0 norm. The complexity of the algorithm will grow exponentially with the

number of columns in the dictionary. When using the basis pursuit model Chen *et al.* [35] proposed the use of the ℓ_1-norm instead of the ℓ_0-norm thus allowing for a less computationally expensive optimisation problem. The ℓ_1-norm can be defined as:

$$\ell_1 \equiv \|\mathbf{z}\|_1 \triangleq \sum_{i=1}^{n} |\mathbf{z}_i|. \tag{5.31}$$

Further, the constraint on Equation 5.30 can be relaxed slightly to reduce the processing time and improve the algorithms robustness and thus the equation becomes

$$\begin{aligned} \{\boldsymbol{\alpha}_1^{opt}, ..., \boldsymbol{\alpha}_k^{opt}\} &= \underset{\{\boldsymbol{\alpha}_1,...,\boldsymbol{\alpha}_k\}}{\operatorname{argmin}} \sum_{i=1}^{k} \|\boldsymbol{\alpha}_i\|_1 \\ &\text{subject to } \|\mathbf{x} - \sum_{i=1}^{k} \boldsymbol{\Phi}_i \boldsymbol{\alpha}_i\|_2 < \sigma. \end{aligned} \tag{5.32}$$

where σ is the noise standard deviation and $\| \, . \, \|_2$ represents the Euclidean norm. The MCA algorithm, described below, is based on an iterative, alternate, matched filtering and thresholding scheme. The algorithm is presented for the case in which two underlying signals are to be separated (i.e. signal and artifact).

1. The dictionaries to be employed are selected and are used to create the overcomplete dictionary $\boldsymbol{\Phi}$. (The choice of dictionaries is described in Section 5.5.2.)

2. The total number of iterations I_{max} and the initial threshold value δ are set. The threshold value is used to help maintain the sparsity of the matrices. The starting threshold (δ_{init}) is set as the minimum of the maximum coefficient of the signal in each dictionary.
   (i.e. calculate $\boldsymbol{\alpha}_i = \boldsymbol{\Phi}_i^T \mathbf{x}$, for $i = 1, 2$. $\delta_{init} = \min(\max(\boldsymbol{\alpha}_1), \max(\boldsymbol{\alpha}_2)))$

3. While the current iteration number is less than I_{max} perform the following steps to calculate the current approximation for the underlying signals $\mathbf{s}_i$ for $i = 1, 2$. For the first iteration $\mathbf{s}_i$ is set to 0;

   (a) Calculate the residual signal to be analysed

   $$\mathbf{r} = \mathbf{x} - \sum_{i=1}^{2} \mathbf{s}_i. \tag{5.33}$$

   (b) The total signal to be analysed using dictionary i is thus

   $$\mathbf{r}_i = \mathbf{r} + \mathbf{s}_i. \tag{5.34}$$

(c) Calculate the coefficients $\boldsymbol{\alpha}_i$ for the signal $\mathbf{r}_i$ by running the fast analysis for the chosen dictionary.

$$\boldsymbol{\alpha}_i = \boldsymbol{\Phi}_i^T \mathbf{r}_i. \tag{5.35}$$

(d) Perform hard thresholding on the coefficients, retaining only the coefficients whose values are above the pre-defined threshold δ, to calculate the new coefficients $\hat{\boldsymbol{\alpha}}_i$. i.e.

$$\hat{\alpha}_i^{(n)} = \begin{cases} \alpha_i^{(n)} & \text{if } \alpha_i^{(n)} > \delta \\ 0 & \text{if } \alpha_i^{(n)} \leq \delta \end{cases} \text{ for } n = \{1, ...N\} \tag{5.36}$$

where N is the number of coefficients. This step ensures the matrices remain as sparse as possible.

(e) Use these new coefficients to reconstruct the new estimate of $\mathbf{s}_i$

$$\hat{\mathbf{s}}_i = \boldsymbol{\Phi}_i \hat{\boldsymbol{\alpha}}_i. \tag{5.37}$$

4. The threshold value δ is reduced after each iteration to allow each dictionary to better represent the residual signal [17]. The threshold is reduced by λ on each iteration where

$$\lambda = \frac{\delta_{init} - \lambda_{min}}{I_{max}}. \tag{5.38}$$

Therefore on the last iteration the threshold value will equal to λ_{min}, where λ_{min} is equal to three times the standard deviation of the noise.

5.5.2 Choice of the optimum dictionaries

As stated previously, the MCA uses dictionaries of atoms for which a fast transform is available [17]. In order to determine the optimum dictionaries to employ to represent the desired and artifact signal a range of different dictionary combinations were analysed. Fadili *et al*. [54] present a number of dictionaries which can be implemented with the MCA algorithm and the tested dictionaries are listed below.

- DCT - Discrete cosine transform (DCT) dictionary. Expresses a sequence of finitely many data points in terms of a sum of cosine functions oscillating at different frequencies.
- LDCT - Local transform using a DCT dictionary. It is local as is computed over windows of the data, similar to the short time fourier transform (STFT).

- ALDCTiv - Adaptive Local DCT-iv transform [103]. DCT-iv is another variant of the DCT transform with a slightly modified definition. The DCT-iv algorithm outperforms the DCT-ii transform used above for large transform sizes [26].
- LDST - Local transform using a discrete sine transform (DST) dictionary. DSTs express a function or a signal in terms of a sum of sinusoids with different frequencies and amplitudes.
- LDSCT - Local transform using a DCT-DST dictionary.
- ATrou - Fast Dyadic wavelet Transform [101]. This algorithm is more famously known as "*algorithme à trous*" in French (the word *trous* means holes in English) which refers to inserting zeros in the filters. It uses a biorthonormal quadratic spline filter pair.
- UDWT - Undecimated wavelet transform. This uses wavelet algorithms that are shift invariant.
- LWP - Wavelet Packet dictionary.

The choice of the optimum dictionary is crucial to the operation of the MCA algorithm. The chosen dictionaries must be capable of accurately representing only the desired signal type. As the dictionaries employing the DCT or DST variations represent similar waveforms they were only compared against the dictionaries which employed wavelets (i.e. ATrou, UDWT, LWP). This resulted in 18 different possible combinations of dictionaries.

In order to chose the optimum dictionary pair the performance was evaluated using the benchmark fNIRS and EEG training datasets introduced in Chapter 4. Using the available "ground truth" signal it is also possible to extract an estimate of the artifact signal (i.e. difference between the noisy signal and the clean "ground truth" signal). The MCA algorithm was run for each dictionary combination on both the EEG and fNIRS training data and the correlations of the separated signals ($\mathbf{s}_1$ and $\mathbf{s}_2$) with the "ground truth" and artifact signals were calculated. The results for the EEG and fNIRS data can be seen in Figure 5.10 and 5.11 respectively.

The first subplot represents the correlation of the first signal $\mathbf{s}_1$ with the "ground truth" signal and the second signal $\mathbf{s}_2$ with the artifact. The second subplot then shows the opposite with the correlation of the first signal $\mathbf{s}_1$ with the artifact signal and the second signal $\mathbf{s}_2$ with the "ground truth". The optimum dictionaries were determined as

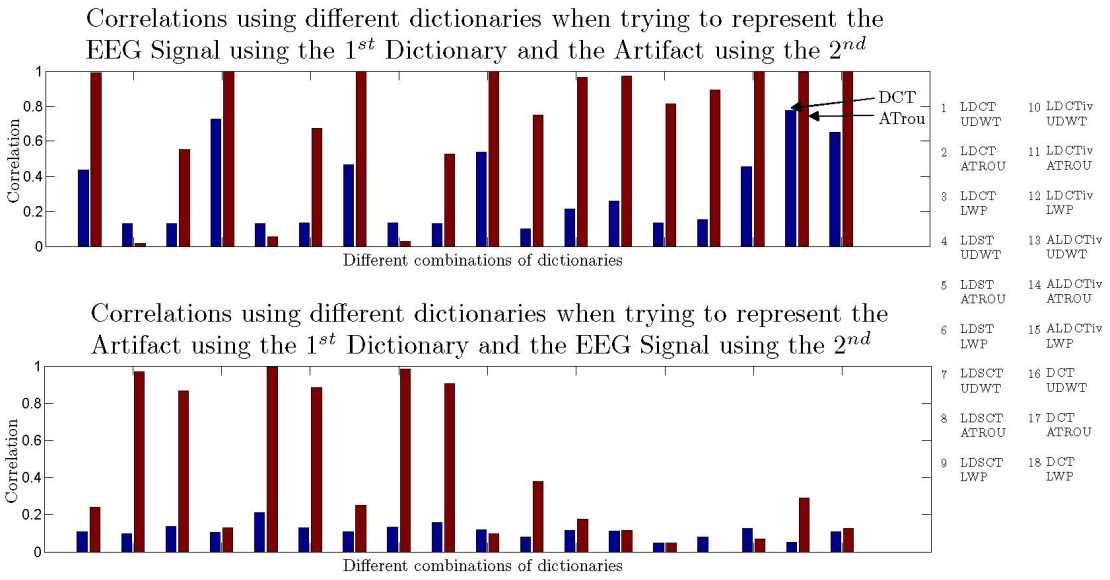

FIGURE 5.10: Correlation of the outputs of the MCA technique with the desired clean EEG signal and the artifact. Combinations of dictionaries are shown on the side. Ideally signals should have high correlation on one plot and very low correlations on the second. It can be seen that the combination of DCT and ATrou gives the best results, with DCT representing the signal and ATrou representing the artifact.

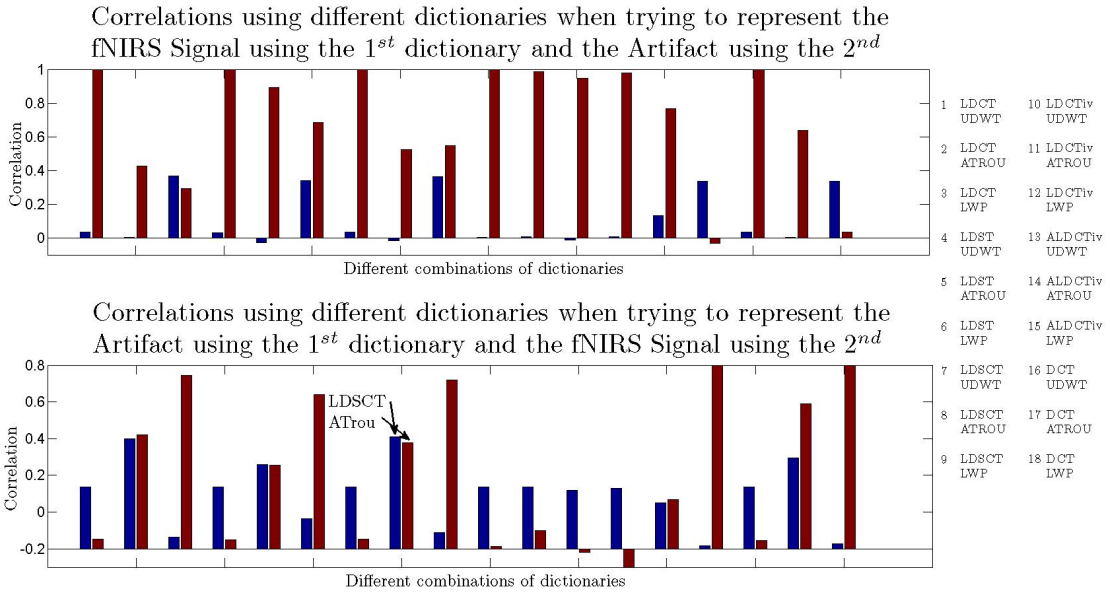

FIGURE 5.11: Correlation of the outputs of the MCA technique with the desired clean fNIRS signal and the artifact. Combinations of dictionaries are shown on the side. Ideally signals should have high correlation on one plot and very low correlations on the second. It can be seen that the combination of LDSCT and ATrou gives the best results, with ATrou representing the signal and LDSCT representing the artifact.

the pair which returned a high correlation for both signals in one subplot, while having a low correlation in the second. This pair could then be said to conform to Equation 5.29.

For the EEG signal it can be seen that the combination of the discrete cosine transform (DCT) and the ATrou dictionaries gives the best results in terms of correlation with the desired signals. This representation of the EEG signal by the DCT dictionary also ties in with the results found by Yong *et al.* [210] [211] when denoising EEG contaminated with spikes, muscle and ocular artifacts. The ATrou dictionary is more proficient at representing the slower changing artifact signal.

For the fNIRS contaminated signal the dictionaries ATrou and LDSCT were deemed to be the optimum in terms of separation. However as the morphology of the artifact signal and the desired signal were not as distinct as for the EEG signals, the dictionaries did not yield results as accurate as those obtained with the EEG data. The local discrete sine cosine transform (LDSCT) dictionary was deemed to be the best at representing the artifact signal while using the ATrou dictionary to represent the desired signal. In truth, the choice of dictionary for the artifact could also have been chosen to be either the DCT or LDCT as all three results are similar.

5.5.3 Optimising the dictionary parameters

After the optimal dictionaries were chosen, the parameters of the dictionaries were tuned so as to give the best results for the lowest computational time. The ATrou dictionary requires a parameter called the scale value as input which determines the number of detail levels to omit in the decomposition. The DCT dictionary takes in a fineness parameter as its input. This parameter determines the fineness or coarseness of the DCT coefficient quantisation; the higher the fineness the more coefficients used to represent the signal. Figure 5.12 shows how the computational time of the MCA technique changes when operating on EEG data, using the ATrou and DCT dictionaries, with changing parameter values. Figure 5.13 then shows how the correlation of the output with the "ground truth" signal changes with changing parameter values. From these figures the optimum parameter values were chosen. The scale parameter for the ATrou was set to 9, and the fineness parameter was set to 2. This ensured that the correlation value remained high while the computational time remains as low as possible.

When using the MCA algorithm on the fNIRS data the LDSCT dictionary is employed. The input parameters for this dictionary are the window width and the amount of overlap of the windows. Figure 5.14 shows how the computational time of the MCA technique changes when operating on the fNIRS data, using the ATrou and LDSCT dictionaries, with changing parameter values. Figure 5.15 then shows how the correlation of the output with the "ground truth" signal changes with these changing parameter

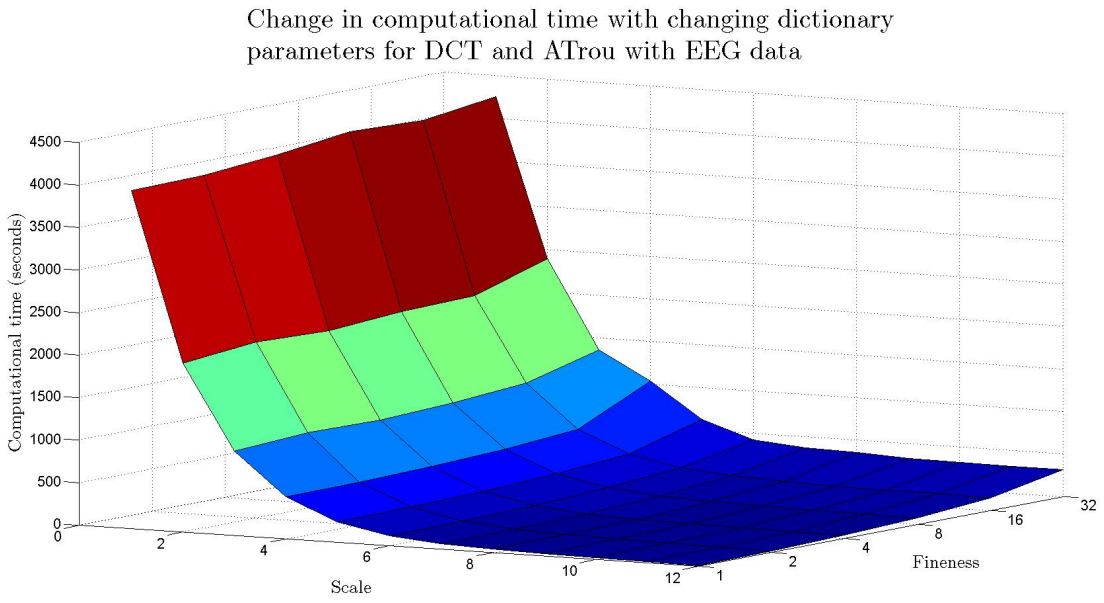

FIGURE 5.12: Change in computational time of the MCA algorithm employed on the corrupted EEG with changing input parameters to the two dictionaries DCT and ATrou.

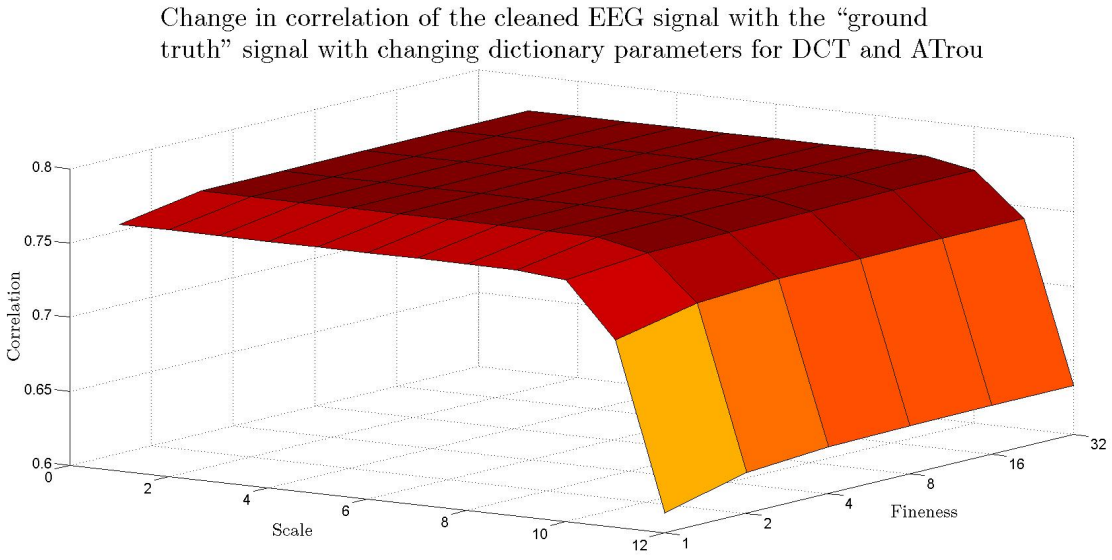

FIGURE 5.13: Change in correlation between the output of the MCA algorithm and the "ground truth" EEG signal with changing input parameters to the two dictionaries DCT and ATrou.

values. From the information shown in these figures the optimum parameters for the LDSCT dictionary were chosen to be 16 for the window width and 0.25 for the overlap. A scale of 10 was also found to be optimum for the ATrou dictionary.

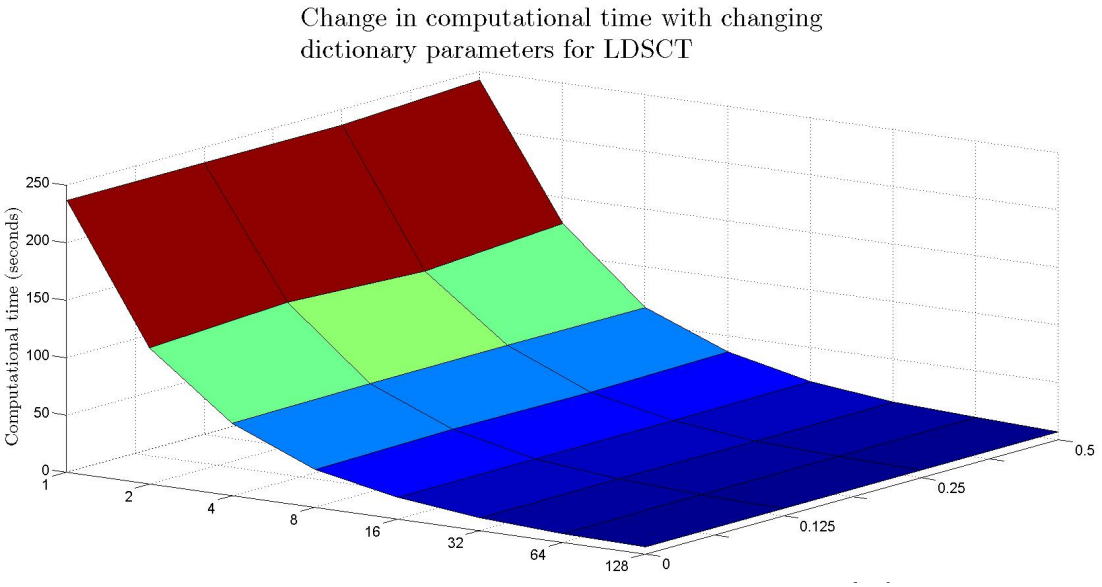

FIGURE 5.14: Change in computational time of the MCA algorithm employed on the corrupted fNIRS with changing input parameters to the two dictionaries LDSCT and ATrou.

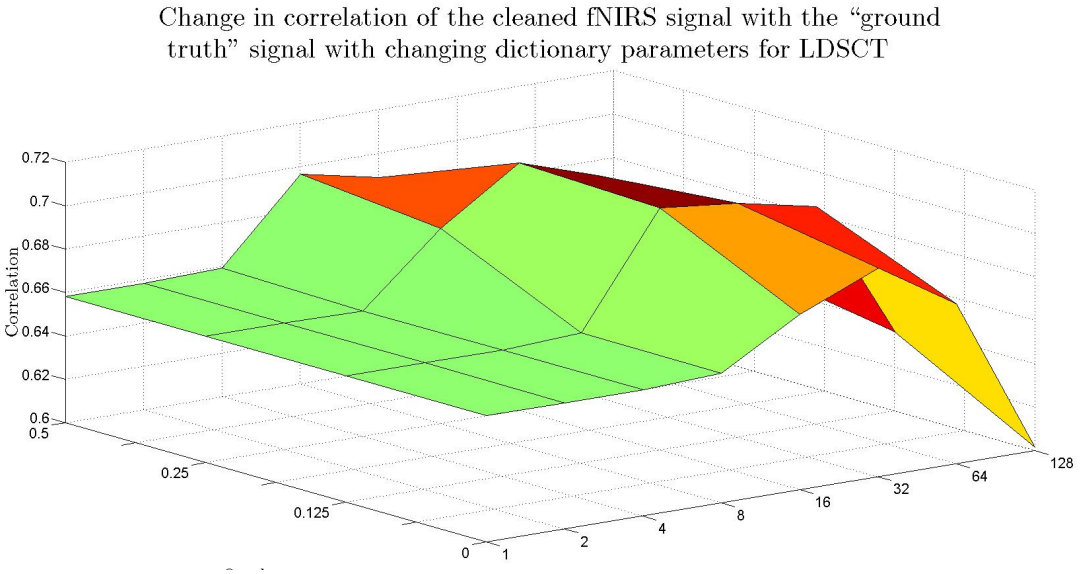

FIGURE 5.15: Change in correlation between the output of the MCA algorithm and the "ground truth" fNIRS signal with changing input parameters to the two dictionaries LDSCT and ATrou.

5.5.4 Employing the MCA algorithm

With the optimum parameters set for the fNIRS and EEG dictionaries the MCA algorithm could be employed to separate the artifact signal from the desired signal for each of the trials in the test dataset. The number of iterations (I_{max}) was set to 100 to allow for a small change in the threshold value (λ) on each iteration and thus a more accurate separation of the signals. Once the signals have been separated using the

employed dictionaries, the cleaned signal can simply be selected. For the fNIRS data this was the signal represented using the ATrou dictionary and for EEG data it was the DCT dictionary. The efficacy results for the technique are presented in Section 5.7 with Figure 5.25 and 5.26 showing an example output of the technique.

If further artifact signals are known to be contaminating the signal, additional dictionaries can be added. Yong *et al.* [210] [211] employed three dictionaries for the removal of spike and muscle artifacts from EEG signals.

5.6 Adaptive Filter

The adaptive filter is an extension to the artifact removal technique employed by the Wiener filter. As stated in Section 5.3 the Wiener filter uses statistical techniques to aid in the removal of the undesired noise from signals of interest. The filter computes the optimal filter coefficients in the situations where the original source signals are known to be stationary. When the signals are stationary the "error" surface $E[\epsilon^2]$ forms a bell shape which is fixed in position, similar to that shown in Figure 5.16. Using statistical properties the minimum of the bell can be found, corresponding to the minimisation of the error. However, when the signals are not stationary this bell shape, corresponding to the error at different filter weights, shifts over time. The optimal weights at one time point will therefore no longer be optimal at another. In these situations an adaptive filtering technique is required which will be capable of adapting the weights over time.

An adaptive filter is defined as a self-designing system that relies on a recursive algorithm for its operation. This enables the filter to perform in environments where there is insufficient knowledge of the statistics of the signals to compute filter parameters *a priori* [72]. The first designed linear adaptive filter algorithm was the least-mean-squared (LMS) algorithm developed by Widrow and Hoff in 1959 [201].

As stated in Section 3.1, the two families of algorithms most commonly implemented for the adaptive filter are the LMS and RLS algorithms. The recursive least square (RLS) algorithm attempts to estimate approximations for $\mathbf{R}_{xx}$ and $\mathbf{r}_{sx}$ from Equation 5.11 and therefore compute $\mathbf{w}_{opt}$. The RLS class of algorithms have very fast convergence, however this benefit comes at a cost of high computational complexity $\mathrm{O}(L^2)$. The LMS based algorithms do not use the statistical properties of the signals to determine $\mathbf{w}_{opt}$ but instead iteratively approximate the gradient of the error surface and use gradient descent to determine the next best approximation for $\mathbf{w}_{opt}$. The LMS algorithms are the most commonly implemented adaptive filter algorithms to date due to their simplicity

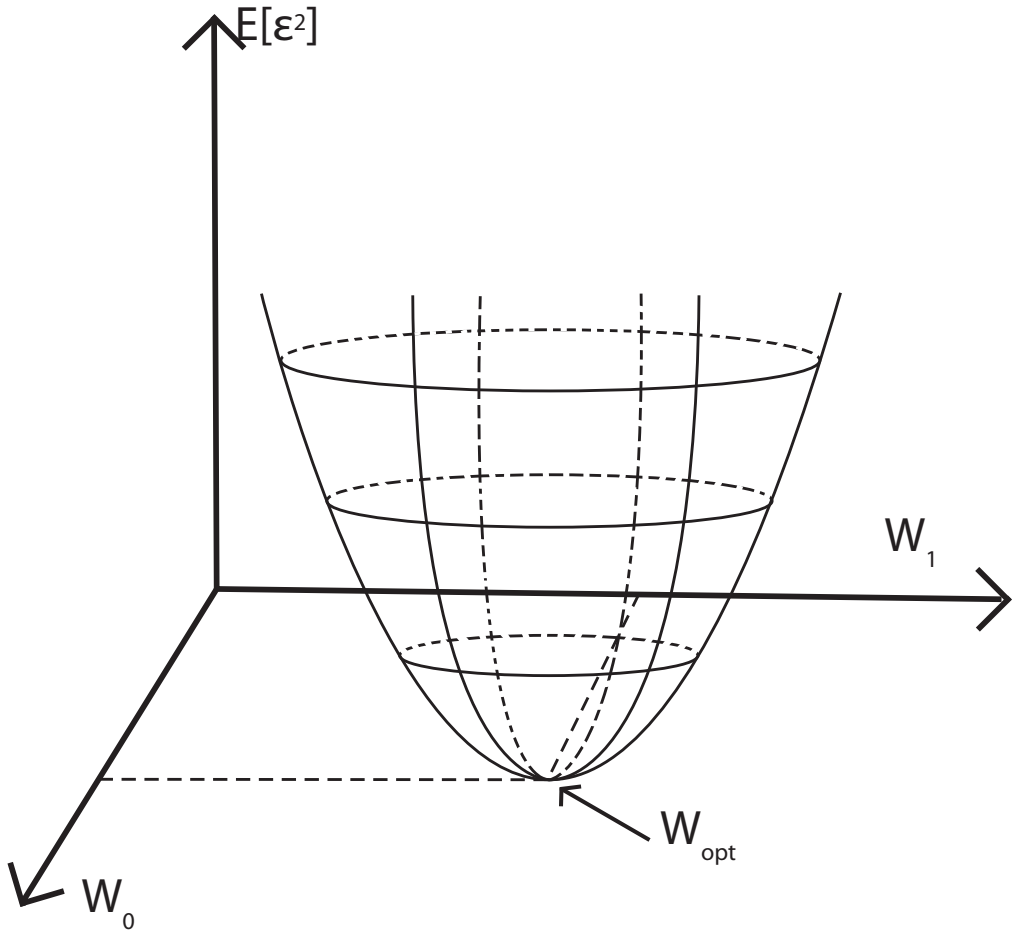

FIGURE 5.16: The Wiener filter finds the optimum weights $\mathbf{w}_{opt}$ using statistical methods so as to reduce the error. However when the signals are non-stationary this bell changes shape and location at each iteration and thus $\mathbf{w}_{opt}$ will no longer be optimum.

and low complexity (O(L)) and are the family of algorithms that were employed for the analysis in this thesis.

Operation of the adaptive filter

From Figure 5.17 it can be seen that the desired signal $\hat{s}(n)$ can be calculated as [94]

$$\begin{aligned} \hat{s}(n) &= x(n) - \hat{v}(n) \\ &= x(n) - \sum_{i=0}^{L-1} w_i(n) u(n-i) \\ &= x(n) - \mathbf{w}^T(n)\mathbf{u}(n), \end{aligned} \tag{5.39}$$

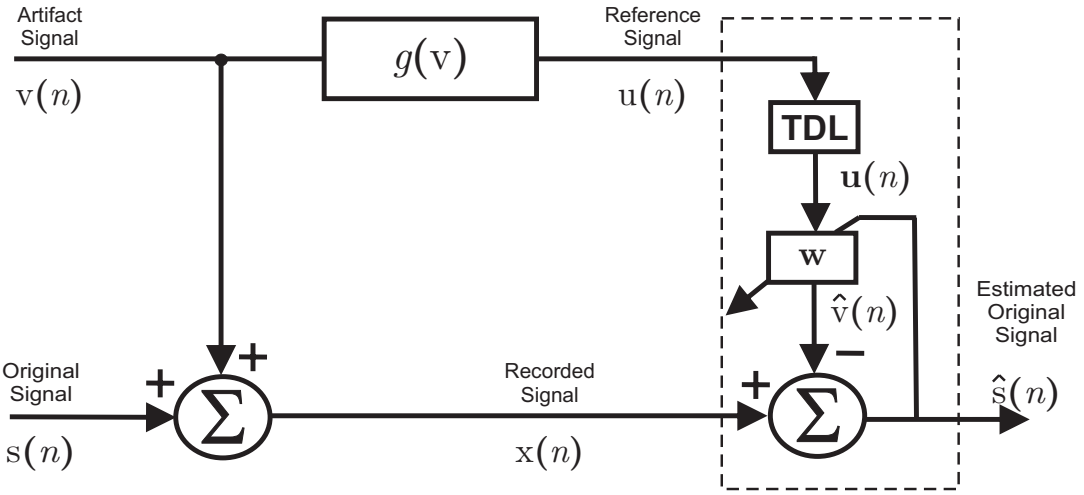

FIGURE 5.17: Adaptive Filter Framework for Artifact Removal

where $x(n)$ is the recorded signal which is contaminated with noise, $u(n)$ is the reference signal and $\hat{v}(n)$ is the output of the adaptive filter. $\mathbf{u}(n)$ is the output of the tap-delay-line and can be defined as $\mathbf{u}(n) = [u(n), ...u(n-L-1)]^T$. The desired signal and the artifact signal are assumed to be uncorrelated and therefore the signal $\hat{v}(n)$ will only be capable of modeling the artifact within the recorded signal $x(n)$. As can be seen in Figure 5.16 the filter aims to find the coefficients which will result in the minimum "error", in this case the minimum $E[\hat{s}^2(n)]$. To reduce the "error" the filter attempts to represent all the artifact in the signal thus leaving the desired approximation of the true signal. To determine the optimum coefficients the adaptive filter uses the gradient descent method.

The purpose of the gradient descent algorithm is to find the direction of maximum gradient of the "error" signal ($\hat{s}^2(n)$) as shown in Figure 5.18. The gradient (∇) points in the steepest uphill direction of the surface at the current location, with its magnitude proportional to the slope at that point. Using this information the LMS algorithm updates the filter coefficients by taking a step in the direction opposite to the gradient, therefore stepping towards the minimum point of the bell.

$$\mathbf{w}(n+1) = \mathbf{w}(n) - \mu\nabla(n). \tag{5.40}$$

μ is the step size and determines how quickly the algorithm will converge to the minimum. If μ is too small the algorithm will require a large number of iterations and thus a long time to converge to the optimum thus giving poor results. However, if μ is too large the algorithm will take steps that are too large and thus the algorithm can become unstable. The choice value for μ will be dealt with later in this section.

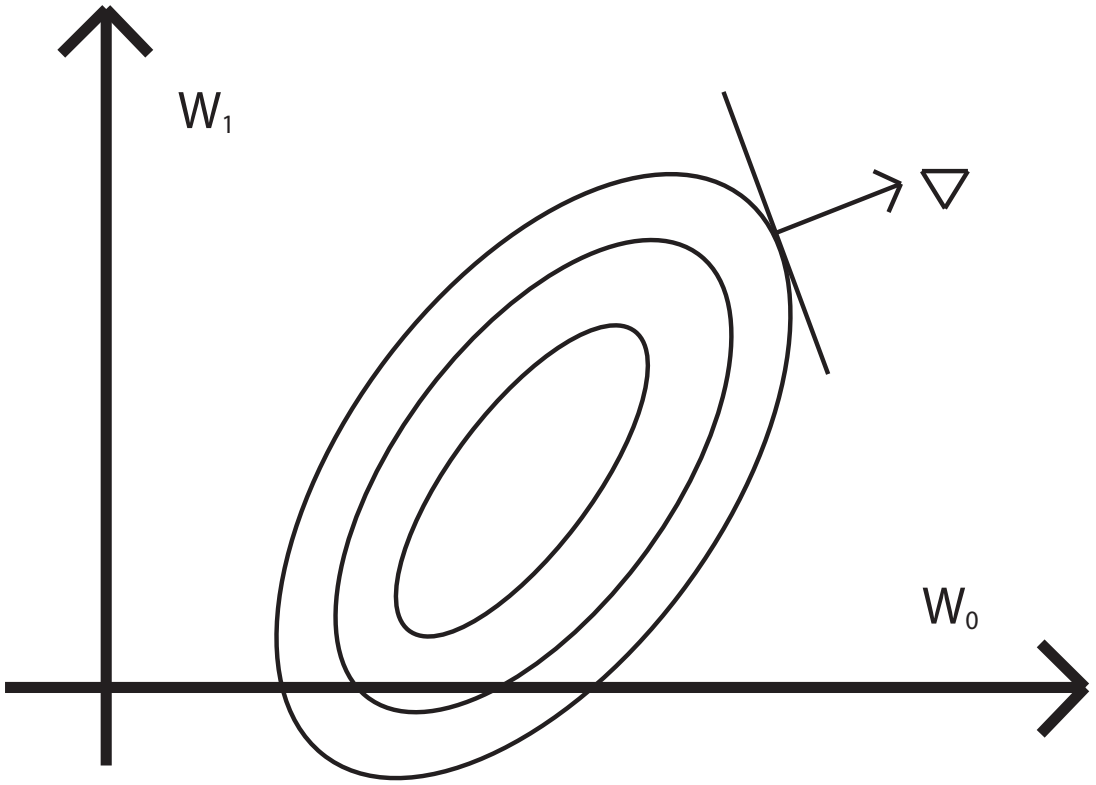

FIGURE 5.18: An example of the gradient of a contour plot. The gradient ∇ shows the steepest uphill direction of the surface at the current position.

In order to be capable of updating the weights, the current gradient ($\nabla(n)$) at each step must first be calculated using:

$$\nabla(n) = \frac{\partial}{\partial \mathbf{w}} \left(E[\hat{s}^2(n)] \right). \tag{5.41}$$

This equation is not tractable, however Widrow and Hoff showed that $\hat{s}^2(n)$ can be used as a noisy approximation to $E[\hat{s}^2(n)]$ and thus Equation 5.41 can be can approximated by:

$$\begin{aligned} \hat{\nabla}(n) &= \frac{\partial}{\partial \mathbf{w}} \left(\hat{s}^2(n) \right) \\ &= 2\hat{s}(n) \frac{\partial}{\partial \mathbf{w}} \left(x(n) - \mathbf{w}^T(n)\mathbf{u}(n) \right) \\ &= -2\hat{s}(n)\mathbf{u}(n). \end{aligned} \tag{5.42}$$

Using this formula the full LMS adaptive filter algorithm can be developed.

$$\begin{aligned}
\hat{v}(n) &= \mathbf{w}^T(n)\mathbf{u}(n) \\
\hat{s}(n) &= x(n) - \hat{v}(n) \\
\mathbf{w}(n+1) &= \mathbf{w}(n) - \mu\hat{\nabla}(n) \\
&= \mathbf{w}(n) - \mu(\ -2\hat{s}(n)\mathbf{u}(n)\ ) \\
&= \mathbf{w}(n) + 2\mu\hat{s}(n)\mathbf{u}(n). \qquad (5.43)
\end{aligned}$$

As stated previously the convergence rate of the filter is dependent on the choice of the step size μ. A number of different authors present different bounds for the values to ensure stability of the system. A common criterion is that the choice of μ be less than λ_{max}^{-1} where λ_{max} is the largest eigenvalue of the autocorrelation matrix $\mathbf{R}$.

$$\mu < \frac{1}{\lambda_{max}}. \qquad (5.44)$$

However λ_{max} may not be known or it could be time varying [94]. A more conservative bound is given as [123]:

$$\mu < \frac{1}{L\sigma_x^2} \qquad (5.45)$$

where σ_x^2 is the mean squared value of the input signal, i.e. the signal power, a quantity that can be readily estimated directly from the input signal and L is the number of filter taps.

This requirement of the LMS algorithm to have a fixed step size for every iteration is a disadvantage [36]. The normalised LMS (NLMS) algorithm was developed as an extension to the LMS algorithm which calculates the maximum step size value. The step size (μ) is now calculated as:

$$\mu = \frac{\hat{\mu}}{\mathbf{u}^T(n)\mathbf{u}(n) + \alpha}. \qquad (5.46)$$

$\hat{\mu}$ is usually set to 0.5 and α is a very small number used to ensure that the denominator doesn't become zero. The step size is proportional to the inverse of the total expected energy of the instantaneous values of the coefficients of the input vector $\mathbf{u}(n)$. The recursive formula for the NLMS algorithm therefore becomes:

$$\mathbf{w}(n+1) = \mathbf{w}(n) + \frac{1}{\mathbf{u}^T(n)\mathbf{u}(n) + \alpha}\hat{s}(n)\mathbf{u}(n). \qquad (5.47)$$

There are also a number of other deviations on this formula, however the displayed recursive formula is the most commonly implemented.

Reference for the adaptive filter

In order to apply the adaptive filter, an appropriate reference signal must be obtained. As stated in Section 3.1 these reference signals can be of a number of different forms. The recording systems employed to record the fNIRS and EEG data, as described in Section 4.1, also incorporated accelerometers and thus these were used to generate the required reference. These accelerometers provide acceleration information on the movement of the recording optodes or electrodes. As this movement can be assumed to be completely independent from the underlying signals of interest the accelerometer outputs became a useful reference source.

The acceleration signal alone was not an accurate enough representation of the contaminating artifact to be an effective reference (in terms of cross-correlation), so a number of processing steps were completed to increase this correlation. A Kalman filter was first employed to model the velocity ($vel(n)$) and positional ($pos(n)$) data from the available noisy acceleration ($acc(n)$) data using the following equations [57]:

$$vel(n+1) = vel(n) + acc(n)\, t \tag{5.48}$$

$$pos(n+1) = pos(n) + vel(n)\, t + \frac{1}{2} acc(n)\, t^2. \tag{5.49}$$

Figure 5.19 shows an example output of the Kalman filter showing the corresponding calculated positional and velocity change for the inputted acceleration. It is also assumed that the position of the optode or electrode always returns to its starting position following the disturbance and thus the positional and velocity graphs have a steady state value of 0.

The acceleration, velocity and positional signals were then used as inputs to a single hidden layer neural network (NN) to generate a model of the artifact signal to use as a reference signal as a simple linear model did not produce the desired correlation with the artifact signal. This NN was trained *a priori* using the available training datasets for both the fNIRS and EEG data. Figure 5.20 presents a comparison between the actual artifact signal (difference between the two recorded channels) and the determined

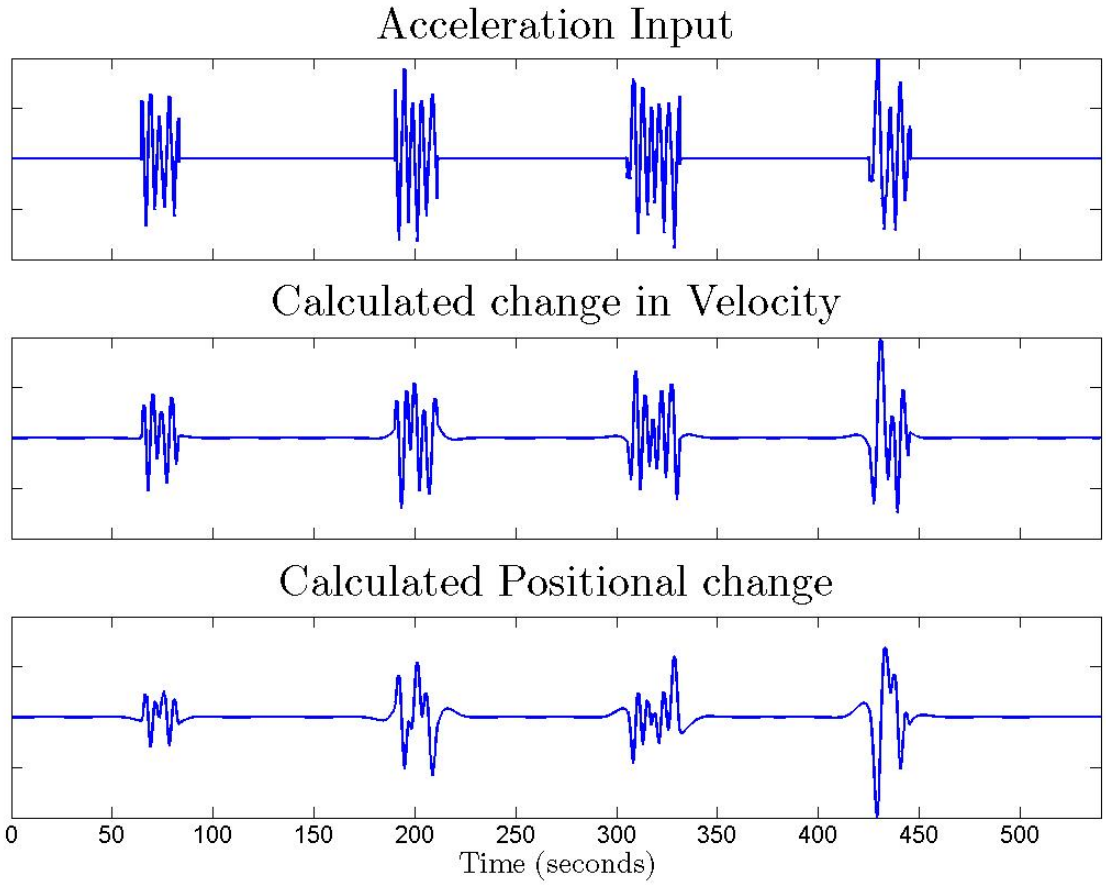

FIGURE 5.19: Calculated change in velocity and position from an example acceleration input signal calculated using a Kalman filter.

reference signal for a given example. The reference signal can be seen to have a high similarity with the artifact signal. For this example the correlation between the artifact signal and the reference was calculated as 0.91 over the full signal.

Employing the adaptive filter

With a valid reference signal, the adaptive filter can then be employed. The adaptive filter coefficients (filter length L, μ and α) were tuned using the available training data so as to produce the best case results. For fNIRS the values were set as $L = 4$, $\mu = 0.5$ and $\alpha = 0.05$. For the EEG data the values were set as $L = 16$, $\mu = 0.5$ and $\alpha = 0.05$. With the coefficients set the adaptive filter could be run on the remaining test data. Once the adaptive filter has been run, the filter output is the original signal with the artifact signal removed. Section 5.7.4 provides an overview of the results obtained when using the adaptive filter on artifact contaminated fNIRS and EEG data with Figure 5.27 and 5.28 showing an example output of the algorithm when employed on the fNIRS and EEG data respectively.

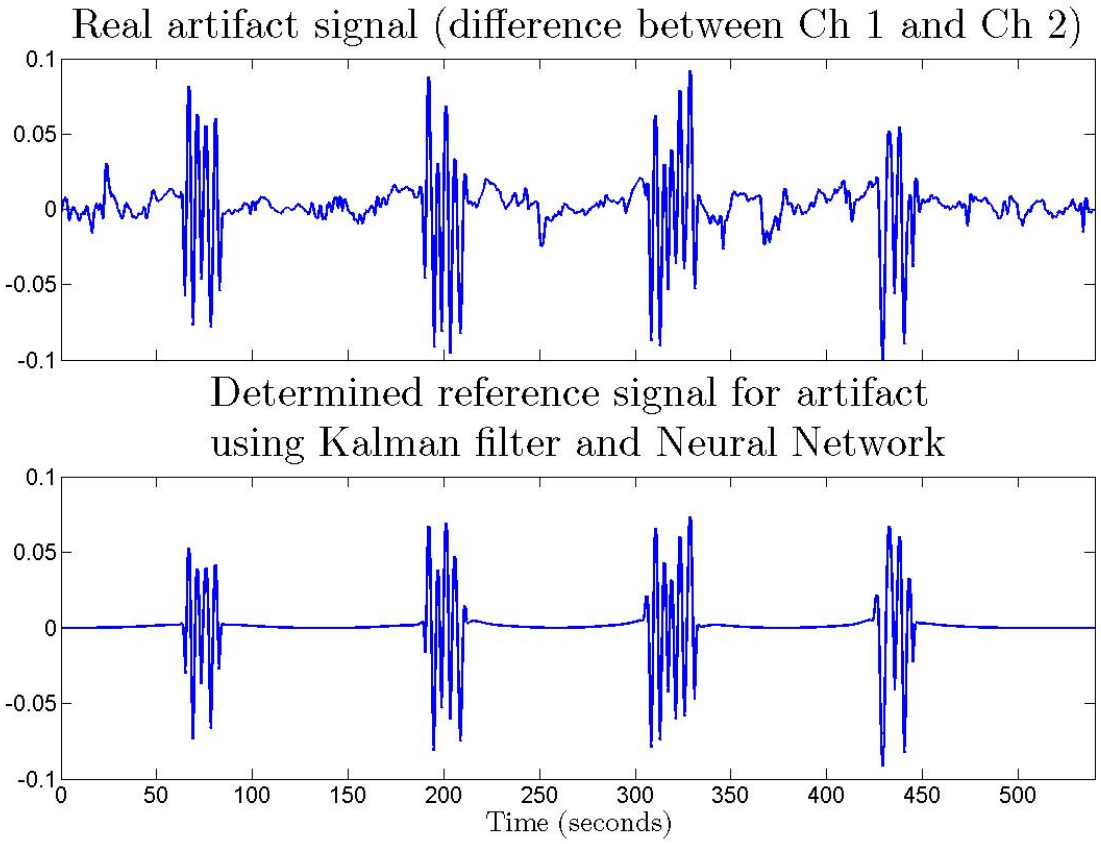

FIGURE 5.20: Calculated reference signal for an example fNIRS trial.

5.7 Results

Using the novel recording methodology, as described in Chapter 4, it is now possible to accurately test the efficacy of artifact removal techniques described in this chapter using the benchmark fNIRS and EEG test datasets. The goal of each artifact removal technique is to return the artifact contaminated signal to its true state. Thus using evaluating metrics, such as Δ SNR (Equation 4.7) and the percentage improvement in correlation (λ) (Equation 4.8), it is possible to quantify the particular technique's ability to remove the undesired artifact.

When analysing the fNIRS dataset, the calculated average correlation over all trials over the epochs of clean data between the "ground truth" signal and the noisy signal was calculated as 0.769 while the average correlation over the whole signal was 0.584. This value of 0.769 can therefore be seen as the realistic best case result for the various artifact removal techniques. In terms of SNR, before employing any of the removal techniques the average SNR over the full signals was -3.65 dB, whereas when calculated solely over the epochs of clean data this value was calculated as 1.53 dB (calculated using the SNR described in Equation 4.7).

For the EEG data the correlation over the clean data was determined to be 0.836, while the correlation over the full signal was 0.397. Finally the SNR prior to employing the various techniques was -6.13 dB when calculated over the average of the full signals. When only the clean epochs were analysed, the SNR rose to 6.06 dB.

The results obtained using the various single stage artifact removal techniques are presented below. For each technique the calculated Δ SNR and λ values are presented as well as plots of sample outputs from the technique when applied to both the fNIRS and EEG data. In addition, any input parameters required are highlighted as well as any deviation from the normal operation of the technique. Two different scenarios are considered:

- Scenario 1: The techniques are applied over the full signals (contaminated epochs and clean epochs).
- Scenario 2: The techniques are only employed on the epochs containing artifact contamination as determined using the data tagging algorithm presented in Section 5.1.

In both scenarios the λ and Δ SNR values are still calculated over the full signal to facilitate direct comparison.

5.7.1 Wiener Filter

As noted in Section 5.3.3, prior to running the Wiener filter the power spectral densities (PSD) of the clean "ground truth" signal and the noise signal were required. This measurement was performed off-line prior to applying the filter as described in Section 5.3.3. Figure 5.21 and Figure 5.22 present an example output of the filter for fNIRS and EEG data respectively. The original noisy signals from these trials can be seen in Figures 4.5 and 4.8.

The efficacy of the artifact removal technique was determined using the Δ SNR and λ metrics described in Section 4.5. For the fNIRS data, the Wiener filter provided an average Δ SNR of 4.67 dB over all trials. The standard deviation of this metric was also calculated to assess the variability of the results. The Δ SNR metric had a standard deviation of 2.55 dB, which in future will be presented in brackets (i.e. Δ SNR was 4.67 dB (2.55)). The percentage improvement in correlation (λ) was calculated as 33.64 % (55.82) therefore providing a new average correlation over all trials of 0.65.

When the data tagging algorithm was employed, the artifact removal techniques were only used during epochs of detected motion. However, to allow for comparison, the λ and Δ SNR values were still calculated over the full signal. The Δ SNR value was calculated as 5.04 dB and the λ value was determined to be 64.03 %.

Similarly, over all trials of the EEG test data, the Δ SNR was calculated as 9.66 dB (3.64) with a λ value of 65.41 % (32.46). This λ value represents an average increase in correlation from 0.29 to 0.68 over all trials. When only employing the algorithms during detected epochs of movement the λ value increased to 86.35 % and the Δ SNR value became 10.31 dB.

5.7.2 Kalman Filter

In order to compare the generic Kalman filter algorithm with the "adaptive" Kalman filter proposed in this thesis, results are presented for both implementations. Prior to applying the Kalman filter the parameters were set as stated in Section 5.4. For the original Kalman filter the measurement noise covariance matrix (R) was set as the variance of the artifact signal (noisy signal minus the "ground truth" signal). For the adaptive Kalman filter R was set as the variance of the artifact signal calculated during epochs of motion when movement was detected by the reference signal and as the variance of the artifact signal calculated during epochs of no movement when the reference signal did not detect any motion.

The results show that the adaptive Kalman filter is far superior to the basic Kalman filter. Using the basic Kalman filter on the fNIRS test dataset the Δ SNR was 4.82 dB (2.3) while λ was -43.74 % (74.18). However for the adaptive Kalman filter with changing R, the Δ SNR was 6.6 dB (2.3) and the percentage improvement in correlation was 74.33 % (68.84). When the Kalman filter was only employed during the determined noisy epochs the Δ SNR was5.37 dB and the λ value was 70.24 %.

Similar results were also observed when operating on the EEG test dataset. The original filter produced a Δ SNR of 7.01 dB (3.63) and a λ of -12.14 % (20.45) whereas the adaptive Kalman filter produced a Δ SNR of 9.98 dB (4.73) and a λ of 82.43 % (38.06). An example of the output produced by the adaptive Kalman filter for fNIRS and EEG data is shown in Figure 5.23 and in Figure 5.24, respectively. When the Kalman filter was employed on the noisy epochs only, the correlation improvement over the full signal became 84.03 % and the Δ SNR value was 9.11 dB.

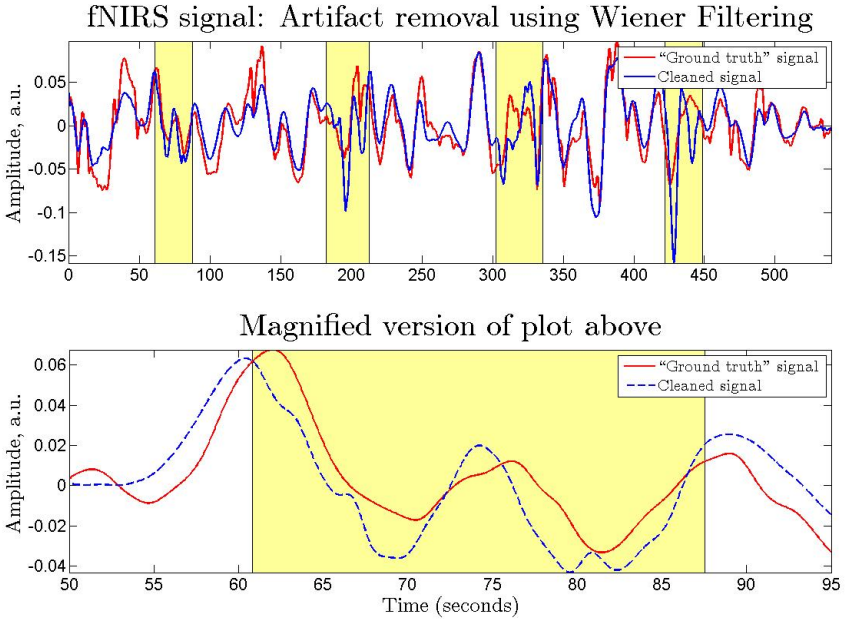

FIGURE 5.21: Example fNIRS trial showing cleaned signal following artifact removal using a Wiener filter.

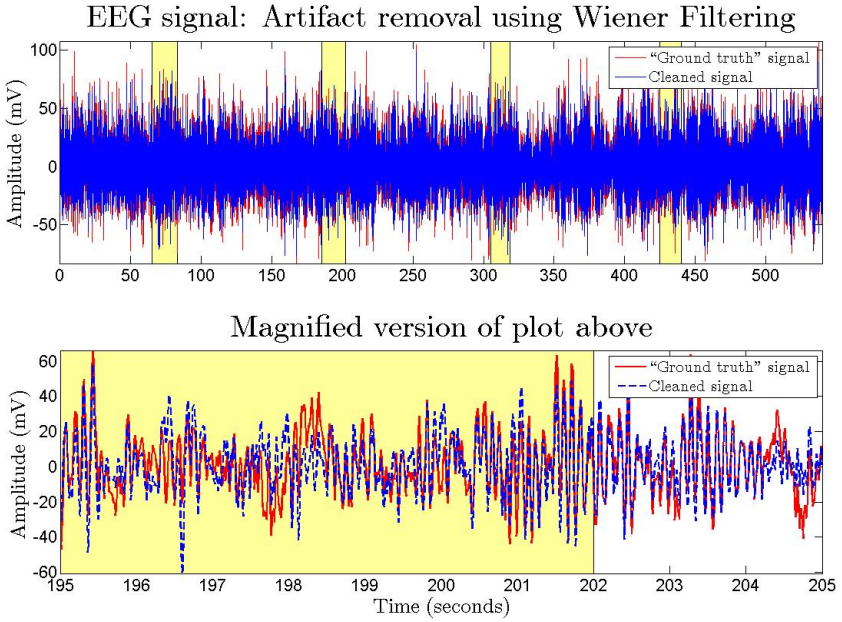

FIGURE 5.22: Example EEG trial showing cleaned signal following artifact removal using a Wiener filter.

5.7.3 Morphological Component Analysis

Once the optimum dictionaries and parameters to employ have been determined (Section 5.5.2 and 5.5.3) the MCA algorithm can be applied to the test datasets. Figure 5.25

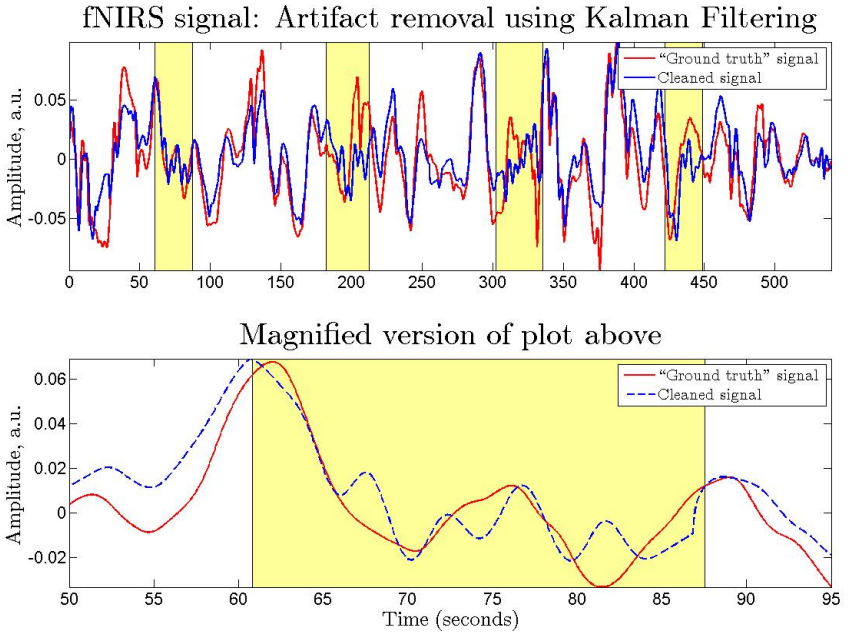

FIGURE 5.23: Example fNIRS trial showing cleaned signal following artifact removal using a Kalman filter.

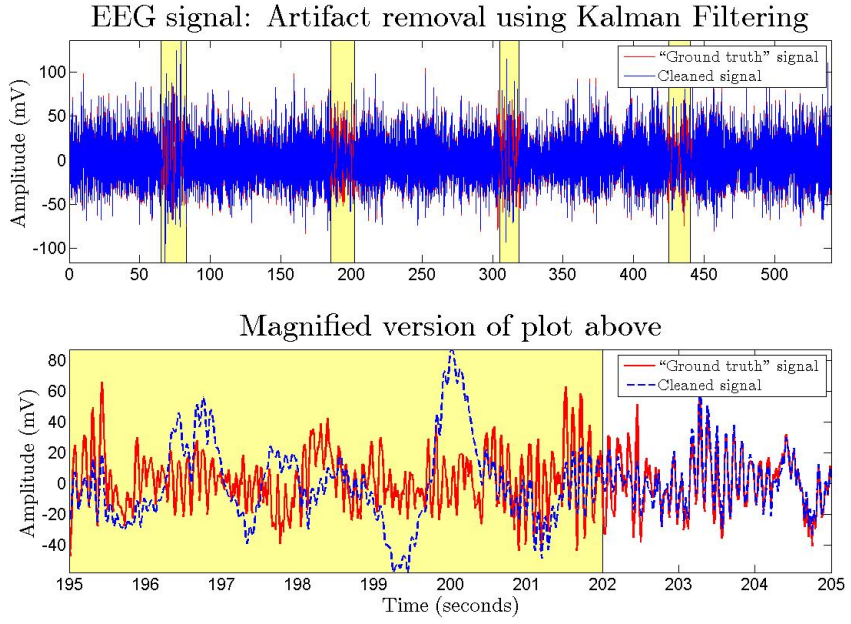

FIGURE 5.24: Example EEG trial showing cleaned signal following artifact removal using a Kalman filter.

shows an example output of the MCA algorithm for a noisy fNIRS input signal. This technique was capable of producing an average Δ SNR of 5.25 dB (1.94) over all trials and a correlation improvement (λ) of 72.9 % (57.53). When the technique was only used during epochs of movement data, the Δ SNR reduced to 4.69 dB and the λ score

reduced to 68.67 %.

Similarly good results were also observed when operating on the EEG data where the technique had a Δ SNR of 9.35 dB (4.5) and a λ of 71.55 % (38.91). Figure 5.26 shows an example output of the MCA algorithm for the EEG data. Again these metrics were also determined when the algorithm was applied over the epochs of movement data only yielding an Δ SNR of 9.29 dB and a λ score of 75.66 %.

5.7.4 Adaptive Filter

As stated in Section 5.6 the adaptive filter parameters were tuned using the training dataset. When operating on the fNIRS data, the adaptive filter was capable of producing Δ SNR of 4.83 dB (2.6) and a percentage improvement in correlation (λ) of 46.86 % (85.16). An example output is shown in Figure 5.27. When employed on the movement epochs only the Δ SNR was 4.75 dB and the λ value was 64.88 %.

When contaminated EEG data is used as the input to the filter the technique had an average Δ SNR of 6.19 dB (2.9) and a λ value of 21 % (25.64). An example output trace can be seen in Figure 5.28. The Δ SNR value increased to 7.29 dB and the λ value became 57.7 % when the adaptive filter was solely employed during epochs of detected motion.

Table 5.1 and Table 5.2 provide an overview of the results obtained with each of the artifact removal techniques on the full signal and the movement epochs only. In the next section a detailed discussion and evaluation of these results will be presented.

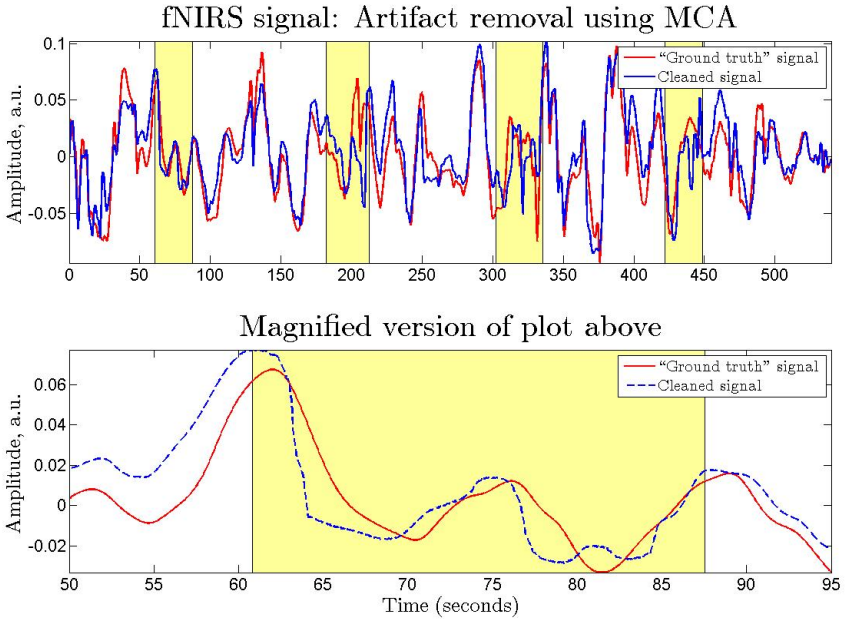

FIGURE 5.25: Example fNIRS trial showing cleaned signal following artifact removal using morphological component analysis (MCA).

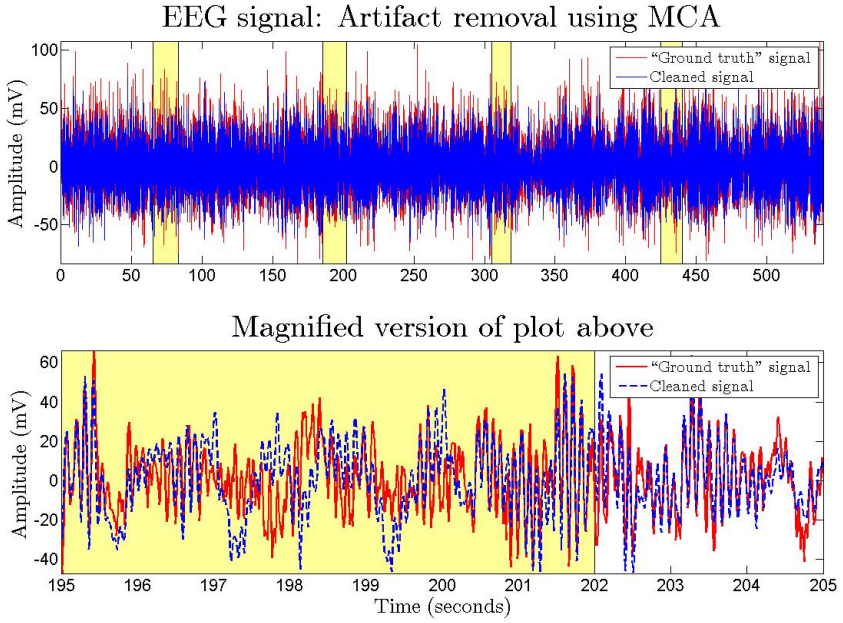

FIGURE 5.26: Example EEG trial showing cleaned signal following artifact removal using morphological component analysis (MCA).

TABLE 5.1: The average % reduction in artifact (λ) and Δ SNR for the benchmark fNIRS and EEG datasets achieved with each of the single stage artifact removal techniques considered in the chapter when applied to the full signal (Scenario 1). The standard deviation of results across trials is indicated in brackets in each case.

		Wiener filter	Kalman filter	Kalman filter (adaptive)	MCA	Adaptive filter
fNIRS	λ	33.64 % (55.82)	-43.74 % (74.18)	**74.33 %** (**68.84**)	72.9 % (57.53)	46.86 % (85.16)
	ΔSNR	4.67 dB (2.55)	4.82 dB (2.3)	**6.6 dB** (**2.46**)	5.25 dB (1.94)	4.83 dB (2.6)
	λ	65.41 %	-12.14 %	**82.43 %**	71.55 %	21.0 %

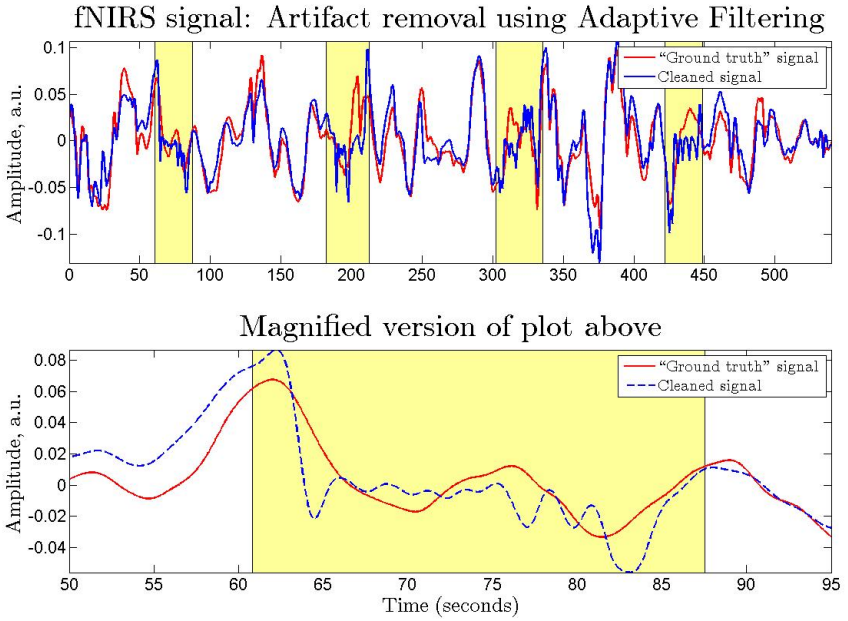

FIGURE 5.27: Example fNIRS trial showing cleaned signal following artifact removal using an NLMS adaptive filter.

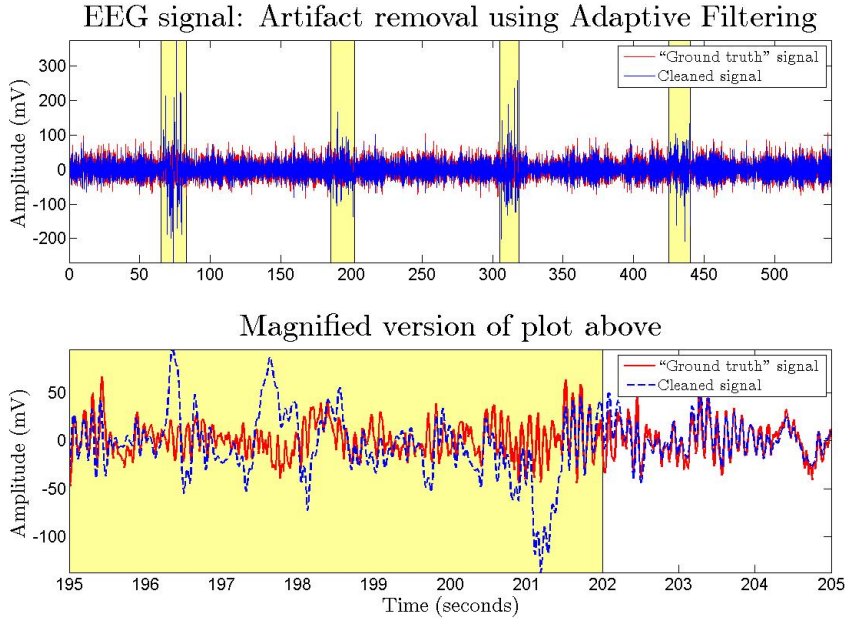

FIGURE 5.28: Example EEG trial showing cleaned signal following artifact removal using an NLMS adaptive filter.

5.8 Discussion and Conclusion

In this section a comparison and evaluation of all of the techniques investigated in this chapter will be performed. The results obtained when analysing the real data are used

TABLE 5.2: The average % reduction in artifact (λ) and Δ SNR for the benchmark fNIRS and EEG datasets achieved with each of the single stage artifact removal techniques considered in the chapter when applied to the motion artifact tagged epochs only (Scenario 2). The standard deviation of results across trials is indicated in brackets in each case.

		Wiener filter	Kalman filter	Kalman filter (adaptive)	MCA	Adaptive filter
fNIRS	λ	64.03 % (54.17)	**70.24 %** (**57.12**)	**70.24 %** (**57.12**)	68.67 % (57.4)	64.88 % (61.62)
	ΔSNR	5.04 dB (2.36)	**5.37 dB** (**2.36**)	**5.37 dB** (**2.36**)	4.69 dB (2.24)	4.75 dB (2.4)
EEG	λ	**86.35 %** (**35.77**)	84.03 % (36.6)	84.03 % (36.6)	75.66 % (37.5)	57.7 % (28.93)
	ΔSNR	**10.31 dB** (**4.4**)	9.11 dB (4.35)	9.11 dB (4.35)	9.29 dB (4.53)	7.29 dB (2.96)

TABLE 5.3: Average computational time for the analysed single stage artifact removal techniques.

	Wiener filter	Kalman filter	MCA	Adaptive filter
fNIRS	0.13 sec (0.24)	4.66 sec (0.31)	18.46 sec (0.30)	0.12 sec (0.002)
EEG	0.31 sec (0.41)	16.12 sec (0.33)	37.24 sec (1.07)	0.39 sec (0.01)

for evaluation, and the chapter concludes by comparing these results to those obtained using the simulated datasets. The availability of the required *a priori* information for each algorithm, the possible requirement for additional sensors for use as a reference, the computational time of the algorithm and the efficacy of the techniques all have a impact on the usefulness of the techniques for employment for artifact removal from physiological signals.

The Wiener filter only requires that the PSD of the clean and noisy signal be available prior to application of the algorithm. This requirement is not overly onerous as test data can easily be recorded prior to using the technique and the PSD of the signals is simple to determine. Compared to a number of the other techniques considered, the Wiener filter performed quite poorly for the fNIRS test dataset. However, when the filter was only applied during the known contaminated epochs, its performance greatly improved with the percentage increase in correlation (λ) almost doubling. This would suggest that, although proficient at removing the artifact from the signal, the Wiener filter also significantly degrades the clean epochs of the signal. This can again be seen with the EEG data, although to a lesser degree. Again there is a significant improvement in the value of λ when the technique is employed over the contaminated epochs only, compared

to application to the full signal. When the algorithm is employed over the movement epochs only, the technique has the highest efficacy of all the analysed techniques for both λ (86.35 %) and for Δ SNR (10.31 dB). The reason for the degradation of the signals over the clean epochs is that the filter is optimised using the PSD of the clean and noisy signals. Therefore when analysing the clean epochs, the PSD of the noisy signal can degrade the quality of the clean, artifact free data. Further complications can arise if the form of the added artifact changes dramatically during analysis from that used to calculate the PSD during training as this PSD would no longer accurately represent the signal. As an added advantage, the Wiener filter is a very fast algorithm with the average computational time for the fNIRS and EEG data calculated as 0.13 seconds (0.24) and 0.31 seconds (0.41) respectively.

As stated in Section 5.4, the Kalman filter analysed in this chapter was run using two different approaches. Firstly the common form of the filter was run, where the noise covariance matrix R remained static throughout the analysis. In order to utilise the algorithm a number of system and process models must first be initialised as discussed in Section 5.4.2. This, similar to the Wiener filter, requires that there be an initial training stage prior to the running of the algorithm. The accuracy of the models used will have an affect on the efficacy of the employed filter. Using the common form of the filter the determined efficacy was extremely poor. The main reason for this was the serious degrading effect of the filter on the clean data as can be seen in Figure 5.9. Due to this poor result, the second form of the Kalman filter was introduced. In this form the noise covariance matrix was altered, depending on the position of the current sample. Therefore when analysing samples within the clean epochs the value of R was different then when analysing data within the contaminated epochs. The results shown in Table 5.1 show the overall improvement after employing the novel technique. For both the fNIRS and EEG data, the Kalman filter with adaptive R performs to the highest standard. Applying the Kalman filter, only during epochs of contaminated data, does not improve results. In fact there is a slight degradation in performance. This maybe because adapting R already takes advantage of the opportunity for improvement. The Kalman filter is a computationally intensive algorithm, and its computational time can be many times greater than some of the other single stage artifact removal techniques investigated. For the fNIRS data the average computational time for the algorithm was 4.66 seconds (0.31) and it was longer again for the EEG data at 16.12 seconds (0.33). The reason for the longer duration with the EEG data is the greater number of data samples in this dataset, due to the higher sampling frequency.

The dictionaries used to represent the underlying signals need to be chosen prior to running MCA. In common with the Wiener and Kalman filters this initialisation step

only has to be completed once so long as the signal and artifact morphologies do not change. If the technique was to be used to remove artifacts of a different nature then a new independent dictionary would be required. MCA performed very well for both the fNIRS and EEG data with λ values of 72.9 % and 71.55 % respectively. Although both efficacy values are below those obtained using the adaptive Kalman filter, MCA does not require the use of the reference signal facilitating a reduction in the complexity of the recording system required. Further using the reference signal as part of the scenario 2 implementation, where MCA is only applied during epochs of clean data does not add substantially to the efficacy of the results. In fact for the fNIRS data both λ and Δ SNR decrease in value. A possible reason for this decrease could be that when performed over the full signal the MCA algorithm removed some of the low amplitude artifacts in the clean signal not due to subject motion. The MCA is a computationally complex algorithm due to the number of iterations required to estimate the morphological component representations of the signals. As specified in Section 5.5.4 the algorithm was run for 100 iterations to allow for a small change in the threshold value on each iteration and thus a more accurate separation of the signals. The algorithm took, on average, 18.46 seconds (0.30) to complete each trial of the fNIRS data and 37.24 seconds (1.07) when employed with the EEG data.

The NLMS adaptive filter parameters were optimised prior to the application of the filter. In comparison to the other single stage artifact removal techniques, the Adaptive filter's efficacy was low for both the fNIRS (46.86 %) and EEG (21.0 %) data. This value increased significantly when only the epochs contaminated with the artifacts were analysed using the technique. During this analysis the adaptive filter had comparable results to both the Wiener and MCA algorithms when utilised on the fNIRS data, whereas for the EEG dataset the algorithm remained sub-par when compared to the other single stage techniques. When comparing the computational time, the adaptive filter is very similar to the Wiener filter in that the average time taken to analyse each trial of fNIRS data is 0.12 seconds (0.002) and for EEG data this becomes 0.39 seconds (0.01).

Overall the MCA algorithm presents itself as a highly efficient algorithm for artifact removal while also having the benefit of not requiring any additional sensors to be used as a reference signal. This algorithm therefore lends itself well to home-health recording systems for which the addition of external sensors is undesired. The computational time of the algorithm and the iterative nature prevents it from being employed in real time. However, the 9 minutes of fNIRS data took, on average, 18.46 seconds to analyse, hence the overall delay in recordings could be quite small if the algorithm was utilised on a shorter data set. The requirement to select and optimise the dictionaries is however

a disadvantage as it restricts the signals which can be used with any particular setup. When the reference signal is available both the Wiener and Kalman filters have a significantly higher efficacy score when applied on the EEG dataset. It can also be seen from Figure 5.22 and 5.24 that the Wiener filter retains the morphology of the EEG signal better than the Kalman filter, which often retains some of the lower frequency oscillations. The Wiener filter is therefore seen as the best single stage artifact removal technique when the reference signal is available as it is very simple to setup, it has a low computation time and provides accurate results.

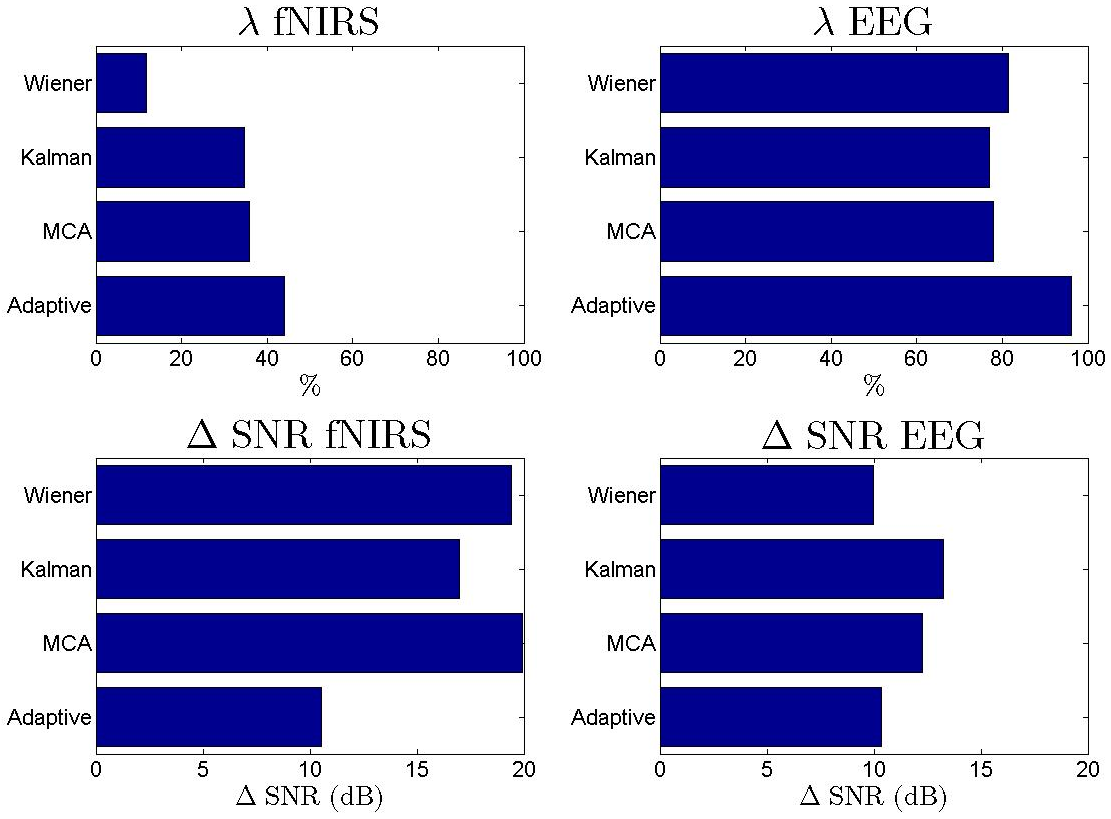

FIGURE 5.29: Determined results using the simulated data. The results shown represent the use of the algorithms over the full signal (both clean and contaminated epochs).

Each of the algorithms above were also tested on the simulated data described in Section 4.8. The bar chart in Figure 5.29 shows the results for λ and Δ SNR for the simulated data when applying the algorithms over the full signal. These results are similar (in terms of the best algorithms) to those obtained using the real data. One striking difference is that the adaptive filter yields the greatest improvement in λ for both the fNIRS and EEG data. The probable reason for the improved performance is the availability of an accurate reference signal for the noise (which was actually the noise signal itself). The Wiener filter provided the poorest results when employed on the simulated contaminated fNIRS data, which is the same pattern observed with the

real data. Similarly, these results greatly improved when the algorithm was applied to the artifact contaminated sections only, becoming competitive with the Kalman filter and the MCA algorithm.

The results presented above highlight the value of two of the contributions of this thesis. Firstly, the use of the novel QOS metric greatly improves the efficacy results obtained by allowing the switching of the algorithms so that they are solely employed when the artifacts are detected. Secondly the results also highlight the importance of the benchmark real dataset obtained by utilising the novel recording methodology. By using exclusively simulated data, the results (such as those for the adaptive filter) can be overly optimistic and can therefore distort the true artifact removal capabilities of particular artifact removal techniques.

Chapter 6

Two Stage Artifact Removal Techniques

In the previous chapter a number of single stage artifact removal techniques, which are capable of performing artifact removal on single channel measurements without the requirement for any additional algorithms, were evaluated. In this chapter two signal processing algorithms which can be employed for two stage artifact removal are detailed, namely wavelet analysis and ensemble empirical mode decomposition. As stated previously, the techniques are labeled two stage as they require the use of additional algorithms to aid in the identification of the artifact components from the decomposed signals. Significantly, these two techniques are also capable of generating a multi-dimensional representation of the single channel signal enabling the use of some of the more intricate multi-dimensional artifact removal algorithms described in Chapter 3. The aim of this joint use of two artifact removal techniques is to further increase the overall artifact removal capability provided by each individual technique.

The combination of the multi-dimensional canonical correlation analysis algorithm with the wavelet transform (W-CCA) and the EEMD algorithm (EEMD-CCA) for artifact removal constitute the novel contributions of this chapter [182]. Importantly the novel EEMD-CCA combination is shown to have an increased artifact removal efficacy compared to the previously available two stage removal techniques when analysing fNIRS data. This result is verified with respect to two previously documented two level techniques, namely Wavelets with independent component analysis (W-ICA) and EEMD with independent component analysis (EEMD-ICA).

The operation of the four aforementioned techniques (Wavelet, EEMD, ICA, CCA) is initially described in detail in the chapter. Following this, a description of both the

novel (EEMD-CCA, W-CCA) and the previously documented combinations (W-ICA, W-CCA) of the techniques are provided. The chapter continues with a comparison of the various techniques discussed in this chapter, using both the benchmark real and simulated fNIRS and EEG datasets where the results are presented in Tables 6.1 and 6.2. It should be again noted that the novel EEMD-CCA algorithm is shown to provide the best efficacy results when analysing the fNIRS data under certain conditions. The chapter concludes with an overall comparison of all techniques (both single and two stage) described in the thesis with a view to providing a suggestion as to the best technique to employ for motion artifact removal from physiological signals.

6.1 Wavelet Transform

Wavelet transform analysis, as it is now known, is a fairly new analysis technique emerging in the early 1980's where it was first developed by Morlet *et al.* [137] to analyse seismic signals. Prior to the development of the wavelet transform, Fourier transforms [196] were the most common method to analyse the frequency content of a signal, and are still widely used today. A Fourier transform takes any function and converts it to an equivalent set of sine and cosine functions and can thus be used to determine the frequency content of the function. However, the basic Fourier transform algorithms (such as the discrete Fourier transform (DFT) and the fast Fourier transform (FFT) [25]) contain time-averaged frequency information (Figure 6.1) and therefore if the signal is non-stationary, the algorithms are incapable of determining the position in the signal where a particular frequency component changes.

This limitation can be overcome, somewhat, by use of the short time Fourier transform (STFT) [2]. The STFT introduces a window function and computes the Fourier transform over specific portions of the input signal. The STFT is therefore capable of determining the sinusoidal frequency and phase content of local sections of a signal as it changes over time. The output of the transform has two parameters, time and frequency (Figure 6.1). However, due to the fixed window size the STFT has a fixed resolution; the width of the windowing function relates to how the signal is represented. If there is a wide window function then the STFT will have a high frequency resolution but poor time resolution whereas if the window is short the function will produce a good time resolution but inadequate frequency resolution.

It was recognized that to represent a signal sufficiently, there was a requirement for a technique capable of both good temporal and frequency resolution (i.e. a short window width for high frequency components and a longer window to represent the slow

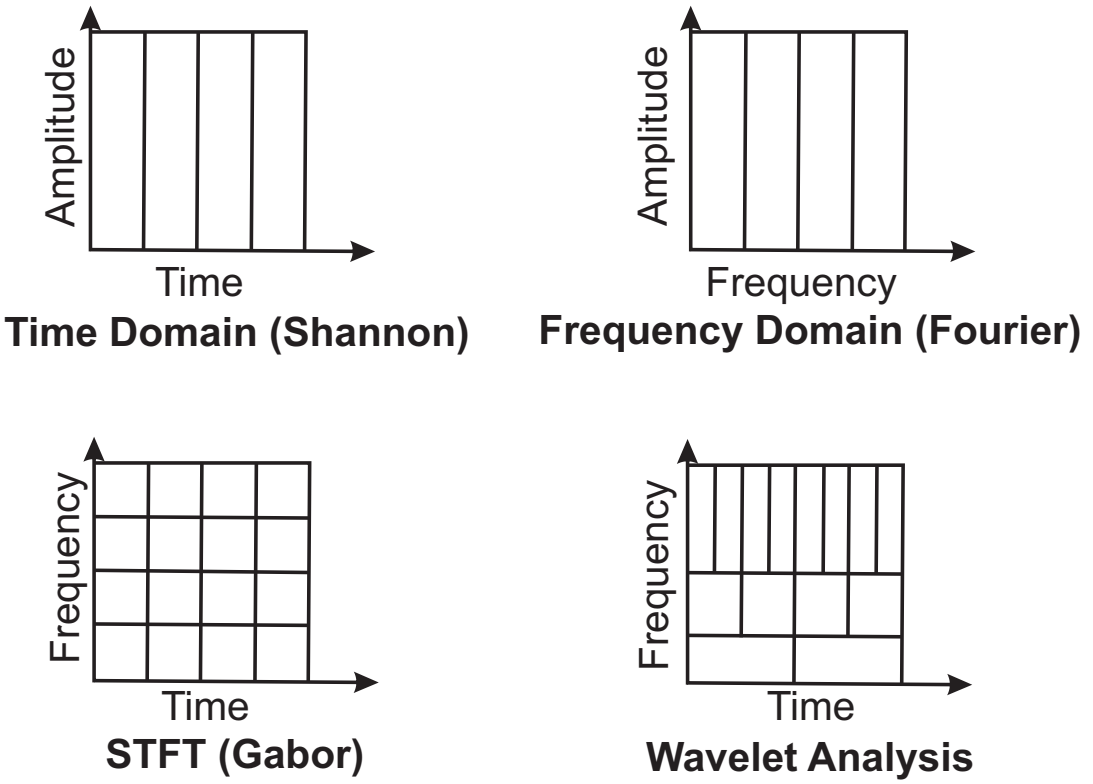

FIGURE 6.1: Figure showing the different information available using some of the different available transforms.

changing low frequency components). This desire lead to the development of the theory of wavelets, where the windowing functions can be scaled and localised to represent the underlying signal components as required. Wavelet theory has been developed over the past three decades by a number of researchers (e.g. [44] [38] [119] [127]) and is now employed in many different areas including science, engineering and mathematics and is particularly useful for the analysis of transients, aperiodicity and other non-stationary signal features.

6.1.1 Continuous Wavelet Transform

Similar to the FFT and other transforms, the wavelet transform is a method of transforming a signal into a different form, allowing for a simpler investigation. The wavelet transform uses localised waveforms ("wavelets") to represent the desired signal in a similar manner to the use of sine waves in the FFT. The continuous wavelet transform (CWT) is defined as:

$$X(a,b) = \frac{1}{\sqrt{a}} \int_{-\infty}^{\infty} x(t)\psi^* \left(\frac{t-b}{a} \right) dt, \begin{cases} a & \in [0, \infty\} \\ b & \in (-\infty, \infty) \end{cases} \tag{6.1}$$

where $X(a,b)$ are known as the wavelet coefficients (or detail coefficients), ψ^* is the complex conjugate of the mother wavelet ψ, a is the scaling (dilation) parameter of the wavelet and b is the location parameter. Note that a is any positive real number and b is any real number. There are a number of different commonly implemented wavelets ψ, (some examples are shown in Figure 6.2) and each must satisfy a number of specified requirements or constraints.

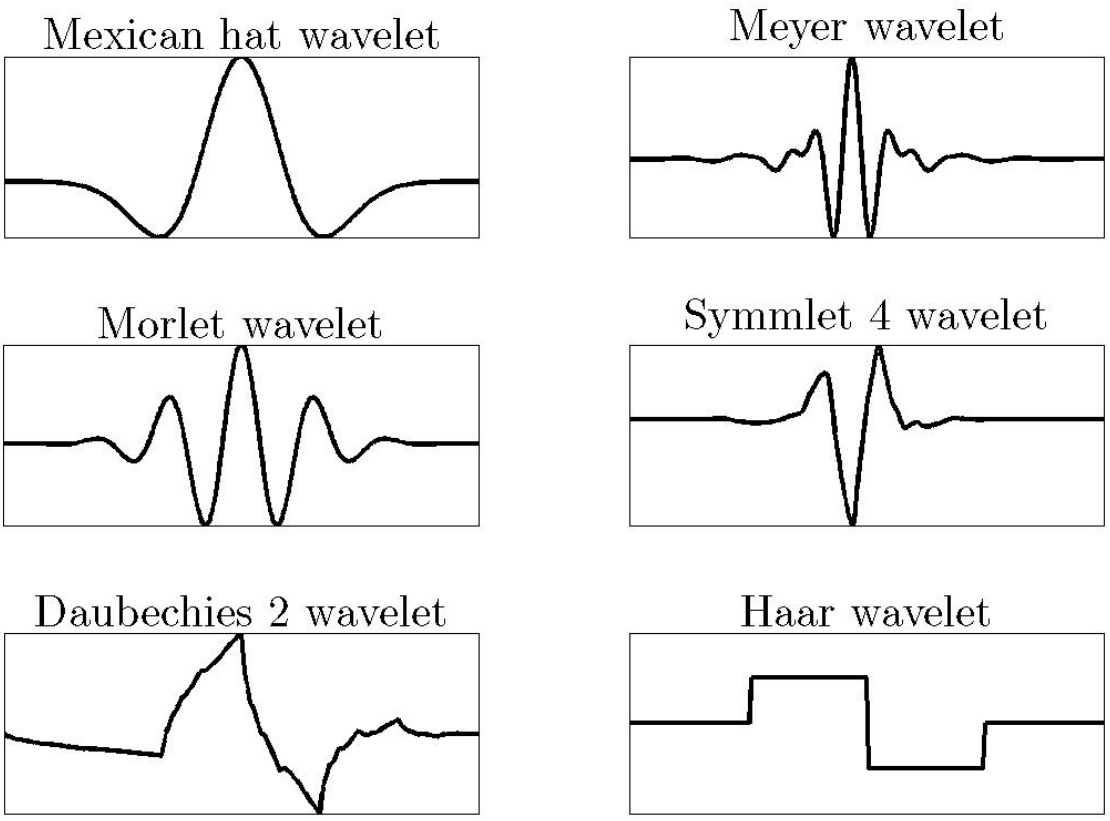

FIGURE 6.2: Examples of some available mother wavelet functions.

1. A wavelet must have *Compact Support* which is to say that the width of the regions where the mother wavelet is not zero is not infinite. Another way of stating this requirement is that the wavelet must have finite energy:

$$E = \int_{-\infty}^{\infty} |\psi(t)|^2 dt < \infty. \tag{6.2}$$

2. The wavelet is required to have at least one *Vanishing Moment*. A wavelet is said to have p vanishing moments if for all positive integers $k < p$, it satisfies [118]

$$\int_{-\infty}^{+\infty} t^k \psi(t) dt = 0. \tag{6.3}$$

   The higher the number of vanishing moments, the more sensitive the wavelet is to the high frequency component of the signal.

3. If $\hat{\psi}(f)$ is the Fourier transform of $\psi(t)$, i.e.

$$\hat{\psi}(f) = \int_{-\infty}^{\infty} \psi(t) e^{-i(2\pi f)t} dt \tag{6.4}$$

   then the following condition must hold:

$$C_\psi = \int_0^{\infty} \frac{|\hat{\psi}(f)|^2}{|f|} df < \infty. \tag{6.5}$$

   If this constraint is met, then the inverse wavelet exists while also ensuring the wavelet will have zero mean.

By taking a closer look at Equation 6.1 it can be seen that it contains both the original signal $x(t)$ and also a dilated and translated wavelet $\psi((t-b)/a)$. Figure 6.3 shows how a change in dilation or translation can affect an example wavelet. An increase in the parameter a corresponds to an increase in the width of the wavelet function. This increase allows the wavelet to more accurately represent the lower frequency components of the signal $x(t)$. The parameter b is then used to determine the position of the wavelet in the signal. The CWT is not commonly used however, as for most functions the transform has no analytical solutions; in order to cover the entire spectrum, an infinite number of decomposition levels would be required. As it is also not possible for a digital computer to computationally compute an integral over the infinite interval (i.e. over b), an extension of the CWT, called the discrete wavelet transform (DWT), was developed.

6.1.2 Discrete Wavelet Transform

When employing the discrete wavelet transform (DWT) the choice of the parameters a and b are no longer arbitrary and are instead constrained to be discrete values, (usually $a = 2^j$ and $b = k2^j$). The wavelet function ψ_{jk} can thus be defined as:

$$\psi_{jk}(t) = \frac{1}{\sqrt{2^j}} \psi\left(\frac{t - k2^j}{2^j}\right), \tag{6.6}$$

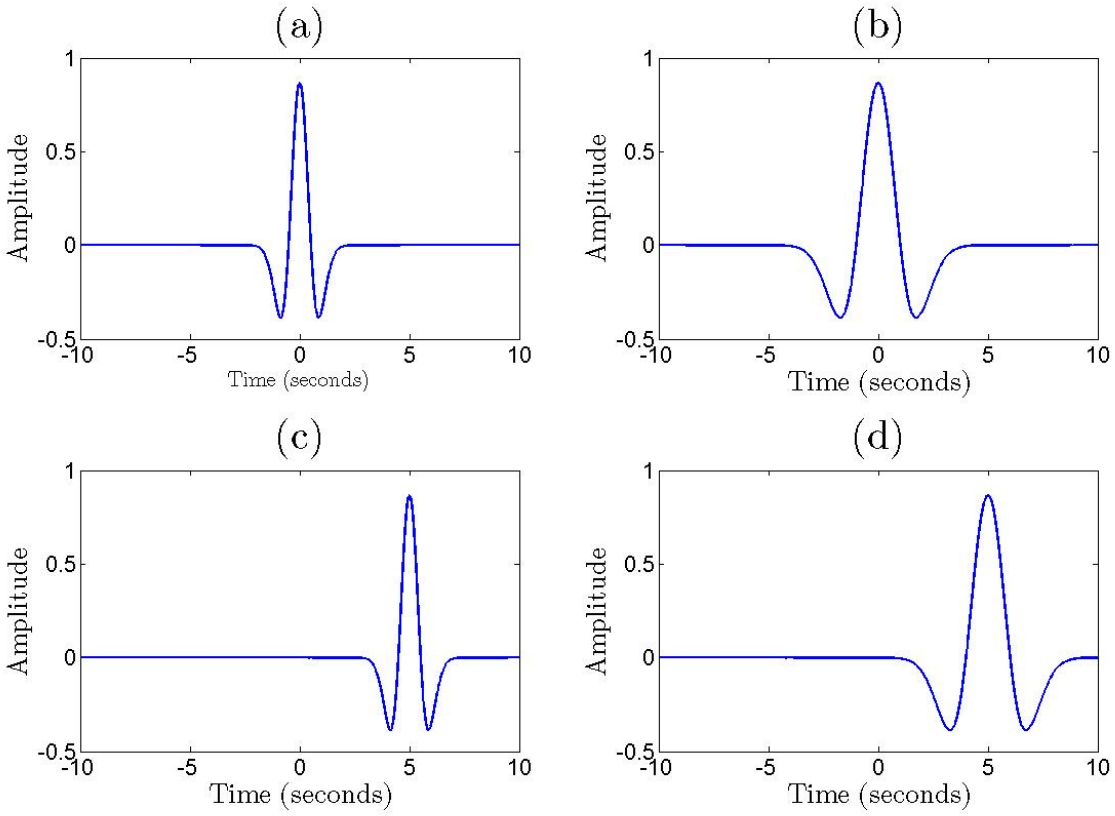

FIGURE 6.3: An example Mexican hat wavelet with changing location (i.e. translation) and scale (i.e. dilation). (a) Original Mother wavelet, (b) dilated version, (c) translated version and (d) translated and dilated version.

where j now controls the wavelet dilation and both j and k control the translation of that particular wavelet function. Therefore, the size of the translation steps is directly proportional to the size of the wavelet dilation, i.e. if the wavelet function width increases by two, so does the step size. It can also be observed that the window width of the wavelet increases by a factor of two with incrementing j and thus the wavelets are also known as dyadic wavelets. The wavelet function can also be regarded as a high-pass filter where each increase in the level, j, has the effect of halving the cutoff frequency. Therefore, to ensure that the full spectrum of the signal is analysed, an (undesirable) infinite number of levels would be required. To overcome this inconvenience, a second function (known as the scaling function) is introduced.

Each individual dyadic discrete wavelet is associated with a *scaling function* φ and its particular dilation equations. This function is similar in form to the wavelet function and can be associated with a smoothing of the signal (i.e. a low-pass filter):

$$\varphi_{jk}(t) = \frac{1}{\sqrt{2^j}}\varphi\left(\frac{t - k2^j}{2^j}\right). \tag{6.7}$$

These scaling functions, for each wavelet family, are selected so their spectrum encompasses the frequencies below the current cut-off frequency of the wavelet function (i.e. the functions are orthogonal). At each step of the decomposition the wavelet function selects the detail components from the signal within the current spectrum and the scaling function selects all frequencies below. These wavelet and scaling functions can then be used to decompose the signal at the first level, i.e. $j = 1$ as shown in Figure 6.4. As the bandwidth of the signal is reducing by half (each function selects half the original bandwidth of the signal), both signals can be down-sampled by a factor of 2 while still conforming with the Nyquist frequency. In doing so, the combination of the output components (approximation ($\mathbf{x}_{1,L}[n]$) and detail ($\mathbf{x}_{1,H}[n]$) components) will always be the same length as the original signal.

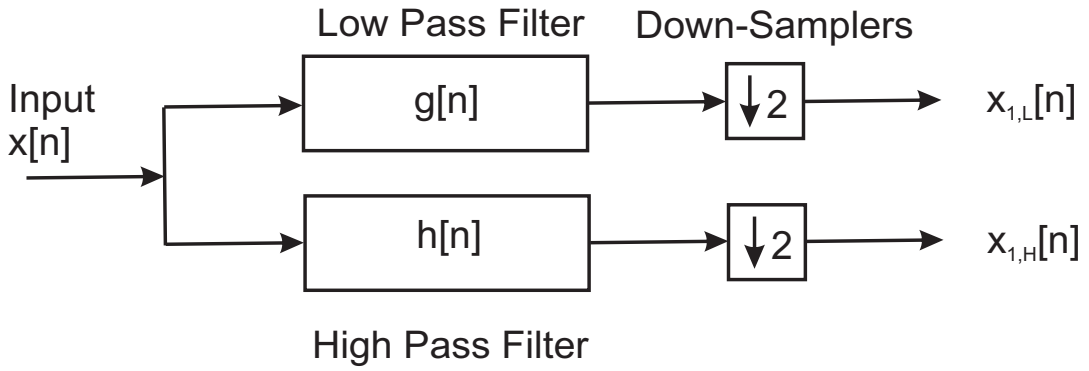

FIGURE 6.4: Single step of the discrete wavelet transform.

To compute the next level of the decomposition, the approximation component is taken as the input and the calculations are repeated for the next scale (i.e. $j = 2$). This decomposition continues up to the chosen M^{th} level as is shown in Figure 6.5. As the number of levels of decomposition increases, so does the level of detail that is extracted from the signal. An example decomposition of a signal using the wavelet transform up to Level 6 is presented in Figure 6.6.

To regenerate the approximation and detail signals and therefore the original signal, each approximation and detail component pair must be passed through the inverse DWT as shown by the diagram presented in Figure 6.7. The output of the synthesis filters ($\bar{g}$ and $\bar{h}$) are the approximation and detail signals respectively. The approximation and detail signals corresponding to the components from Figure 6.6 are shown in Figure 6.8.

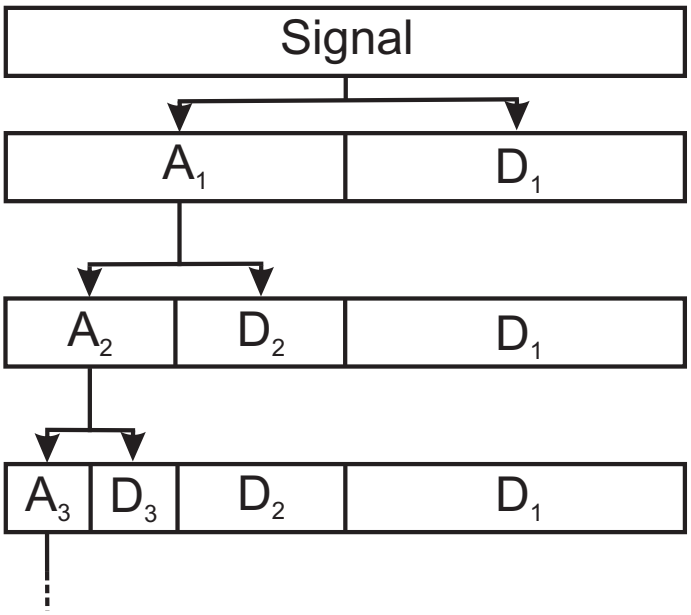

FIGURE 6.5: Diagram of the decomposition of a signal using the wavelet transform.

The complete discrete wavelet expansion of a signal ($x(t)$) can thus be written as [9]:

$$x(t) = \sum_{k} c_{Mk}\varphi_{Mk}(t) + \sum_{j=1}^{M}\sum_{k} d_{jk}\psi_{jk}(t), \tag{6.8}$$

where

$$c_{jk} = \int x(t)\varphi^{*}_{jk}(t)dt \tag{6.9}$$

are called the scaling coefficients and the scaling functions φ are as defined in Equation 6.7. The wavelet coefficients (d) for the wavelet function ψ (Equation 6.6) are given by:

$$d_{jk} = \int x(t)\psi^{*}_{jk}(t)dt. \tag{6.10}$$

These scaling and wavelet coefficients are then used to determine the details and approximations of the discrete wavelet transform at each level (j):

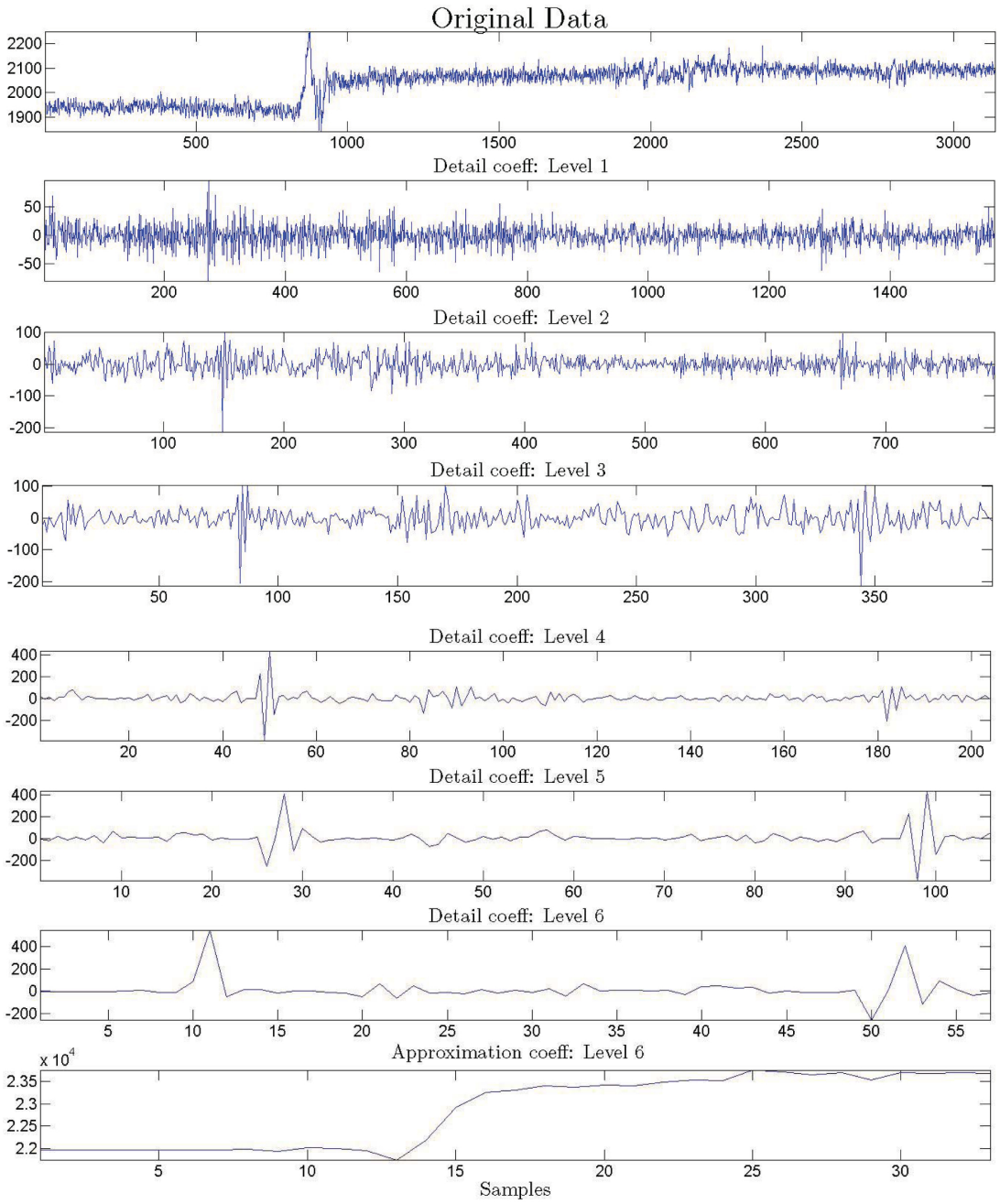

FIGURE 6.6: An example decomposition of an EEG signal using the wavelet transform (Mother wavelet - Daubechies 5). The Details (or wavelet coefficients) correspond to d_{jk} for $j = 1 : M$ and the approximation (or scaling coefficients) correspond to c_{Mk} for $M = 6$ from Equation 6.8.

$$A_j(t) = \sum_{k=-\infty}^{+\infty} c_{jk}\varphi_{jk}(t)$$
$$D_j(t) = \sum_{k=-\infty}^{+\infty} d_{jk}\psi_{jk}(t). \tag{6.11}$$

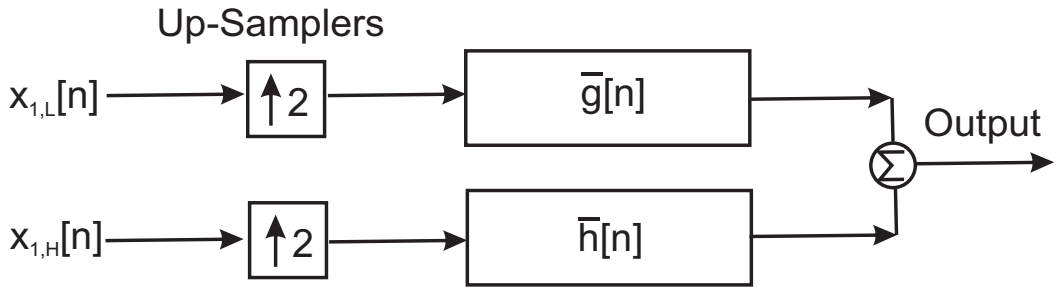

FIGURE 6.7: Single step of the Inverse DWT

The original signal $x(t)$ can be easily reconstructed by adding up all the details calculated and also the approximation for the final level (M), i.e.

$$\mathbf{x} = A_M + \sum_{n=1}^{M} D_n. \tag{6.12}$$

6.1.3 Employing the wavelet transform

To perform artifact removal using the wavelet transform the contaminated signal is selected as the input to the algorithm and the output details D_j and approximation A_M are set as the source components. The Daubechies 5 mother wavelet was chosen as the mother wavelet. As wavelet transform based artifact removal is a two stage approach, the components relating to artifacts are not yet known and therefore an additional technique must be employed for them to be determined. There are a number of approaches currently employed to determine the artifact components for various signals. Section 4.7 described the artifact selection techniques considered in this thesis. As previously mentioned, the wavelet transform can also be used to permit the usage of multi-dimensional artifact removal techniques. The transforms novel employment with the CCA algorithm is described in Section 6.5. Section 6.7 describes the efficacy of the wavelet transform based artifact removal technique when employed on both the fNIRS and EEG datasets and finally Section 6.8 provides a comparison, first with the other two stage techniques analysed in this chapter and then with all of the techniques described in the thesis.

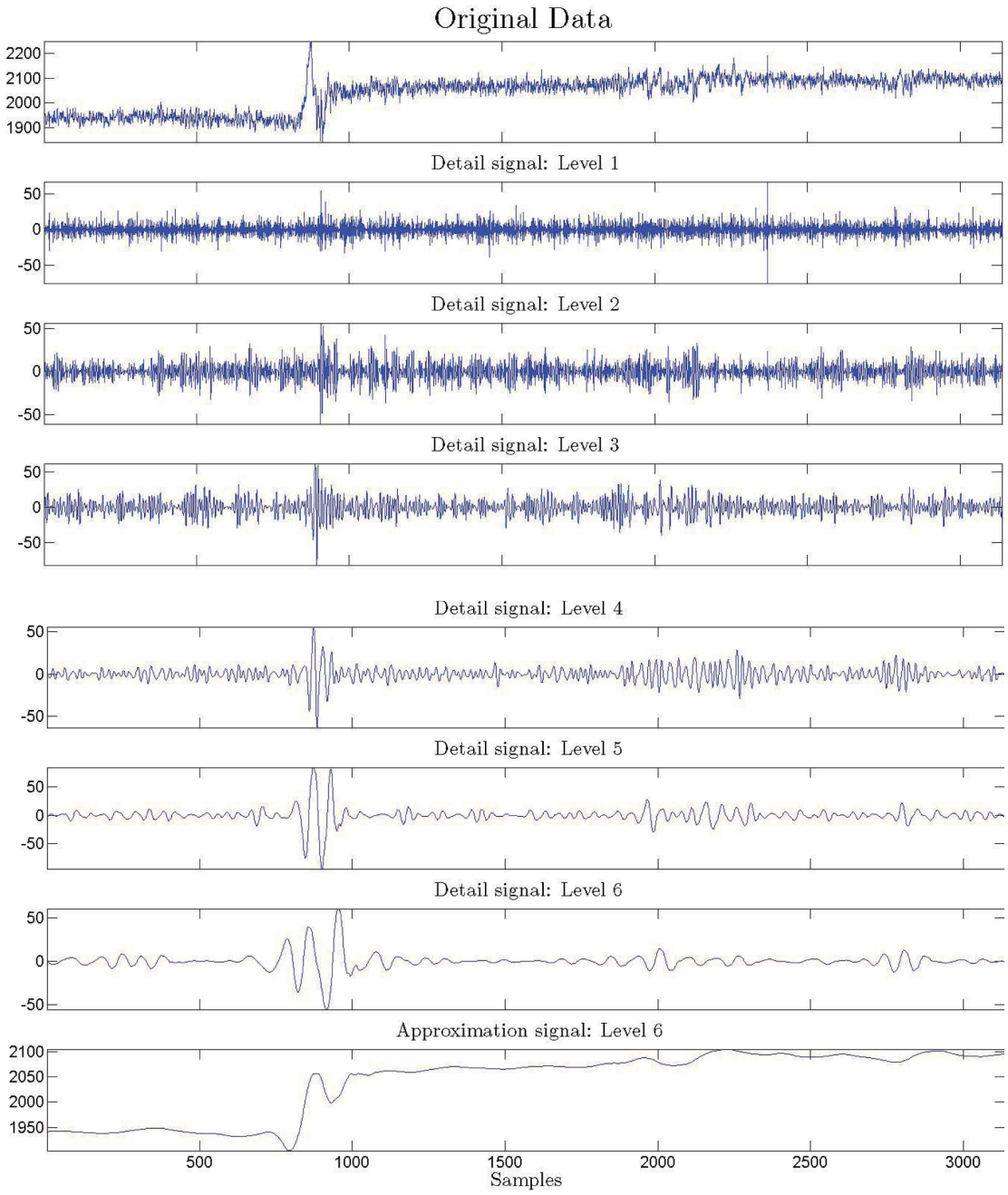

FIGURE 6.8: Approximation and detail signals corresponding to the components shown in Figure 6.6. The detail signals correspond to $D_j(t)$ for $j = 1 : M$ and the approximation signal corresponds to $A_M(t)$ for $M = 6$ from Equation 6.11.

6.2 Empirical Mode Decomposition

Empirical mode decomposition (EMD) was first introduced by Huang *et al.* [79] as a method to decompose a signal into components, called intrinsic mode functions (IMFs), that admit well behaved Hilbert transforms. The Hilbert transform is similar to the well known Fourier transform. The Fourier transform, however, has some restrictions

in contrast to the Hilbert transform in that the transform requires the input data to be both linear and stationary and is capable of representing the data in only the energy-frequency domain. However, as the Hilbert transform does not require the data to be stationary (or linear) it is capable of representing the data in the energy-frequency-time domain, similar to wavelet analysis. An advantage of the EMD algorithm, compared to wavelets, is its adaptive nature, as its IMFs derive their basis from the data, unlike wavelet analysis whose basis is chosen *a priori*.

The EMD algorithm is therefore a very useful algorithm which is capable of decomposing an input signal into its corresponding IMF adaptively, where the signal can be both non-linear and non-stationary.

6.2.1 Operation of the technique

As stated previously, the EMD algorithm operates by decomposing an input signal into a small number of intrinsic mode functions (IMFs) which admit well behaved Hilbert transforms. An IMF is defined as a function that satisfies the following two conditions [79]:

1. The number of extrema (i.e. maxima or minima) and the number of zero crossings of the IMF over the full data set must be equal or differ by at most one.
2. Over all points, the mean of the envelope that is defined by the local maxima and the envelope that is defined by the local minima is zero.

The first condition ensures that the determined IMF will be a stationary Gaussian signal while the second condition will ensure that the IMF signal will not be asymmetric, and thus the resulting instantaneous frequencies will not have any undesired fluctuations. An example of an IMF is shown in Figure 6.9.

As the majority of real world signals do not meet the criteria required for an IMF, the EMD algorithm is used to decompose the original data into a small number of sub-signals that do. As stated previously, this decomposition is adaptive with the basis used for the decomposition derived directly from the data. The basic foundation of the approach is to identify the individual intrinsic oscillatory modes by their characteristic time scales in the data empirically, and then to decompose the data accordingly [79]. This foundation is based on a number of assumptions regarding the data:

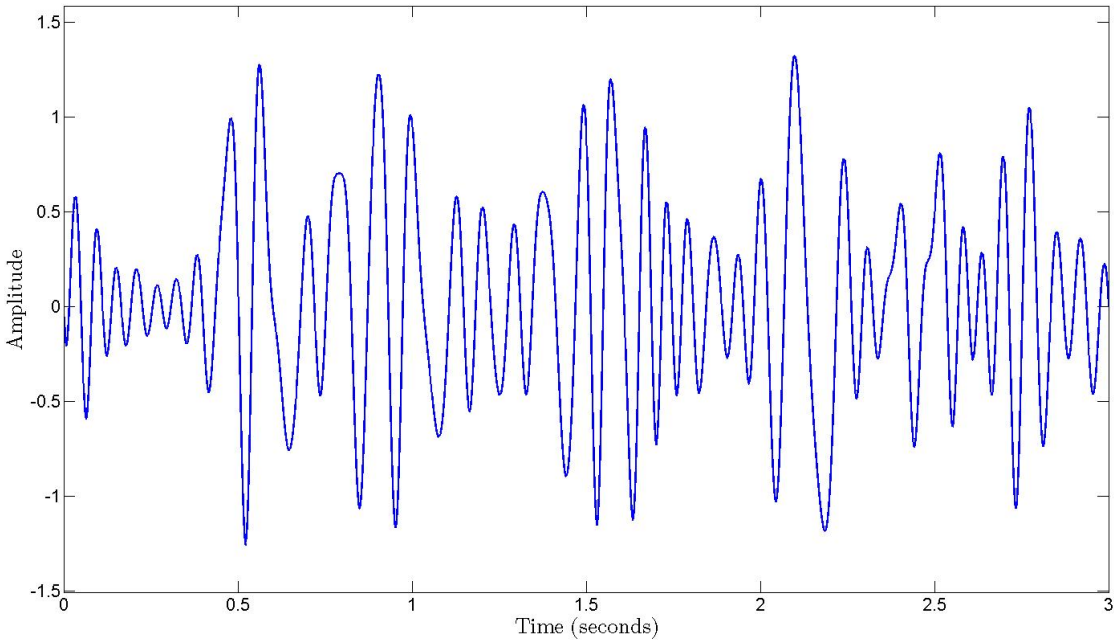

FIGURE 6.9: The first intrinsic mode function determined using the EMD algorithm from the data shown in Figure 6.10 (a). It can be seen that the number of extrema and the number of zero crossings are identical and the signal has zero mean.

1. There are at least two extrema in the signal; one maximum and one minimum.

2. The characteristic time scale of the mode is described by the time between the local extrema.

3. If there are no extrema present in the data but there are inflection points, the data can be differentiated to locate the extrema. The final results can then be obtained by integration of the components [79].

Once the data is determined to conform to the assumptions described above, the EMD algorithm can then be employed to determine the individual IMF of the data. The EMD algorithm is a simple algorithm that uses envelopes of the extrema of the data to determine the IMF. The algorithm can be broken down into a number of simple operations. The first step in the algorithm is to determine the positions of all the extrema of the input signal $\mathbf{x}$ (example shown in Figure 6.10 (a)). Once all the extrema have been found, an upper and lower envelope are created. The upper envelope is created by connecting a cubic spline to all the maxima of the data and the lower envelope is the connection of all the minima, again by a cubic spline. These envelopes can be seen in Figure 6.10 (b). The mean ($\mathbf{m}_1$) of the two envelopes is then calculated (Figure 6.10 (c)) and the first component $\mathbf{h}_1$ is calculated as:

$$\mathbf{h}_1 = \mathbf{x} - \mathbf{m}_1, \tag{6.13}$$

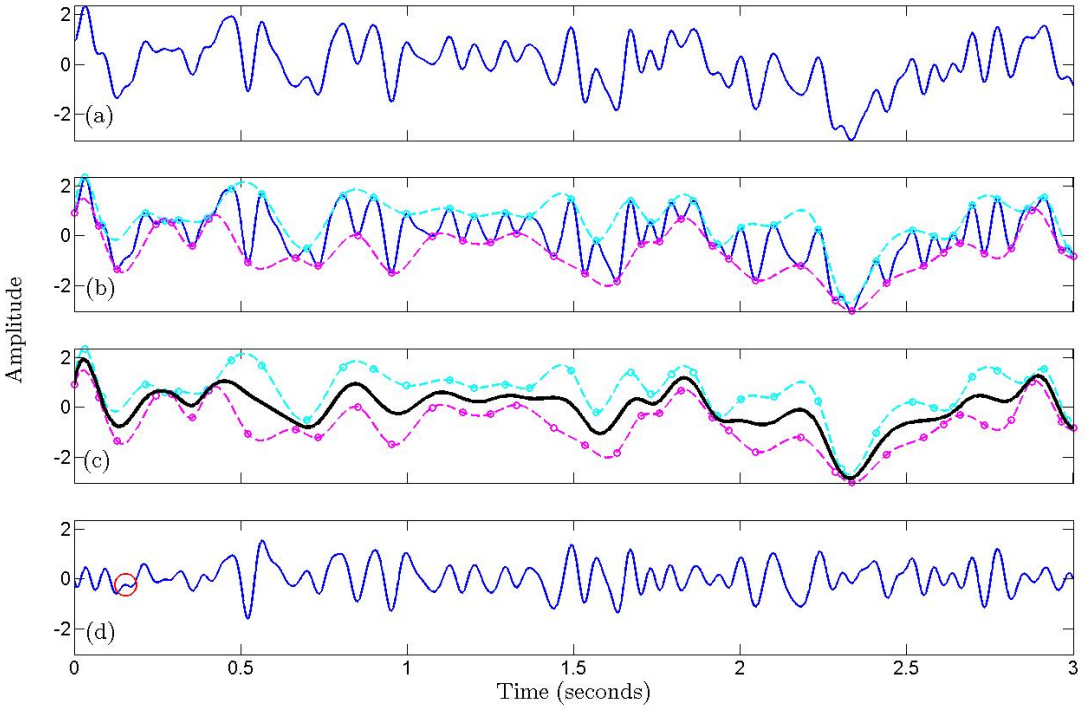

FIGURE 6.10: Example of the EMD sifting process: (a) the original example input data ($\mathbf{x}(t)$); (b) the upper and lower envelopes (dashed lines) determined from the maxima and minima of the data; (c) the mean of the two envelopes (thick solid line); (d) the first component $\mathbf{h}_1$ calculated as the residual of the original data minus the mean of the envelopes. The current component cannot be considered an IMF due to the undershoot of the signal, highlighted using the red circle.

and can be observed in Figure 6.10 (d).

Although the steps described above were developed to create IMF it is not usually the case that the resulting components ($\mathbf{h}_1$ in this case) can always be considered an IMF. This is due to the components themselves often having some overshoots or undershoots which will result in the number of extrema and zero crossings not differing by at most one as specified in the IMF requirements. An example of an undershoot can be observed in Figure 6.10 (d), highlighted using the red circle. In order to determine the first true IMF component, the sifting process must be repeated until the output component conforms with the conditions of the IMF. For the second iteration, the output component of the first step, $\mathbf{h}_1$, is treated as the data, and thus the upper and lower envelopes of this signal are determined. After repeating the steps outlined above it follows that:

$$\mathbf{h}_{11} = \mathbf{h}_1 - \mathbf{m}_{11}. \tag{6.14}$$

Again this component is analysed to determine if it is a true IMF (more detail of how this is determined below). If this component is also determined not to be an IMF the steps above are repeated until

$$\mathbf{h}_{1n} = \mathbf{h}_{1(n-1)} - \mathbf{m}_{1n} \tag{6.15}$$

is an IMF. An example of the first IMF from the data shown in Figure 6.10 (a) is shown in Figure 6.9. It can clearly be seen from this figure that the number of zero crossings and the number of extrema (maxima or minima) are equal and also that the signal has zero mean. Once the first IMF has been determined it is retained, i.e.

$$\mathbf{c}_1 = \mathbf{h}_{1n} \tag{6.16}$$

and then the EMD process is repeated with the new data ($\mathbf{r}_1$) set as the original data minus the calculated first IMF:

$$\mathbf{r}_1 = \mathbf{x} - \mathbf{c}_1. \tag{6.17}$$

In order to ensure that the resulting IMF continue to retain some sense in terms of physical meaning for both amplitude and frequency, it is necessary to have a stopping criterion to limit the number of iterations of the sifting process. If the sifting process is continued, then the resulting IMF signal will be a pure frequency modulated signal of constant amplitude [79]. The original stopping criterion proposed by Huang *et al.* was associated with limiting the size of the standard deviation of two consecutive sifting components. The standard deviation between two consecutive components can be calculated as:

$$SD = \sum_{t=0}^{K} \left[\frac{|h_{1(n-1)}(t) - h_{1n}(t)|^2}{h^2_{1(n-1)}(t)} \right] \tag{6.18}$$

with a typical value for the threshold set to 0.2 or 0.3. However this stopping criterion can be problematic as the appearance of new extrema post sifting can cause large deviations in SD. A simple and adequate stopping criterion is just when the number of extrema matches the number of zero crossings. The sifting process continues until the residual signal $\mathbf{r}_n$ becomes monotonic (i.e. a function that is constantly increasing or decreasing, see Figure 6.12). When this occurs, the original signal $\mathbf{x}$ is said to be decomposed into its n IMFs and can be described as:

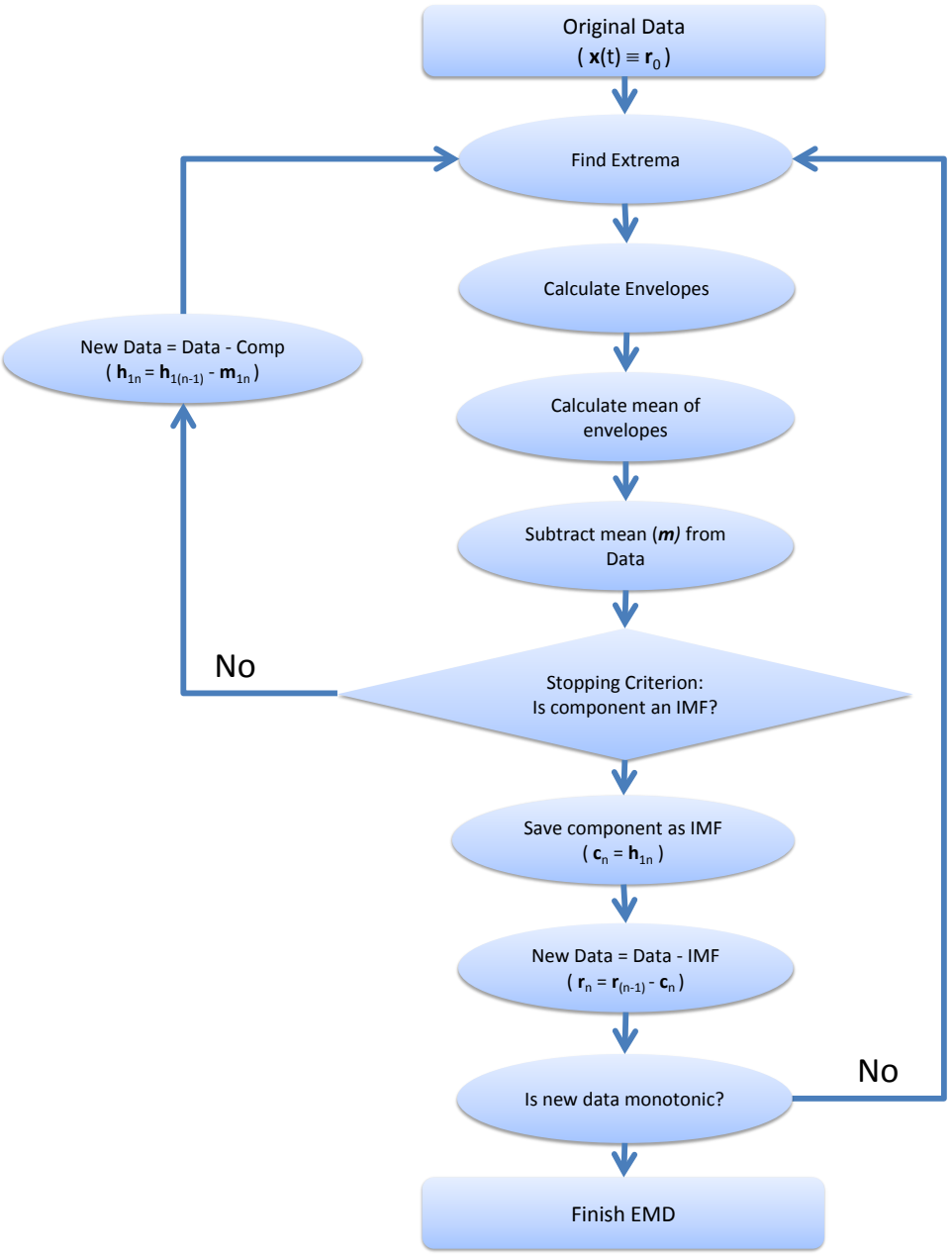

FIGURE 6.11: A flow chart of the steps involved in determining the intrinsic mode functions of an input data signal.

$$\mathbf{x} = \sum_{i=1}^{n} \mathbf{c}_i + \mathbf{r}_n. \tag{6.19}$$

A flow chart describing the steps of determining the intrinsic mode functions is presented in Figure 6.11. Figure 6.12 displays the resulting IMF after running the EMD algorithm for the same example data used to illustrate wavelet decomposition.

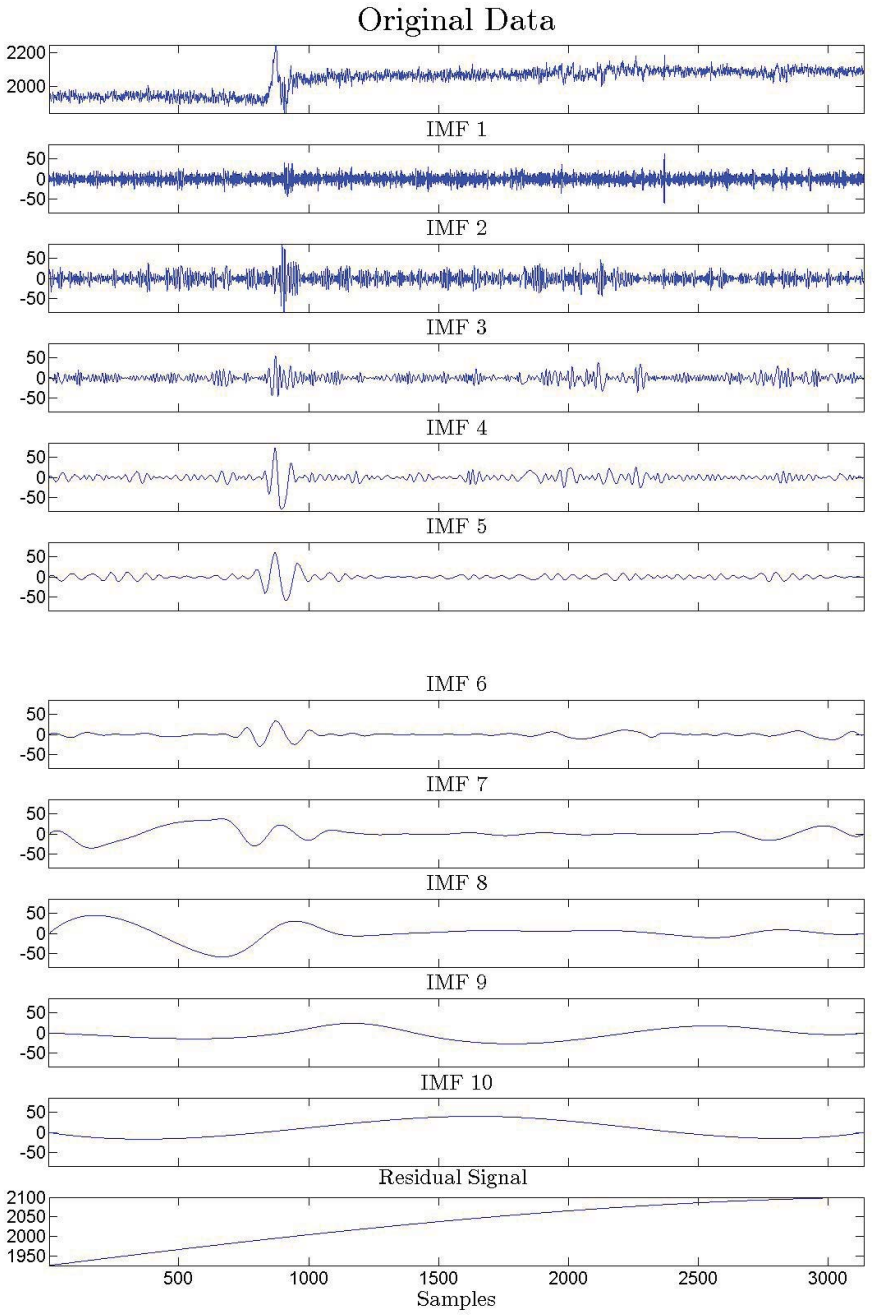

FIGURE 6.12: Figure presents the original noisy signal (same as Figure 6.8) along with the individual IMF outputs from the EMD algorithm.

6.2.2 Ensemble Empirical Mode Decomposition (EEMD)

One of the major complications with the EMD algorithm is that often the determined IMF can be affected by "mode mixing". Mode mixing is said to have occurred if a single IMF consists of signals of vastly different scales or if signals (e.g. Figure 6.13) of similar

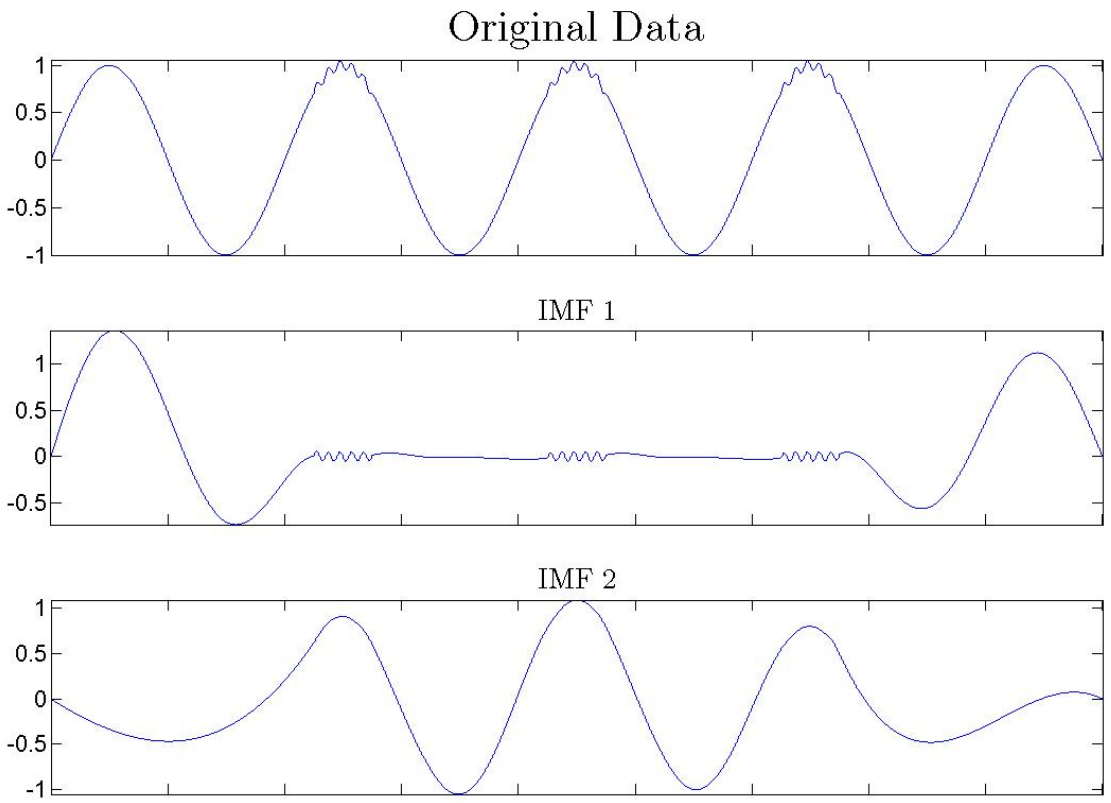

FIGURE 6.13: This figure shows an example of mode mixing in a signal. The signal intermittency in the original data has resulted in the first IMF containing signals of vastly different scales. Only the first two IMF are shown.

scales are present in different IMFs. The presence of mode mixing in the IMF can cause aliasing in the time-frequency distribution and/or cause the physical meaning of the IMF to become unclear. Initially, Huang *et al.* [78] defined an intermittency test based on period length to separate waves of different period into different modes. However, by using this intermittency test, the EMD algorithm was no longer adaptive and thus the test negated some of the advantages of the algorithm.

Wu *et al.* [205] developed an extension to the EMD algorithm in 2009 called ensemble EMD (EEMD), following on from the pioneering work by Gledhill [64] and Flandrin *et al.* [55]. This new noise assisted data analysis method defined the newly calculated IMF to be the average of an ensemble of trials and in doing so eliminated the mode mixing problem without discarding the adaptive nature of the algorithm. The foundation of the algorithm is the addition of white noise to a given number of ensembles of the original data. Therefore the new ensemble data can be thought of as a number of observations of the same data, each contaminated by different random white noise of similar standard deviation. By adding this uniform noise, the components of the signal of different scales are automatically projected onto proper scales of reference, established by the white

noise in the background. The EEMD algorithm, run on the same data as shown in Figure 6.13, is shown in Figure 6.14. It can be seen that the previous problem of mode mixing has been removed and the true signal can be clearly seen in IMF 5.

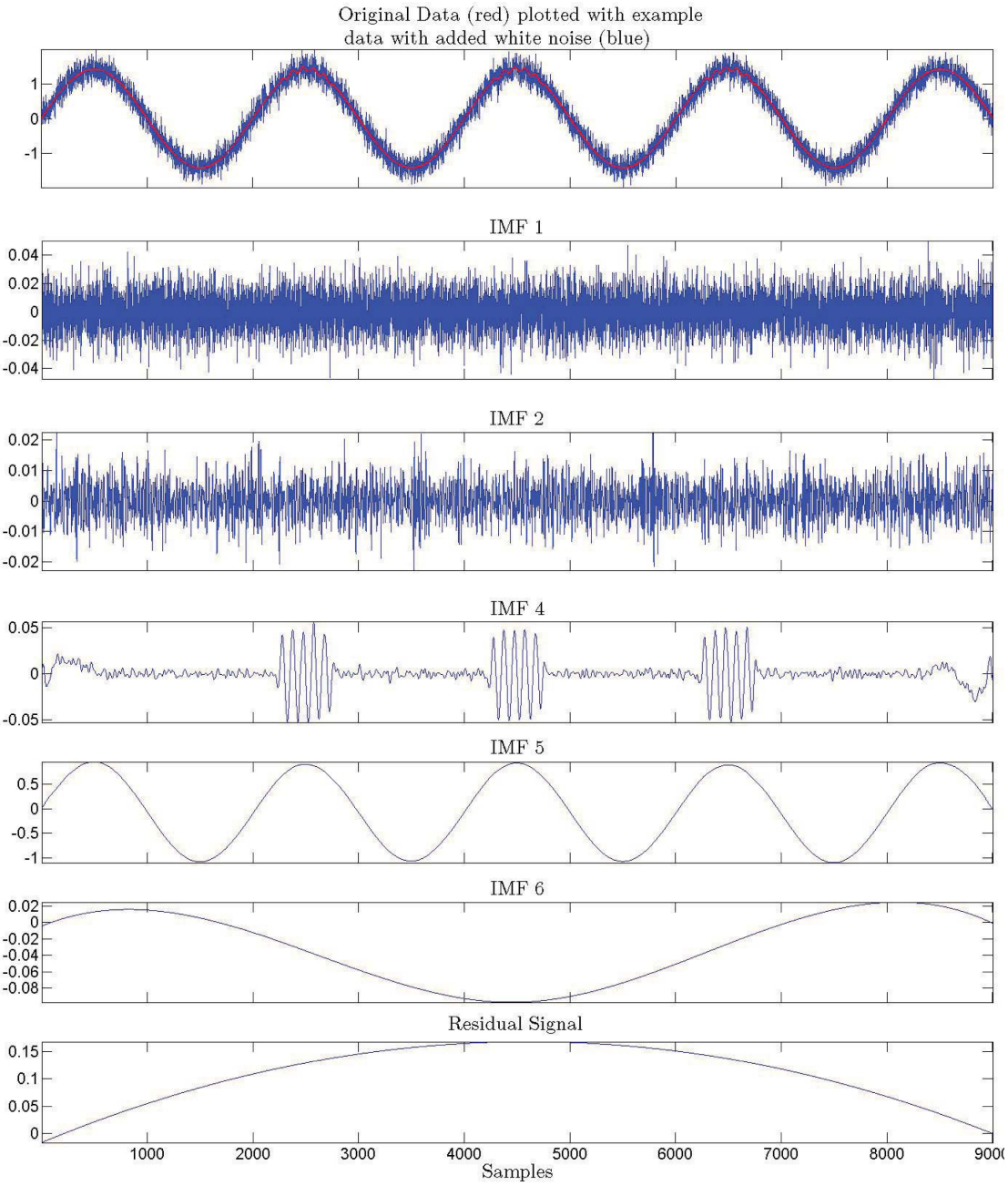

FIGURE 6.14: This figure shows an example of how the EEMD algorithm solves the mode mixing problem. The original data, similar to that shown in Figure 6.13, is shown in red in the first subplot, with the original data mixed with an example white noise shown in blue. Scaling is independent for each IMF to better illustrate the contained components.

The steps to perform EEMD are similar to those undertaken when employing EMD shown in Figure 6.11. There are however 3 additional steps that must be taken:

1. Prior to running the EMD algorithm, white noise (whose standard deviation is a set ratio of that of the original signal) is added to the original input data $\mathbf{x}$. The n IMFs are then calculated as described previously and shown in Figure 6.11.

2. Step one above is repeated (for the chosen number of ensembles) with a random white noise added to the original data on each iteration.

3. The final output IMFs of the EEMD algorithm can then be calculated as the mean of the ensemble of the previously calculated IMFs.

When running the EEMD algorithm there are two parameters that need to be set prior to implementation; the amplitude of the added white noise and the number of ensembles to run. The noise amplitude is required to be of a significant level to ensure that it introduces the change in extrema that the EEMD algorithm relies on. However if the amplitude is too large then a greater number of ensembles is required to negate the resulting additive noise. It follows that the number of ensembles required should be large enough to negate the effect of adding the random white noise, however as the number of ensembles increases so too does the computational time of the algorithm. Wu *et al*. suggest the added noise should have a standard deviation of approximately 0.2 times the standard deviation of the data and so was thus set for the performed analysis. The number of ensembles can then be chosen empirically ensuring that the mode mixing problem has been negated and the added white noise has been canceled sufficiently. The number of ensembles was set to 3 when analysing the fNIRS data and to 5 when analysing the EEG data.

Once the IMFs have been determined, the components deemed to be artifacts can be removed. For the results produced in this thesis the artifact components were determined as specified in Section 4.7. The resulting cleaned signal can then be calculated as the sum of the remaining "clean" IMFs. The determined efficacy of the EEMD technique is presented in Section 6.7 where an example output of the algorithm is also presented for the fNIRS and EEG data.

In Section 6.5 the EEMD algorithm is used to create a multi-dimensional signal from the signal channel fNIRS and EEG data, allowing the novel use of the CCA algorithm [182]. This novel combination will be shown to provide the best efficacy results when employed on the fNIRS data under certain circumstances.

6.3 Independent Component Analysis

As stated in Section 3.4.1 independent component analysis (ICA) is a blind source separation technique in which recorded, multi-channel signals are separated into their independent constituent components or sources [83]. Figure 6.15 demonstrates the purpose of the ICA algorithm; given recorded sources $x(t)$, the algorithm endeavours to acquire an estimate $\hat{s}(t)$ of the true underlying sources $s(t)$ by use of an un-mixing matrix $\mathbf{W}$, i.e.

$$\hat{\mathbf{s}} \;=\; \mathbf{W}\mathbf{x}. \tag{6.20}$$

As the underlying sources $\mathbf{s}$ are often contaminated by noise $\mathbf{n}$, the recorded sources are often described as $\mathbf{x} = \mathbf{A}\mathbf{s} + \mathbf{n}$. However, the contaminating noise can be assumed to be independent of the underlying sources and thus it can be incorporated into $\hat{s}$ through increasing the dimension. Therefore the noise signal will emerge as an independent component (IC) of $\hat{\mathbf{s}}$. As ICA is a blind source separation (BSS) problem, neither the original sources $\mathbf{s}$ or the mixing matrix $\mathbf{A}$ are known. Accordingly, in order to be feasible to separate the underlying sources, additional assumptions must be made. The ICA algorithm makes a number of assumptions (as detailed in Section 3.4.1) with the most important stating that all underlying sources are assumed independent of each other, that is to say that the output of one source has no impact on any other.

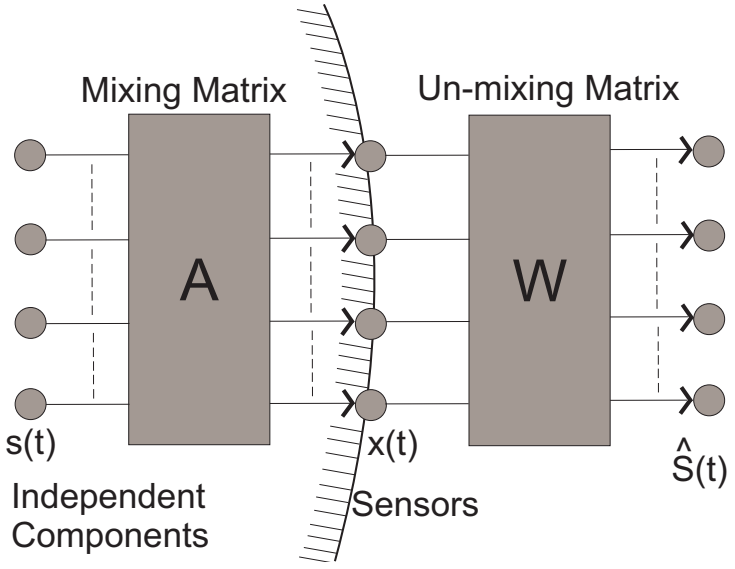

FIGURE 6.15: Model of the ICA algorithm. The sensors $\mathbf{x}$ detect a linear mix of the underlying independent sources $\mathbf{s}$, ie. $\mathbf{x} = \mathbf{A}\mathbf{s}$. The goal of the ICA algorithm is to create the un-mixing matrix $\mathbf{W}$ such that $\hat{\mathbf{s}} = \mathbf{W}\mathbf{x}$

Using this assumption of independence, Comon [39] showed that if the sources contain at most one Gaussian component then the sources could be separated with the only indeterminacies being scaling and permutation [187]. These indeterminacies can be outlined as follows:

$$\begin{aligned} \mathbf{x} &= \mathbf{A}\mathbf{s} \\ &= \sum_{i=1}^{n} \mathbf{a}_i s_i \\ &= \sum_{i=1}^{n} \left(\frac{1}{\alpha_i} \mathbf{a}_i \right) (\alpha_i s_i), \end{aligned} \tag{6.21}$$

where $\alpha_i \in \mathbb{R}$, $\alpha_i \neq 0$. As multiplying the sources by a non-zero constant (α_i) does not change their independence, each column of $\mathbf{A}$ can only be found up to a scaling factor. Further, as permuting the sum in the equation does not change the result, only the columns of $\mathbf{A}$ can be found and not their order.

The central limit theorem states that the sum of independent random variables (IRVs) lies closer to a Gaussian than the independent random variables themselves:

$$\text{Gaussianity}\left(\sum \text{IRVs}\right) > \text{Gaussianity}\left(\text{IRVs}\right) \tag{6.22}$$

and thus by increasing the non-Gaussianity of the random variables you simultaneously increase their independence. A number of different algorithms use differing techniques to separate the sources based on their non-Gaussian nature such as negentropy and kurtosis as described in Section 3.4.1. FastICA [84] is currently one of the most widely employed ICA techniques and therefore it is the approach adopted for this work. The rest of this section will deal exclusively with the implemented FastICA algorithm and the technique of maximising the kurtosis to separate the sources.

6.3.1 FastICA

FastICA is currently one of the most referenced ICA techniques available. First described in 1997 [84] this algorithm has many advantages over alternative ICA implementations. The algorithm uses an efficient fixed-point iteration scheme for finding the local extrema of the kurtosis of a linear combination of the observed variables. To separate the sources using non-Gaussianity, the aim is to maximise the magnitude of the kurtosis. The

kurtosis is a measure of the "peakedness" of the probability distribution of a real-valued random variable and is described for a zero-mean random variable x as

$$\text{kurt}(x) = E\{x^4\} - 3(E\{x^2\})^2. \tag{6.23}$$

The kurtosis is negative for source signals whose amplitude has sub-Gaussian probability densities, positive for super-Gaussian and zero for Gaussian densities [193]. An example of some distributions is presented in Figure 6.16. Thus, maximising the norm of the kurtosis forces the sources to be as non-Gaussian as possible.

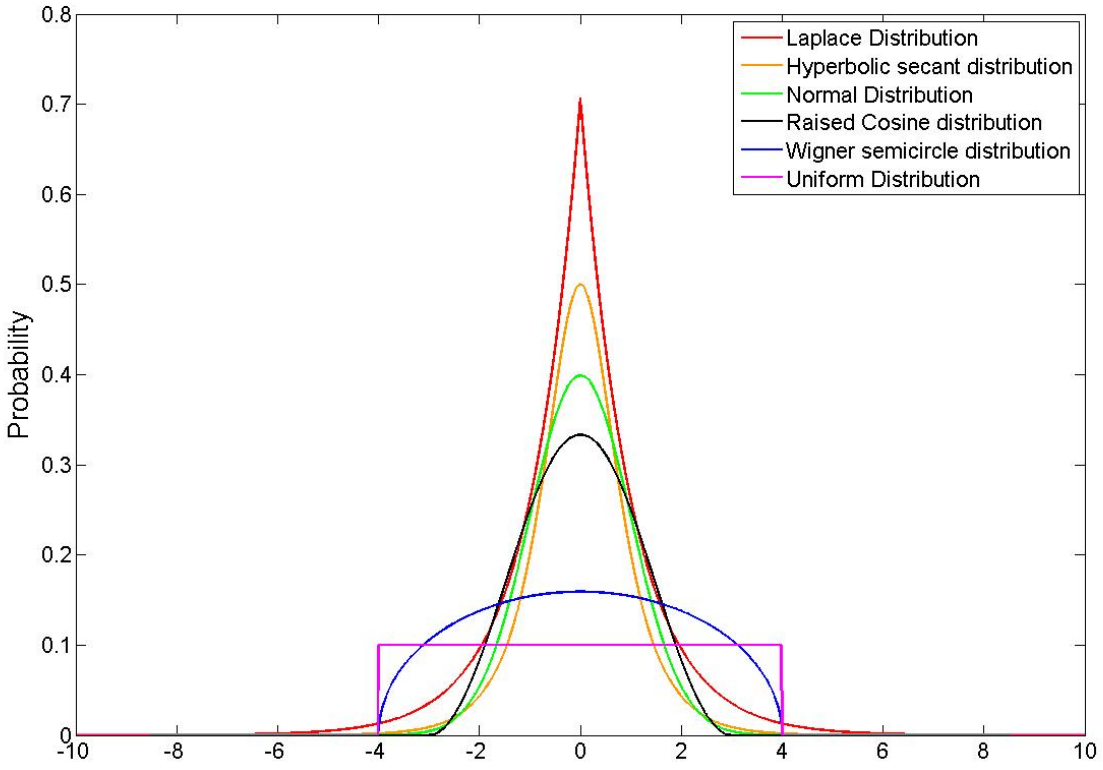

FIGURE 6.16: Figure shows the change in kurtosis from super-Gaussian to Gaussian to sub-Gaussian signals. The normal distribution is a Gaussian function and thus has a kurtosis of 0. The Laplace and hyperbolic secant distributions are super-Gaussian and have a positive kurtosis. The raised cosine, Wigner semicircle and the Uniform distributions all have sub-Gaussian distributions with a kurtosis less than 0.

The FastICA algorithm has many advantages over other implemented ICA methods, with some listed below [84]:

- The algorithm is very simple to utilise as there is no learning rate or other adjustable parameters as required in other techniques.
- The convergence speed of similar fixed-point algorithms is often linear in nature. The FastICA algorithm's convergence rate is cubic. This increased convergence

rate usually ensures the FastICA algorithm is 10 to 100 times faster then other implemented ICA methods.

- The algorithm is capable of finding the independent components in series (deflation approach) rather then in parallel (symmetric approach) like other methods. This allows certain independent components to be estimated, without the required computation of detecting all components, again decreasing the computational time of the algorithm.

One preprocessing step commonly performed before employing the FastICA algorithm is pre-whitening. The use of pre-whitening considerably simplifies the BSS problem by removing any autocorrelations present in the time series data in both space and time. Using a technique such as principal component analysis (PCA) [93], to pre-whiten the signal, results in the number of parameters to be determined being reduced from n^2 to $\frac{1}{2}n(n+1)$ [212] thus further increasing the speed of the FastICA algorithm.

Following the whitening of the data, the deflation FastICA algorithm can be expressed as follows:

1. Initialise the algorithm by setting $p := 1$ (Where p is the current independent component number).

2. Choose $\mathbf{w}_p(0) \in S^{n-1}$. $\mathbf{w}_p(0)$ represents the weights for IC p and S^{n-1} denotes the (n-1) dimensional unit sphere, that is:

$$S^{n-1} := \{\mathbf{x} \in \mathbb{R}^n | \, |\mathbf{x}| = 1\}. \tag{6.24}$$

3. Perform a single fixed-point kurtosis maximisation step:

$$\mathbf{v}_p(t+1) := \mathbf{E}\left(\left(\mathbf{w}_p(t)^T\mathbf{z}\right)^3\mathbf{z}\right) - 3\mathbf{w}_p(t), \tag{6.25}$$

   where $\mathbf{z}$ is the data whitened using a technique such as PCA.

4. To ensure that the current weight vector $\mathbf{v}_p$ is orthogonal to all previously found weights $\mathbf{w}_j$, the so-called deflationary orthogonalisation can be performed after each FastICA update iteration.

$$\mathbf{u}_p(t+1) := \mathbf{v}_p(t+1) - \sum_{j=1}^{p-1}\left(\mathbf{v}_p(t)\mathbf{w}_j\right)\mathbf{w}_j. \tag{6.26}$$

5. Normalise the weight vector to ensure it stays on the S^{n-1} sphere:

$$\mathbf{w}_p(t+1) := \frac{\mathbf{u}_p(t+1)}{|\mathbf{u}_p(t+1)|}. \tag{6.27}$$

6. Check for the convergence of the algorithm using the stopping criterion. A commonly used stopping criterion for the FastICA algorithm is when the mean-squared difference of $\mathbf{w}_p$ is less than a given ϵ [212], i.e.

$$|1 - |\mathbf{w}_p(t+1)^T \mathbf{w}_p(t)| \,| < \epsilon. \tag{6.28}$$

   If the algorithm has not converged, return to step 3 and perform a further kurtosis maximisation step.

7. If the stopping criterion has been met and the value of p is less than the desired number of independent components, increment p and return to step 2. If the value of p is equal to the desired number of independent components, return the final $\mathbf{W} = [\mathbf{w}_1, \mathbf{w}_2, \mathbf{w}_3, ...\mathbf{w}_p]$ matrix.

Although FastICA is a simple technique to implement, it can be affected by a few troublesome issues. One of the problems with FastICA, and ICA in general, occurs with oscillatory activity within the signal, which is often present in brain signals. The kurtosis of this oscillatory signal changes depending on length of the bursts of activity. For short bursts there is a positive kurtosis and this kurtosis goes negative the longer the duration of the bursts become. However, at a given length of oscillatory activity the kurtosis can be zero [193]. This causes the signal to appear Gaussian to the FastICA algorithm with the result that it is no longer able to separate it from the other sources. This situation is, however, improbable but future techniques may have to overcome this problem by using approaches based on the time correlation in the data [11].

Although the kurtosis of a signal is extremely simple to calculate, because it is a fourth-order statistic it's estimators are highly sensitive to outliers in the data [6]. The kurtosis value can sometimes be based on only a few samples in the tails of the distributions which can lead to poor statistical significance. Therefore, although the sources continue to be separated, they may not be as independent as possible. Finally, the use of pre-whitening can sometimes impose a restriction on separation performance and for short data sizes can sometimes introduce an estimation bias due to residual source bias [212]. However, due to the improvement in computational time and the use of long data sets, the pre-whitening stage was retained.

After using the FastICA algorithm to determine the un-mixing matrix $\mathbf{W}$, and therefore the estimated underlying sources $\hat{\mathbf{s}}$, the sources that are deemed to be artifactual in nature can be set to zero. The methods employed to determine which sources are artifacts are discussed in Section 4.7. The remaining sources $\hat{\mathbf{s}}_{CLEAN}$ are then understood to be the artifact free sources and the artifact free signals at the recording site can be determined as follows:

$$\mathbf{x}_{CLEAN} = \mathbf{A}\hat{\mathbf{s}}_{CLEAN}, \tag{6.29}$$

where $\mathbf{A}$ (the mixing matrix) is the inverse of the determined un-mixing matrix (i.e. $\mathbf{A} = \mathbf{W}^{-1}$. If $\mathbf{W}$ is not square it is not possible to compute the true inverse of the matrix, however the pseudoinverse can be calculated which can serve as a good approximation for the "true" inverse. Although the ICA algorithm can not itself be employed on the fNIRS and EEG datasets analysed in this thesis, its combination with the wavelet transform and the EEMD technique is described in Section 6.6. The FastICA algorithm does not require any additional parameters to be set prior to employing the algorithm.

6.4 Canonical Correlation Analysis

Canonical correlation analysis (CCA) [77] is a multi-channel blind source separation (BSS) technique (Section 3.4) for separating a number of mixed or contaminated signals. The CCA technique, similar to the ICA method described in Section 6.3, requires that there be a greater than or equal number of recorded signals $\mathbf{x}$ as underlying sources $\mathbf{s}$ and thus cannot be used on single channel measurements. However, unlike ICA, the CCA algorithm separates the underlying sources using the assumption that the sources are uncorrelated with each other. The CCA method uses second order statistics (SOS) to generate components derived from their uncorrelated nature. CCA solves the BSS problem by forcing the sources to be maximally autocorrelated (at lag one) and mutually uncorrelated [46], i.e. CCA makes $x_i(t)$ and $x_i(t+1)$ as correlated as possible while ensuring $x_i(t)$ and $x_j(t)$ are uncorrelated (as they are statistically independent). Separating components due to their uncorrelated nature is a weaker condition than the statistical independence required by ICA (independent components are also uncorrelated, but the opposite is not necessarily true) but is also less computationally complex due to the use of SOS rather than higher order statistics (HOS) used by ICA.

6.4.1 Operation of CCA

With a zero mean input signal $\mathbf{x}$, let $\mathbf{y}$ be a linear combination of neighbouring (but not overlapping) samples (i.e. $y(t) = x(t-1) + x(t+1)$). From these two available vectors two new scalar random variables x and y, called the canonical variates, can be generated as a linear combination of the components in $\mathbf{x}$ and $\mathbf{y}$.

$$x = w_{x_1}x_1 + w_{x_1}x_2 + ... + w_{x_m}x_m = \mathbf{w}_\mathbf{x}^T\mathbf{x} \tag{6.30}$$

$$y = w_{y_1}y_1 + w_{y_1}y_2 + ... + w_{y_m}x_m = \mathbf{w}_\mathbf{y}^T\mathbf{y} \tag{6.31}$$

CCA attempts to find the weight vectors $\mathbf{w_x}$ and $\mathbf{w_y}$ that will maximise the correlation ρ between x and y [23]. The simple solution of $\mathbf{w}_x = \mathbf{w}_y = 0$ is not permitted. By maximising this correlation it is possible to conclude that the algorithm will not select a mixture of the source signals as this mixture would have a lower correlation than if one of the original source signals was chosen. When the first pair of weight vectors $(\mathbf{w}_x, \mathbf{w}_y)_1$ has been determined, the CCA algorithm then continues to find a second pair of weights $(\mathbf{w}_x, \mathbf{w}_y)_2$ that produces canonical variates that are also maximally correlated but simultaneously uncorrelated with the canonical variates produced using the first set of weights. The CCA algorithm is a recursive algorithm and therefore proceeds to find a total of m variates, where m is the number of recording sites. To find the maximum correlation between the variates x and y the following equation must be solved:

$$\begin{aligned}
\rho &= \frac{E[xy]}{\sqrt{E[x^2]E[y^2]}} \\
&= \frac{E[\mathbf{w}_\mathbf{x}^T\mathbf{x}\mathbf{y}^T\mathbf{w}_\mathbf{y}]}{\sqrt{E[\mathbf{w}_\mathbf{x}^T\mathbf{x}\mathbf{x}^T\mathbf{w}_\mathbf{x}]]E[\mathbf{w}_\mathbf{y}^T\mathbf{y}\mathbf{y}^T\mathbf{w}_\mathbf{y}]]}} \\
&= \frac{\mathbf{w}_\mathbf{x}^T\mathbf{C}_{xy}\mathbf{w}_\mathbf{y}}{\sqrt{\mathbf{w}_\mathbf{x}^T\mathbf{C}_{xx}\mathbf{w}_\mathbf{x}\mathbf{w}_\mathbf{y}^T\mathbf{C}_{yy}\mathbf{w}_\mathbf{y}}}.
\end{aligned} \tag{6.32}$$

The matrix $\mathbf{C}_{xy}$ is the between-sets covariance matrix and $\mathbf{C}_{xx}$ and $\mathbf{C}_{yy}$ are the nonsingular within-set covariance matrices, i.e.

$$\mathbf{C} = E\left[\begin{pmatrix}\mathbf{x}\\ \mathbf{y}\end{pmatrix}\quad\begin{pmatrix}\mathbf{x}\\ \mathbf{y}\end{pmatrix}^T\right] = \begin{bmatrix}\mathbf{C}_{xx} & \mathbf{C}_{xy}\\ \mathbf{C}_{yx} & \mathbf{C}_{yy}\end{bmatrix}. \tag{6.33}$$

The calculation of the maximum of ρ can be found by setting the derivatives of Equation 6.32 to zero with respect to $\mathbf{w_x}$ and $\mathbf{w_y}$. This equation then results in the following equations [60] [59]:

$$\begin{cases} \mathbf{C}_{xy}\hat{\mathbf{w}}_\mathbf{y} = \rho\lambda_x \mathbf{C}_{xx}\hat{\mathbf{w}}_\mathbf{x} \\ \mathbf{C}_{yx}\hat{\mathbf{w}}_\mathbf{x} = \rho\lambda_y \mathbf{C}_{yy}\hat{\mathbf{w}}_\mathbf{y}, \end{cases} \tag{6.34}$$

where the scaling factors λ_x and λ_y are calculated as

$$\lambda_x = \lambda_y^{-1} = \sqrt{\frac{\hat{\mathbf{w}}_\mathbf{y}^T \mathbf{C}_{yy}\hat{\mathbf{w}}_\mathbf{y}}{\hat{\mathbf{w}}_\mathbf{x}^T \mathbf{C}_{xx}\hat{\mathbf{w}}_\mathbf{x}}}. \tag{6.35}$$

Substituting $\mathbf{w_x}$ for $\mathbf{w_y}$ and vice versa in Equation 6.34 results in the following two eigenvalue problems:

$$\begin{aligned} \mathbf{C}_{xx}^{-1}\mathbf{C}_{xy}\mathbf{C}_{yy}^{-1}\mathbf{C}_{yx}^T\hat{\mathbf{w}}_\mathbf{x} &= \rho^2\hat{\mathbf{w}}_\mathbf{x} \\ \mathbf{C}_{yy}^{-1}\mathbf{C}_{yx}\mathbf{C}_{xx}^{-1}\mathbf{C}_{xy}^T\hat{\mathbf{w}}_\mathbf{y} &= \rho^2\hat{\mathbf{w}}_\mathbf{y}. \end{aligned} \tag{6.36}$$

$\mathbf{w_x}$ and $\mathbf{w_y}$ can be determined as the eigenvectors of the matrices $\mathbf{C}_{xx}^{-1}\mathbf{C}_{xy}\mathbf{C}_{yy}^{-1}\mathbf{C}_{yx}^T$ and $\mathbf{C}_{yy}^{-1}\mathbf{C}_{yx}\mathbf{C}_{xx}^{-1}\mathbf{C}_{xy}^T$ respectively and the corresponding eigenvalues ρ^2 are the squared canonical correlations. As $\mathbf{x}$ is our original signal it is sufficient to only calculate $\hat{\mathbf{w}}_\mathbf{x}$ from Equation 6.36; if desired $\hat{\mathbf{w}}_\mathbf{y}$ can then be calculated using Equation 6.34. This approach ensures that $\hat{\mathbf{w}}_\mathbf{x}$ and $\hat{\mathbf{w}}_\mathbf{y}$ have correct signs to produce the desired positive canonical correlation coefficient. The first pair of variates are the eigenvectors of $\mathbf{w_x}$ and $\mathbf{w_y}$ that correspond to the largest square correlation coefficient (or eigenvalue) ρ_{max}^2. The following pairs of variates $(\mathbf{w}_x, \mathbf{w}_y)_{2\ldots m}$ are then the remaining eigenvectors in decreasing order of correlation [3]. The canonical correlation analysis technique therefore creates a weight matrix $\mathbf{W}_x = [\mathbf{w}_{x1}, \mathbf{w}_{x2} \ldots \mathbf{w}_{xm}]^T$ that can be used to separate the recorded sources $\mathbf{x}$ into the self correlated and mutually uncorrelated sources.

$$\hat{\mathbf{s}} = \mathbf{W}_x\mathbf{x}. \tag{6.37}$$

Artifact removal can then be conducted, in a similar manner to the ICA algorithm as previously described in Section 6.3.1. Components in the output matrix $\hat{\mathbf{s}}$ which are deemed to have been produced by artifact sources are identified and the corresponding

columns are set to zero (Section 4.7). In doing so the artifact components will not have an affect on the cleaned signal after reconstruction, i.e.

$$\mathbf{x}_{CLEAN} = \mathbf{A}\hat{\mathbf{s}}, \tag{6.38}$$

where $\mathbf{A} = \mathbf{W}^{-1}$. If $\mathbf{W}$ is not a square matrix (i.e. the number of sources is not equal to the number of signals) then it does not have an inverse. However, in these cases the pseudoinverse of the matrix can be calculated which can serve as a good approximation for the "true" inverse.

One major advantage of the CCA algorithm over the ICA algorithm is its ability to take temporal correlations into account [23]. With ICA, the samples can be arranged arbitrarily in time and the ICA algorithm will return the same result. In doing so the ICA can lose a lot of information about the signal and can make the separation technique more difficult then it is required to be. CCA addresses this issue and is capable of finding uncorrelated components that, in addition, have maximum spatial or temporal correlation within each component. In doing so, the CCA algorithm will always return the same result in terms of source separation which is not true for the ICA algorithm. Further, it is known that if a random vector has a multivariate normal distribution then any two or more of its components that are uncorrelated are also independent [21] and thus CCA can often return the same result as ICA. If this is not the case, then CCA will return components which are uncorrelated but not necessarily independent.

The CCA algorithm does not require any additional parameters to be set prior to employing the algorithm. Similar to the ICA algorithm, the CCA technique cannot be applied directly to the fNIRS and EEG datasets generated in this thesis as they are single channel signals. Section 6.5 below describes the novel combination of the CCA algorithm with both the EEMD algorithm and the wavelet transform, which overcomes this limitation.

6.5 Novel Combination of EEMD/Wavelets with CCA

As stated in Section 6.4 the CCA source separation technique is only capable of operating when a multichannel signal is available at its input. When these signals are available the technique has been shown to be highly efficient at removing the artifacts from contaminated signals [46]. Therefore, if this technique is to be used in conjunction with a contaminated single channel measurement, this measurement must first be converted into a multichannel signal. The two decomposition methods described in this

chapter (EEMD and wavelet transform) are two of a number of techniques currently available which can generate these desired signals. In this section we combine the signal decomposition methods with the CCA source separation techniques, providing two novel techniques, with the aim of further increasing the artifact removal capability achievable when using the signal decomposition methods alone.

The novel use of EEMD in combination with CCA for source separation of single channel measurements was described by the authors in [182]. The EEMD technique can be used to create a multi-channel signal $\mathbf{X}$, comprised of IMFs, from a single channel recording $\mathbf{x}$ (see Section 6.2.1). This matrix $\mathbf{X}$ can then be employed as the input to the CCA algorithm with the aim of estimating the underlying true sources $\hat{\mathbf{S}}$ (Equation 6.37). The individual sources determined to be artifacts are selected (Section 4.7) and the corresponding columns of the matrix $\hat{\mathbf{S}}$ are set to zero. The source matrix is then passed through the inverse of the un-mixing matrix $\mathbf{A}$ to return the multi-channel signals $\mathbf{X}_{CLEAN}$ which are now, ideally, free of artifacts (Equation 6.38). The original single channel signal $\hat{\mathbf{x}}$, now free of artifacts, can be determined by simply adding the columns of the matrix $\mathbf{X}_{CLEAN}$.

As there are two levels to these techniques, i.e. EEMD followed by CCA, the removal of the artifact components can take place either solely after the CCA stage as described above, or alternatively can be performed both after the EEMD decomposition stage and the CCA stage. By performing the artifact removal using this second method, much of the dominating artifact will have been removed prior to the employment of the CCA technique and so the source separation technique can have a better chance of removing the lower amplitude artifact components. The results presented in Section 6.7 of this chapter will present the efficacy metrics calculated for each of the employed techniques on both the fNIRS and EEG test datasets. For this purpose, the results obtained when removing the artifact components only after the CCA technique will be known as the one level artifact removal method and when removed after both the wavelet transform and the CCA techniques will be known as the two level method.

The use of the wavelet transform in combination with CCA for source separation of single channel measurements operates in a similar manner to that described for the EEMD based technique above. When using the W-CCA technique, the input to the CCA algorithm comprises of the details and approximation of the original single channel signal determined using the wavelet transform (Equation 6.12). Again, the CCA technique separates these input signals into components which are uncorrelated with one another while also being maximally autocorrelated. The signals are then regenerated following the removal of the artifact components and the original input signal to the W-CCA technique can be determined by again adding all of the CCA outputs. Similar to the

EEMD-CCA technique, the artifact removal can also take place in two separate manners and are again described as one level/two level artifact removal methods.

The next section describes two previously available two stage techniques which will allow for a rigourous comparison with the novel techniques described above.

6.6 Combination of EEMD/Wavelets with ICA

In order to provide a fair comparison to the novel artifact removal techniques described in Section 6.5, the operation of two previously described two stage techniques (namely EEMD-ICA and W-ICA) are described below.

Wavelet-ICA, or W-ICA, was first documented by Azzerboni *et al.* [9] in 2004 as a means for removing artifacts from surface EMG signals and has since also been employed by a number of authors for the removal of artifacts from EEG signals [85]. The combined use of the EEMD decomposition method with ICA was first documented by Mijović in 2010 for the removal of ECG artifact from EMG signals and the removal of seizure events from EEG signals [129] [130].

These two techniques operate in a similar manner to the EEMD-CCA and W-CCA technique described previously. However, the output of the signal decomposition methods is now passed into the input of the ICA technique (Section 6.3). This technique separates the input components into the underlying source signals which are generated due to their independent nature. With the source signals generated, the sources deemed to be artifacts can again be removed (Section 4.7). The remaining sources can then be used to re-generate the input components (minus the removed artifacts).

The novel introduction of the CCA algorithm to the wavelet transform or the EEMD algorithm has many advantages over the EEMD-ICA and W-ICA techniques described above. The use of the CCA algorithm greatly reduces the computational complexity of the algorithm as can be seen from Figure 6.17. This figure shows the average time taken to run each algorithm over 100 runs of 540 seconds of fNIRS data. Therefore the CCA algorithm can also lend itself towards use in systems based outside of the hospital environment where the computational complexity of an algorithm can often reduce the run time of monitoring devices. Secondly the CCA algorithm has been shown to be more capable of removing artifacts from some signals than the ICA algorithm [46] and thus may provide superior results when employed on the fNIRS or EEG data.

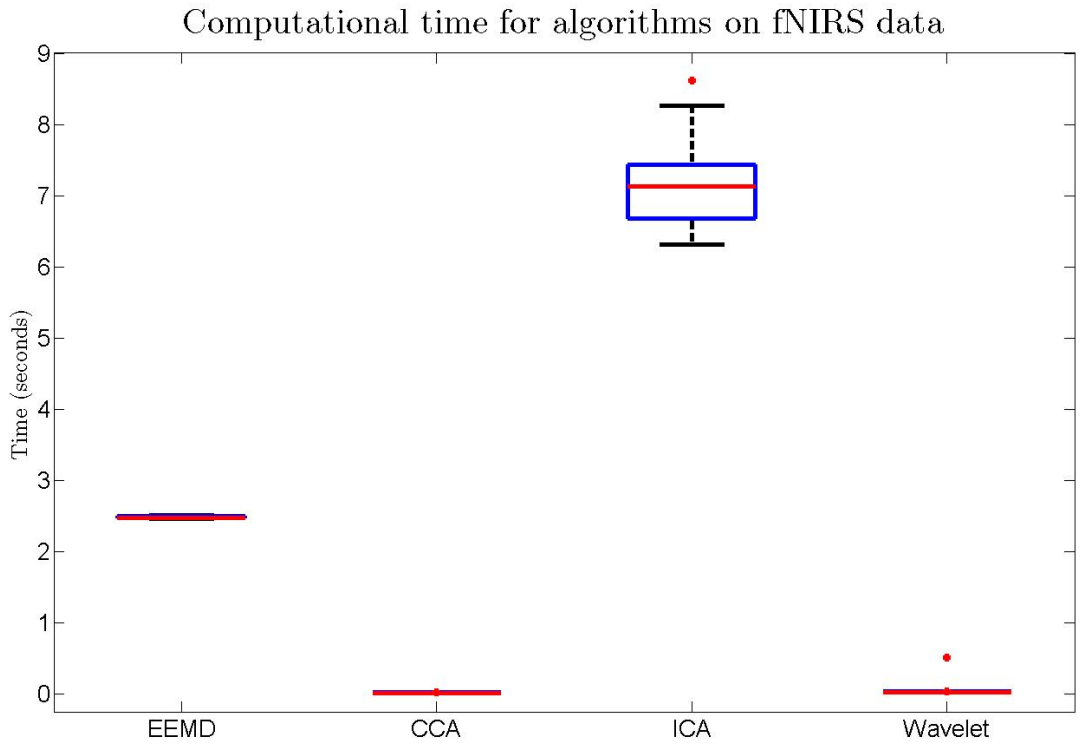

FIGURE 6.17: Mean computational time, over 100 runs, of the EEMD, CCA, ICA and wavelet algorithms on fNIRS data, with variation also shown. ICA can be seen to have a high variation compared to the other analysed techniques.

Section 6.7 provides results for each of the four composite artifact removal techniques (W-ICA, EEMD-ICA, W-CCA, EEMD-CCA) on both the fNIRS and EEG datasets. Results are provided for both the one level and two level implementation in each case.

6.7 Results

The results in this chapter are organised in a similar manner to those presented in Chapter 5. The efficacy of the multiple artifact removal techniques are compared using two metrics; first, the improvement in signal-to-noise ratio (Δ SNR from Equation 4.7) and second the percentage improvement in correlation (λ from Equation 4.8).

Unlike the algorithms detailed in Chapter 5, the two stage algorithms require a technique to classify the separated components into either desired signal or artifact. When employing the artifact removal techniques on the fNIRS test dataset, two different artifact identification methods are used. The first, known as the GTC selection technique, uses the available "ground truth" signal to aid in the selection of the artifact components as described in Section 4.7.1. Using this technique provides the best case results for the

analysed techniques. However, as this "ground truth" signal will not normally be available, a second artifact component selection technique is also analysed which uses the autocorrelation function to determine the appropriate artifact components as described in Section 4.7.2. When employing the artifact techniques on the contaminated EEG data a third artifact selection technique is also analysed which uses the Hurst exponent of the individual components to determine if they are artifacts (Section 4.7.3).

The results obtained using the various two stage artifact removal techniques are presented below and are summarised in Table 6.1. Table 6.2 provides a summary of the results when the algorithms are solely employed on the epochs contaminated with artifacts, as determined using the data tagging technique outlined in Section 5.1. Results are presented for all the artifact selection techniques described, however a figure of an example output from the technique when employed on both the fNIRS and EEG data is presented only when employing the GTC selection technique. In addition, any input parameters required are highlighted as well as any deviation from the normal operation of the technique. Section 6.8 concludes the chapter by providing a comparison and discussion of the performance of each of the two stage techniques followed by an overall comparison of all the techniques analysed in the thesis.

6.7.1 Wavelet Transform

As stated in Section 6.1 the output of the wavelet transform is separated into a number of components known as details and approximations. The choice of the optimum components to remove to produce the best results were determined using the GTC selection technique. For the fNIRS test data this selection technique in conjunction with the wavelet transform provided a Δ SNR of 3.05 dB (2.15) and a λ value of 43.63 % (48.32). When employing the autocorrelation function to determine the artifact components the results became 2.57 dB (2.13) for Δ SNR and the percentage of correlation improvement dropped to 32.68 % (51.91). An example output of the wavelet transform with artifacts identified using the GTC selection technique is shown in Figure 6.18.

When employed on the EEG test data three different artifact selection techniques were analysed. Again the GTC selection technique provided the best case results and produced a Δ SNR of 8.8 dB (4.01) and a λ value of 55.25 % (35.43). Artifact selection using the autocorrelation function produced a Δ SNR of 8.89 dB (3.74) and a λ value of 50.98 % (40.34). The third artifact selection technique used with the EEG data is the Hurst exponent which generated a Δ SNR of 8.7 dB (3.98) and a percentage correlation

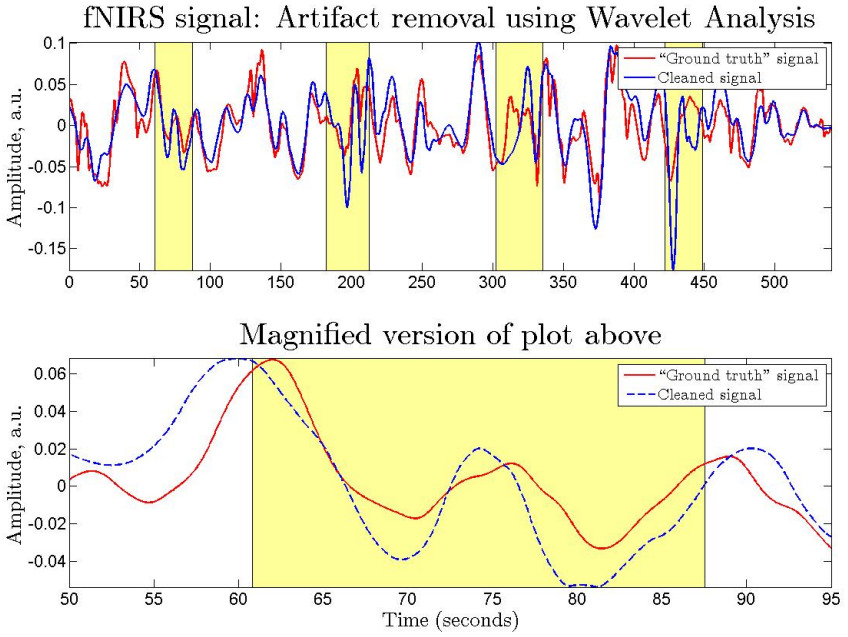

FIGURE 6.18: Example fNIRS trial showing cleaned signal following artifact removal using wavelet analysis.

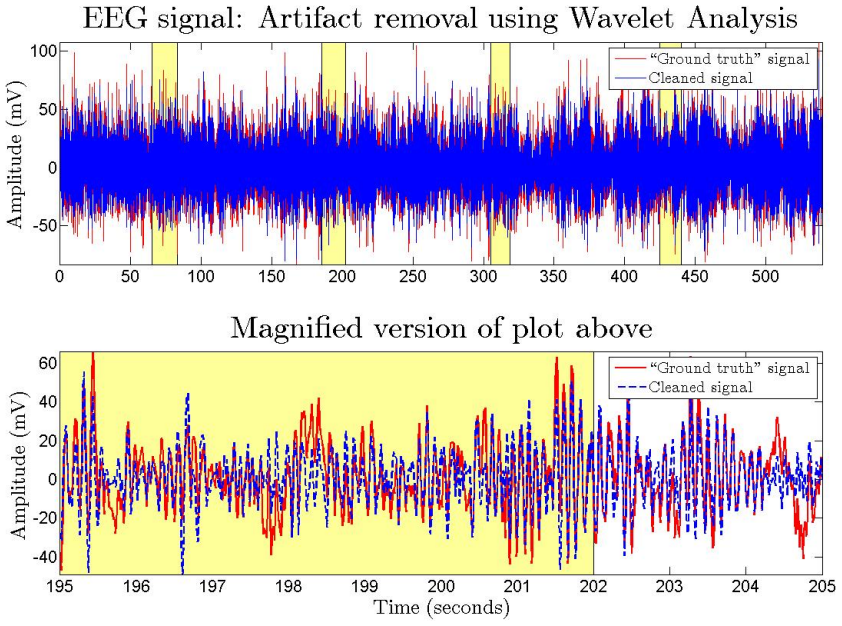

FIGURE 6.19: Example EEG trial showing cleaned signal following artifact removal using wavelet analysis.

increase of 51.26 % (39.15). Figure 6.19 presents an example output of the wavelet transform when employed on the EEG data using the GTC selection technique.

6.7.2 (Ensemble) Empirical Mode Decomposition

Similarly to the wavelet transform described above, the EEMD technique was tested with a number of different artifact selection techniques employed for the second stage. Figure 6.20 displays the output of the EEMD technique when using the GTC selection technique for the removal of the artifact components from the fNIRS test data. This technique provided a Δ SNR of 3.31 dB (2.21) and a λ value of 46.95 % (48.68). This corresponds to an average correlation rise from 0.584 prior to the artifact removal to 0.671 after. Using the autocorrelation function the percentage improvement in correlation was 32.49 % (45.41) and the Δ SNR was 2.38 dB (1.63).

The output of the two stage algorithm when employed on an example contaminated EEG signal is shown in Figure 6.21. The best case results, produced using the GTC selection technique, showed a 8.35 dB (4.0) increase in Δ SNR and a 52.24 % (36.34) increase in λ. As with the wavelet transform, the EEMD technique was also tested when using the autocorrelation function and the Hurst exponents to determine the artifact components. The autocorrelation function presented a 46.7 % (46.32) increase in λ and the SNR rose by 8.72 dB (3.7) whereas the Hurst exponent selection technique produced a 5.84 dB (3.98) value for Δ SNR and a λ value of 18.65 % (44.1).

In order to verify that the EEMD technique is required rather than the simpler EMD algorithm, the EMD algorithm was also run with the GTC selection technique. When employed on the fNIRS data the technique produced results of 2.05 dB (1.46) for Δ SNR and 18.97 % (27.38) for λ. Also for the EEG data the Δ SNR was calculated as 7.89 dB (3.89) and the percentage improvement in correlation was determined to be 43.29 % (31.19).

6.7.3 Wavelet-ICA

When employing the wavelet-ICA algorithm there are two separate ways to generate the artifact free signal (see Section 6.7), the first is to perform artifact component selection and removal only after the ICA technique, and so the wavelet transform is solely used to create the multichannel signal. This shall be called the one level method. The second method performs artifact component selection and removal at each step and therefore the multidimensional input to the ICA algorithm has already had some of the artifact signal removed and will be known as the two level method.

These two different artifact removal procedures were performed on both the available fNIRS and EEG test datasets. When employed on the fNIRS data, the one level method

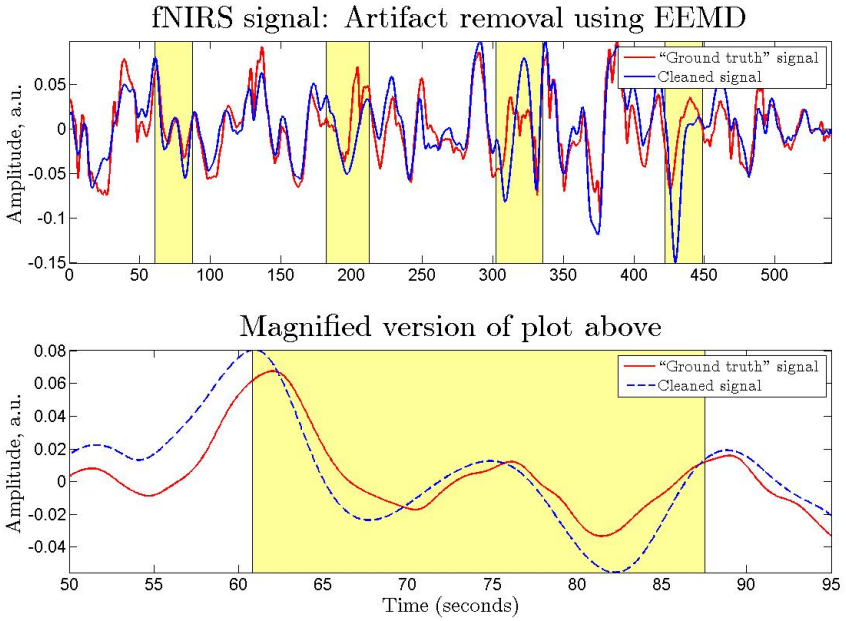

FIGURE 6.20: Example fNIRS trial showing cleaned signal following artifact removal using ensemble empirical mode decomposition (EEMD).

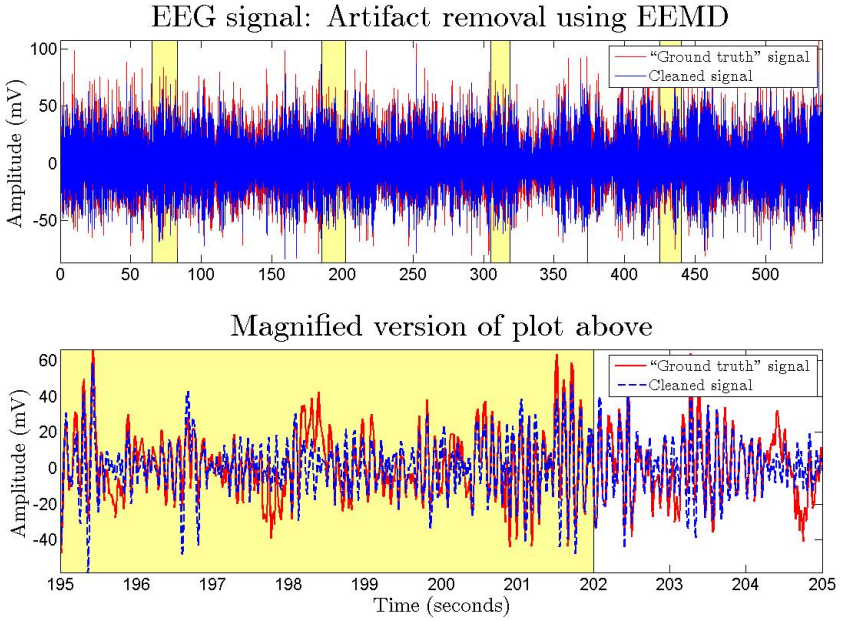

FIGURE 6.21: Example EEG trial showing cleaned signal following artifact removal using ensemble empirical mode decomposition (EEMD).

generated an average Δ SNR of 2.54 dB (2.12) and a λ value of 30.54 % (41.03). The artifact components were selected using the GTC selection technique. Using the same selection technique when employing the two level method the technique resulted in a

Δ SNR value of 3.03 dB (2.17) and a value for λ of 43.6 % (48.1). Using the autocorrelation function to select the artifact components, the λ value became 33.55 % (51.32) and the Δ SNR value became 2.51 dB (2.17). An example output of the wavelet-ICA algorithm using the two level technique with the GTC selection technique is shown in Figure 6.22.

The EEG data was analysed in the same manner as the fNIRS above with the addition of the Hurst exponent artifact selection criterion. When using the one level method, again using the GTC selection technique, the algorithm produced an average Δ SNR of 8.34 dB (3.4) and a λ of 55.5 % (35). When tested using the two level method, the algorithm produced similar results with a λ of 55.4 % (35.2) and Δ SNR of 8.82 dB (3.99). An example output of the algorithm using these parameters is shown in Figure 6.23. When using the autocorrelation function the acquired λ value dropped to 52.8 % (36.7) and the average value for Δ SNR became 8.73 dB (4.03). Finally, employing the Hurst exponent to select the artifact components over the two levels produced a Δ SNR of 8.21 dB (4.55) and a λ of 52.69 % (36.73).

6.7.4 Wavelet-CCA

The novel combination of the wavelet transform and the CCA technique was tested in the same manner as the W-ICA technique in that both the one level and two level methods were analysed. Using just the one level artifact selection method produced a Δ SNR of 3.06 dB (2.16) and a λ of 43.64 % (48.29). When employing the two level artifact selection technique the results were seen to diminish slightly. For the GTC selection technique, a λ of 37.30 % (52.17) and a Δ SNR of 2.77 dB (2.17) were obtained. The results obtained when using the autocorrelation technique to determine the artifacts components were 33.26 % (51.54) for λ and 2.54 dB (2.15) for Δ SNR. An example output of the algorithm is shown in Figure 6.24 for an input fNIRS signal where two level artifact removal was performed using the GTC selection technique.

When employed on the EEG data the results were comparable to the W-ICA technique. For the one level method, the average value for λ was 55.26 % (35.29) and the value obtained for Δ SNR was 8.74 dB (3.94). When analysing the two level methods, the three different artifact selection techniques were again analysed. The GTC selection technique provided an average Δ SNR of 8.80 dB (4.01) and a λ value of 55.25 % (35.43). When using the autocorrelation function to aid in the selection of the components relating to artifacts the λ value achieved was 52.80 % (36.71) and the improvement in SNR was determined to be 8.73 dB (4.03). Finally the Hurst exponent provided a λ of

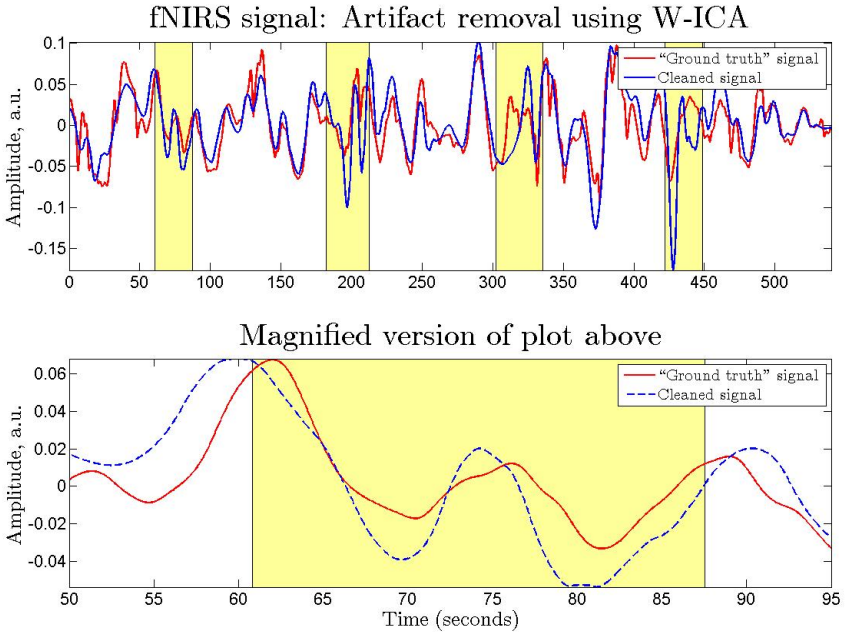

FIGURE 6.22: Example fNIRS trial showing cleaned signal following artifact removal using wavelet-ICA.

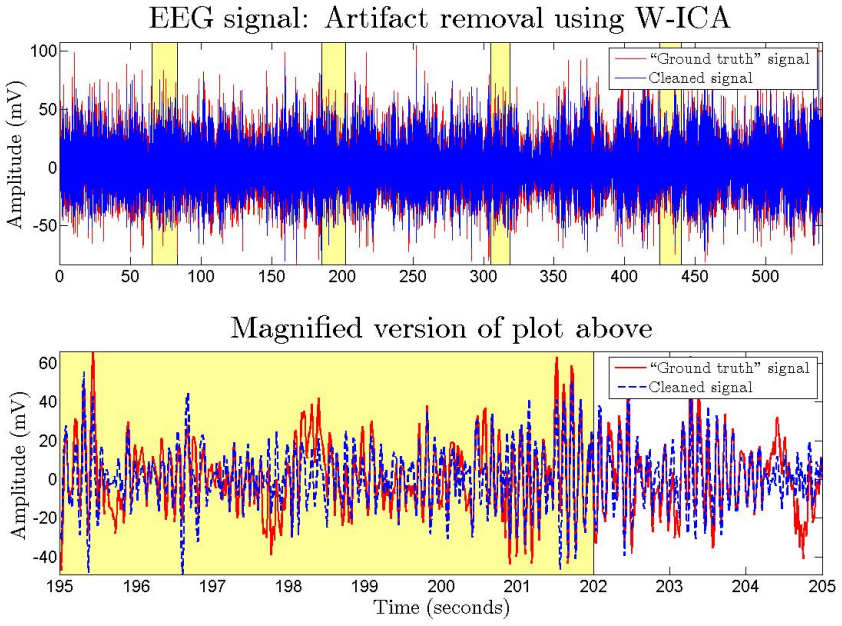

FIGURE 6.23: Example EEG trial showing cleaned signal following artifact removal using wavelet-ICA.

52.59 % (36.78) and a Δ SNR of 8.17 dB (4.56). Figure 6.25 presents an example output when analysing the EEG data.

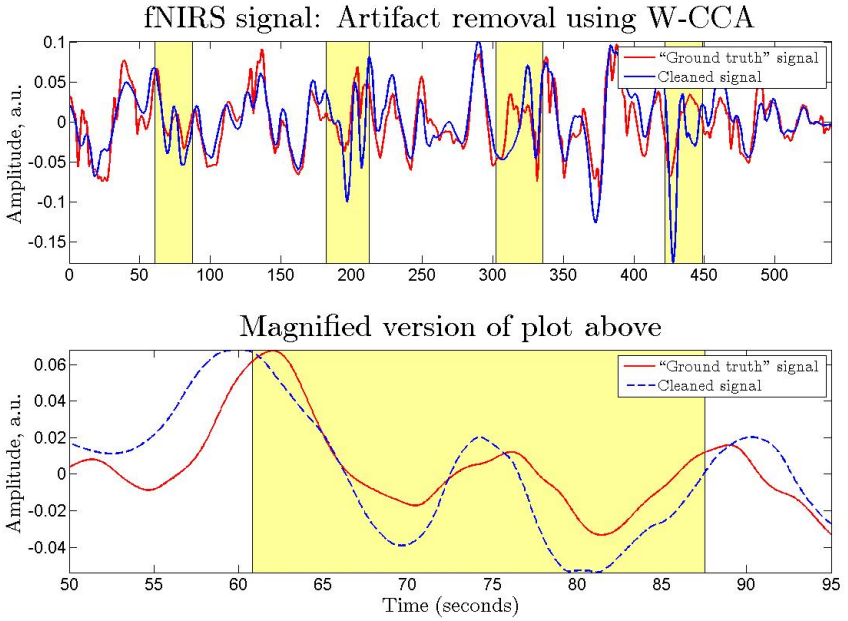

FIGURE 6.24: Example fNIRS trial showing cleaned signal following artifact removal using wavelet-CCA.

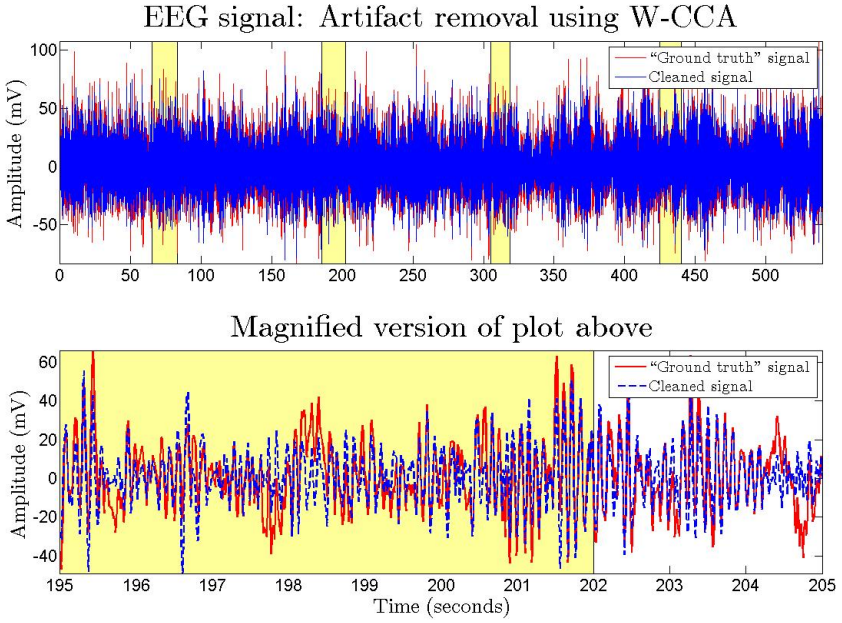

FIGURE 6.25: Example EEG trial showing cleaned signal following artifact removal using wavelet-CCA.

6.7.5 EEMD-ICA

As the EEMD-ICA technique converts a single channel signal into a multichannel signal before separating them into the underlying sources (similar to the steps of the W-ICA

and W-CCA techniques) the one level and two level artifact removal methods can again be employed. When operating on contaminated fNIRS data the one level artifact removal method generated a value of 37.21 % (50.45) for λ and a value of 2.91 dB (2.33) for Δ SNR. However when the artifact components were removed after each step using the GTC selection technique, the determined values for λ and Δ SNR improved. The new λ was 43.43 % (49.89) and the Δ SNR was 3.32 dB (2.26). When using the autocorrelation of the components to aid in the selection of the artifact components the calculated λ was 28.43 % (44.17) and the Δ SNR became 2.25 dB (1.83). Figure 6.26 shows an example output of the algorithm when using the GTC selection technique.

For the EEG data the one level technique generated a λ of 50.17 % (36.15) and a Δ SNR of 7.76 dB (3.86). These values again increased when using the two level artifact removal method. The calculated λ was 52.37 % (26.23) and Δ SNR was 8.25 dB (3.87) when using the GTC selection technique. The values dropped slightly when using the components autocorrelation to select the artifact components with the Δ SNR value becoming 7.62 dB (4.43) and the λ value becoming 51.06 % (37.58). Finally removal of the artifact components based on the Hurst exponent produced a λ value of 23.53 % (40.31) and a Δ SNR value of 4.71 dB 4.93). Figure 6.27 shows the output of the algorithm when employed on contaminated EEG data.

6.7.6 EEMD-CCA

Finally, the novel EEMD-CCA algorithm was also run on the fNIRS and EEG test datasets. When using just the single level artifact selection method on the fNIRS data, the algorithm produced a Δ SNR of 2.75 db (2.03) and a 40.06 % (49.06) increase in correlation. These values increased to 49.38 % (48.71) for λ and 3.60 dB (2.14) for Δ SNR when removing the artifacts both after the EEMD and the CCA stage using the GTC selection technique, and an example output can be seen in Figure 6.28. When using the autocorrelation of the components to select the artifact components the average λ value was calculated as 34.05 % (48.81) and the Δ SNR was 2.44 dB (1.77).

A plot of the output of the EEMD-CCA algorithm when applied to the contaminated EEG data can be seen in Figure 6.29. When only removing the artifact components after the CCA algorithm the average λ value was calculated to be 50.01 % (37.06) and the average Δ SNR over all trials was calculated as 8.16 db (4.37). The algorithm performed better when the artifact components were removed after each stage using the GTC selection technique ($\lambda = 51.84$ % (36.42) and Δ SNR = 8.19 dB (3.82)). Removing

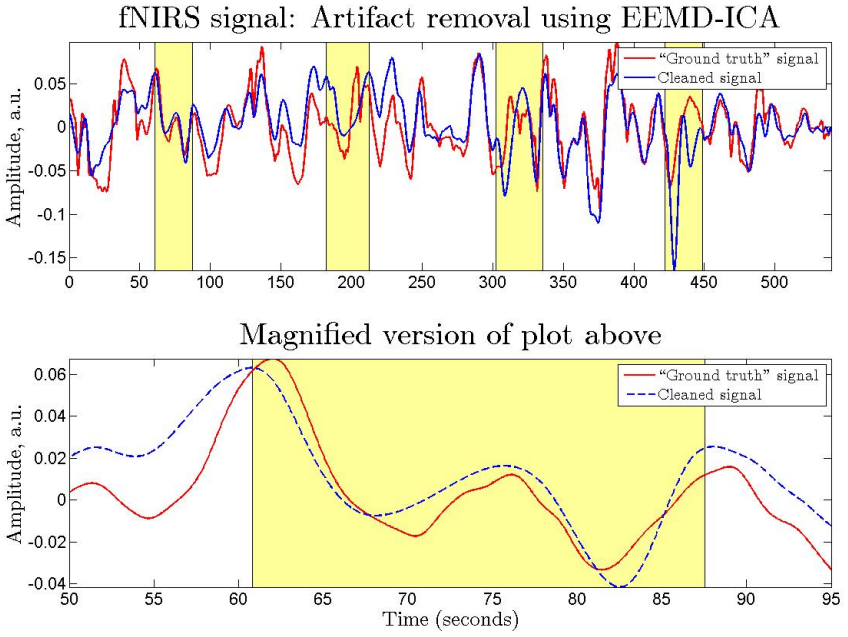

FIGURE 6.26: Example fNIRS trial showing cleaned signal following artifact removal using EEMD-ICA.

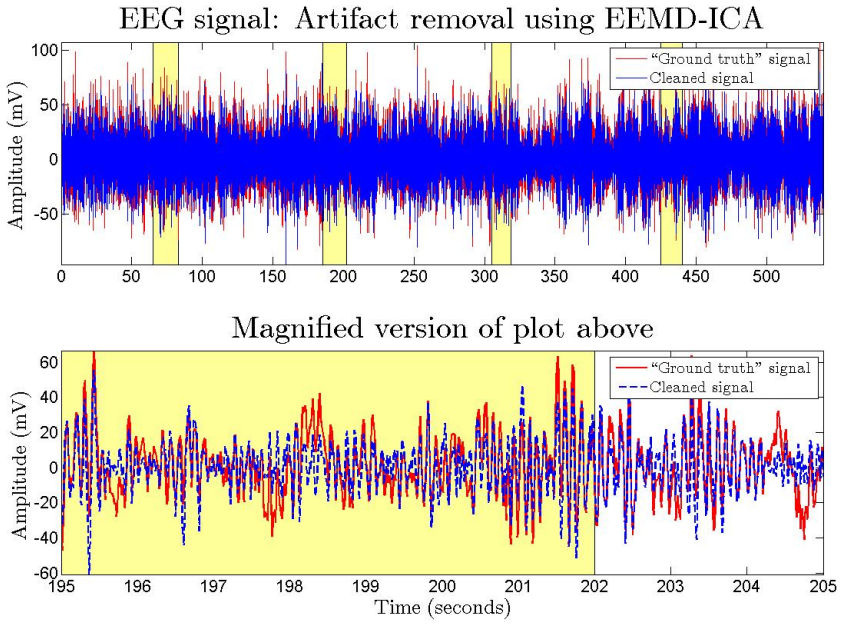

FIGURE 6.27: Example EEG trial showing cleaned signal following artifact removal using EEMD-ICA.

the components based on their autocorrelation was seen to perform well for the EEMD-CCA algorithm with the technique producing a λ score of 51.22 % and 7.61 dB (4.43) for the increase in Δ SNR. Finally, choosing the components to remove depending on their corresponding Hurst exponent produced a λ value of 23.16 % (42.21) and an increase in

Δ SNR of 4.62 dB (5.02).

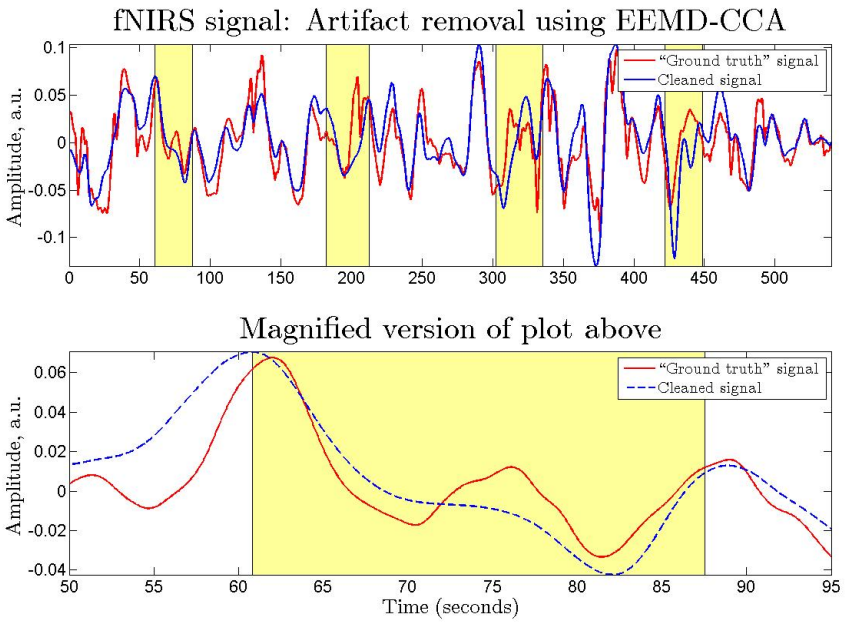

FIGURE 6.28: Example fNIRS trial showing cleaned signal following artifact removal using EEMD-CCA.

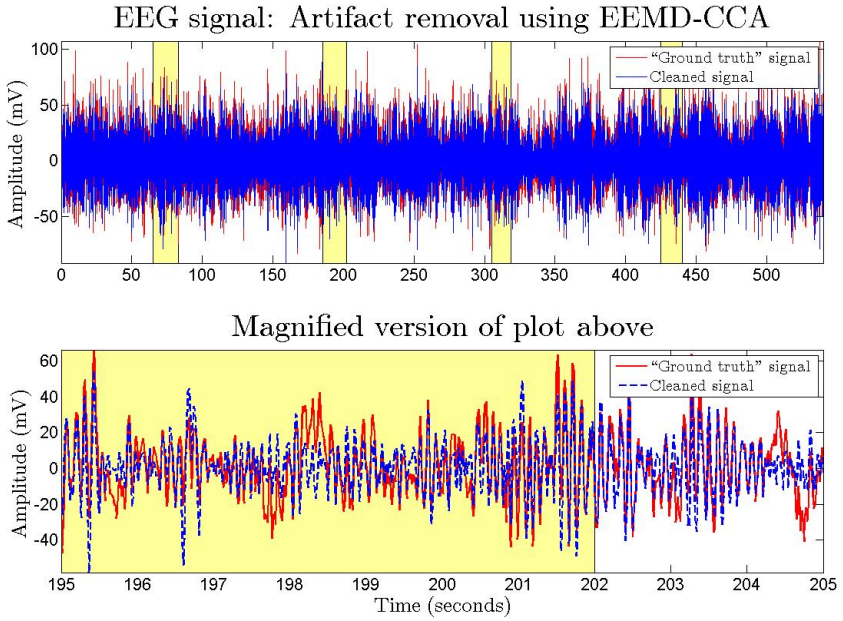

FIGURE 6.29: Example EEG trial showing cleaned signal following artifact removal using EEMD-CCA.

The results presented in this section are summarised in Table 6.1 and will be analysed and discussed in the following section. The results of the techniques when employed solely on the epochs contaminated with artifacts are presented in Table 6.2. A final

comparison between these two stage artifact removal techniques and the single stage techniques presented in Chapter 5 will also be presented which details the best techniques to employ for given situations.

6.8 Discussion and Conclusion

The previous discussion in Chapter 5 presented a comparison and evaluation of the single stage artifact removal techniques detailed in that chapter. This discussion section will expand on that by initially providing an evaluation and comparison of the two stage techniques, using the real and simulated data, followed by an overall comparison and discussion of all of the techniques detailed in the thesis. All of the techniques analysed in this chapter are known as two stage techniques as they each require a method of identifying the artifact components from the separated or decomposed signals. This requirement necessitates the use of an additional algorithm or function and a discussion of the findings of which technique is best for the tested algorithms is also provided.

The wavelet transform requires that the mother wavelet to be used must be chosen prior to the employment of the technique. This requirement restricts the transform slightly compared to some of the other analysed techniques in that the technique is not adaptive to the data. However with the correct mother wavelet chosen, the wavelet transform performs very well for both the fNIRS and EEG data with a lambda value of 43.63 % and 55.25 % respectively. This value obtained when employed with the EEG data approximately equals the best result obtained by any of the two stage techniques. This trend continues when analysing the results obtained when the techniques are employed only on the epochs of contaminated data. Here the λ value for the EEG data rises to 87.76 % and the Δ SNR value is calculated as 10.02 dB. This result, in addition to the low computational time of 0.39 seconds (1.48) as can be seen from Figure 6.17 makes it a very useful method in the artifact removal domain. When selecting the artifact components to remove, the GTC selection technique will always perform the best as specified in Section 4.7. However the autocorrelation function and hurst exponents both provided comparable results to this GTC selection technique with the autocorrelation function providing approximately equal values in terms of λ.

The EMD technique was analysed so as to verify the requirement for the ensemble version of the algorithm. The EMD is an adaptive algorithm in that its IMF are determined straight from the data. Therefore no a priori information is required prior to employing the algorithm. As expected, the EMD algorithm did not provide good results

TABLE 6.1: Percentage reduction in artifact (λ) (Equation 4.8) and the Δ SNR (Equation 4.7) for each two stage artifact removal technique applied to the fNIRS and EEG data (with corresponding standard deviations shown in brackets).

		Wavelet GTC	Wavelet Rxx	Wavelet Hurst	EMD	EEMD GTC	EEMD Rxx	EEMD Hurst
fNIRS	λ	43.63 % (48.32)	32.68 % (51.91)	- -	18.97 % (27.38)	46.95 % (48.68)	32.49 % (45.41)	- -
	ΔSNR	3.05 dB (2.15)	2.57 dB (2.13)	- -	2.05 dB (1.46)	3.31 dB (2.21)	2.38 dB (1.63)	- -
EEG	λ	55.25 % (35.43)	50.98 % (40.34)	51.26 % (39.15)	43.29 % (31.19)	52.24 % (36.34)	46.47 % (46.62)	18.65 % (44.10)
	ΔSNR	8.80 dB (4.01)	**8.89 dB** (**3.74**)	8.70 dB (3.98)	7.89 dB (3.89)	8.35 dB (4.00)	8.72 dB (3.70)	5.84 dB (3.98)

		W-ICA 1 Level GTC	W-ICA GTC	W-ICA Rxx	W-ICA Hurst	W-CCA 1 Level GTC	W-CCA GTC	W-CCA Rxx	W-CCA Hurst
fNIRS	λ	30.54 % (41.03)	43.61 % (48.10)	33.55 % (51.32)	- -	43.64 % (48.29)	37.30 % (52.17)	33.26 % (51.54)	- -
	ΔSNR	2.54 dB (2.12)	3.03 dB (2.17)	2.51 dB (2.17)	- -	3.06 dB (2.16)	2.77 dB (2.17)	2.54 dB (2.15)	- -
EEG	λ	**55.55 %** (**35.00**)	55.39 % (35.19)	52.80 % (36.71)	52.69 % (36.73)	55.26 % (35.29)	55.25 % (35.43)	52.80 % (36.71)	52.59 % (36.78)
	ΔSNR	8.34 dB (3.40)	8.82 dB (3.99)	8.73 dB (4.03)	8.21 dB (4.55)	8.74 dB (3.94)	8.80 dB (4.01)	8.73 dB (4.03)	8.17 dB (4.56)

		EEMD-ICA 1 Level GTC	EEMD-ICA GTC	EEMD-ICA Rxx	EEMD-ICA Hurst	EEMD-CCA 1 Level GTC	EEMD-CCA GTC	EEMD-CCA Rxx	EEMD-CCA Hurst
fNIRS	λ	37.21 % (50.45)	43.43 % (49.89)	28.43 % (44.17)	- -	40.06 % (49.06)	**49.38 %** (**48.71**)	34.05 % (48.81)	- -
	ΔSNR	2.91 dB (2.33)	3.32 dB (2.26)	2.25 dB (1.83)	- -	2.75 dB (2.03)	**3.60 dB** (**2.14**)	2.44 dB (1.77)	- -
EEG	λ	50.17 % (36.15)	52.37 % (36.23)	51.06 % (37.58)	23.53 % (40.31)	50.01 % (37.06)	51.84 % (36.42)	51.22 % (37.48)	23.16 % (42.21)
	ΔSNR	7.76 dB (3.86)	8.25 dB (3.87)	7.62 dB (4.43)	4.71 dB (4.93)	8.16 dB (4.37)	8.19 dB (3.82)	7.61 dB (4.43)	4.62 dB (5.02)

TABLE 6.2: Percentage reduction in artifact (λ) (Equation 4.8) and the Δ SNR (Equation 4.7) for each two stage artifact removal technique applied to the fNIRS and EEG data (with corresponding standard deviations shown in brackets). Data shows results when artifact removal techniques employed only during epochs of detected movement. (-) signifies test was not carried out using that particular technique.

		Wavelet GTC	Wavelet Rxx	Wavelet Hurst	EMD	EEMD GTC	EEMD Rxx	EEMD Hurst
fNIRS	λ	48.51 % (54.28)	39.82 % (59.10)	- -	32.68 % (47.05)	45.48 % (51.95)	32.87 % (45.15)	- -
	ΔSNR	3.04 dB (2.19)	2.64 dB (2.25)	- -	2.30 dB (1.82)	3.05 dB (2.11)	2.34 dB (1.63)	- -
EEG	λ	87.76 % (39.62)	87.21 % (34.08)	80.94 % (37.50)	78.27 % (37.82)	**87.99 %** (**40.11**)	87.92 % (33.14)	53.83 % (44.32)
	ΔSNR	10.02 dB (4.80)	10.22 dB (4.05)	9.72 dB (4.71)	9.13 dB (4.40)	9.66 dB (4.67)	**10.39 dB** (**3.85**)	6.69 dB (4.62)

		W-ICA 1 Level GTC	W-ICA GTC	W-ICA Rxx	W-ICA Hurst	W-CCA 1 Level GTC	W-CCA GTC	W-CCA Rxx	W-CCA Hurst
fNIRS	λ	40.44 % (53.79)	49.05 % (54.31)	39.19 % (59.54)	- -	48.54 % (54.38)	43.93 % (58.47)	39.63 % (59.23)	- -
	ΔSNR	2.62 dB (2.24)	3.03 dB (2.20)	2.57 dB (2.31)	- -	3.04 dB (2.19)	2.81 dB (2.25)	2.62 dB (2.27)	- -
EEG	λ	80.35 % (37.16)	84.94 % (39.39)	84.29 % (39.49)	77.60 % (43.53)	83.67 % (39.02)	84.76 % (39.62)	84.29 % (39.49)	76.86 % (43.64)
	ΔSNR	9.48 dB (4.04)	10.04 dB (4.78)	9.87 dB (4.70)	9.28 dB (5.33)	9.90 dB (4.71)	10.02 dB (4.80)	9.87 dB (4.70)	9.23 dB (5.35)

		EEMD-ICA 1 Level GTC	EEMD-ICA GTC	EEMD-ICA Rxx	EEMD-ICA Hurst	EEMD-CCA 1 Level GTC	EEMD-CCA GTC	EEMD-CCA Rxx	EEMD-CCA Hurst
fNIRS	λ	43.08 % (55.86)	45.93 % (51.56)	33.09 % (50.85)	- -	43.56 % (50.42)	**51.00 %** (**52.44**)	33.86 % (48.85)	- -
	ΔSNR	2.93 dB (2.39)	**3.13 dB** (**2.21**)	2.26 dB (1.91)	- -	2.80 dB (2.08)	3.09 dB (2.12)	2.39 dB (1.77)	- -
EEG	λ	77.83 % (42.36)	80.76 % (39.89)	78.11 % (46.43)	43.87 % (53.36)	86.69 % (42.62)	86.02 % (39.79)	78.34 % (46.16)	41.46 % (53.40)
	ΔSNR	9.12 dB (4.64)	9.55 dB (4.56)	9.03 dB (5.31)	5.41 dB (5.81)	9.61 dB (5.06)	9.48 dB (4.50)	9.06 dB (5.28)	5.33 dB (5.97)

for either the fNIRS or EEG data with the results obtained through use of the algorithm only during epochs of movement again lower then those obtained using either the EEMD algorithm or the wavelet transform. The average time taken for the EMD algorithm to run was calculated as 0.76 seconds (0.25) for the fNIRS data and 3.37 seconds (0.4) when employed on the EEG data.

The EEMD algorithm performs well compared to the rest of the techniques analysed in this chapter. The λ value obtained for the fNIRS data is second only to that obtained when using EEMD-CCA with the value for the EEG data only 3 % less than for the wavelet transform. The value obtained for the EEG data when employing the EEMD algorithm only during movement epochs improves considerably and becomes the top score for λ at 87.99 %. Further the use of the autocorrelation of the components to aid in the selection of the artifact components provides very similar results and also provides the largest Δ SNR for EEG for all techniques at 10.39 dB. The use of the Hurst exponent performs poorly for the EEMD data. As an ensemble of 5 is used for the algorithm, the computational time is longer than the EMD technique and was calculated as 2.56 seconds (0.15) on average for the fNIRS data and 16.86 seconds (0.72) for the EEG data.

The wavelet-ICA combination was first presented by Azzerboni *et al.* [9] and was tested to determine if the addition of the ICA algorithm to the wavelet decomposition technique presented any improvement to the efficacy of the technique. Results for the technique show that the combination of the techniques does not generate any major advantage. The results for both λ and Δ SNR are either approximately the same or slightly worse then those that can be obtained using the wavelet transform alone. This is true whether analysing the results generated when the algorithm was employed over the full signal or solely over the epochs of contaminated data. Further, the additional computational time of the ICA algorithm as can be seen from Figure 6.17 would suggest that the addition if the ICA algorithm to the wavelet technique does not provide significant enough value to be employed.

Similar conclusions as those specified above for the wavelet-ICA algorithm are relevant when evaluating the wavelet-CCA algorithm. Again, the addition of the CCA algorithm to the wavelet decomposition method does not provide any significant improvement in efficacy when removing artifacts of this type. However, one point to note is that (similar to the W-ICA technique) the selection of the artifact components depending on their autocorrelation function provides results comparable to those obtained using the GTC selection technique.

The combination of the EEMD with the ICA algorithm fails to greatly improve the results obtained using the EEMD algorithm alone. However, the results again show that the use of the Hurst exponent to select the artifact components does not work for the EEMD based algorithms as the determined λ value is almost half that detected using the GTC selection technique.

The novel EEMD-CCA algorithm does however provide results which are significantly improved on those obtained using the other analysed two stage algorithms when employed on the fNIRS data. When analysing the full signal the EEMD-CCA technique produces a λ value 6 % greater than anything achieved using the wavelet based techniques and 3 % better than the EEMD technique. This improvement can also be seen when viewing the Δ SNR values. When reducing the span of the algorithm and focusing on the epochs of movement data, the EEMD-CCA algorithm again has the best results for the fNIRS data with a λ value of 51.00 %. Unlike the ICA algorithm, the addition of the CCA algorithm to the EEMD algorithm provides very little increase in computational cost as the average computational time of the CCA algorithm for fNIRS and EEG is 0.03 seconds (0.01) and 0.19 seconds (0.28) respectively and thus can be implemented without major concern for the additional computational load.

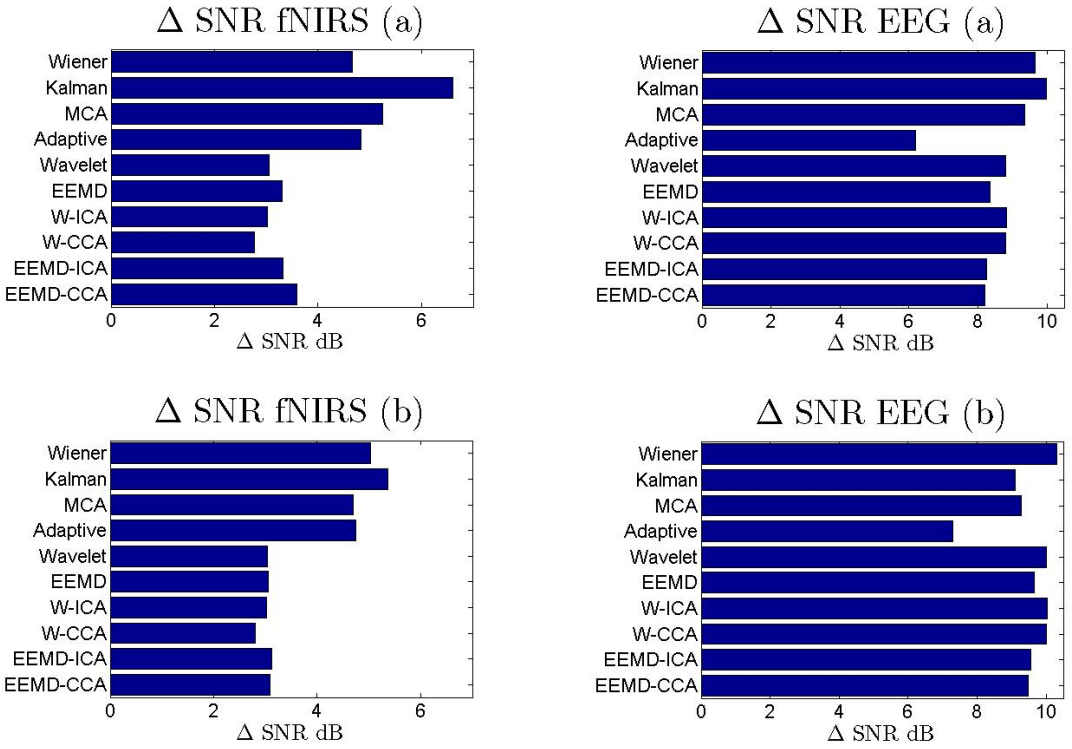

FIGURE 6.31: Improvement in signal-to-noise ratio (Δ SNR, Equation 4.7) due to the use of the multiple artifact removal techniques. (a) Results obtained when the algorithms were employed over the full fNIRS/EEG signals. (b) Results when the algorithms are employed only during epoch containing contaminating artifacts. Δ SNR still is calculated over the full signal.

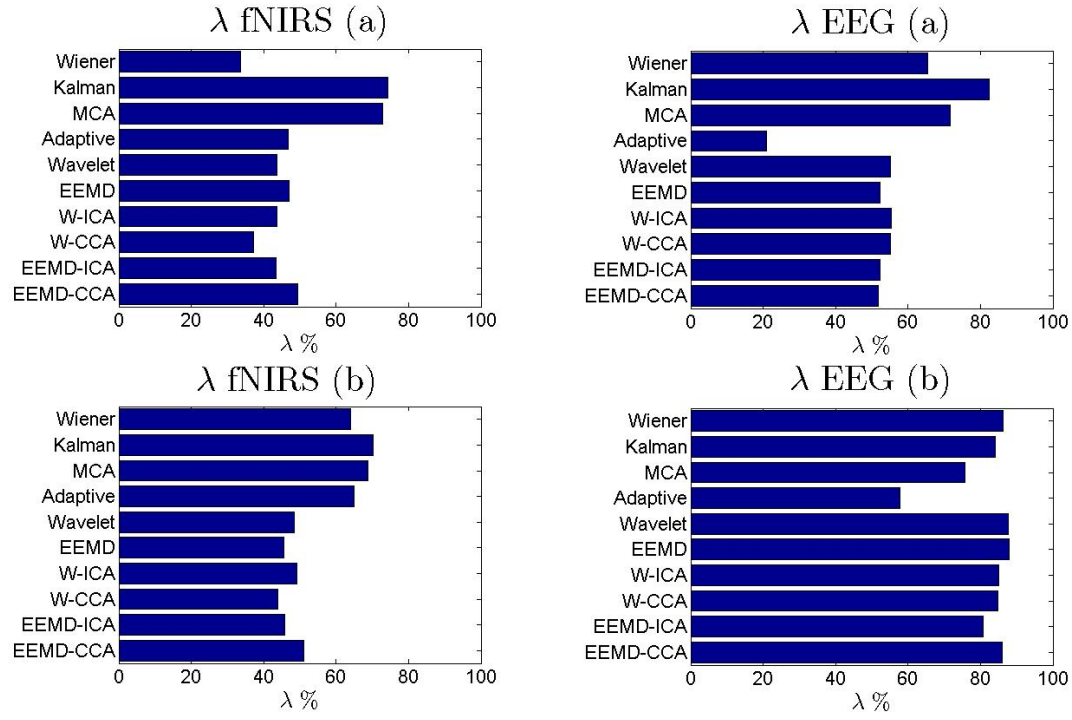

FIGURE 6.30: Percentage improvement in correlation (λ, Equation 4.8) due to the use of the multiple artifact removal techniques. (a) Results obtained when the algorithms were employed over the full fNIRS/EEG signals. (b) Results when the algorithms are employed only during epoch containing contaminating artifacts. λ still is calculated over the full signal.

The bar charts presented in Figure 6.30 and Figure 6.31 provide an overview of the results shown in Table 5.1, 5.2, 6.1 and 6.2. Figure 6.32 provides a bar chart of the λ and Δ SNR values obtained when employing the simulated data. The results obtained when using the two stage techniques on the simulated fNIRS and EEG data are similar to those shown above. Although the determined values for λ and Δ SNR may have differed between the use of real or simulated data (as expected), the improved results of the EEMD-CCA algorithm compared to the other tested techniques when employed on the fNIRS data still hold true. Further, the wavelet transform and its associated combinations (W-ICA, W-CCA) have a higher λ value then their corresponding EEMD based methods as was shown with the real data. The high correlation between the results obtained between the real and simulated data further proves that the methodology used to record the novel dataset succeeds in providing an accurate representation of the true contamination of the signals.

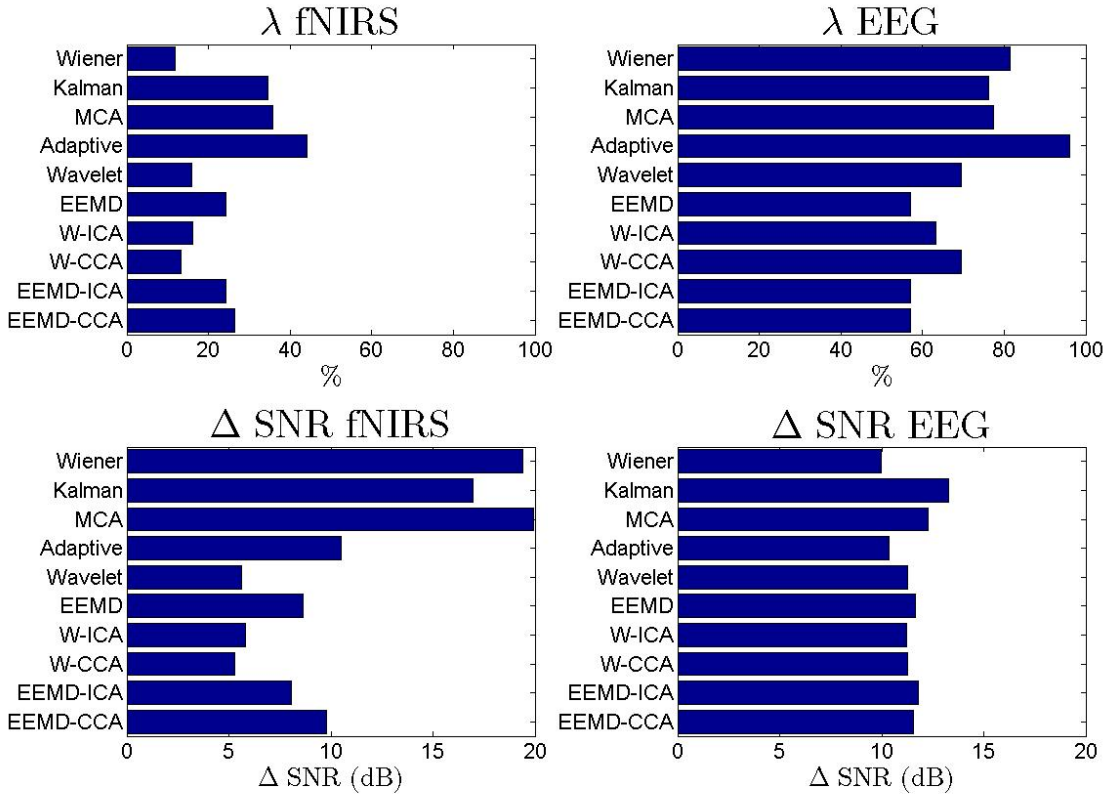

FIGURE 6.32: Calculated λ and Δ SNR values for the simulated fNIRS and EEG data.

When employing all of the tested techniques (both single stage and two stage) on the contaminated fNIRS data, when no reference signal is available, the MCA technique delivers the best results in terms of λ while also outperforming all other techniques for Δ SNR. As was shown in Figure 4.7 when artifacts are present in the recorded fNIRS signal the Hb and HbO components become more correlated causing the trajectory plot to become distorted. Figure 6.33 provides an example output of the affect that utilising

the MCA algorithm has on the corresponding HbO and Hb values of the fNIRS. It can be observed that the use of the MCA algorithm has succeeded in removing the vast majority of the contaminating artifact. It should also be remembered that the Kalman filter results shown above are for the adaptive Kalman filter where a reference signal is required. When the reference signal is available the other single stage techniques increase their performance and all outperform each of the two stage techniques. In this situation the Kalman filter has the best λ value but is very closely followed by the MCA algorithm.

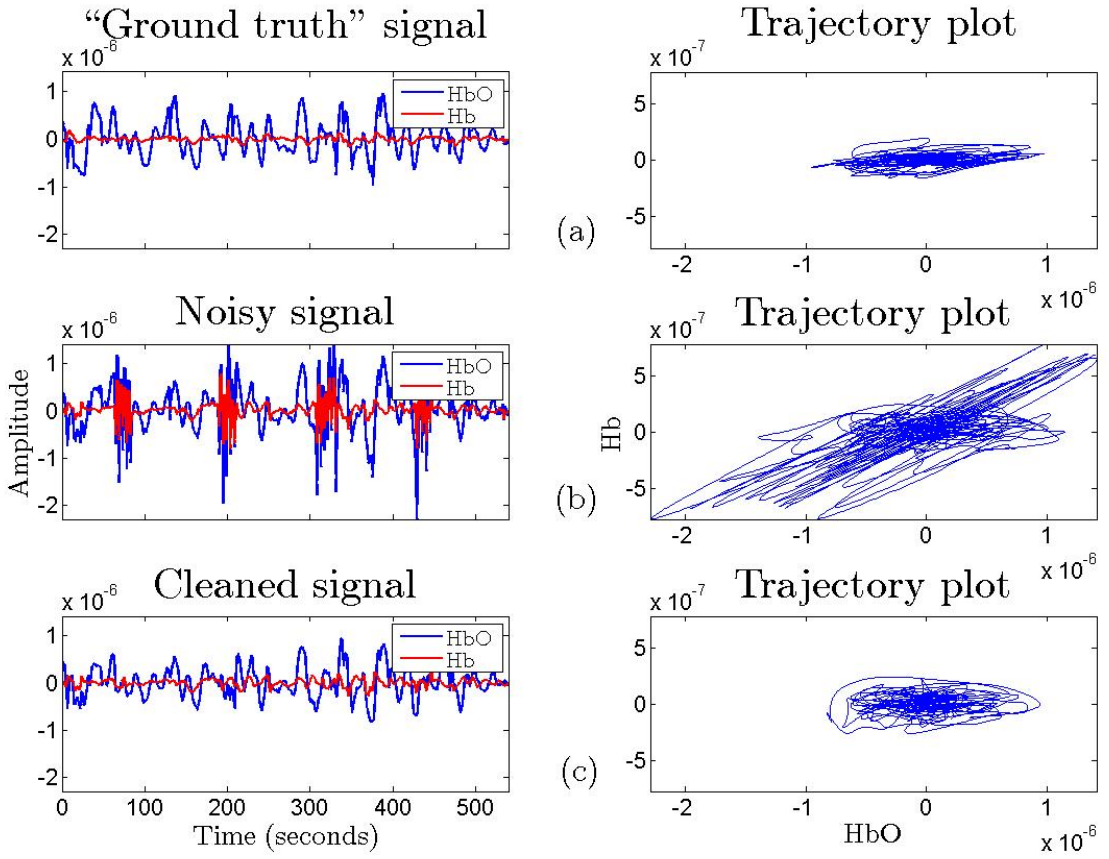

FIGURE 6.33: Improvement in signal quality can also be observed using a trajectory plot. (a) "Ground truth" signal (b) Noisy fNIRS signal contaminated with motion artifact (c) Cleaned signal using the MCA technique.

It has been stated previously that the MCA algorithm requires that the signal dictionaries be chosen prior to the employment of the technique and therefore if additional, un-characterised artifacts contaminate the signal they may not be separated from the desired signal. If the artifact type is unknown and a reference signal is not available, the two stage techniques may perform best with the EEMD-CCA technique currently the highest performing algorithm when dealing with fNIRS data.

When analysing the EEG data when no reference signal is available the MCA algorithm again performs to the highest standard in terms of λ value with the Wiener filter also performing well. The MCA algorithm generates a new correlation value of 0.71 following the removal of the artifact (up from 0.396). These two techniques also perform well in terms of the Δ SNR values with the Wiener filter generating a 9.66 dB improvement. When a reference signal does become available the two stage techniques efficacy improves greatly with both the wavelet transform and the EEMD technique obtaining over 87 % improvement in correlation following the use of the techniques. Although these techniques do require the reference signal to become comparable to the single stage techniques, they do not require any *a priori* information. The choice of the artifact selection technique to use is important however.

When analysing the signals using the EEMD, EEMD-ICA or EEMD-CCA techniques the Hurst exponent performs very poorly and should not be used to determine the artifact components in the signal. The choice of components based on their autocorrelation however does provide adequate results when compared to the results obtained when using the GTC selection technique with only an average reduction in λ of 14.56 % for the fNIRS data and 2.02 % for the EEG data. When using the wavelet based techniques both the Hurst exponent and the autocorrelation function performed well. The λ value obtained using the Hurst exponent was 5.24 % and for the autocorrelation based function the reduction was 1.83 %, thus proving that for both the EEG and the fNIRS datasets analysed in this thesis the autocorrelation based function should be used to determine the artifact components in the situations where the "ground truth" signal is not available.

Chapter 7

Case Study

Over the past number of chapters this thesis first described a novel methodology which allows for the simultaneous recording of both a "ground truth" and artifact corrupted signal. Two unique benchmark datasets were recorded with this methodology, one for fNIRS and one for EEG. The main advantage of these datasets is that they permit the accurate measurement of the efficacy of any analysed artifact removal technique. Using these unique datasets, a number of single stage and two stage techniques were then evaluated in Chapters 5 and 6 and the best artifact removal techniques to employ to remove the contaminating motion artifact were determined. However, the determined techniques can only be deemed the best when the form of the artifact is similar to that created during the data acquisition (artifacts due to the intermittent movement of the recording optodes or electrodes), as specified in Section 4.2.

In this chapter a case study is presented in which ambulatory EEG data, intermittently corrupted with artifact, is recorded. Over a number of recordings a number of distinct motion artifact signals are produced, ranging from head movement while seated to full body movement while running. For each of the presented artifact types the most proficient algorithms tested in Chapters 5 and 6 are used to try to remove the varying levels of contamination. In doing so, the techniques can be tested with real ambulatory data for a number of the most common artifacts present in recordings performed outside of the hospital environment.

The remainder of the chapter is organised as follows: Firstly, the ambulatory EEG measuring device used to record the data will be detailed, including the positions of the recording electrodes. Following this, a description is given of the various subject head and body movements which were undertaken to generate the varied artifact types. For each of the tested artifacts, sample plots are presented to illustrate the corresponding

contamination of the EEG data. The reasons for testing each particular type of movement will also be detailed. Next, a description of the metrics and figures that will be used to test the efficacy of the techniques will be described. The efficacy metrics used in the previous chapters cannot be employed in this chapter as the "ground truth" signal is no longer available. Finally, a number of the most proficient algorithms already tested will be employed and their outputs and results will be described.

7.1 EEG Measurement System

The EEG data was recorded using the Starstim® (Neuroelectrics, Barcelona, Spain) measurement system. This is a wireless recording system capable of monitoring 8 channels of EEG concurrently. The system uses Silver-Silver-Chloride (Ag-AgCl) electrodes similar to those employed when recording using the BioSemi ActiveTwo system described in Chapter 4. In addition to these 8 measurement electrodes, there are also 2 additional electrodes used, namely the driven right leg (DRL) and common mode sense (CMS) electrodes. The purpose of these additional electrodes has been previously described in Section 4.1.2. The measurements are recorded with 24 bit resolution (0.05 μV) and are sampled at 500 Hz.

All the recorded data is stored on an on-board SD memory card which is housed in a control box. This control box contains the battery pack of the system (allowing for up to 8 hours of EEG recording), the connectors to the EEG electrodes, the SD card, a Bluetooth communication module and a tri-axial accelerometer. The control box is connected to the cap at the rear of the head using velcro as can be seen in Figure 7.1. The overall weight of the control box is only 65 grams which ensures that the system can be easily carried by the user without any restriction to movement. The included Bluetooth device allows for consistent communication between the monitoring device and the host computer, however as previously mentioned, the data can also be stored on the SD card for later analysis. The accelerometer device contained in the control box is orientated to allow for accurate measurement of the movement of the device in the median sagittal, the transverse and the frontal planes. This availability of the accelerometer signal allows for the tagging of the data as well as allowing for the additional use of a number of the techniques described in the thesis which require a reference signal. This StarStim system is also capable of transcranial current stimulation, however this property was not employed during the described recording.

The cap used to secure the control box and the electrodes to the scalp can be seen in Figure 7.1. This cap is made from Neoprene and thus is highly flexible allowing it

FIGURE 7.1: StarStim® ambulatory EEG recording system.

to be easily applied and secured to the head. As stated previously, the EEG control box is then secured to the rear of the head using velcro. The 8 recording electrodes were positioned at locations AF7, F7, T7, P7, O2, PO8, C2 and C4. These locations can be seen from Figure 7.2 which shows the 10-20 electrode placement including the intermediate 10 % electrode positions. The electrode locations were chosen in order to represent the various cortical areas of the brain. The CMS electrode was place at the Cz position and the DRL was secured to the mastoid.

In addition to the recording of the EEG data a number of supplementary data files were also chronicled. Firstly, each recording was videoed to allow for a validation of the tagging of the data post recording and secondly an external trigger was employed to mark the start and end of each different epoch of movement. This trigger value was sent using TCP/IP over Bluetooth to the control box allowing for simple data tagging during analysis.

7.2 Artifact Generation Protocol

In order to test the artifact removal techniques described in this thesis with ambulatory recorded EEG data, a number of different types of contaminating motion artifacts were required to be generated. The varying forms of the induced artifacts were chosen so as to reflect those which are most commonly recorded in the ambulatory recording domain. These differing forms of artifacts can be grouped into two separate categories.

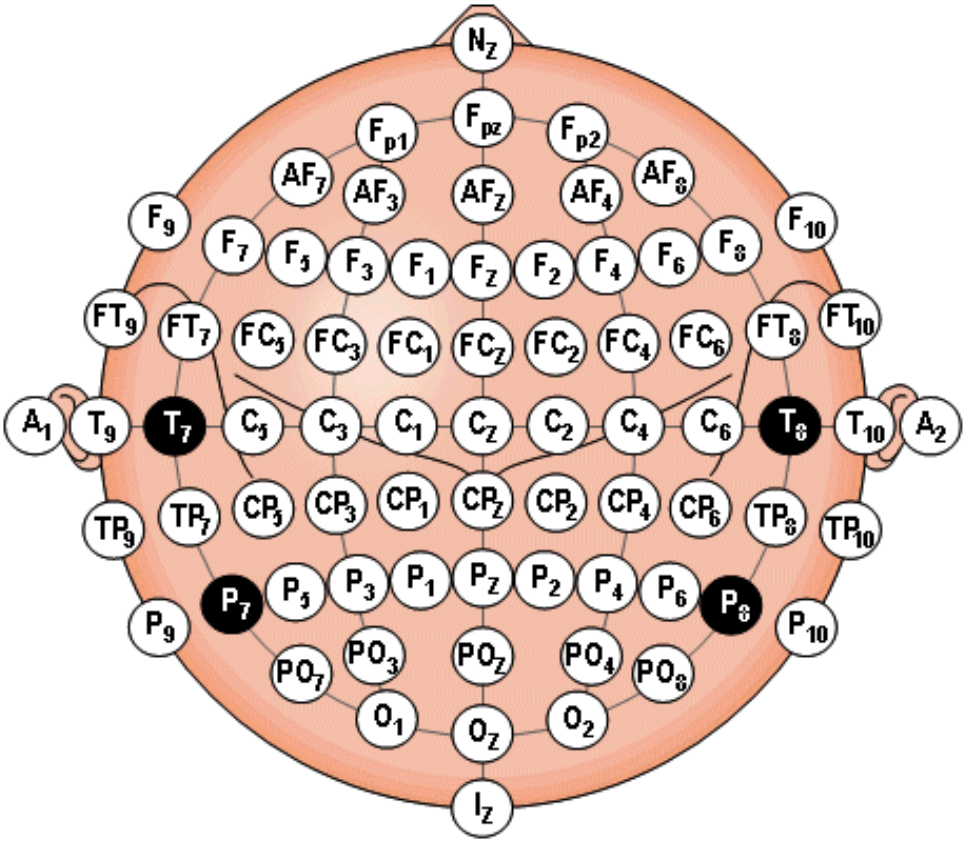

FIGURE 7.2: Location and nomenclature of the intermediate 10 % electrodes of the 10-20 system, as standardised by the American Electroencephalographic Society [120].

The first category comprised of movements of the subjects head or facial muscles. O'Regan *et al*. [147] detailed the recording of EEG data during 5 different artifact generating movements. These movements included shaking of the head (right and left), nodding of the head (forward and backward), rolling the head (around the axis of the neck), clenching the jaw muscles and the raising and lowering of the eyebrows. As these movements accurately simulated some of the major motion artifacts detected in ambulatory EEG data, they were each analysed for the case study. These movements were recorded while in a seated position and were approximately 30 seconds in duration each. Each movement was performed twice and there was a 30 second epoch of no movement between each ensuing movement. A lengthy recording of 40 mins was also performed in which the subject performed routine activities at a computer. No restrictions were imposed on the movement of the subject during recording aside from that they should remain in a seated position.

The second group of generated contaminating artifacts were due to the combined movement of both the subjects body and head. During each of these trials the subject was asked to perform a task which required full body movement. This, again, was to reflect the normal movements of a subject whose EEG was being monitored in an

ambulatory setting. The first trial consisted of the subject performing the standard sit-to-stand task [50]. This task is commonly used to determine the mobility and muscle power of a subject. During this task the subject is asked to go from a seated position to a fully standing position before returning to the seat. The time taken to perform the task can then be used to determine the patients mobility. In order to lengthen the duration of the induced artifact, the subject was asked to perform three sit-to-stand movements consecutively. Four trials were recorded. The second movement based trial consisted of the also commonly employed timed-up and go (TUG) test. During this test the subject is asked to rise from a chair, walk three meters, turn around, walk back to the chair and then sit down. This study is often used to test a subjects mobility as well as their static and dynamic balance [66]. In addition to the two common tests described, data was also recorded for: 1) a 4 minute tour of a building which included activities such as passing through doors and climbing stairs, and 2) 17 minutes of walking and running on a treadmill. These additional datasets were recorded to represent real long term monitoring of ambulatory EEG.

Table 7.1 summarises the multiple movements used to generate the artifact contaminated data analysed in this chapter.

7.3 Efficacy Metrics

As the "ground truth" signal used to test the efficacy in the previous chapters of the thesis is no longer available, the efficacy metrics employed in this chapter differ slightly. The percentage improvement in correlation (λ) cannot be employed as there is not a true signal with which to compare. However a version of the Δ SNR metric can be employed and is defined as

$$\Delta SNR = 10\ \log_{10}\left(\frac{\sigma^2_{true}}{\sigma^2_{after}}\right) - 10\ \log_{10}\left(\frac{\sigma^2_{true}}{\sigma^2_{before}}\right) \tag{7.1}$$

where σ^2_{true} is the variance of an epoch of data free from movement artifact, σ^2_{before} is the variance of the artifact contaminated data prior to employing the particular artifact removal technique and σ^2_{after} is the variance of the same epoch following the use of the removal technique.

In addition to providing results for the increase in SNR, due to the use of the various artifact removal techniques, example outputs from the techniques, both in the time and frequency domain will be presented showing the effect of the techniques on

TABLE 7.1: The different movements undertaken during ambulatory EEG monitoring case study.

Movement Type	Description	Duration
Shake Head	Move the head from side to side with varying speed	≈ 30 sec
Nod Head	Move the head up and down with varying speed	≈ 30 sec
Roll Head	Roll the head around the axis of the neck. Varying direction	≈ 30 sec
Jaw Clenching	Engage the jaw muscles. Mimic the chewing action	≈ 30 sec
Eyebrow Movement	Raise and lower the eyebrows with varying amplitude and duration	≈ 30 sec
Sit-to-Stand	From a seated position, stand up out of the chair fully before reseating. Perform three times	≈ 15 sec
Timed-Up and Go (TUG)	From a seated position, stand up, walk to a line on the floor, turn around and walk back to the chair and sit down. Walk at regular pace.	≈ 10 sec
Walking	Walk around the department including passing through 6 sets of push/pull doors and 4 flights of stairs	≈ 4 mins
Walking/Running	Treadmill running. Intervals of 1 min rest, 3 mins walking, 3 mins running, 3 mins walking, 3 mins running, 3 mins walking and 1 min of rest.	≈ 17 mins
Working on Computer	General light movement while working at a PC	≈ 40 mins

the morphology of the signals. As increasing the SNR does not guarantee improvement in the quality of the true signal (since $\lim_{\sigma^2_{after}\to 0} 10\ \log_{10}\left(\frac{\sigma^2_{true}}{\sigma^2_{after}}\right) = \infty$), the concurrent evaluation of the techniques using both the time and frequency domain plots is essential.

7.4 Artifact Removal

For the purpose of the case study, 4 of the techniques described previously in the thesis were employed. Namely these techniques were the Wiener filter, morphological component analysis (MCA), wavelet analysis and ensemble empirical mode decomposition (EEMD), all of which were previously shown to perform well when removing motion artifacts from the EEG signal. These 4 techniques were chosen as, between them, they covered the full range of analysed techniques (i.e. filtering, separation; single stage, two stage). The EEG data, recorded as specified in Section 7.2, was separated into epochs of clean artifact free data and epochs of known artifact contamination using the available accelerometer signals. This separation was confirmed using the available video and data tagging information.

Each technique was individually employed on all epochs of contaminated data and the resulting improvement in SNR calculated. Figure 7.3 shows an example of 5 of the artifact contaminated epochs due to the different head movements. Each of the 5 protocols used to generate head movement artifacts were performed twice and as there was 8 channels of EEG recorded this resulted in a total of 16 epochs of contaminated data per movement type.

Figure 7.4 shows the artifacts generated due to the protocols involving full body movement. Again, each protocol was undertaken twice and therefore 16 trials of contaminated data were available for each. In the sections below, an example output of each artifact removal technique is presented for each artifact type and the resulting improvement in SNR is provided. Table 7.2 provides a summary of the determined Δ SNR for each of the techniques.

By analysing Figure 7.3 and 7.4 it can be seen that the generated artifacts seriously degrade the quality of the recorded EEG signals. The artifact signals can also be observed to be very different in nature, with some having a very periodic morphology (i.e. running/walking artifact) while others are more random in nature. This can also be deduced from the frequency domain representation of the signal where the lower frequency components of the artifact signals are observed to have a very high power with respect to the power of the clean epoch.

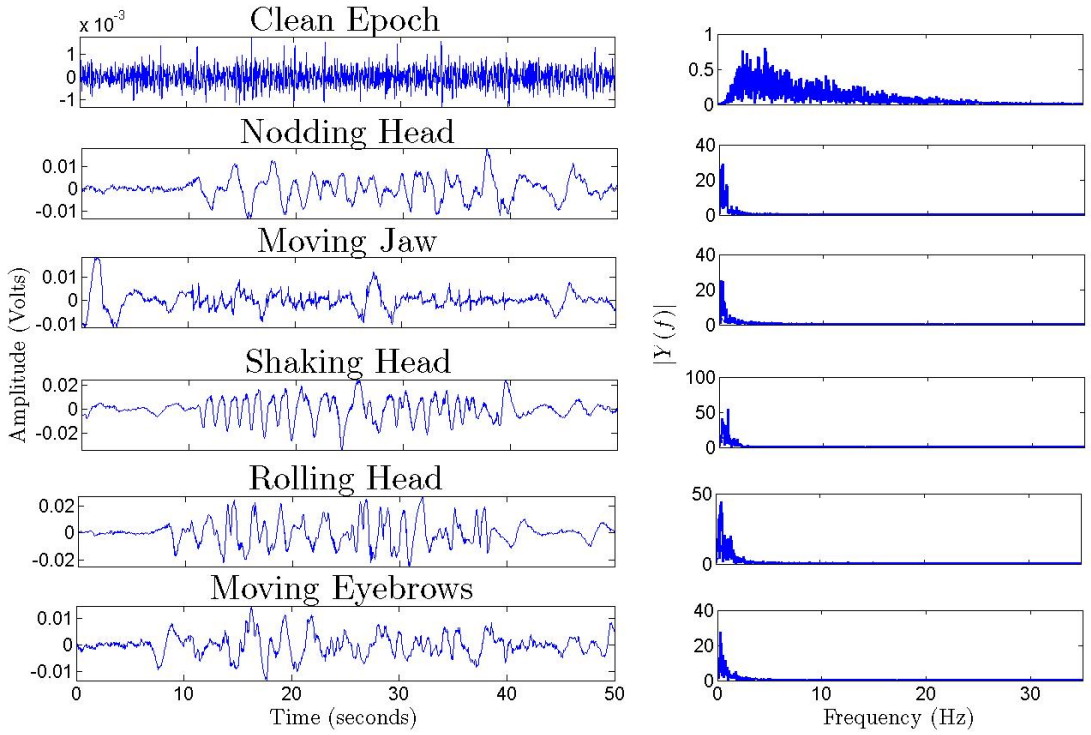

FIGURE 7.3: Example recordings of EEG during the 5 Head movements (Nodding, Jaw movement, Shaking, Rolling and Eyebrow movement) shown in the time and frequency domain.

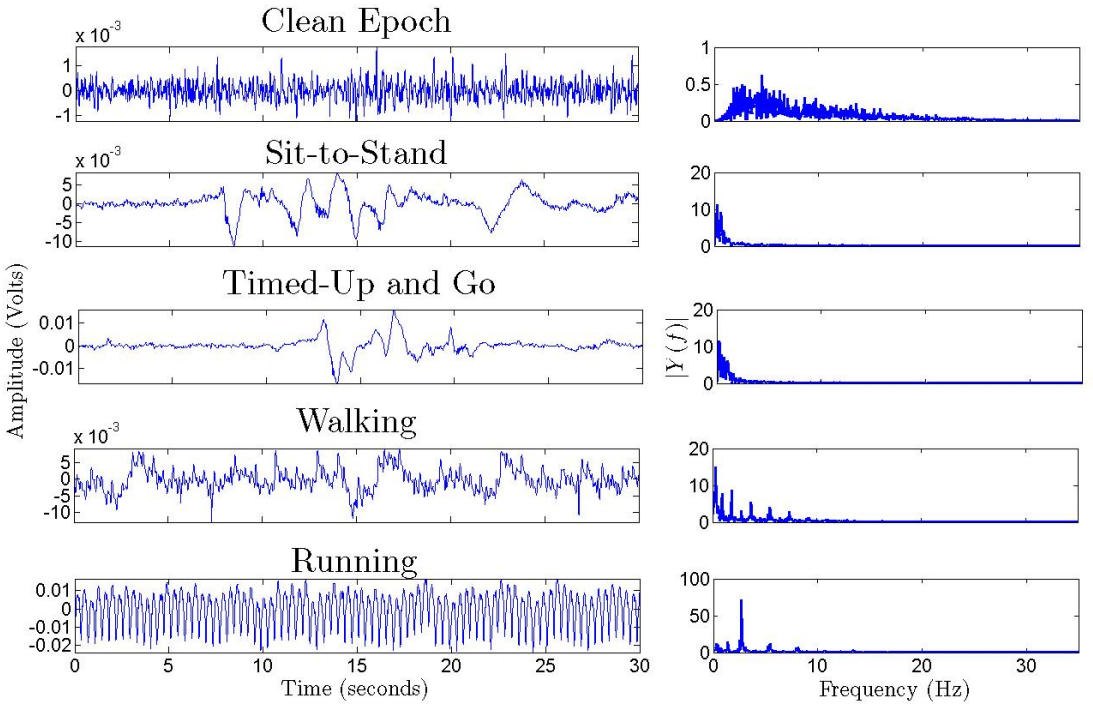

FIGURE 7.4: Example recordings of EEG during the 4 full body movements (Sit-to-Stand, Timed-Up and Go (TUG), Treadmill Walking, Treadmill Running) shown in the time and frequency domain.

7.4.1 Wiener Filter

The Wiener filter was applied as was described in Chapter 5. The PSD of an epoch of known clean data was first calculated. The PSD of the artifact contaminated signal could then be used for each individual trial examined. Using these PSD's the Wiener filter could then be generated, where separate filter coefficients were calculated for each artifact type. Figure 7.5 and 7.6 present example outputs of the filter for the contaminated data shown in Figure 7.3 and 7.4.

As can be seen in Table 7.2, the Wiener filter was highly efficient in removing the power from the noise signal with an average Δ SNR over all artifact types of 18.94 dB. Further, through comparison of the time and frequency domain figures, the artifact removal technique can be deemed proficient at removing the contaminating artifacts. There are, however, some residual artifact components in the "walking" and "running" signals, which can be observed as periodic waves in the time domain and spikes in the frequency domain. Also, the signal power for these two signals is quite low over the known EEG frequencies which could signify a loss in true signal power.

7.4.2 MCA

Prior to the running of the MCA algorithm, the appropriate dictionaries were again required to be chosen as specified in Section 5.5. As the "ground truth" signal was not available, the choice of dictionaries was performed manually for each artifact type. The combinations of dictionaries described in Section 5.5.2 were again analysed and the pair which best separated the artifact from the signal were chosen. When analysing the signals contaminated with the 5 different head movements the optimal dictionaries were determined to be the DCT and ATrou dictionaries. These can be seen to be equivalent to the dictionaries chosen to remove the motion artifact described in Chapter 5. However, when analysing the data contaminated with artifacts due to the movement of the subject, a different pair of dictionaries were optimal. These were the LDCT and LWP dictionaries. The mother wavelet chosen to represent the artifact (as required by the LWP dictionary) was the Daubechies 6 wavelet.

Figure 7.7 presents example outputs from the MCA algorithm for inputs contaminated with artifacts due to the movement of the subjects head. Again the artifact removal algorithm can be observed to perform well as the representation of the signals in both the time and frequency domain closer resemble the clean signal then the original noisy signal. The same conclusion can be taken from the epochs of contaminated data

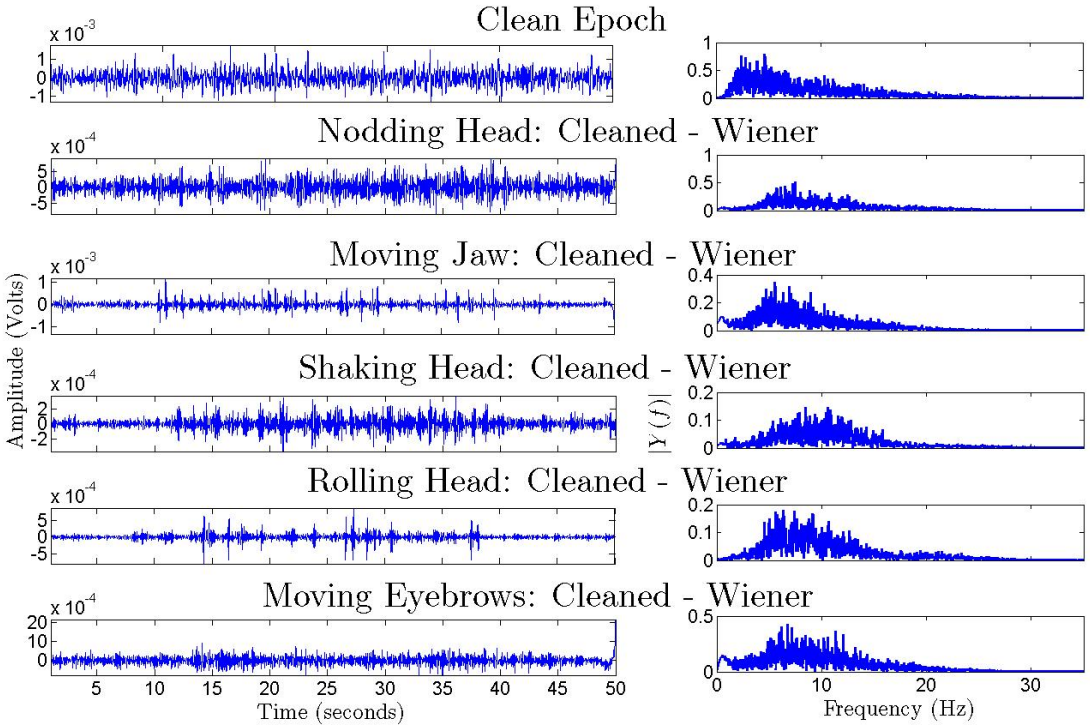

FIGURE 7.5: Artifact removal performed using the Wiener filter on EEG epochs contaminated due to movements of the head.

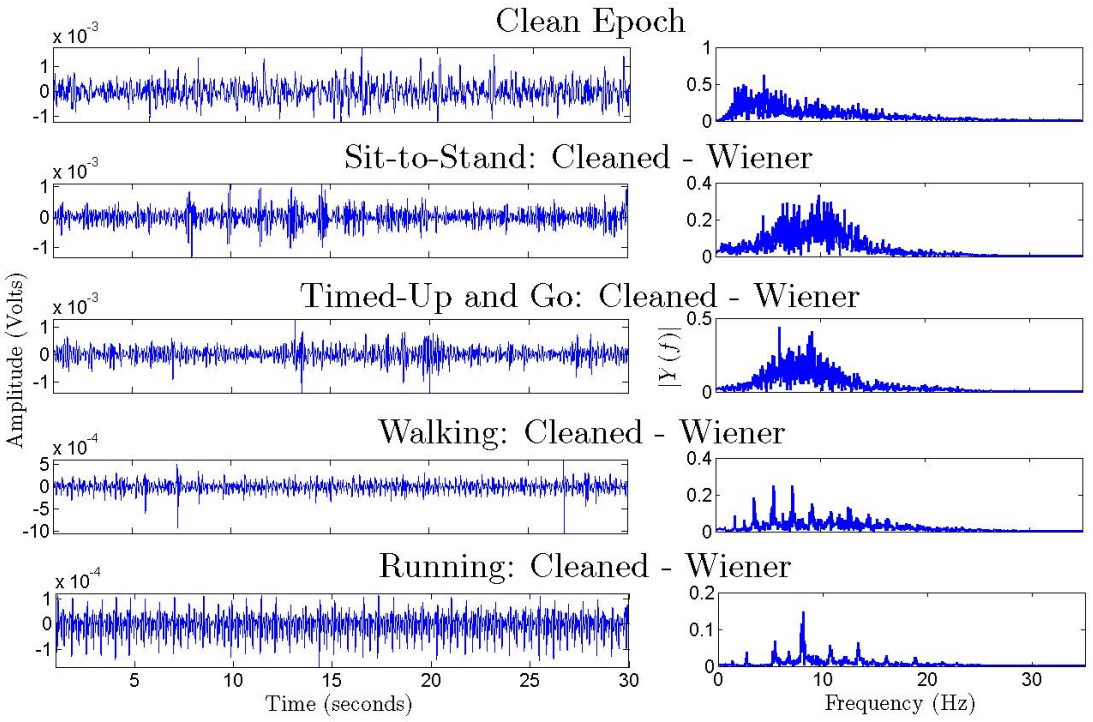

FIGURE 7.6: Artifact removal performed using the Wiener filter on EEG epochs contaminated due to movements of the body.

due to full body movement (Figure 7.8). Unlike when employing the Wiener filter, the "walking" and "running" artifact contaminated signals are not corrupted with periodic artifacts, although they do contain a number of spike artifacts. These could possibly be removed through the use of additional dictionaries. Finally, over all the contaminated epochs the average calculated Δ SNR was 13.67 dB.

7.4.3 Wavelet Transform

The wavelet transform was also chosen to clean the artifact contaminated data as it provided a high efficacy for both λ and Δ SNR when employed on the known contaminated data from Chapter 6. The technique was employed as described in Section 6.1 however, as the "ground truth" signal was not available the autocorrelation of the decomposed components was used to determine the artifact components. This technique was chosen above the use of the Hurst exponent as it was shown, on average, to provide the best results for the experiments undertaken in Chapter 6. The choice of the threshold value was determined empirically and was set to 0.999 for all artifact types. All components whose autocorrelation at lag one was above this threshold were then determined to be artifacts and were thus removed from the reconstructed signal.

Figure 7.9 and Figure 7.10 present example outputs of the technique for all the described artifact types. The time domain outputs can be seen to contain more residual artifacts than those for the other techniques investigated. One possible reason for this may be the choice of the artifact threshold value. As this value is static, artifact components of different morphologies may not all be separated. Future analysis could look into the use of a variable threshold value, possibly employing the accelerometer signals as a reference. These artifacts are also apparent in the "walking" and "running" trials similar to the Wiener filter outputs. Over all epochs the wavelet transform technique yielded a Δ SNR value of 4.92 dB.

7.4.4 EEMD

Similar to the wavelet transform the EEMD technique was employed as was described in Section 6.2.2 with the sole difference being the value of the threshold used to separate the artifact components from the desired signal. Again the autocorrelation function was used to determine these components and the threshold was set to 0.999. This threshold resulted in the removal of the artifact components which can be seen from both Figure 7.11 and 7.12. As was observed with the wavelet transform and the Wiener

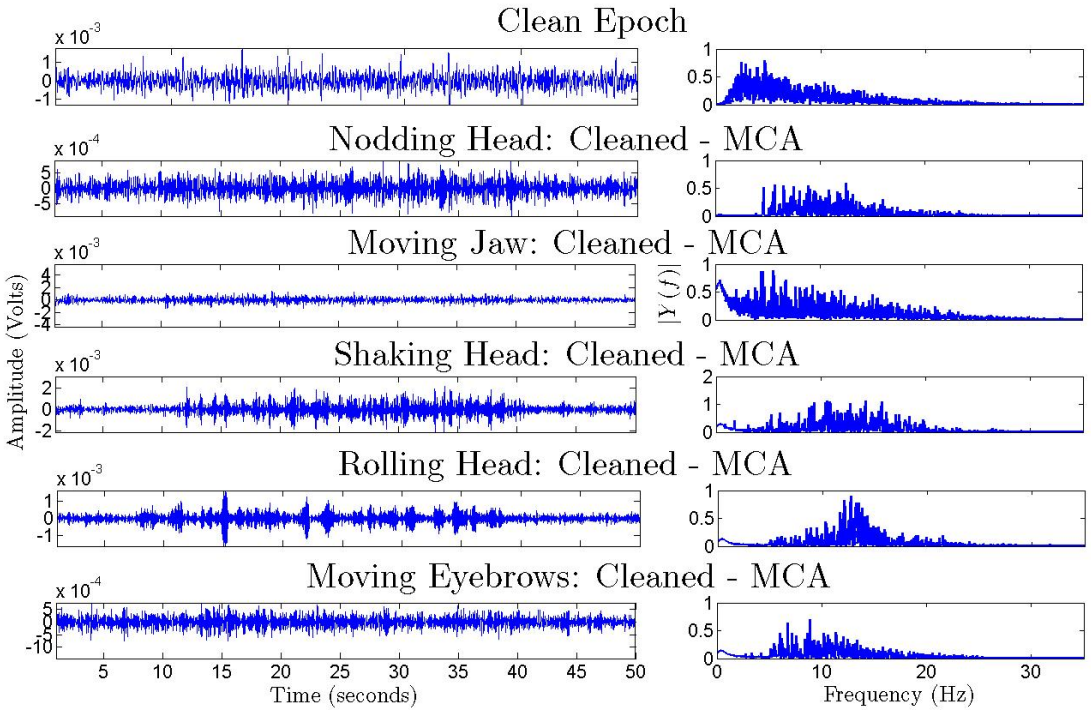

FIGURE 7.7: Artifact removal performed using morphological component analysis (MCA) on EEG epochs contaminated due to movements of the head.

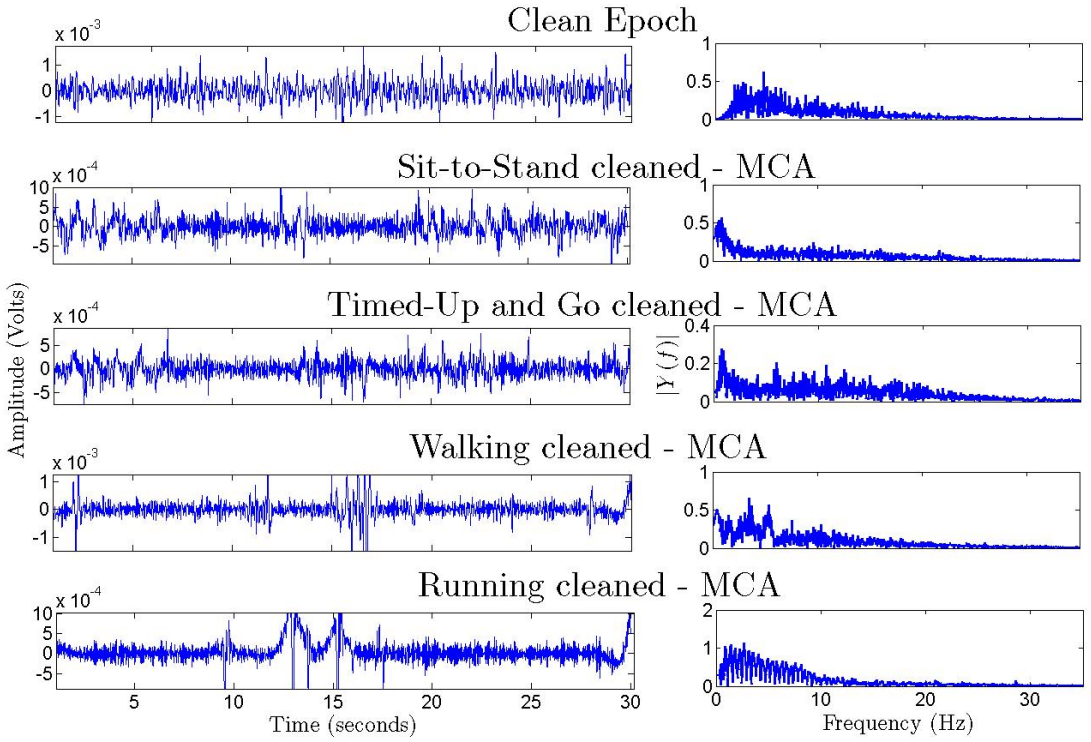

FIGURE 7.8: Artifact removal performed using morphological component analysis (MCA) on EEG epochs contaminated due to movements of the body.

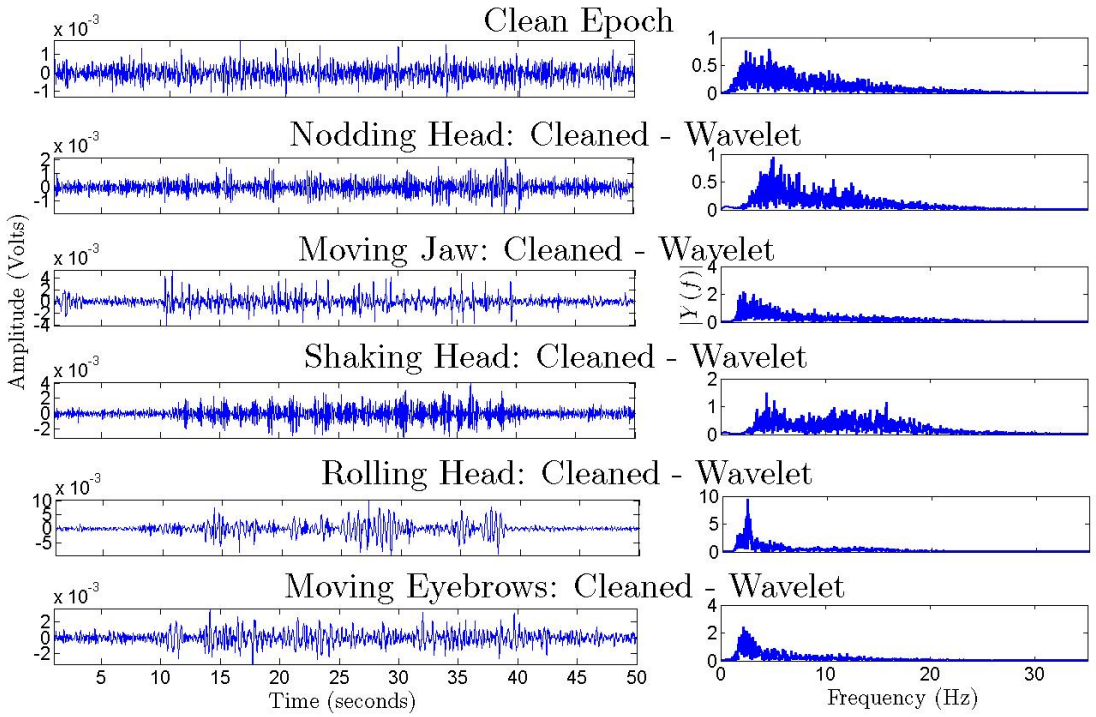

FIGURE 7.9: Artifact removal performed using the wavelet transform on EEG epochs contaminated due to movements of the head.

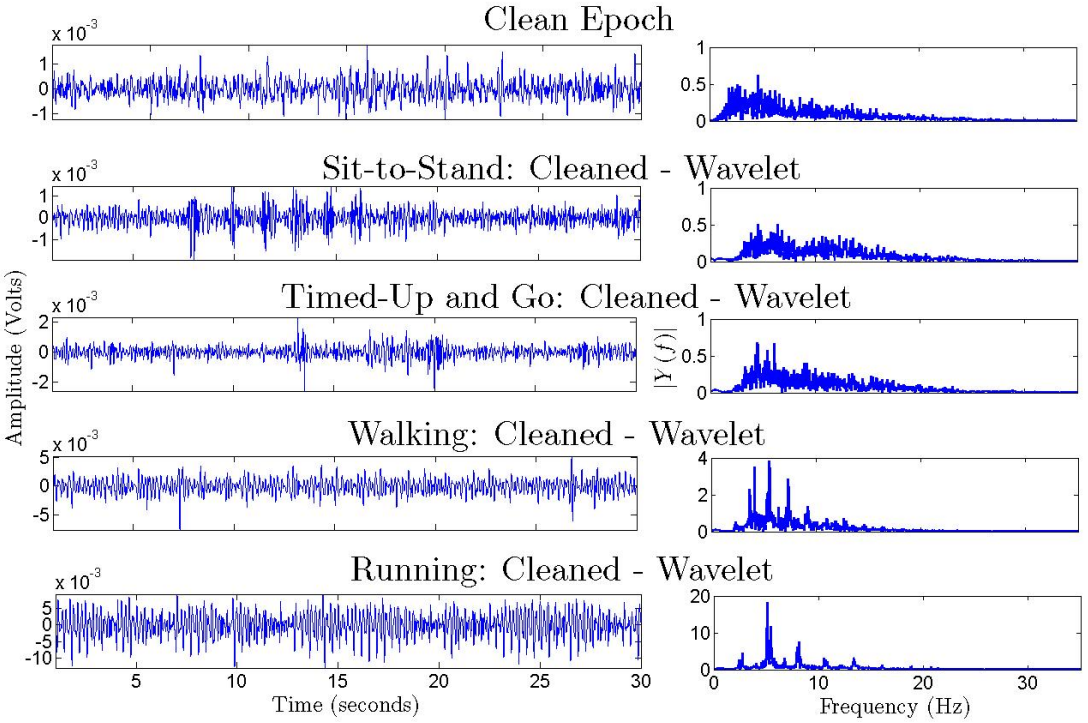

FIGURE 7.10: Artifact removal performed using the wavelet transform on EEG epochs contaminated due to movements of the body.

filter, the epochs of data contaminated with artifacts due to the subject "running" and "walking" retain some periodic artifacts. However, when compared to the contaminated artifacts shown in Figure 7.3 and Figure 7.4, the majority of the artifact components can be seen to be removed. This can also be shown by the increase in SNR. Over all epochs the average Δ SNR value was calculated as 6.14 dB.

7.5 Discussion

Table 7.2 summaries the improvements in SNR obtained through the use of the various artifact removal techniques. These results are consistent with the previous analysis of the techniques presented in Chapters 5 and 6. The Wiener filter produces the largest average improvement in SNR in 7 of the 9 trials tested while having results only slightly lower than MCA in the other two. This result affirms the results shown in Figure 6.31 which also shows the Wiener filter to be best in terms of SNR improvement.

In the analysis performed in this case study, the MCA algorithm provided the 2^{nd} best results. Unlike the Wiener filter, which only requires the PSD of the true and noisy signal to operate, the MCA algorithm requires that the correct dictionaries be chosen to represent the underlying signals prior to implementation. When employing the algorithm on the signals contaminated with artifacts due to movement of the body a new selection of dictionaries was required as the previous choice did not satisfactorily separate the signals. This requirement for the selection of the dictionaries could restrict the use of the technique in situations where the exact form of the contaminating artifact is not known.

The EEMD and wavelet transform techniques perform significantly worse, in terms of Δ SNR, than the previously mentioned algorithms particularly in the walking and running scenarios. The overall reduction in performance could be due to the use of the autocorrelation function to determine the artifact components to remove. As was shown in Section 6.8, although the technique does perform well, it may not always provide the best results (previously shown using the "ground truth" signal).

As can be seen from both the figures and the SNR results, the epochs contaminated due to the subject walking or running are the most difficult to remove. The Wiener filter, wavelet transform and EEMD have removed some of the artifacts but the frequency plots continue to show large signal power at the particular step frequencies and their aliases. The MCA algorithm is capable of removing these periodic artifacts but the outputs still contain some residual artifacts as can be seen from Figure 7.8. However, the power and

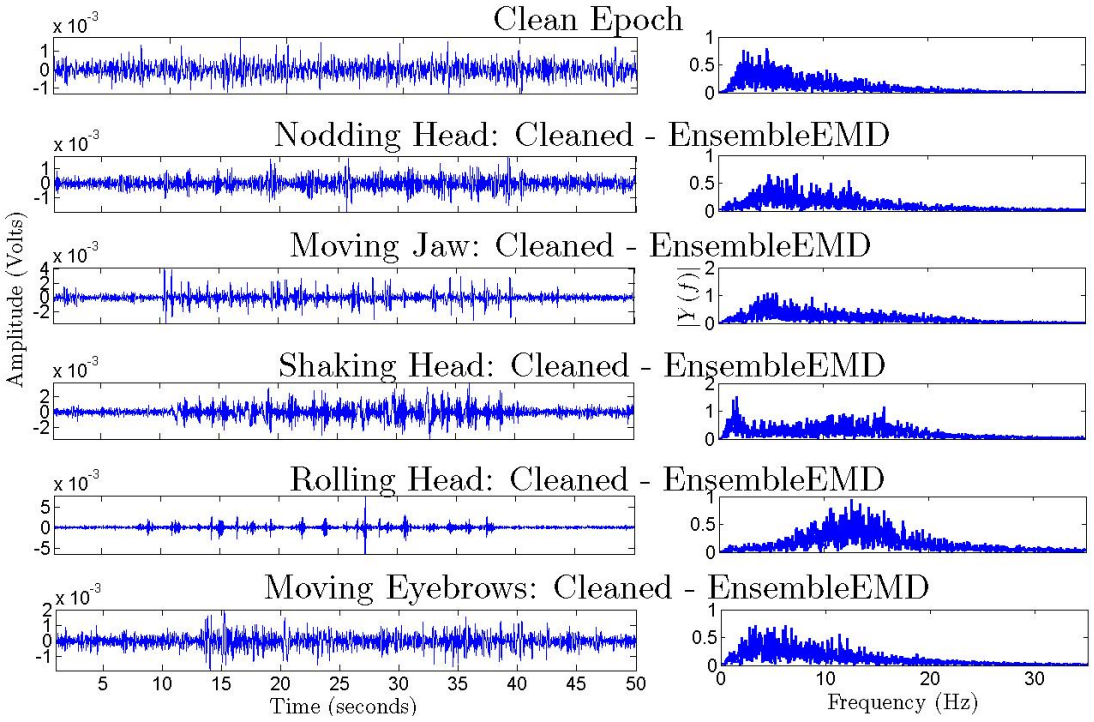

FIGURE 7.11: Artifact removal performed using ensemble empirical mode decomposition (EEMD) on EEG epochs contaminated due to movements of the head.

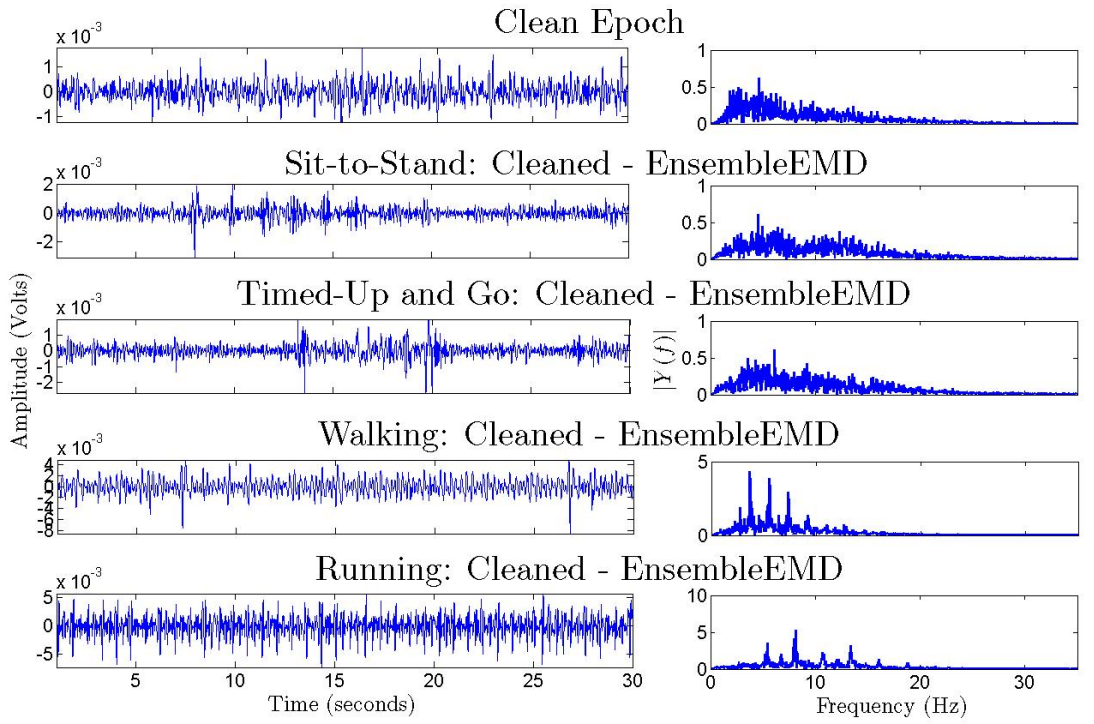

FIGURE 7.12: Artifact removal performed using ensemble empirical mode decomposition (EEMD) on EEG epochs contaminated due to movements of the body.

amplitude of the frequency and time plots of the cleaned signal using MCA have the closest resemblance to that of the true clean signal. It should be noted that the Wavelet transform and the EEMD technique can perform to a higher accuracy if the threshold value is adjusted. Therefore an adaptive threshold value is required if these techniques are to be employed for automatic artifact removal.

It should be stated again that the SNR is not a precise metric for analysing the artifact removal capability as it does not take account of how much of the actual desired signal has also been removed. It is not possible to quantify this degradation to the true signal as the form of the original true signal is not known. It was for this reason that the visual inspections were also included in the analysis. Future work on ambulatory artifact removal should look into the use of the accelerometer signals to determine the frequency of the artifact signals when walking and running and to use this information to help remove the contaminating artifacts.

TABLE 7.2: Improvement in SNR following the use of the various artifact removal techniques.

Δ SNR	Wiener	MCA	Wavelet	EEMD
Nodding Head	12.20 dB (1.83)	13.89 dB (3.39)	5.68 dB (1.43)	5.89 dB (1.53)
Moving Jaw	8.79 dB (4.00)	5.61 dB (3.86)	2.42 dB (2.43)	2.42 dB (2.44)
Shaking Head	21.40 dB (4.36)	12.81 dB (3.33)	8.04 dB (1.25)	9.00 dB (3.64)
Rolling Head	21.99 dB (3.30)	17.29 dB (4.17)	6.08 dB (2.30)	8.07 dB (3.54)
Moving Eyebrows	17.33 dB (15.83)	16.63 dB (14.28)	4.15 dB (1.61)	7.62 dB (7.43)
Sit-to-Stand	16.32 dB (3.61)	17.46 dB (1.88)	11.47 dB (1.99)	11.03 dB (2.79)
Timed-Up and Go	19.17 dB (3.90)	18.10 dB (2.44)	12.68 dB (2.70)	12.37 dB (3.57)
Walking	17.70 dB (3.77)	5.53 dB (5.85)	-3.95 dB (4.79)	-4.53 dB (5.44)
Running	35.57 dB (2.23)	15.67 dB (4.27)	-2.30 dB (2.73)	3.37 dB (2.68)

Chapter 8

Conclusion

This thesis presents the comprehensive evaluation and comparison of novel and existing artifact removal techniques that can be employed for motion artifact removal from physiological signals. Artifacts are present in all recordings independent of the recording environment. However, as health monitoring moves from the hospital-centric to the p-health environment, the possibility for contamination of signals with undesired artifacts increases. This contamination can be due to a number of factors including: a lack of trained clinicians to apply the recording system correctly, increased environmental noise, and unconstrained movement of the subject. Therefore, the requirement for techniques capable of accurately removing the artifact components is of utmost importance. The best performing artifact removal techniques should facilitate their use both within the hospital environment and in the p-health domain by performing adequately, and having a low computational and hardware cost.

Progress on the artifact removal problem had previously been limited by 3 main factors: 1) No comprehensive review of the literature existed, 2) few combinations of techniques had been compared and 3) no dataset was available from which an accurate evaluation of all of the techniques could be made. In this thesis each of these factors have been addressed in this thesis and a complete evaluation of a range of leading artifact removal techniques provided. The thesis concludes by proposing the best artifact removal techniques to use for physiological signals under different circumstances.

The following sections detail the overall conclusions and contributions of the research as well as highlighting possible avenues for future investigation.

8.1 Summary of Contributions

Literature Review

As no previous review had been conducted in the area prior to the initiation of the thesis, a comprehensive literature review of the state-of-the-art in artifact removal techniques pertaining to physiological signal analysis was presented (Chapter 3). This work reviewed the techniques which are currently among the most commonly employed. The review also provided a taxonomy under which the artifact removal techniques could be grouped. "Single stage artifact removal techniques" were defined as artifact removal techniques which suppress unwanted signals without the requirement for an intermediate artifact identification stage and, furthermore, are capable of operating on the available single channel measurements. These techniques do, however, require some *a priori* knowledge of the true and/or noisy signal to function correctly. "Two stage artifact removal techniques" may or may not require *a priori* information but do require the use of additional algorithms to aid in the identification of the artifact components from the decomposed signals.

The review concluded that the majority of artifact removal techniques were evaluated using simulated data and a method of analysing the techniques on real data was required. Also, very few of the different algorithms had been compared with each other and therefore a detailed comparison was needed.

Novel Recording Methodology

To facilitate the evaluation of the multiple artifact removal techniques investigated, a novel method of testing the efficacy was developed. Existing efficacy metrics rely on the use of simulated data, where the true signal is known but the mixing of the artifact is overly simplistic, or on contaminated real data where the form of the true signal is unknown. Using either data type can generate unrealistic results (as shown for the adaptive filter employed on the simulated data in Section 5.8). Chapter 4 details the novel recording methodology which was developed to allow for accurate testing of the efficacy of the individual algorithms. The novel methodology, designed for the recording of both electroencephalography (EEG) and functional near-infrared spectroscopy (fNIRS) data, permits the recording of two separate but highly correlated channels, allowing for the recording of a noise-contaminated and a noise-free signal concurrently. This correlated noise-free signal, labeled the "ground truth" signal can then be used as a reference for

the true signal underlying the artifact contaminated signal. The artifact removal techniques can be tested on their ability to remove the contaminating noise by determining how well the cleaned signal matches the "ground truth" signal. This matching was determined using two efficacy metrics, the percentage improvement in correlation (λ from Equation 4.8) and the improvement in signal-to-noise ratio (Δ SNR from Equation 4.7).

This new dataset allowed for a more accurate evaluation of the efficacy of the removal techniques. This was particularly shown when employing the adaptive filter. When using simulated data, the adaptive filter provided very good results due to the availability of an accurate reference signal. However when employing real data, this accurate reference is not available and thus the efficacy results of the technique drops significantly.

Novel Tagging Algorithm

A novel tagging algorithm, used to generate an original quality-of-signal (QOS) metric, was proposed in Chapter 5. This QOS metric contrasted with any quality metric which had been previously described due to its use of dual accelerometers. This allowed for the recording of overall subject motion, along with any differential movement of the electrodes/optodes with respect to the skin. Using these two references, the QOS metric is able of perform three separate functions.

- Similar to previously available QOS metrics, the technique allows for an accurate indication of the epochs of a signal where an artifact component is likely to be present. This information can aid a trained technician in evaluating the differences between signal irregularities of interest and contaminating artifacts. However, unlike previous metrics the novel QOS technique is able to distinguish between different artifact types. The presence of motion does not always generate artifacts on a given signal, as shown in Figure 5.5.
- The novel QOS metric provides an accurate representation as to the position and type of artifact contaminating the signal, allowing the appropriate artifact removal technique to be chosen for each artifact type.
- The QOS metric permits the switching of the artifact removal techniques. Switching allows for the artifact removal techniques to only be employed as required and also allows for different artifact removal techniques to be employed for different artifact types. Results, shown in Tables 5.1, 5.2, 6.1 and 6.2, have demonstrated that this switching greatly increases the efficacy of the employed techniques.

Therefore the novel QOS metric provides the information necessary to determine when to employ the artifact removal techniques while also aiding in the decision as to which techniques to employ.

EEMD-CCA Artifact Removal Technique

A novel artifact removal technique is proposed in Chapter 6. When reviewing the multiple artifact removal techniques in Chapter 3, it was shown that the canonical correlation analysis (CCA) algorithm often returns quantitatively the same results as the independent component analysis (ICA) algorithm and it was also shown to be capable of outperforming the ICA algorithm for particular data types. This finding prompted the development of a novel algorithm combining the ensemble empirical mode decomposition algorithm (EEMD) with the CCA algorithm, allowing the CCA algorithm to be employed on recordings with low channel numbers. This algorithm was shown to have significantly lower computational cost than the similar EEMD-ICA technique, while demonstrating similar efficacy.

Results showed that the novel EEMD-CCA algorithm was the best artifact removal algorithm to employ when analysing fNIRS data when a reference signal is not available and the form of the artifact is unknown.

Evaluation and Comparison of Techniques

Given the difficulty in acquiring high quality signals, in the uncontrolled environment present in modern connected health, understanding, from a comparative perspective, the performance of the various techniques developed for this purpose is valuable and has been hitherto unavailable. Through providing a comparison in a controlled and rigourous fashion, this thesis should help connected health engineers better understand the options open to them. It was found that the choice of the best removal technique to use is dependent on a number of different factors: 1) the availability of a reference signal 2) the signal modality and 3) whether or not the form of the artifact is known. If no reference signal is available, but the form of the artifact is known, then the morphological component analysis (MCA) algorithm provides the best results for both the fNIRS and EEG data. The Wiener filter also performs well in these situations when applied to the EEG data. However, if the morphology of the artifact is not known then the MCA algorithm will not be capable of separating the signal from the noise. The EEMD-CCA technique becomes the best performing algorithm in that situation for the fNIRS data, while the Wiener filter performs similarly to before with the EEG data. In situations

where a reference signal is available, the tagging algorithm, can be used to determine when to apply the techniques (in real time), so they are only employed when necessary and for the right artifacts. In this context, all of the single stage techniques perform well. As before, the MCA algorithm is only effective when the form of the artifact is known. For the EEG data, the Wiener filter along with the Wavelet and EEMD techniques provide the best results. The requirement of the two stage techniques for algorithms capable of determining the artifact components is a disadvantage, suggesting the Wiener filter as the best option for implementation. A summary of these results is given in Table 8.1 which provides a direct comparison between the techniques presented.

TABLE 8.1: Best artifact removal techniques to employ for the EEG and fNIRS data under different situations.

		EEG	fNIRS
Not Tagged	Known Artifact Type	MCA Wiener	MCA
	Unknown Artifact Type	Wiener	EEMD-CCA
Tagged	Known Artifact Type	Wiener Wavelet EEMD	Kalman MCA Wiener Adaptive
	Unknown Artifact Type	Wiener Wavelet EEMD	Kalman Wiener Adaptive

In conclusion, the Wiener filter can be seen as the best performing algorithm for the EEG data as it performs best over all situations while also having a very low computational load and is relatively easy to setup prior to implementation. For the fNIRS data, the best technique depends on each particular situation. When a reference is available the Wiener filter should be used as it has the lowest computational cost which can be important when operating in the p-health domain to improve operating time.

Comparison of Two Stage Artifact Selection Techniques

As previously stated, each of the analysed two stage artifact removal techniques require an additional algorithm to aid in the selection of the appropriate components relating to artifacts from the separated signals. A comparison of two of these selection techniques was provided in Chapter 6.

1. The first technique used the components autocorrelation coefficient at lag one to classify whether a component was artifact or desired signal
2. The second technique used the Hurst exponent, which is a measure of the rate of change of autocorrelation over time

The Hurst exponent technique was found to be in-capable of selecting the correct components when employed on the fNIRS data and so, for this signal modality, only the autocorrelation function was used. However, when employed on EEG data, both techniques were capable of separating the signal and artifact components and thus were compared. The results provided using the two techniques were compared against those obtained using the information provided by the "ground truth" signal, in order to determine the optimum components. It was found that the Hurst exponent function performed poorly when employed with any of the techniques that used the EEMD function, but provided adequate results for the Wavelet based techniques. However, the autocorrelation based technique provided better results for both the EEMD and Wavelet based techniques with correlation values only about 1-2 % lower then the determined best case results.

It is therefore concluded that the individual components autocorrelation information should be used to determine the artifact components from the decomposed signals. The requirement to determine the optimum threshold levels to separate the artifact and true signal components could restrict the use of these techniques in the future.

Case Study

Chapter 7 presented a case study which employed four of the best algorithms derived in Chapter 6 on ambulatory recorded EEG data. This novel dataset comprised of EEG data corrupted with artifacts arising due to movements, ranging from simple head movements to full body movement while running. This case study provided an opportunity to test the algorithms on artifacts which commonly affect recordings made in the p-health domain. Using both a SNR efficacy metric and the visual assessment of improvement in signal quality, both in the time and frequency domain, the Wiener filter, and the MCA, Wavelet and EEMD techniques were evaluated. In agreement with the results from Chapter 6, the Wiener filter provided the largest average improvement in 7 of the 9 tested trials. Its should be noted however that the MCA technique provided the best results visually for both trials contaminated due to the subject walking and running. This proves that if the artifact signal has a known morphology, the MCA algorithm may be the best technique to employ.

Due to the consistency of the results, it is concluded that the Wiener filter is the best tested removal technique to employ for motion artifact removal from ambulatory EEG data, however the MCA technique could possibly provide better results for artifacts due to walking or running.

Benchmark Datasets

The final contributions of the thesis are the benchmark datasets collected to test the efficacy of the artifact removal techniques, namely the fNIRS and EEG data recorded using the methodology described in Chapter 4 and the EEG data recorded for the case study in Chapter 7. These datasets will be made available online to the research community, providing a valuable resource for future artifact removal research. In particular, the fNIRS and EEG datasets provide a benchmark from which to test future artifact removal techniques, allowing for a quick and easy comparison with each of the techniques described in this thesis. In addition, these datasets provide researchers who do not have access to the required recording systems to record their own data, with the opportunity to test new artifact removal techniques on real motion artifact contaminated data rather than having to exclusively rely on simulated data.

8.2 Future Work

During the research performed for this thesis a number of future avenues for further research have been identified. Below, three of these different avenues are elaborated upon.

Extension of the Recording Methodology

The methodology proposed in Chapter 4 allows for an accurate measure of the efficacy of artifact removal techniques due to the availability of a "ground truth" signal. In order to further test the artifact removal capabilities of the techniques, further trials could be recorded with an extension to the recording protocol described in Section 4.2.3 and 4.2.4.

In the protocol described in the thesis, the subjects were not asked to perform any mental tasks during the recording of the fNIRS or EEG data. For these trials, an interpretation of the physical meaning of the underlying signals was not of importance. If this protocol was altered, therefore requiring the subjects to perform a mental task intermittently during recording, an additional test of the removal techniques could be

performed. The form of this mental task would depend on the electrode/optode position during the recording. Using the "ground truth" signal, a classifier could first be trained to detect the activation and rest epochs of the signal, as performed by Leamy and Ward [106]. By implementing this new revised protocol, the individual artifact removal techniques could be also compared on their ability to return the contaminated signal to a form where the trained classifier is capable of determining the associated active and rest epochs.

In addition, to generate a more controlled artifact signal a mechanical process could be used to disturb the recording optode/electrode instead of the pulling of the leads manually. By use of a device such as a stepper motor to pull on the lead, the exact movements can be determined allowing for an exact knowledge of the waveform representing the disturbance.

Adaptive Artifact Selection Threshold

When employing any of the described two stage techniques for automatic artifact removal there is a requirement for additional algorithms capable of determining the components relating to artifacts from the separated signals. One difficulty with using these automatic component selection techniques is the choice of the threshold value to use to separate the artifact from the true signal components. An incorrect threshold value can result in either the failure to remove some of the artifact components or in the removal of a number of components relating to the desired true signal.

A further avenue for research is the development of algorithms capable of automatically determining the optimum threshold values for combinations of random signal and artifact modalities. In doing so, an adaptive nature is introduced to the artifact selection techniques where only the artifact signal is removed, thus improving the overall efficacy of the techniques.

Data Tagging Algorithm without Reference

A further avenue which would benefit from further analysis is the tagging of artifact epochs of a data signal. In this thesis, as described in Section 5.1, the tagging of data is performed using the available reference accelerometer signals.

The current tagging method requires that a reference signal for the artifact in the form of an accelerometer is available. In order to reduce the power consumption and the hardware requirements of the developed p-health monitoring system, there is a desire

to eliminate the requirement for this reference signal. Changes in the statistical or morphological properties of the analysed signals may be able to be used to self tag the data, providing a basic QOS metric which could be used to control the artifact removal techniques.

8.3 Concluding Remarks

The focus of this thesis was to determine the best techniques to employ for motion artifact removal from physiological signals. This is an important topic of research, since until the artifacts that commonly contaminate physiological signals can be accurately removed, the measurements will not be capable providing the required level of accurate information often required by clinicians. Further, such artifacts are hindering the pervasion of p-health technology in a rapidly ageing society.

The thesis focused primarily on the fNIRS and EEG signal types as these are two of the more challenging signal modalities to measure both within and outside the laboratory. A novel methodology was devised to provide datasets from which the artifact removal techniques could be evaluated accurately and fairly. The numerous techniques were evaluated and compared with the best proposed technique for EEG deemed to be the Wiener filter. For the fNIRS data, the best technique depended on the particular situation examined (i.e. was a reference signal available etc).

With the ever increasing capabilities of technology and the use of ever more efficient artifact removal techniques, the next number of decades will hopefully see a dramatic increase in both the number and the accuracy of physiological measurements performed in the p-health domain. These measurements will help to reduce the ever increasing cost of healthcare, while eradicating the requirement of hospital-visits to perform routine monitoring and checkups, resulting in a better quality of life for the patient.

Appendix A

Publications Arising from this Work

Sweeney, K.T. Ward, T.E. and McLoone, S.F., A simple bio-signals quality measure for in-home monitoring, *In proceedings of the 7th IASTED International Conference*, 2010.

> Electrocardiography (ECG) is a test that measures the electrical activity of the heart. The use of ECG for recording in ambulatory settings is becoming more prominent due to an increase in in-home monitoring. By virtue of the ambulatory nature of the recordings, artifacts have a large effect on the signals, with the most significant artifact a result of motion. This paper describes an accelerometer system used to detect differential movement between the recording electrodes on the body. This system is then used to determine a Quality of Signal (QOS) metric for the ECG signal. The results show that the use of differential movement of the recording electrodes with respect to one another is a better representative of the motion artifact, then overall body movement. This simple Signal Quality metric is used to more accurately flag the appropriate noisy ECG data which can be rejected from the signal. The simplicity of this system also allows it to be easily embedded into any in-home monitoring system.

Sweeney, K.T. Leamy, D.J. and Ward, T.E. and McLoone, S.F., Intelligent artifact classification for ambulatory physiological signals, *In proceedings of the IEEE Engineering in Medicine and Biology Society (EMBC)*, 2010.

Connected health represents an increasingly important model for healthcare delivery. The concept is heavily reliant on technology and in particular remote physiological monitoring. One of the principal challenges is the maintenance of high quality data streams which must be collected with minimally intrusive, inexpensive sensor systems operating in difficult conditions. Ambulatory monitoring represents one of the most challenging signal acquisition challenges of all in that data is collected as the patient engages in normal activities of everyday living. Data thus collected suffers from considerable corruption as a result of artifact, much of it induced by motion and this has a bearing on its utility for diagnostic purposes. We propose a model for ambulatory signal recording in which the data collected is accompanied by labeling indicating the quality of the collected signal. As motion is such an important source of artifact we demonstrate the concept in this case with a quality of signal measure derived from motion sensing technology viz. accelerometers. We further demonstrate how different types of artifact might be tagged to inform artifact reduction signal processing elements during subsequent signal analysis. This is demonstrated through the use of multiple accelerometers which allow the algorithm to distinguish between disturbance of the sensor relative to the underlying tissue and movement of this tissue. A brain monitoring experiment utilising EEG and fNIRS is used to illustrate the concept.

Sweeney, K.T. Kelly, D. Ward, T.E. and McLoone, S.F., A Review of the State of the Art in Artifact Removal Technologies as used in an Assisted Living Domain, *IET Conference on Assisted Living*, 2011.

There has been significant growth in the area of ubiquitous, pervasive, distributed healthcare technologies due to the increasing burden on the healthcare system and the impending demographic shift towards an aging population. The move from a hospital-centric healthcare system towards in-home health assessment is aimed to alleviate the burden on healthcare professionals, the health care system and caregivers. Advances in signal acquisition, data storage and communication channels provide for the collection of reliable and useful in-home physiological data. Artifacts, arising from environmental, experimental and physiological factors, degrade signal quality and reduce the utility of the affected part of the signal. The degrading effect of the artifacts significantly increases when data collection is moved from the clinic into the home. Advances in signal processing have brought about significant improvement in artifact removal over the last number of years. This paper reviews the most common physiological and location-indicative signals recorded in the home and documents the artifacts which occur most often. A discussion of some of the most common artifact removal techniques is then provided. An evaluation of the advantages and disadvantages of each is given with reference to the assisted living environment.

Sweeney, K.T. Ayaz, H. Ward, T.E. Izzetoglu, M. McLoone, S.F. and Onoral, B., A Methodology for Validating Artifact Removal Techniques for fNIRS *In proceedings of the IEEE Engineering in Medicine and Biology Society (EMBC)*, 2011.

fNIRS recordings are increasingly utilised to monitor brain activity in both clinical and connected health settings. These optical recordings provide a convenient measurement of cerebral hemodynamic changes which can be linked to motor and cognitive performance. Such measurements are of clinical utility in a broad range of conditions ranging from dementia to movement rehabilitation therapy. For such applications fNIRS is increasingly deployed outside the clinic for patient monitoring in the home. However, such a measurement environment is poorly controlled and motion, in particular, is a major source of artifacts in the signal, leading to poor signal quality for subsequent clinical interpretation. Artifact removal techniques are increasingly being employed with an aim of reducing the effect of the noise in the desired signal. Currently no methodology is available to accurately determine the efficacy of a given artifact removal technique due to the lack of a true reference for the uncontaminated signal. In this paper we propose a novel methodology for fNIRS data collection allowing for effective validation of artifact removal techniques. This methodology describes the use of two fNIRS channels in close proximity allowing them to sample the same measurement location; allowing for the introducing of motion artifact to only one channel while having the other free of contamination. Through use of this methodology, for each motion artifact epoch, a true reference for the uncontaminated signal becomes available for use in the development and performance evaluation of signal processing strategies. The advantage of the described methodology is demonstrated using a simple artifact removal technique with an accelerometer based reference.

Sweeney, K.T. Ward, T.E. and McLoone, S.F., Artifact Removal in Physiological Signals -Practices and Possibilities, *IEEE Transactions on Information Technology in Biomedicine*, vol. 16, no. 3, pp 488-500, May, 2012.

The combination of reducing birth rate and increasing life expectancy continues to drive the demographic shift toward an aging population. This, in turn, places an ever-increasing burden on healthcare due to the increasing prevalence of patients with chronic illnesses and the reducing income-generating population base needed to sustain them. The need to urgently address this healthcare "time bomb "; has accelerated the growth in ubiquitous, pervasive, distributed healthcare technologies. The current move from hospital-centric healthcare toward in-home health assessment is aimed at alleviating the burden on healthcare professionals, the health care system and caregivers. This shift will also further increase the comfort for the patient. Advances in signal acquisition, data storage and communication provide for the collection of reliable and useful in-home physiological data. Artifacts, arising from environmental, experimental and physiological factors, degrade signal quality and render the affected part of the signal useless. The magnitude and frequency of these artifacts significantly increases when data collection is moved from the clinic into the home. Signal processing advances have brought about significant improvement in artifact removal over the past few years. This paper reviews the physiological signals most likely to be recorded in the home, documenting the artifacts which occur most frequently and which have the largest degrading effect. A detailed analysis of current artifact removal techniques will then be presented. An evaluation of the advantages and disadvantages of each of the proposed artifact detection and removal techniques, with particular application to the personal healthcare domain, is provided.

Sweeney, K.T. Ayaz, H. Ward, T.E. Izzetoglu, M. McLoone, S.F. and Onaral, B., A methodology for validating artifact removal techniques for physiological brain signals, *IEEE Transactions on Information Technology in Biomedicine*, vol. 16, no. 5, pp 918-926, Sept., 2012.

> Artifact removal from physiological signals is an essential component of the biosignal processing pipeline. The need for powerful and robust methods for this process has become particularly acute as healthcare technology deployment undergoes transition from the current hospital-centric setting towards a wearable and ubiquitous monitoring environment. Currently, determining the relative efficacy and performance of the multiple artifact removal techniques available on real world data can be problematic, due to incomplete information on the uncorrupted desired signal. The majority of techniques are presently evaluated using simulated data and therefore the quality of the conclusions is contingent on the fidelity of the model used. Consequently, in the biomedical signal processing community, there is considerable focus on the generation and validation of appropriate signal models for use in artifact suppression. Most approaches rely on mathematical models which capture suitable approximations to the signal dynamics or underlying physiology and therefore introduce some uncertainty to subsequent predictions of algorithm performance. This paper describes a more empirical approach to the modeling of the desired signal that we demonstrate for functional brain monitoring tasks which allows for the procurement of a "ground truth" signal which is highly correlated to a true desired signal that has been contaminated with artifacts. The availability of this "ground truth", together with the corrupted signal, can then aid in determining the efficacy of selected artifact removal techniques. A number of commonly implemented artifact removal techniques were evaluated using the described methodology to validate the proposed novel test platform.

Sweeney, K.T. Ward, T.E. and McLoone, S.F., The use of empirical mode decomposition with canonical correlation analysis as a novel artifact removal technique, *IEEE Transactions on Biomedical Engineering, (Accepted)*, 2012.

Biosignal measurement and processing is increasingly being deployed in ambulatory situations particularly in connected health applications. Such an environment dramatically increases the likelihood of artifacts which can occlude features of interest and reduce the quality of information available in the signal. If multichannel recordings are available for a given signal source then there are currently a considerable range of methods which can suppress or in some cases remove the distorting effect of such artifacts. There are however considerably fewer techniques available if only a single channel measurement is available and yet single channel measurements are important where minimal instrumentation complexity is required. This paper describes a novel artifact removal technique for use in such a context. The technique known as ensemble empirical mode decomposition with canonical correlation analysis (EEMD-CCA) is capable of operating on single channel measurements. The EEMD technique is first used to decompose the single channel signal into a multi-dimensional signal. The CCA technique is then employed to isolate the artifact components from the underlying signal using second order statistics. The new technique is tested against the currently available wavelet denoising and EEMD-ICA techniques using both electroencephalography (EEG) and functional near-infrared spectroscopy (fNIRS) data and is shown to produce significantly improved results.

Appendix B

Data Sheet and Schematic for Accelerometer System

ANALOG DEVICES

Small, Low Power, 3-Axis ±2 *g* Accelerometer

ADXL327

FEATURES

3-axis sensing
Small, low profile package
4 mm × 4 mm × 1.45 mm LFCSP
Low power: 350 µA typical
Single-supply operation: 1.8 V to 3.6 V
10,000 *g* shock survival
Excellent temperature stability
Bandwidth adjustment with a single capacitor per axis
RoHS/WEEE lead-free compliant

APPLICATIONS

Cost-sensitive, low power, motion- and tilt-sensing applications
Mobile devices
Gaming systems
Disk drive protection
Image stabilization
Sports and health devices

GENERAL DESCRIPTION

The ADXL327 is a small, low power, complete 3-axis accelerometer with signal conditioned voltage outputs. The product measures acceleration with a minimum full-scale range of ±2 *g*. It can measure the static acceleration of gravity in tilt-sensing applications, as well as dynamic acceleration, resulting from motion, shock, or vibration.

The user selects the bandwidth of the accelerometer using the C_X, C_Y, and C_Z capacitors at the X_{OUT}, Y_{OUT}, and Z_{OUT} pins. Bandwidths can be selected to suit the application with a range of 0.5 Hz to 1600 Hz for X and Y axes and a range of 0.5 Hz to 550 Hz for the Z axis.

The ADXL327 is available in a small, low profile, 4 mm × 4 mm × 1.45 mm, 16-lead, plastic lead frame chip scale package (LFCSP_LQ).

FUNCTIONAL BLOCK DIAGRAM

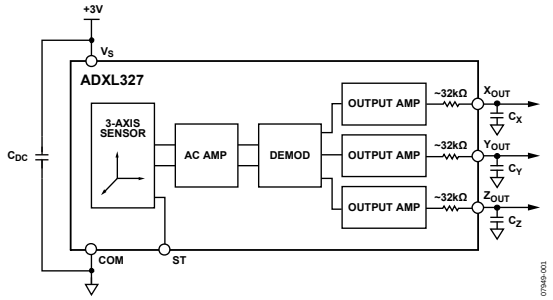

Figure 1.

Rev. 0

One Technology Way, P.O. Box 9106, Norwood, MA 02062-9106, U.S.A.
Tel: 781.329.4700 **www.analog.com**
Fax: 781.461.3113

SPECIFICATIONS

T_A = 25°C, V_S = 3 V, C_X = C_Y = C_Z = 0.1 µF, acceleration = 0 *g*, unless otherwise noted. All minimum and maximum specifications are guaranteed. Typical specifications are not guaranteed.

Table 1.

Parameter	Conditions	Min	Typ	Max	Unit
SENSOR INPUT	Each axis				
Measurement Range		±2	±2.5		*g*
Nonlinearity	Percent of full scale		±0.2		%
Package Alignment Error			±1		Degrees
Interaxis Alignment Error			±0.1		Degrees
Cross Axis Sensitivity[1]			±1		%
SENSITIVITY (RATIOMETRIC)[2]	Each axis				
Sensitivity at X_{OUT}, Y_{OUT}, Z_{OUT}	V_S = 3 V	378	420	462	mV/*g*
Sensitivity Change Due to Temperature[3]	V_S = 3 V		±0.01		%/°C
ZERO *g* BIAS LEVEL (RATIOMETRIC)					
0 *g* Voltage at X_{OUT}, Y_{OUT}	V_S = 3 V	1.3	1.5	1.7	V
0 *g* Voltage at Z_{OUT}	V_S = 3 V	1.2	1.5	1.8	V
0 *g* Offset vs. Temperature			±1		m*g*/°C
NOISE PERFORMANCE					
Noise Density X_{OUT}, Y_{OUT}, Z_{OUT}			250		µ*g*/√Hz rms
FREQUENCY RESPONSE[4]					
Bandwidth X_{OUT}, Y_{OUT}[5]	No external filter		1600		Hz
Bandwidth Z_{OUT}[5]	No external filter		550		Hz
R_{FILT} Tolerance			32 ± 15%		kΩ
Sensor Resonant Frequency			5.5		kHz
SELF TEST[6]					
Logic Input Low			+0.6		V
Logic Input High			+2.4		V
ST Actuation Current			+60		µA
Output Change at X_{OUT}	Self test 0 to 1	−210	−450	−850	mV
Output Change at Y_{OUT}	Self test 0 to 1	+210	+450	+850	mV
Output Change at Z_{OUT}	Self test 0 to 1	+210	+770	+1400	mV
OUTPUT AMPLIFIER					
Output Swing Low	No load		0.1		V
Output Swing High	No load		2.8		V
POWER SUPPLY					
Operating Voltage Range		1.8		3.6	V
Supply Current	V_S = 3 V		350		µA
Turn-On Time[7]	No external filter		1		ms
TEMPERATURE					
Operating Temperature Range		−40		+85	°C

[1] Defined as coupling between any two axes.
[2] Sensitivity is essentially ratiometric to V_S.
[3] Defined as the output change from ambient-to-maximum temperature or ambient-to-minimum temperature.
[4] Actual frequency response controlled by user-supplied external filter capacitors (C_X, C_Y, C_Z).
[5] Bandwidth with external capacitors = 1/(2 × π × 32 kΩ × C). For C_X, C_Y = 0.003 µF, bandwidth = 1.6 kHz. For C_Z = 0.01 µF, bandwidth = 500 Hz. For C_X, C_Y, C_Z = 10 µF, bandwidth = 0.5 Hz.
[6] Self test response changes cubically with V_S.
[7] Turn-on time is dependent on C_X, C_Y, C_Z and is approximately 160 × C_X or C_Y or C_Z + 1 ms, where C_X, C_Y, C_Z are in µF.

ABSOLUTE MAXIMUM RATINGS

Table 2.

Parameter	Rating
Acceleration (Any Axis, Unpowered)	10,000 *g*
Acceleration (Any Axis, Powered)	10,000 *g*
V_S	−0.3 V to +3.6 V
All Other Pins	(COM − 0.3 V) to (V_S + 0.3 V)
Output Short-Circuit Duration (Any Pin to Common)	Indefinite
Temperature Range (Powered)	−55°C to +125°C
Temperature Range (Storage)	−65°C to +150°C

Stresses above those listed under Absolute Maximum Ratings may cause permanent damage to the device. This is a stress rating only; functional operation of the device at these or any other conditions above those indicated in the operational section of this specification is not implied. Exposure to absolute maximum rating conditions for extended periods may affect device reliability.

ESD CAUTION

ESD (electrostatic discharge) sensitive device. Charged devices and circuit boards can discharge without detection. Although this product features patented or proprietary protection circuitry, damage may occur on devices subjected to high energy ESD. Therefore, proper ESD precautions should be taken to avoid performance degradation or loss of functionality.

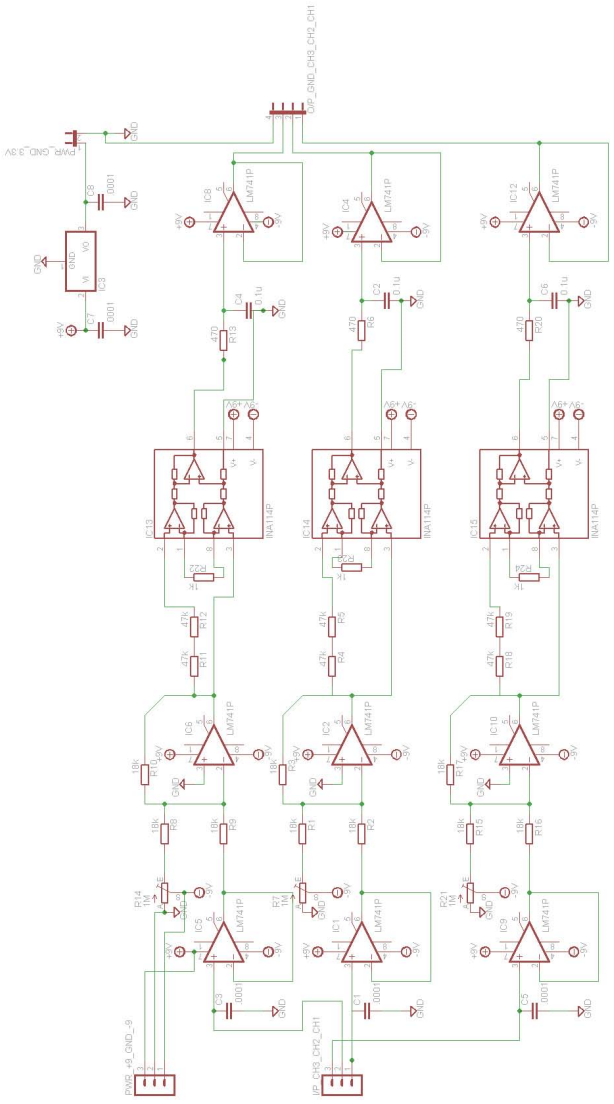

FIGURE B.1: Accelerometer Circuitry

References

[1] M T. Akhtar, W. Mitsuhashi, and C.J. James. Employing spatially constrained ICA and wavelet denoising, for automatic removal of artifacts from multichannel EEG data. *Signal Processing*, 92(2):401 – 416, Feb. 2012.

[2] J. Allen. Short term spectral analysis, synthesis, and modification by discrete Fourier transform. *Acoustics, Speech and Signal Processing, IEEE Transactions on*, 25(3):235 – 238, Jun. 1977.

[3] T W. Anderson. *An Introduction to Multivariate Statistical Analysis.* Wiley-Interscience, 2003.

[4] J L. Andreassi. *Psychophysiology: human behavior and physiological response.* Lawrence Erlbaum Associates Inc, 2000.

[5] M. Arezki, A. Benallal, and D. Berkani. Improvement of the Simplified Fast Transversal Filter Type Algorithm for Adaptive Filtering . *Journal of Computer Science*, 5(5):347–354, 2010.

[6] F G. Ashby. *Statistical analysis of fMRI data.* Cambridge, Mass. MIT Press,, 2011.

[7] H Aurlien, I.O Gjerde, J.H Aarseth, G Eldoen, B Karlsen, H Skeidsvoll, and N.E Gilhus. EEG background activity described by a large computerized database. *Clinical Neurophysiology*, 115(3):665 – 673, Mar. 2004.

[8] H. Ayaz, P. Shewokis, A. Curtin, M. Izzetoglu, K. Izzetoglu, and B. Onaral. Using MazeSuite and Functional Near Infrared Spectroscopy to Study Learning in Spatial Navigation. *Journal of Visualized Experiments*, 56:3443, Oct. 2011.

[9] B. Azzerboni, M. Carpentieri, F. La Foresta, and F.C. Morabito. Neural-ICA and wavelet transform for artifacts removal in surface EMG. In *Neural Networks, 2004. Proceedings. 2004 IEEE International Joint Conference on*, volume 4, pages 3223 –3228, 2004.

[10] Y. Barkana and M. Belkin. Laser Eye Injuries. *Survey of Ophthalmology*, 44(6):459 – 478, 2000.

[11] A.K. Barros, R. Vigario, V. Jousmaki, and N. Ohnishi. Extraction of event-related signals from multichannel bioelectrical measurements. *Biomedical Engineering, IEEE Transactions on*, 47(5):583 –588, May 2000.

[12] A. J. Bell and T J. Sejnowski. An information-maximization approach to blind separation and blind deconvolution. *Neural Computation*, 7(6):1129–1159, Nov. 1995.

[13] C J. Bell, P Shenoy, R. Chalodhorn, and R P N. Rao. Control of a humanoid robot by a noninvasive brain-computer interface in humans. *Journal of Neural Engineering*, 5(2):214–220, 2008.

[14] T. Benesty, J. Gansler. New Insights into the RLS Algorithm. *EURASIP Journal on Applied Signal Processing*, pages 331–339, Mar. 2004.

[15] C. Berka, D J. Levendowski, M M. Cvetinovic, M M. Petrovic, G. Davis, M N. Lumicao, V T. Zivkovic, M V. Popovic, and R. Olmstead. Real-Time Analysis of EEG Indexes of Alertness, Cognition, and Memory Acquired With a Wireless EEG Headset. *International Journal of Human-Computer Interaction*, 17(2):151–170, 2004.

[16] C. Berka, D. J. Levendowski, G. Davis, M Lumicao, C Ramsey, K Stanney, L Reeves, S Harkness, and P.D. Tremoulet. EEG Technology Review: Wireless Sensor Headset, B-Alert® Software, Alertness and Memory Profiler (AMP). *Advanced Brain Monitoring, Inc*, 2005.

[17] J. Bobin, J.-L. Starck, J.M. Fadili, Y. Moudden, and D.L. Donoho. Morphological component analysis: An adaptive thresholding strategy. *Image Processing, IEEE Transactions on*, 16(11):2675 –2681, Nov. 2007.

[18] J. Donnelly P. Bogan, D. Spence. *Connected Health in Ireland: An All-Island Review*. BioBusiness Northern Ireland, May 2010.

[19] G. Bonmassar, P L. Purdon, I P. Jääskeläinen, V. Chiappa, K.and Solo, E N. Brown, and J W. Belliveau. Motion and Ballistocardiogram Artifact Removal for Interleaved Recording of EEG and EPs during MRI. *NeuroImage*, 16(4):1127 – 1141, Aug. 2002.

[20] M H. Boostani, R. Moradi. Evaluation of the forearm EMG signal features for the control of a prosthetic hand. *Physiological Measurement*, 24(2):309, 2003.

[21] M. Borga and C M. Borga. *Learning Multidimensional Signal Processing.* PhD thesis, Linkoping University, S-581 83 Linkoping, Sweden, 1998.

[22] M. Borga, O. Friman, P. Lundberg, and H. Knutsson. A Canonical Correlation Approach to Exploratory Data Analysis in fMRI. In *Proceedings of the ISMRM Annual Meeting*, Honolulu, Hawaii, May 2002.

[23] M. Borga and H. Knutsson. A canonical correlation approach to blind source separation. Technical Report LiU-IMT-EX-0062, Linkoping University, Sweeden, Jun. 2001.

[24] A. Bozkurt, A. Rosen, H. Rosen, and B. Onaral. A portable near infrared spectroscopy system for bedside monitoring of newborn brain. *BioMedical Engineering OnLine*, 4(29):29–35, April 2005.

[25] E.O. Brigham. *The Fast Fourier Transform.* Prentice Hall, N.J., 1974.

[26] V. Britanak. *The Transform and Data Compression Handbook.* CRC Press LLC, 2001.

[27] R T. Brouillette, A Morielli, A Leimanis, K A. Waters, R Luciano, and F M. Ducharme. Nocturnal Pulse Oximetry as an Abbreviated Testing Modality for Pediatric Obstructive Sleep Apnea. *Pediatrics*, 105(2):405–412, Feb. 2000.

[28] S.C. Bunce, M. Izzetoglu, K. Izzetoglu, B. Onaral, and K. Pourrezaei. Functional near-infrared spectroscopy. *Engineering in Medicine and Biology Magazine, IEEE*, 25(4):54–62, July-Aug. 2006.

[29] LR. Buxton, RB. Frank. A model for the coupling between cerebral blood flow and oxygen metabolism during neural stimulation. *Journal of Cerebral Blood Flow & Metabolism*, 17(1):64–72, Jan. 1997.

[30] R. B. Buxton, E. C. Wong, and L. R. Frank. Dynamics of blood flow and oxygenation changes during brain activation: the balloon model. *Magnetic Resonance in Medicine*, 39(6):855–864, Jun. 1998.

[31] J V. Candy. *Bayesian Signal Processing: Classical, Modern and Particle Filtering Methods (Adaptive and Learning Systems for Signal Processing, Communications and Control Series).* Wiley-Interscience, Apr. 2009.

[32] A J. Casson and E. Rodriguez-Villegas. On data reduction in EEG monitoring: Comparison between ambulatory and non-ambulatory recordings. *Engineering in Medicine and Biology Society, 2008. EMBS 2008. 30th Annual International Conference of the IEEE*, pages 5885–5888, Aug. 2008.

[33] A.J. Casson, D.C. Yates, S. Patel, and E. Rodriguez-Villegas. Algorithm for AEEG data selection leading to wireless and long term epilepsy monitoring. *Engineering in Medicine and Biology Society, 2007. EMBS 2007. 29th Annual International Conference of the IEEE*, pages 2456–2459, Aug. 2007.

[34] M.P.S. Chawla, H.K Verma, and Vinod Kumar. Artifacts and noise removal in electrocardiograms using independent component analysis. *International Journal of Cardiology*, 129(2):278 – 281, Aug 2008.

[35] S S. Chen, D L. Donoho, and M A. Saunders. Atomic Decomposition by Basis Pursuit. *SIAM Journal on Scientific Computing*, 20(1):33–61, 1998.

[36] R. Chinaboina, D S. Ram Kiran, and K P. Srinivas. Adaptive Algorithms for Acoustic Echo Cancellation in speech Processing. *International Journal of RRAS*, 7(1), Apr. 2011.

[37] S. Choi, A. Cichocki, H. Park, and S. Lee. REVIEW Blind Source Separation and Independent Component Analysis: A Review. *Neural Information Processing - Letters and Reviews*, 6(1):1–57, Dec. 2004.

[38] A. Cohen and R.D. Ryan. *Wavelets and Multiscale Signal Processing*. Chapman & Hall, 1995.

[39] P. Comon. Independent component analysis, a new concept? *Signal Processing*, 36(3):287–314, Apr. 1994.

[40] G. Comtois and Y. Mendelson. A noise reference input to an adaptive filter algorithm for signal processing in a wearable pulse oximeter. In *Bioengineering Conference, 2007. NEBC '07. IEEE 33rd Annual Northeast*, pages 106–107, Mar. 2007.

[41] M. Cope. *The Application Of Near Infrared Spectroscopy To Non Invasive Monitoring Of Cerebral Oxygenation In The Newborn Infant*. PhD thesis, University of London, 1991.

[42] S. Coyle, D. Morris, K-T. Lau, D. Diamond, N. Taccini, D. Constanzo, P. Salvo, F. Di Francesco, MG. Trivella, JA. Porchet, and J. Luprano. Textile sensors to measure sweat pH and sweat-rate during exercise. In *Pervasive Health 2009*. Institute of Electrical and Electronics Engineers, Apr. 2009.

[43] X. Cui, S. Bray, and A L. Reiss. Functional near infrared spectroscopy (NIRS) signal improvement based on negative correlation between oxygenated and deoxygenated hemoglobin dynamics. *Neuroimage*, 49:3039–46, Nov. 2010.

[44] I. Daubechies. Ten lectures on wavelets. *CBM-SNSF Regional Conference Series in Applied Mathematics*, 1992.

[45] M E. Davies and C. J. James. Source separation using single channel ICA. *Signal Processing*, 87(8):1819 – 1832, Aug. 2007.

[46] W. De Clercq, A. Vergult, B. Vanrumste, W. Van Paesschen, and S. Van Huffel. Canonical correlation analysis applied to remove muscle artifacts from the electroencephalogram. *Biomedical Engineering, IEEE Transactions on*, 53(12):2583 –2587, Nov. 2006.

[47] M. De Vos, W. Deburchgraeve, P J. Cherian, V. Matic, R M. Swarte, P. Govaert, G H. Visser, and S. Van Huffel. Automated artifact removal as preprocessing refines neonatal seizure detection. *Clinical Neurophysiology*, 122(12):2345 – 2354, Dec. 2011.

[48] J J. Ding. Intoduction of Wiener Filter. Technical report, Department of Electrical Engineering, National Taiwan University, 2010.

[49] P. Diniz. *Adaptive filtering: algorithms and practical implementation*. Springer Science + Business Media L.L.C., 2008.

[50] E.P. Doheny, Chie Wei Fan, T. Foran, B.R. Greene, C. Cunningham, and R.A. Kenny. An instrumented sit-to-stand test used to examine differences between older fallers and non-fallers. In *Engineering in Medicine and Biology Society,EMBC, 2011 Annual International Conference of the IEEE*, pages 3063 –3066, 30 2011-sept. 3 2011.

[51] A. Doucet, N. De Freitas, and N. Gordon. *Sequential Monte Carlo Methods in Practice (Statistics for Engineering and Information Science)*. Springer-Verlag, 2001.

[52] B A. Draper, K. Baek, M. Stewart Bartlett, and J R. Beveridge. Recognizing faces with PCA and ICA. In *Computer vision and image understanding, special issue on face recognition*, pages 115–137, July 2003.

[53] J. Escudero, R. Hornero, D E. Abásolo, A. Fernández, and M L. Coronado. Artifact Removal in Magnetoencephalogram Background Activity With Independent Component Analysis. *IEEE Transactions on Biomedical Engineering*, 54(11):1965–1973, Nov. 2007.

[54] J.M. Fadili, J.-L. Starck, M. Elad, and D.L. Donoho. Mcalab: Reproducible research in signal and image decomposition and inpainting. *Computing in Science Engineering*, 12(1):44 –63, Jan.-Feb. 2010.

[55] P. Flandrin, P. Gonçalves, and G. Rilling. Emd equivalent filter banks, from interpretation to applications. In N.E. Huang and S.S.P. Shen, editors, *The Hilbert-Huang Transform and Its Applications*, pages 55–74. Interdisciplinary Mathematical Sciences, 2005.

[56] Organisation for Economic Co-operation and Development (2010). OECD Health Data. OECD Health Statistics (database).

[57] J. Forshaw and G. Smith, editors. *Dynamics and Relativity*. John Wiley & Sons, 2009.

[58] D. Fox, J. Hightower, L. Liao, D. Schulz, and G. Borriello. Bayesian Filtering for Location Estimation. *IEEE Pervasive Computing*, 2:24–33, Jul. 2003.

[59] O. Friman. *Adaptive Analysis of Functional MRI Data*. PhD thesis, Linköping University, Sweden, 2003. Dissertation No 836, ISBN 91-7373-699-6.

[60] O. Friman, J. Carlsson, P. Lundberg, M. Borga, and H. Knutsson. Detection of neural activity in functional MRI using canonical correlation analysis. *Magnetic Resonance in Medicine*, 45(2):323–330, February 2001.

[61] V S. Frost, J A. Stiles, K. S. Shanmugan, and J C. Holtzman. A Model for Radar Images and Its Application to Adaptive Digital Filtering of Multiplicative Noise. *Pattern Analysis and Machine Intelligence, IEEE Transactions on*, PAMI-4(2):157 –166, Mar. 1982.

[62] Gao., Junfeng., Zheng., Chongxun., Wang., and Pei. Online Removal of Muscle Artifact from Electroencephalogram Signals Based on Canonical Correlation Analysis. *Clinical EEG and Neuroscience*, 41(1):53–9, Jan 2010.

[63] Gartner-Inc. eHealth for a Healthier Europe, July 2009.

[64] R J. Gledhill. *Methods for Investigating Conformational Change in Biomolecular Simulations*. PhD thesis, University of Southampton, 2003.

[65] G. Gomez-Herrero, W. De Clercq, H. Anwar, O. Kara, K. Egiazarian, S. Van Huffel, and W. Van Paesschen. Automatic removal of ocular artifacts in the eeg without an eog reference channel. In *Signal Processing Symposium, 2006. NORSIG 2006. Proceedings of the 7th Nordic*, pages 130 –133, Jun. 2006.

[66] B.R. Greene, A.O. Donovan, R. Romero-Ortuno, L. Cogan, C. Ni Scanaill, and R.A. Kenny. Quantitative falls risk assessment using the timed up and go test. *Biomedical Engineering, IEEE Transactions on*, 57(12):2918 –2926, Dec. 2010.

[67] A.C Guyton, J.E. Hall, and W. Schmitt. *Human Physiology and Mechanisms of Disease*. Elsevier Health Sciences, 6th edition, Oct. 1996.

[68] P.S. Hamilton and M.G. Curley. Adaptive removal of motion artifact [ECG recordings] . In *Engineering in Medicine and Biology Society, 1997. Proceedings of the 19th Annual International Conference of the IEEE*, volume 1, pages 297–299, Oct-2 Nov 1997.

[69] P.S. Hamilton, M.G. Curley, R.M. Aimi, and C. Sae-Hau. Comparison of methods for adaptive removal of motion artifact. In *Computers in Cardiology 2000*, pages 383–386, 2000.

[70] Todd C. Handy, editor. *Event-Related Potentials: A Methods Handbook*. MIT Press, 2004.

[71] M. Hassan, S. Boudaoud, J. Terrien, B. Karlsson, and C. Marque. Combination of Canonical Correlation Analysis and Empirical Mode Decomposition Applied to Denoising the Labor Electrohysterogram. *Biomedical Engineering, IEEE Transactions on*, 58(9):2441 –2447, Sept. 2011.

[72] S. Haykin. *Adaptive Filter Theory*. Prentice Hall, 2002.

[73] P. He, G. Wilson, and C. Russell. Removal of ocular artifacts from electroencephalogram by adaptive filtering. *Medical and biological engineering and computing*, 42(3):407–412, May 2004.

[74] J. Healey and B. Logan. Wearable wellness monitoring using ECG and accelerometer data. In *Wearable Computers, 2005. Proceedings. Ninth IEEE International Symposium on*, pages 220–221, Oct. 2005.

[75] L. Hejjel and L. Kellenyi. The corner frequencies of the ECG amplifier for heart rate variability analysis. *Physiological measurement*, 26:39–47, Feb 2005.

[76] P. Hongxia and M. Jifang. De-noising method research on bearing fault signal based on particle filter. In *Nature and Biologically Inspired Computing (NaBIC), 2010 Second World Congress on*, pages 311 –315, Dec. 2010.

[77] H Hotelling. Relations between two sets of variates. *Biometrika*, 28(3-4):321–377, 1936.

[78] N E Huang, Z. Shen, and S R Long. A new view of nonlinear water waves: The Hilbert Spectrum. *Annual Review of Fluid Mechanics*, 31(1):417–457, 1999.

[79] N. E. Huang, Z. Shen, S. R. Long, M. C. Wu, H. H. Shih, Q. Zheng, N. C. Yen, C. C. Tung, and H. H. Liu. The empirical mode decomposition and the Hilbert

spectrum for nonlinear and non-stationary time series analysis. *Proceedings of the Royal Society of London. Series A: Mathematical, Physical and Engineering Sciences*, 454(1971):903–995, Mar. 1998.

[80] E. Huigen, A. Peper, and C A. Grimbergen. Investigation into the origin of the noise of surface electrodes. *Medical & Biological Engineering & Computing*, 40:332–338, 2002.

[81] T J. Huppert, S G. Diamond, M A. Franceschini, and D A. Boas. HomER: a review of time-series analysis methods for near-infrared spectroscopy of the brain. *Applied Optics*, 48(10):D280–D298, Apr. 2009.

[82] J. W. Hurst. Naming of the Waves in the ECG, With a Brief Account of Their Genesis. *Circulation*, 98(18):1937–1942, 1998.

[83] A. Hyvärinen, J. Karhunen, and E. Oja. *Independent Component Analysis*. Wiley-Interscience, June 2001.

[84] A. Hyvärinen and E. Oja. A fast fixed-point algorithm for independent component analysis. *Neural Computation*, 9(7):1483–1492, Oct. 1997.

[85] G. Inuso, F. La Foresta, N. Mammone, and F.C. Morabito. Wavelet-ICA methodology for efficient artifact removal from Electroencephalographic recordings. In *Neural Networks, 2007. IJCNN 2007. International Joint Conference on*, pages 1524 –1529, Aug. 2007.

[86] K Izzetoglu, S Bunce, B Onaral, K Pourrezaei, and B Chance. Functional Optical Brain Imaging Using Near-Infrared During Cognitive Tasks. *International Journal of human-computer interaction*, 17:211–227, 2004.

[87] M. Izzetoglu, P. Chitrapu, S. Bunce, and B. Onaral. Motion artifact cancellation in NIR spectroscopy using discrete Kalman filtering. *BioMedical Engineering OnLine*, 9(1):16–31, Mar. 2010.

[88] M. Izzetoglu, A. Devaraj, S. Bunce, and B. Onaral. Motion artifact cancellation in NIR spectroscopy using Wiener filtering. *Biomedical Engineering, IEEE Transactions on*, 52(5):934–938, May 2005.

[89] D. Jabaudon, J. Sztajzel, K. Sievert, T. Landis, and R. Sztajzel. Usefulness of Ambulatory 7-Day ECG Monitoring for the Detection of Atrial Fibrillation and Flutter After Acute Stroke and Transient Ischemic Attack. *American Heart Association*, 35(7):1647–51, Jul. 2004.

[90] C J. James and C W. Hesse. Independent component analysis for biomedical signals. *Physiological Measurement*, 26(1):15–39, Feb. 2005.

[91] C J. James and D. Lowe. Extracting multisource brain activity from a single electromagnetic channel. *Artificial Intelligence in Medicine*, 28(1):89 – 104, May 2003.

[92] C.J. James. On the use of single-channels for sensing multisource activity in biomedical signals. In *Information Technology Applications in Biomedicine, 2003. 4th International IEEE EMBS Special Topic Conference on*, pages 366 – 369, Apr. 2003.

[93] I. T. Jolliffe. *Principal Component Analysis*. Springer, 2, illustrated edition, 2002.

[94] D L. Jones, S. Appadwedula, M. Berry, M. Haun, D. Moussa, and D. Sachs. Adaptive Filtering: LMS Algorithm. Technical report, 2009.

[95] T P. Jung, S. Makeig, M. Westerfield, J. Townsend, E. Courchesne, and T J. Sejnowski. Removal of eye activity artifacts from visual event-related potentials in normal and clinical subjects. *Clinical Neurophysiology*, 111(10):1745 – 1758, Oct. 2000.

[96] R E. Kalman. A New Approach to Linear Filtering and Prediction Problems. *Transactions of the ASME–Journal of Basic Engineering*, 82(Series D):35–45, 1960.

[97] J. Karvanen, J. Eriksson, and V. Koivunen. Maximum Likelihood Estimation Of Ica Model For Wide Class Of Source Distributions. In *Signal Processing*, pages 445–454, 2000.

[98] Y. Kishimoto, Y. Kutsuna, and K. Oguri. Detecting Motion Artifact ECG Noise During Sleeping by Means of a Tri-axis Accelerometer. In *EMBS 2007. 29th Annual International Conference of the IEEE*, pages 2669–2672, Aug. 2007.

[99] B M. Klein, S. Thorne. *Biological psychology*. Worth Publishers, 2007.

[100] J N. Knight. Signal Fraction Analysis and Artifact Removal in EEG. Master's thesis, Department of Computer Science, Colorado State University, 2003.

[101] I. Koren and A. Laine. A Discrete Dyadic Wavelet Transform for Multidimensional Feature Analysis. In *Time Frequency and Wavelets in Biomedical Signal Processing, IEEE Press series in biomedical engineering*, pages 425–448. IEEE Press, 1997.

[102] D Z Kowey, P R. Kocovic. Ambulatory Electrocardiographic Recording. *American Heart Association*, 108, 2003.

[103] R. Öktem, K. Egiazarian, V V. Lukin, N N. Ponomarenko, and O V. Tsymbal. Locally Adaptive DCT Filtering for Signal-Dependent Noise Removal. *EURASIP Journal on Advances in Signal Processing*, pages 1–10, Jan. 2007.

[104] P S. Kumar, R. Arumuganathan, K. Sivakumar, and C. Vimal. Removal of Ocular Artifacts in the EEG through Wavelet Transform without using an EOG Reference Channel. *International Journal of Open Problems in Computer Science and Mathematics*, 1, 2008.

[105] D L. Xu J Q. Murphy S L. Kung, H C. Hoyert. Deaths: Final Data for 2005. *National Vital Statistics Reports*, 56(10), 2008.

[106] D.J. Leamy and T.E. Ward. A novel co-locational and concurrent fnirs/eeg measurement system: Design and initial results. In *Engineering in Medicine and Biology Society (EMBC), 2010 Annual International Conference of the IEEE*, pages 4230 –4233, Sept. 2010.

[107] D.J. Leamy, T.E. Ward, and K.T. Sweeney. Functional near infrared spectroscopy (fnirs) synthetic data generation. In *Engineering in Medicine and Biology Society,EMBC, 2011 Annual International Conference of the IEEE*, pages 6589 –6592, Sept. 2011.

[108] J. C. Lee. Using a Low-Cost Electroencephalograph for Task Classification. In *HCI Research*, pages 81–90, 2006.

[109] Sukhan Lee and G. Saridis. The control of a prosthetic arm by EMG pattern recognition. *Automatic Control, IEEE Transactions on*, 29(4):290–302, Apr 1984.

[110] T W. Lee, M. Girolami, and T J. Sejnowski. Independent Component Analysis Using an Extended Infomax Algorithm for Mixed Subgaussian and Supergaussian Sources. *Neural Computation*, 11(2):417–441, Feb. 1999.

[111] P. LeVan. A system for automatic artifact removal in ictal scalp EEG based on independent component analysis and Bayesian classification. Master's thesis, Department of Biomedical Engineering and Montreal Neurological Institute,McGill University, Montréal, Canada, 2006.

[112] R. Li and J C. Principe. Blinking artifact removal in cognitive EEG data using ICA. *Conference Proceedings of the International Conference of IEEE Engineering in Medicine and Biology Society*, 1(3):5273–5276, 2006.

[113] Y. Li, Z. Ma, W. Lu, and Y. Li. Automatic removal of the eye blink artifact from EEG using an ICA-based template matching approach. *Physiological Measurement*, 27(4):425, Mar. 2006.

[114] H. Liang and Z. Lin. Stimulus artifact cancellation in the serosal recordings of gastric myoelectric activity using wavelet transform. *Biomedical Engineering, IEEE Transactions on*, 49(7):681 –688, Jul. 2002.

[115] J. Lin and A. Zhang. Fault feature separation using wavelet-ICA filter. *NDT & E International*, 38(6):421 – 427, Sept. 2005.

[116] L.-G. Lindberg and P.Å. Öberg. Photoplethysmograph from a laser source. *Medical and Biological Engineering and Computing*, 30:568–568, Sept. 1992.

[117] S. Liu, Q. He, R X. Gao, and P. Freedson. Empirical mode decomposition applied to tissue artifact removal from respiratory signal. In *Engineering in Medicine and Biology Society, 2008. EMBS 2008. 30th Annual International Conference of the IEEE*, pages 3624 –3627, Aug. 2008.

[118] S. Mallat and W.L. Hwang. Singularity detection and processing with wavelets. *Information Theory, IEEE Transactions on*, 38(2):617–643, Mar 1992.

[119] S G. Mallat. A theory for multiresolution signal decomposition: the wavelet representation. *IEEE Transactions on Pattern Analysis and Machine Intelligence*, 11:674–693, Jul. 1989.

[120] J. Malmivuo and R. Plonsey, editors. *Bioelectromagnetism - Principles and Applications of Bioelectric and Biomagnetic Fields*. Oxford University Press, New York, 1995.

[121] D G. Manolakis, V K. Ingle, and S M. Kogon. *Statistical and Adaptive Signal Processing*. McGraw-Hill Science/Engineering/Math, 1999.

[122] C. Marque, C. Bisch, R. Dantas, S. Elayoubi, V. Brosse, and C. Pérot. Adaptive filtering for ECG rejection from surface EMG recordings. *Journal of Electromyography and Kinesiology*, 15(3):310 – 315, Jun. 2005.

[123] J. Mathews and S. Douglas. *Adaptive Filters*. Prentice Hall PTR, 2009.

[124] R. Matthews, P.J. Turner, N. J. McDonald, K. Ermolaev, T. Mc Manus, R.A. Shelby, and M. Steindorf. Real time workload classification from an ambulatory wireless EEG system using hybrid EEG electrodes. *Engineering in Medicine and Biology Society, 2008. EMBS 2008. 30th Annual International Conference of the IEEE*, pages 5871–5875, Aug. 2008.

[125] P S. Maybeck. *Stochastic models, estimation, and control*, volume 141 of *Mathematics in Science and Engineering*. 1979.

[126] K. McMorrow and W. Roeger. *The economic consequences of ageing populations: A comparison of the EU, US and Japan.* CECA, May 2012.

[127] Y. Meyer and R.D. Ryan. *Wavelets: Algorithms & Applications.* SIAM, May 1993.

[128] P. Middleton, C. Tang, G. Chan, S. Bishop, A. Savkin, and N. Lovell. Peripheral photoplethysmography variability analysis of sepsis patients. *Medical and Biological Engineering and Computing*, 49:337–347, Mar. 2011.

[129] B. Mijović, M. De Vos, I. Gligorijevic and, J. Taelman, and S. Van Huffel. Source Separation From Single-Channel Recordings by Combining Empirical-Mode Decomposition and Independent Component Analysis. *Biomedical Engineering, IEEE Transactions on*, 57(9):2188 –2196, Sep. 2010.

[130] B. Mijović, M. De Vos, I. Gligorijevic and, and S. Van Huffel. Combining EMD with ICA for extracting independent sources from single channel and two-channel data. In *Engineering in Medicine and Biology Society (EMBC), 2010 Annual International Conference of the IEEE*, pages 5387 –5390, Sep. 2010.

[131] M. Milanesi, N. Martini, N. Vanello, V. Positano, M.F. Santarelli, R. Paradiso, D. De Rossi, and L. Landini. Multichannel Techniques for Motion Artifacts Removal from Electrocardiographic Signals. In *EMBS '06. 28th Annual International Conference of the IEEE*, pages 3391–3394, Sep. 2006.

[132] M. N Milanesi, N Martini, V Vanello, Positano M. F, Santarelli, and L Landini. Independent component analysis applied to the removal of motion artifacts from electrocardiographic signals. *Medical and Biological Engineering and Computing*, 46(3):251–261, Mar. 2008.

[133] T Mildner, D G Norris, C Schwarzbauer, and C J Wiggins. A qualitative test of the balloon model for bold-based mr signal changes at 3t. *Magnetic Resonance in Medicine*, 46(5):891–899, 2001.

[134] M.K. Moaveni. *A Multiple Scattering Field Theory Applied to Whole Blood.* PhD thesis, Dept. of Electrical Engineering, University of Washington, 1970.

[135] A. Mognon, J. Jovicich, L. Bruzzone, and M. Buiatti. ADJUST: An automatic EEG artifact detector based on the joint use of spatial and temporal features. *Psychophysiology.*, 16, Jul. 2010.

[136] F. Morbidi, A. Garulli, D. Prattichizzo, C. Rizzo, and S. Rossi. Application of Kalman Filter to Remove TMS-Induced Artifacts from EEG Recordings. *Control Systems Technology, IEEE Transactions on*, 16(6):1360 –1366, Nov. 2008.

[137] J. Morlet, G. Arens, E. Fourgeau, and D. Giard. Wave propagation and sampling theory; Part I, Complex signal and scattering in multilayered media. *Geophysics*, 47(2):203–221, 1982.

[138] J. Muhlsteff, O. Such, R. Schmidt, M. Perkuhn, H. Reiter, J. Lauter, J. Thijs, G. Musch, and M. Harris. Wearable approach for continuous ECG - and activity patient-monitoring. In *IEMBS 2004. 26th Annual International Conference of the IEEE*, volume 1, pages 2184–2187, Sept. 2004.

[139] United Nations, editor. *World Population Prospects: The 2008 Revision*. United Nations Publications, 2010.

[140] United Nations. World population ageing 2009. Technical report, Department of Economic and Social Affairs, Oct. 2012.

[141] E Niedermeyer and F. Lopes da Silva. *Electroencephalography: Basic Principles, Clinical Applications and Related Fields*. Lippincot Williams & Wilkins, 1999.

[142] U.S. Department of Commerce. International Data Base (IDB) — World Population. Technical report, June 2010.

[143] U.S. Department of Commerce. U.S. Census Bureau – World POPClock Projection, July 2012–July 2013 data. Technical report, 2012.

[144] Office of the Actuary. National Health Care Expenditures Data, Jan. 2010.

[145] R. Oostenveld and P. Praamstra. The five percent electrode system for high-resolution EEG and ERP measurements. *Clinical neurophysiology*, 112(4):713–719, Apr. 2001.

[146] A V. Oppenheim and G C. Verghese. Introduction to Communication, Control, and Signal Processing. Class notes for 6.011, Massachusetts Institute of Technology, Cambridge, Spring 2010.

[147] S. O'Regan, S. Faul, and W. Marnane. Automatic detection of EEG artefacts arising from head movements using EEG and gyroscope signals. *Medical Engineering & Physics*, (0):–, Sept. 2012.

[148] World Health Organization. *Global status report on noncommunicable diseases 2010*. Apr. 2011.

[149] C. Papadelis, C. Kourtidou-Papadeli, P.D. Bamidis, I. Chouvarda, D. Koufogiannis, E. Bekiaris, and N. Maglaveras. Indicators of Sleepiness in an ambulatory EEG study of night driving. *EMBS '06. 28th Annual International Conference of the IEEE*, pages 6201–6204, Sep. 2006.

[150] J P. Phillips, P A. Kyriacou, D P. Jones, K H. Shelley, and R M. Langford. Pulse oximetry and photoplethysmographic waveform analysis of the esophagus and bowel. *Current Opinion in Anesthesiology*, 21(6):779–783, Dec. 2008.

[151] MD. Prahlow, Nathan D., MD Buschbacher, and Ralph M. An Introduction to Electromyography: An Invited Review. *Journal of Long-Term Effects of Medical Implants*, 13, 2003.

[152] M.A.D. Raya and L.G. Sison. Adaptive noise cancelling of motion artifact in stress ECG signals using accelerometer. In *24th Annual EMBS/BMES Conference , 2002. Proceedings of the Second Joint*, volume 2, pages 1756–1757, 2002.

[153] K. Restom, KJ. Bangen, MW. Bondi, JE. Perthen, and TT. Liu. Cerebral blood flow and bold responses to a memory encoding task: a comparison between healthy young and elderly adults. *Neuroimage*, 37(2):430–9, Aug 2007.

[154] K. Rheinberger, T. Steinberger, K. Unterkofler, M. Baubin, A. Klotz, and A. Amann. Removal of CPR Artifacts From the Ventricular Fibrillation ECG by Adaptive Regression on Lagged Reference Signals. *Biomedical Engineering, IEEE Transactions on*, 55(1):130 –137, Jan. 2008.

[155] F. C. Robertson, T. S. Douglas, and E. M. Meintjes. Motion Artifact Removal for Functional Near Infrared Spectroscopy: A Comparison of Methods. *Biomedical Engineering, IEEE Transactions on*, 57(6):1377 –1387, Jun. 2010.

[156] G. Robertson, G. Caldwell, J. Hamill, G. Kamen, and S. Whittlesey. *Research Methods in Biomechanics*. 2004.

[157] J A. Robichaud, K D. Pfann, C L. Comella, and D M. Corcos. Effect of medication on EMG patterns in individuals with Parkinson's disease. *Movement Disorders*, 17:950–960, 2002.

[158] M Rohalova, P Sykacek, M Koska, and G. Dorffner. Detection of the EEG Artifacts by the Means of the (Extended) Kalman Filter. *Measurement Science Review*, 1:59–62, 2001.

[159] S N. Roper and R L. Gilmore. Orbitofrontal resections for intractable partial seizures. *Journal of Epilepsy*, 8(2):146 – 152, 1995.

[160] O A. Rosso, A. Figliola, J. Creso, and E. Serrano. Analysis of wavelet-filtered tonic-clonic electroencephalogram recordings. *Medical & Biological Engineering & Computing*, 42:516–523, Jul. 2004.

[161] R. Sameni, M.B. Shamsollahi, C. Jutten, and M. Babaie-Zadeh. Filtering noisy ECG signals using the extended kalman filter based on a modified dynamic ECG model. In *Computers in Cardiology, 2005*, pages 1017 –1020, 2005.

[162] R. Sameni, M.B. Shamsollahi, C. Jutten, and G.D. Clifford. A Nonlinear Bayesian Filtering Framework for ECG Denoising. *Biomedical Engineering, IEEE Transactions on*, 54(12):2172 –2185, Dec. 2007.

[163] A. Schlögl, C. Keinrath, D. Zimmermann, R. Scherer, R. Leeb, and G. Pfurtscheller. A fully automated correction method of EOG artifacts in EEG recordings. *Clinical Neurophysiology*, 118(1):98 – 104, Jan. 2007.

[164] J.M. Schmitt. Optical measurement of blood oxygenation by implantable telemetry. Technical Report G558-15, Stanford, 1986.

[165] J L. Semmlow, editor. *Biosignal and Medical Image Processing, Second Edition.* CRC Press, 2nd edition, 2008.

[166] S. Seyedtabaii and L. Seyedtabaii. Kalman Filter Based Adaptive Reduction of Motion Artifact from Photoplethysmographic Signal. *International Journal of Electronics, Circuits and Systems*, 2(1):31–34, 2008.

[167] K H. Shelley, D H. Jablonka, A A. Awad, R G. Stout, H Rezkanna, and D G. Silverman. What Is the Best Site for Measuring the Effect of Ventilation on the Pulse Oximeter Waveform? *Anesthesia & Analgesia*, 103(2):372–377, Aug. 2006.

[168] S. Shelley, K. Shelley. Pulse Oximeter Waveform: Photoelectric Plethysmography. pages 420–428, 2001.

[169] A. Shoeb, S. Schachter, D. Schomer, B. Bourgeois, S.T. Treves, and J. Guttag. Detecting seizure onset in the ambulatory setting: Demonstrating feasibility. *EMBS 2005. 27th Annual International Conference*, pages 3546–3550, Jan. 2005.

[170] L. Sornmo and P. Laguna. *Electrocardiogram (ECG) signal processing*, volume 2. Wiley, 2006.

[171] J L. Starck, Y. Mouden, J. Bobin, M. Elad, and Donoho D L. Morphological Component Analysis. *Proceedings of SPIE*, 5914, 2005.

[172] C. Starr L. Starr, C. Evers. *Biology: Today and Tomorrow With Physiology.* Yolanda Cossio, 2009.

[173] R. Stevens, T. Galloway, and C. Berka. Integrating EEG Models of Cognitive Load with Machine Learning Models of Scientific Problem Solving. 2006.

[174] Y. Su, A. Wolczowski, M.H. Fisher, G.D. Bell, D. Burn, and R. Gao. Towards an EMG Controlled Prosthetic Hand Using a 3D Electromagnetic Positioning System. *Instrumentation and Measurement Technology Conference, 2005. IMTC 2005. Proceedings of the IEEE*, 1:261–266, May 2005.

[175] T.J. Sullivan, S.R. Deiss, Tzyy-Ping Jung, and G. Cauwenberghs. A brain-machine interface using dry-contact, low-noise EEG sensors. *Circuits and Systems, 2008. ISCAS 2008. IEEE International Symposium on*, pages 1986–1989, May 2008.

[176] K. T. Sweeney, H. Ayaz, T.E. Ward, M. Izzetoglu, S.F. McLoone, and B. Onaral. A methodology for validating artifact removal techniques for fNIRS. In *Engineering in Medicine and Biology Society,EMBC, 2011 Annual International Conference of the IEEE*, pages 4943 –4946, Sep. 2011.

[177] K. T. Sweeney, H. Ayaz, T.E. Ward, M. Izzetoglu, S.F. McLoone, and B. Onaral. A Methodology for Validating Artifact Removal Techniques for Physiological Signals. *Information Technology in Biomedicine, IEEE Transactions on*, 16(5):918 –926, Sep. 2012.

[178] K T. Sweeney, D. Kelly, T. Ward, and S. McLoone. A Review of the State of the Art in Artifact Removal Technologies as used in an Assisted Living Domain. In *IET Conference on Assisted Living 2011*, pages 1–6, Apr. 2011.

[179] K T. Sweeney, D.J. Leamy, T.E. Ward, and S. McLoone. Intelligent artifact classification for ambulatory physiological signals. In *Engineering in Medicine and Biology Society (EMBC), 2010 Annual International Conference of the IEEE*, pages 6349 –6352, Sep. 2010.

[180] K T. Sweeney, T. Ward, and S. McLoone. A simple bio-signals quality measure for in-home monitoring. In *Proceedings of the 7th IASTED International Conference*. IASTED, Feb. 2010.

[181] K. T. Sweeney, T.E. Ward, and S.F. McLoone. Artifact Removal in Physiological Signals -Practices and Possibilities. *Information Technology in Biomedicine, IEEE Transactions on*, 16(3):488 –500, May 2012.

[182] K.T. Sweeney, S.F. McLoone, and T.E. Ward. The Use of Ensemble Empirical Mode Decomposition With Canonical Correlation Analysis as a Novel Artifact Removal Technique. *Biomedical Engineering, IEEE Transactions on*, 60(1):97 – 105, Jan. 2013.

[183] H. Tamura, M. Omori, and M. Choui. NIRS trajectories in Oxy-Deoxy Hb plane and the trajectory map to understand brain activities related to human interface.

In *Proceedings of the 2007 conference on Human interface: Part I*, pages 994–1003, 2007.

[184] G. Tang and A. Qin. ECG De-noising Based on Empirical Mode Decomposition. In *Young Computer Scientists, 2008. ICYCS 2008. The 9th International Conference for*, pages 903 –906, Nov. 2008.

[185] A.R. Teixeira, A.M. Tome, E.W. Lang, P. Gruber, and A. Martins da Silva. Automatic removal of high-amplitude artefacts from single-channel electroencephalograms. *Computer Methods & Programs in Biomedicine*, 83(2):125–138, Aug. 2006.

[186] N.V. Thakor and Y.-S. Zhu. Applications of adaptive filtering to ECG analysis: noise cancellation and arrhythmia detection. *Biomedical Engineering, IEEE Transactions on*, 38(8):785–794, Aug. 1991.

[187] A Theis, F J. Meyer-Bäse. *Biomedical Signal Analysis - Contemporary Methods and Applications.* MIT Press, 2010.

[188] D.A. Tong, K.A. Bartels, and K.S. Honeyager. Adaptive reduction of motion artifact in the electrocardiogram. In *24th Annual EMBS/BMES Conference, 2002. Proceedings of the Second Joint*, volume 2, pages 1403–1404, 2002.

[189] Information Unit. Population and Population Projections. Technical report, An Roinn Slainte (Department of Health), 2010.

[190] S P. van den Broek, F. Reinders, M. Donderwinkel, and M J. Peters. Volume conduction effects in EEG and MEG. *Electroencephalography and Clinical Neurophysiology*, 106(6):522 – 534, Jun. 1998.

[191] M A C. van Rijn, A. Peper, and C. A. Grimbergen. High-quality recording of bioelectric events. Part 1. Interference reduction, theory and practice. *Medical & Biological Engineering & Computing*, 28(5):389–97, Sep. 1990.

[192] C. Vaya, J.J. Rieta, C. Sanchez, and D. Moratal. Convolutive blind source separation algorithms applied to the electrocardiogram of atrial fibrillation: Study of performance. *Biomedical Engineering, IEEE Transactions on*, 54(8):1530 –1533, Aug. 2007.

[193] R. Vigario, J. Sarela, V. Jousmiki, M. Hamalainen, and E. Oja. Independent component approach to the analysis of EEG and MEG recordings. *Biomedical Engineering, IEEE Transactions on*, 47(5):589 –593, May 2000.

[194] FC. Viola, J. Thorne, B. Edmonds, T. Schneider, T. Eichele, and S. Debener. Semi-automatic identification of independent components representing EEG artifact. *Clinical Neurophysiology*, 120(5):868–877, May 2009.

[195] A. Vorobyov, S. Cichocki. Blind noise reduction for multisensory signals using ICA and subspace filtering, with application to EEG analysis. *Biological cybernetics*, 86(4):293–303, Apr. 2002.

[196] J S. Walker. *Fast Fourier Transforms*. CRC Press, Aug 1996.

[197] Q. Wang, D.Y. Chen, and Y.T. Zhang. Motion Artifact Reduction In Photoplethysmography Utilizing Empirical Mode Decomposition Method. 2010.

[198] E. Waterhouse. New horizons in ambulatory electroencephalography. *Engineering in Medicine and Biology Magazine, IEEE*, 22(3):74–80, May-Jun. 2003.

[199] P. Wei, R. Guo, J. Zhang, and Y.T. Zhang. A new wristband wearable sensor using adaptive reduction filter to reduce motion artifact. In *Technology and Applications in Biomedicine, 2008. ITAB 2008. International Conference on*, pages 278–281, May 2008.

[200] G. Welch and G. Bishop. An introduction to the Kalman filter. Technical report, 2006.

[201] M E. Widrow, B. Hoff. Adaptive Switching Circuits. In *IRE WESCON Convention Record*, pages 96–104, 1960.

[202] N. Wiener. *Extrapolation, Interpolation, and Smoothing of Stationary Time Series*. New York: Wiley, 1949.

[203] J R. Wolpaw and D J. McFarland. Control of a two-dimensional movement signal by a noninvasive brain-computer interface in humans. *Proceedings of the National Academy of Sciences of the United States of America*, 101(51):17849–17854, Dec. 2004.

[204] L.B. Wood and H.H. Asada. Noise Cancellation Model Validation for Reduced Motion Artifact Wearable PPG Sensors Using MEMS Accelerometers. In *Engineering in Medicine and Biology Society, 2006. EMBS '06. 28th Annual International Conference of the IEEE*, pages 3525–3528, Sep. 2006.

[205] Z. Wu and N E. Huang. Ensemble Empirical Mode Decomposition: a Noise-Assisted Data Analysis Method. *Advances in Adaptive Data Analysis*, 1(1):1–41, 2009.

[206] A. Yamazaki, T. Tajima, and K. Matsuoka. Convolutive independent component analysis of EEG data. In *SICE 2003 Annual Conference*, volume 2, pages 1227 –1231, Aug. 2003.

[207] G. Yang, J. Chen, H. Tenhunen, and LR. Zheng. Intelligent electrode design for long-term ECG monitoring at home: Prototype design using FPAA and FPGA. In *Pervasive Computing Technologies for Healthcare, 2009. PervasiveHealth 2009. 3rd International Conference on*, pages 1 –4, Apr. 2009.

[208] N. Yeung, R. Bogacz, C. B. Holroyd, and J. D. Cohen. Detection of synchronized oscillations in the electroencephalogram: An evaluation of methods. *Psychophysiology*, 41:822–832, Nov. 2004.

[209] N. Yeung, R. Bogacz, C B. Holroyd, S. Nieuwenhuis, and J D. Cohen. Theta phase-resetting and the error-related negativity. *Psychophysiology*, 44(1):39–49, Jan. 2007.

[210] X. Yong, R.K. Ward, and G.E. Birch. Artifact removal in EEG using Morphological Component Analysis. In *Acoustics, Speech and Signal Processing, 2009. ICASSP 2009. IEEE International Conference on*, pages 345 –348, Apr. 2009.

[211] X. Yong, R.K. Ward, and G.E. Birch. Generalized Morphological Component Analysis for EEG source separation and artifact removal. In *Neural Engineering, 2009. NER '09. 4th International IEEE/EMBS Conference on*, pages 343 –346, april 2009.

[212] V. Zarzoso and P. Comon. Robust independent component analysis by iterative maximization of the kurtosis contrast with algebraic optimal step size. *Neural Networks, IEEE Transactions on*, 21(2):248 –261, Feb. 2010.

[213] C. Zhao and T. Qiu. An automatic ocular artifacts removal method based on wavelet-enhanced canonical correlation analysis. In *Engineering in Medicine and Biology Society,EMBC, 2011 Annual International Conference of the IEEE*, pages 4191 –4194, Sep. 2011.

[214] M Zia Ur Rahman, R A. Shaik, and D V R K. Reddy. Cancellation of artifacts in ECG Signals using sign based normalized adaptive filtering technique. In *Industrial Electronics & Applications, 2009. ISIEA 2009. IEEE Symposium on*, volume 1, pages 442–445, Oct. 2009.

[215] A.K. Ziarani and A. Konrad. A nonlinear adaptive method of elimination of power line interference in ECG signals. *Biomedical Engineering, IEEE Transactions on*, 49(6):540–547, Jun. 2002.

[216] M. Zibulevsky and B A. Pearlmutter. Blind Separation Of Sources With Sparse Representations In A Signal Dictionary. In *International Workshop on Independent Component Analysis and Blind Source Separation*, pages 86388–2, 2001.

[217] A. Ziehe, G. Nolte, T. Sander, K.-R. Müller, and G. Curio. A comparison of ICA-based artifact reduction methods for MEG. In *12th international conference on Biomagnetism*, pages 895–898, 2000.

[218] M Zima, P Tichavský, K Paul, and V Krajča. Robust removal of short-duration artifacts in long neonatal EEG recordings using wavelet-enhanced ICA and adaptive combining of tentative reconstructions. *Physiological Measurement*, 33(8):N39, Aug. 2012.